

Phosphine- and Indenylidene-Based Z-Selective Ruthenium Olefin Metathesis Catalysts and Catalyst Stability: Decomposition, Olefin Isomerization and Regeneration

Wietse Smit

Thesis for the degree of Philosophiae Doctor (PhD)
University of Bergen, Norway
2019

UNIVERSITY OF BERGEN



**Phosphine- and Indenylidene-Based Z-Selective
Ruthenium Olefin Metathesis Catalysts and Catalyst
Stability: Decomposition, Olefin Isomerization and
Regeneration**

Wietse Smit



Thesis for the degree of Philosophiae Doctor (PhD)
at the University of Bergen

Date of defense: 22.11.2019

© Copyright Wietse Smit

The material in this publication is covered by the provisions of the Copyright Act.

Year: 2019

Title: Phosphine- and Indenylidene-Based *Z*-Selective Ruthenium Olefin Metathesis Catalysts and Catalyst Stability: Decomposition, Olefin Isomerization and Regeneration

Name: Wietse Smit

Print: Skipnes Kommunikasjon / University of Bergen

O sol che sani ogni vista turbata,
tu mi contenti sì quando tu solvi,
che, non men che saver, dubbiar m'aggrata.

Divina Commedia, *Inf.*, XI. 91–93,

DANTE ALIGHIERI

Acknowledgements

First of all, I would like to thank my supervisor Vidar R. Jensen and cosupervisor Giovanni Occhipinti for giving me the opportunity to complete this work in their group. In addition, I would like to acknowledge Marco Foscatto, Julien Engel, Jonas B. Ekeli, Vitali Koudriavtsev and Bartosz Woźniak for their contribution to the papers included in this thesis.

Many thanks go to: Bjarte Holmelid for recording sometimes difficult to obtain mass spectra; Jose Carlos Reyes Guerrero, Jarl Underhaug and Nils Åge Frøystein for their assistance with NMR experiments; Karl W. Törnroos for performing X-ray diffraction measurements and resolving the crystal structures; Erwan Le Roux for his advice on and help with laboratory-related issues; and to Inger Johanne Fjellanger for assistance with the elemental analysis.

I would like to especially thank my fellow office mates, colleagues and friends Maria Del Prado Carrión-Ramirez, Tim Ahnfeldt, Anders Teigland, Coralie C. Quadri, Emily M. MacCready, Iván Flores Linares, Hajar Nsiri, Anna Sobolewska, Lalrempuia Ralte, Sondre H. Hopen Eliasson, Anamitra Chatterjee, Andrey Bezrukov, Breogan Pato Doldan and everybody that I might have forgotten to mention, for creating a good social climate, despite the hardships that eventually arose.

At last, but most certainly not least, I want to thank my husband Stefano for his everlasting support and his help with proofreading this thesis. Meeting you was the best thing Bergen brought me! *“Ti voglio bene!”*

Bergen, July 2019

Wietse Smit

Abstract

This thesis describes the development and synthesis of phosphine-bearing first-generation *Z*-selective olefin metathesis catalysts that give 70–95% of the *Z*-isomer product in homocoupling of terminal alkenes such as allylbenzene, 1-octene, allyl acetate, and 2-allyloxyethanol. Density functional theory (DFT) calculations revealed the importance of sufficient steric interaction between the PR_3 ligand and the bulky 2,4,6-triphenylbenzenethiolate and showed that limiting rotation around the P–Ru bond with chelating anionic phosphine ligands such as *o*-(di-*tert*-butylphosphino)phenolate improves *Z*-selectivity. The most prolific catalyst, $[\text{P}(-6\text{-O-C}_6\text{H}_4)(^t\text{Bu})_2](-\text{S}-2,4,6\text{-Ph-C}_6\text{H}_2)\text{Ru}(\text{=CH}-o\text{-O}^i\text{PrC}_6\text{H}_4)$ (**37**), performs homocoupling metathesis with *Z*-selectivity > 80% with internal olefins such as 1-octene and allylbenzene, and > 90% with allylacetate. In addition, while the catalysts described here are somewhat less active compared to their N-heterocyclic carbene (NHC) bearing second-generation counterparts, they show less substrate and product isomerization and thus higher yields.

The strategy described above was extended to prepare the first *Z*-selective indenylidene-bearing ruthenium catalysts $\text{RuCl}(\text{NHC})(-\text{S}-2,4,6\text{-Ph-C}_6\text{H}_2)(\text{Py})$ - (3-phenylindenylidene) (NHC = IMes = 1,3-bis(2,4,6-trimethylphenyl)imidazol-2-ylidene (**40**) or SIMes = 1,3-bis(2,4,6-trimethylphenyl)-4,5-dihydroimidazol-2-ylidene (**42**)). Together with showing *Z*-selectivity, these catalysts were envisaged to combine two additional desirable properties: improved thermal stability, via substitution of the traditional benzylidene moiety for 3-phenylindenylidene; and fast initiation of olefin metathesis, by using pyridine as stabilizing donor ligand. Interestingly, the molecular structures obtained from X-ray diffraction show that steric pressure resulting from the three bulky ligands (the NHC, the arylthiolate, and the indenylidene) forces the thiolate ligand to position itself *trans* to the NHC ligand, a configuration thought as being incompatible with *Z*-selectivity or high catalytic activity. To our surprise, these new complexes turn out to initiate rapidly,

even at room temperature. Furthermore, they offer up to 80% *Z*-selectivity in homocoupling of a range of 1-alkenes and are relatively stable in catalysis (TONs up to 2200). Unfortunately, despite the presence of the indenylidene ligand, thermal stability is rather poor. DFT calculations show that pyridine dissociates easily, explaining the fast initiating character. Furthermore, the 14-electron complex, obtained after pyridine dissociation, isomerizes to yield the active species; in here, the thiolate is, analogue to other monothiolate-based *Z*-selective catalysts, found *trans* w.r.t. to Cl.

Catalyst decomposition, to species that promote double-bond migration of the substrate and product, is responsible for undesired by-products observed in metathesis experiments. Although this is an important problem, the pathways that lead to catalyst decomposition are not well understood, especially those that originate in intermediates of the olefin metathesis catalytic cycle. Here, using DFT calculations, the Hoveyda–Grubbs second-generation catalyst was decomposed with allylbenzene via ring expansion of the metallacyclobutane intermediate. This facile decomposition pathway leads to loss of the alkylidene ligand and formation of spin-triplet 12-electron complex (SIMes)RuCl₂ (**³R21**). DFT calculations predicted this to be a key species to double-bond migration: upon direct reaction with the substrate, the η^3 -allyl mechanism is entered, while spin inversion to **R21**, followed by formation of a cyclometalated Ru-hydride complex, activates the hydride mechanism. Synthesis of *p*-cymene-stabilized **R21** (**44**) allowed for experimental confirmation of the computational predictions. Catalytic testing showed that, under conditions that promote dissociation of *p*-cymene, alkene isomerization is favoured. Furthermore, trends in the selectivities towards metathesis and isomerization are shared between Hoveyda–Grubbs second-generation catalyst and **44**, indicating that the same reaction network applies to both of them.

The loss of the alkylidene moiety was presumed to be irreversible; yet, when alkylidene-free **44** or its congeners are reacted with olefins, metathesis products are observed. With the alkylidene being a prerequisite to perform olefin metathesis, *in situ* regeneration is implied. DFT calculations suggest dinuclear ruthenium activation of alkene as a viable pathway. Moreover, we experimentally prove that ruthenium alkylidenes can be generated from **44** and catalyst poison ethene.

List of Publications

Paper I

“Phosphine-Based *Z*-Selective Ruthenium Olefin Metathesis Catalysts”

Wietse Smit, Vitali Koudriavtsev, Giovanni Occhipinti, Karl W. Törnroos, and Vidar R. Jensen

Organometallics **2016**, 35, 1825–1837

Paper II

“Loss and Reformation of Ruthenium Alkylidene: Connecting Olefin Metathesis, Catalyst Deactivation, Regeneration, and Isomerization”

Julien Engel, Wietse Smit, Marco Foscato, Giovanni Occhipinti, Karl W. Törnroos, and Vidar R. Jensen

Journal of the American Chemical Society **2017**, 139, 16609–16619

Paper III

“Reviving Metathesis: Ethylene-Triggered Formation of Ruthenium Alkylidene from Decomposed Catalyst”

Wietse Smit, Giovanni Occhipinti, and Vidar R. Jensen

Submitted to the *Journal of the American Chemical Society*, currently under revision.

Paper IV

“*Z*-Selective Ru-Indenylidene Olefin Metathesis Catalysts with Remarkable Structural Features”

Wietse Smit, Giovanni Occhipinti, Jonas B. Ekele, Bartosz Woźniak, Karl W. Törnroos and Vidar R. Jensen

Manuscript to be submitted to *Organometallics*.

Abbreviations

AAc	Allyl acetate
AB	Allylbenzene
ADMET	Acyclic diene metathesis
AOE	2-Allyloxyethanol
AQ	Acquisition time
ATMS	Allyltrimethylsilane
CM	Cross-metathesis
Cy	Cyclohexyl
DBM	Double-bond migration
DCM	Dichloromethane
DEDAM	Diethyl diallylmalonate
DFT	Density functional theory
GC	Gas chromatography
HC	Homocoupling
IMes	1,3-Bis(2,4,6-trimethylphenyl)imidazol-2-ylidene
LPV	Low-pressure/vacuum
MCB	Metallacyclobutane
Mes	Mesitylene, 2,4,6-trimethylbenzene
NHC	N-Heterocyclic carbene
OCT	1-Octene
PB	4-Phenyl-1-butene
PPA	Phenylphosphoric acid
qNMR	Quantitative NMR
QUI	2,6-Dichloro-1,4-benzoquinone
RCB	Ruthenacyclobutane
RCM	Ring-closing metathesis
ROCM	Ring-opening/cross-metathesis

ROM	Ring-opening metathesis
ROMP	Ring-opening metathesis polymerization
RT	Room temperature
RuNPs	Ruthenium nanoparticles
SIMes	1,3-Bis(2,4,6-trimethylphenyl)-4,5-dihydroimidazol-2-ylidene
TCPO	Tricyclohexylphosphine oxide
THF	Tetrahydrofuran
TOF	Turnover frequency
TON	Turnover number

Contents

Acknowledgements	v
Abstract	vii
List of Publications	ix
Abbreviations	xi
1 Introduction	1
1.1 Aim of the Thesis	2
1.2 Outline of the Thesis	4
2 Discovery and Initial Development	5
2.1 Hérisson–Chauvin Mechanism	6
2.2 Well-Defined Olefin Metathesis Catalysts	7
2.2.1 From Free to Metal-Bound Carbenes	7
2.2.2 Schrock-Type Olefin Metathesis Catalysts	9
2.2.3 Grubbs-Type Olefin Metathesis Catalysts	10
2.2.4 Mechanism of Ru-Catalyzed Olefin Metathesis	13
2.2.5 Activity of First- vs. Second-Generation Catalysts	15
3 Selectivity in Olefin Metathesis	17
3.1 Enabling Z-Selectivity	18
3.2 The Origin of Z-Selectivity	20
4 Catalyst decomposition	25
4.1 Isomerization	25
4.2 Ruthenium Hydrides	27
4.3 Ruthenium Nanoparticles	30

4.4	Substrate-Induced Decomposition	30
5	Methods	35
5.1	Synthesis of Organometallic Compounds	35
5.2	Quantitative NMR	36
5.3	Generation of Ethene	37
5.4	Reduction of the NMR-Tube Headspace	38
6	Z-Selective First-Generation Catalysts	39
6.1	Monodentate Phosphine Ligands	39
6.2	Restricting Phosphine Rotation	43
6.3	Reducing the Size of the P–O Chelate	45
6.4	Different Reaction Conditions	50
7	Z-Selective Ru-Indenylidene Catalysts	53
7.1	Catalyst Synthesis	53
7.2	Performance in Catalysis	57
7.3	Computational Investigation	59
8	Ru-Alkylidene Loss and Isomerization	61
8.1	Evaluation of Known Mechanisms	62
8.2	Decomposition via RCB Ring-Expansion	62
8.3	Identifying a Key Isomerization Culprit	63
8.3.1	The Allylic Isomerization Cycle	64
8.3.2	C-H Bond Activation and the Hydride Cycle	66
8.4	Experimental Verification of the Predictions	66
8.4.1	Synthesis of the Precatalyst	68
8.4.2	Experimental Evaluation in Allylbenzene	68
9	Ru-Alkylidene Regeneration	73
9.1	Dinuclear Ruthenium Alkene Activation	73
9.2	Ethene-Triggered Ru-Alkylidene Formation	74
9.2.1	Propene as Ru-Methylidene Indicator	75
9.2.2	Ru-Alkylidene Formation at Higher Temperature	77
9.2.3	Decomposition of G-II _m	80
9.2.4	Notable Differences w.r.t. Temperature	81
9.2.5	Regenerated Catalyst in Olefin Metathesis	81

CONTENTS	xv
Conclusions	83
Outlook to the Future	87
References	89
Paper I	99
Paper II	115
Paper III	129
Paper IV	137
Paper I: Supporting Information	147
Paper II: Supporting Information	167
Paper III: Supporting Information	227
Paper IV: Supporting Information	275

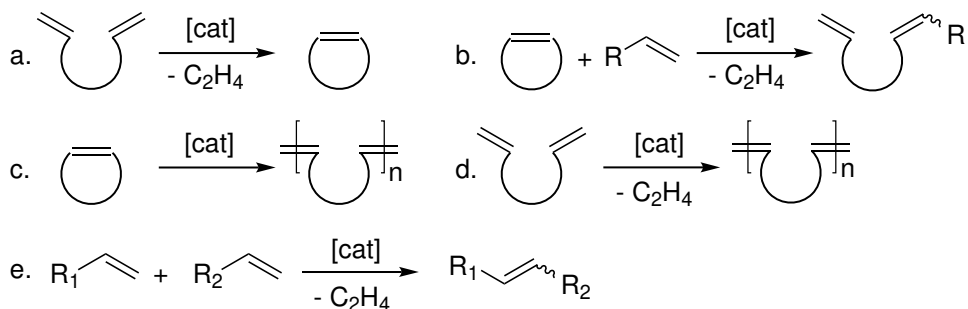
Chapter 1

Introduction

The ability to form carbon–carbon double bonds is of utmost importance in organic and polymer chemistry. However, traditional methods for the preparation of unsaturated compounds used in organic synthesis, such as the Wittig, Corey–Winter, Ramberg–Bäcklund, Julia–Lythgoe, and Peterson olefination reactions, frequently require the presence of specific functional groups. Moreover, toxic and highly-reactive reagents (Na/Hg, CCl₂S, KH, BuLi, etc.) need to be used. These classical methods involve multiple steps and require tedious workup to obtain the end-product; this generates an excessive amount of waste, containing organic and inorganic P, S, Si, and Hg compounds.

Olefin metathesis provides us with the ability to form C=C bonds in a relatively clean and efficient way, releasing only ethene or other olefins and allowing the construction of complex organic molecules. This makes olefin metathesis a powerful and irreplaceable tool in the synthesis of natural products^{1–3} that are often supposed to be medicinally active in battling cancers, neurological diseases, and infections. Furthermore, many different polymers^{4,5} are synthesized with olefin metathesis, and the reaction has also found its niche in oleochemistry.⁶ Application in the synthesis of insect sex pheromones yields green, nontoxic and environmentally friendly pesticides.⁷

Although technically regarded as one single chemical reaction, olefin metathesis can generally be divided into different subreactions (Scheme 1). For instance, ring-closing metathesis (RCM) is an essential step in the synthesis of biologically active spirocyclic isoindoles that have been identified as neuroprotective and anticancer agents.⁸ Going in the reverse direction, ring-opening metathesis (ROM) converts cyclic alkenes back into linear dienes.^{9,10} Electro-active polymer networks, used in sensors, flexible electronics and in applications where electrochromism is desired,

Scheme 1: Different subtypes of the olefin metathesis reaction.^a

^a**a.** ring-closing metathesis (RCM), **b.** ring-opening metathesis (ROM), **c.** ring-opening metathesis polymerization (ROMP), **d.** acyclic diene metathesis (ADMET), **e.** homocoupling (HC)/self-metathesis ($\text{R}_1 = \text{R}_2$), cross-metathesis ($\text{R}_1 \neq \text{R}_2$).

can be obtained through ring-opening metathesis polymerization (ROMP) of unsaturated ring systems.^{11,12} Moreover, this type of reaction is commercially used to produce large amounts of polymers such as Vestenamer[®], Norsorex[®], Telene[®], Pentam[®], Zeonex[®] and Metton[®].¹³

Products such as polymers and macrocycles can also be obtained from linear dienes through acyclic diene metathesis (ADMET).^{14–17} Cross-metathesis (CM), the coupling of two different linear alkenes, has been used in the synthesis of (+)-aspicilin, a natural product found in lichen from the *Lecanoraceae* family;¹⁸ in addition, carbon-carbon coupling of two equivalents of the same linear alkene is known as homocoupling (HC) or self-metathesis. In ethenolysis an internal alkene is reacted with ethene to obtain primary alkenes; for instance, in the production of neohexene, an intermediate in the synthesis of synthetic musk.¹³

Other industrial processes in which olefin metathesis plays an important role are: the Shell higher olefins process (SHOP), yielding C_{11} – C_{14} internal alkenes from ethene via a combination of oligomerization, double-bond isomerization and olefin metathesis; the OCT process, in which ethene and 2-butene are converted to propene; and the Phillips triolefin process, essentially the OCT process in reverse direction.¹³

1.1 Aim of the Thesis

The purpose of this thesis is to explore whether the design of *Z*-selective ruthenium-based olefin metathesis catalysts, developed by Jensen and co-workers,^{19,20} can be expanded successfully: in **Paper I** the possibility of obtaining *Z*-selective

first-generation catalysts is investigated. Up to that point, practically all known ruthenium-based *Z*-selective catalysts were derived from second-generation parents; regrettably, because first-generation catalysts have the advantage of being less prone to double-bond migration (DBM) and secondary metathesis reactions.^{21,22} This, and the possibility to obtain additional insight into the factors that determine selectivity and other catalyst properties, were key motivators for this paper.

The higher thermal stability of Ru-indenylidene catalysts, compared to those based on benzylidene,²³ stimulated us to use the same technique, i.e. exchanging one of the anionic ligands for a large aryl thiolate, to obtain a novel branch of *Z*-selective catalysts. This work, represented by **Paper IV**, also investigates the influence of pyridine on the selectivity and uses calculations to explain why the remarkable solid-state structures of the catalysts are *Z*-selective at all.

Catalyst decomposition leads to ruthenium species that promote double-bond migration (isomerization) which may compete with olefin metathesis, compromising selectivity and yield. In addition, *Z/E* isomerization strongly diminishes the yield of *Z*-olefin in reactions with *Z*-selective catalysts. Possible culprits, such as ruthenium hydrides and nanoparticles, give only a partial explanation: ruthenium hydrides were found to be of only low isomerization activity and ruthenium nanoparticles seem at best to account for only 50% of the total substrate isomerization during olefin metathesis.^{21,24} Moreover, the pathways that lead to the formation of these nanoparticles and to the isomerization-active molecular species remained unknown. In **Paper II**, the lack of a proper explanation for the observed double-bond migration activity stimulated exploration of new substrate-induced catalyst decomposition pathways, which resulted in elucidation of substrate isomerization mechanisms and identification of isomerization-active molecular species.

Observation of olefin metathesis activity with compounds that do not possess the minimum requirements for catalysts that normally perform this reaction inspired the work in **Paper III**. More importantly, the possibility that decomposed catalyst could be resurrected by ethene, a known olefin metathesis catalyst poison, was a key motivator for this paper.

1.2 Outline of the Thesis

Chapter 2 gives an overview of the discovery and historical development of olefin metathesis, from the earliest observation of this reaction and postulation of the Hérisson–Chauvin mechanism, to well-defined catalysts. Henceforth, after a short discussion of the tungsten- and molybdenum-based systems developed by Schrock, this chapter focuses on the characteristics and mechanistic aspects of Grubbs-type ruthenium-based olefin metathesis catalysts. The development of olefin metathesis catalysts that display selectivity towards the *Z*-product olefin is discussed in *Chapter 3*. In addition, theoretical studies are used to explain the origin of *Z*-selectivity. In *Chapter 4*, the problem involving catalyst decomposition and double bond migration are explored, including different suspects such as ruthenium hydrides and ruthenium nanoparticles. Nonstandard experimental methods used to obtain the results in **Paper I–Paper IV** are found in *Chapter 5*.

Following this, *Chapters 6–9* contain a summary of the main results: the development of *Z*-selective first-generation catalysts (**Paper I**) in *Chapter 6*; the novel *Z*-selective ruthenium-indenylidene catalysts (**Paper IV**) in *Chapter 7*; ruthenium alkylidene loss and isomerization (**Paper II**) in *Chapter 8*; and finally *Chapter 9* describes ruthenium alkylidene regeneration (**Paper II** and **Paper III**).

Discussion of the papers is followed by general *Conclusions* and an *Outlook to the Future*. After the *References*, the *Papers* used in this manuscript are attached, together with their respective *Supporting Information*.

Chapter 2

Discovery and Initial Development

Throughout the 1950s and 1960s several independent groups observed an unknown chemical reaction: olefinic products both of higher and lower molecular weight were observed when asymmetric unsaturated hydrocarbons were led over molybdenum on alumina.^{25,26} Shortly thereafter, a similar conversion was obtained under homogeneous conditions.²⁷ Formation of these products can only be explained if one imagines the C=C bond in substrate olefins being “cut-in-half”, followed by scrambling of the resulting fragments before they are “glued” together again; subsequently, this reaction was dubbed “olefin metathesis” (Gr. *μετάθεσις* = to transpose), and efforts to elucidate its reaction mechanism soon commenced.

Through careful analysis of the products obtained with several different substrate combinations,^{28,29} combined with deuterium and carbon-14 labeling of the substrate,^{30–32} a “quasi-cyclobutane” species was suggested to be the key intermediate in the reaction mechanism. While this explained the distribution of isotope labels and the obtained products, existence of this intermediate was difficult to comprehend, since it would imply a [2 + 2] cycloaddition of two olefins, which is forbidden according to the Woodward–Hoffmann rules. Thus, to make this reaction allowed, the “quasi-cyclobutane” would somehow have to be coordinated to the metal;^{30,33} however, cyclobutane does not have any free valences available to achieve this. In addition, cyclobutane was absent in the reaction mixtures of metathesis experiments, and it is not accepted as substrate either;³³ moreover, the product distribution and kinetics observed in ROM remained unexplained.^{34,35}

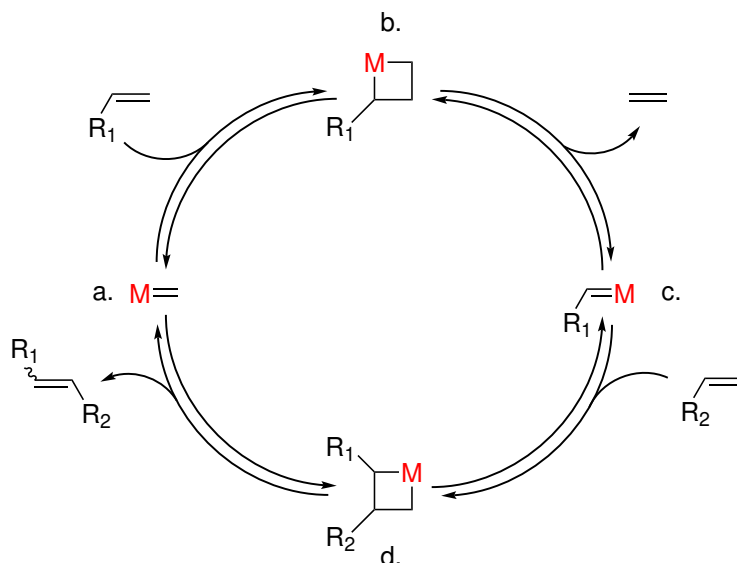
Eventually, based on existing literature,^{25,36,37} Chauvin and Hérisson postulated that a metal-carbene, or more specifically a metal-alkylidene, plays a key role in olefin metathesis.³⁴

2.1 Hérissou–Chauvin Mechanism

Hérissou and Chauvin proposed a mechanism based on the $[2 + 2]$ cycloaddition between an alkene and metal-alkylidene.³⁴ Today, this essentially constitutes the generally accepted mechanism for olefin metathesis: first, reaction of an initial metal-methylidene complex (**a.**, Scheme 2) with a molecule of substrate gives a monosubstituted metallacyclobutane (MCB, **b.**); subsequently, this MCB collapses via a $[2 + 2]$ retro-addition forming a metal-alkylidene and releasing ethene (**c.**). Following this, reaction with an additional equivalent of substrate affords disubstituted MCB **d.**; the ensuing MCB collapse releases the product olefin and regenerates the initial metal-methylidene complex (**a.**).

Because two new C=C bonds are formed at the cost of breaking two other C=C bonds, the olefin metathesis reaction is essentially thermoneutral, with the exception of ROM(P) and RCM of highly strained substrates: for instance, in ROMP of norbornene, a bridged cyclic alkene, energy is released through relieve

Scheme 2: The Hérissou–Chauvin mechanism for olefin metathesis.^a



^a**a.** initial metal-methylidene complex, **b.** monosubstituted MCB formed after reaction with substrate, **c.** new metal-alkylidene complex formed together with the release of ethene, **d.** disubstituted MCB formed after reaction with an additional equivalent of substrate, followed by product release and regeneration of the initial metal-methylidene complex.

of ring strain.³⁸ In addition, incorporation of ring strain in RCM demands the use of high substrate dilution to make the reaction kinetically favored over other metathesis reactions, such as CM/HC. In general, the driving force of the olefin metathesis reaction is the increase of entropy obtained through the release of small, often gaseous, alkenes such as ethene or propene.

2.2 Well-Defined Olefin Metathesis Catalysts

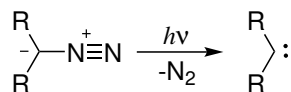
Initially, olefin metathesis was performed with ill-defined mixtures containing salts or complexes of molybdenum (MoO_3), tungsten (WCl_6 , WOCl_4) and rhenium (Re_2O_7) used either homogeneously or heterogeneously (adsorbed on alumina or silica).^{25-27,39} These reactions were performed under harsh conditions and gave mixed results; the yield was often heavily dependent on the use of Lewis acids/alkylating agents as additives (Bu_4Sn , EtAlCl_2 , etc.) that were supposed to function as co-catalysts. Therefore, synthesis and isolation of an alkyl-substituted metal-carbene, and thus a well-defined olefin metathesis catalyst, was required in order to obtain control over the reaction;³⁵ after all, such compounds were proposed by Hérisson and Chauvin as the olefin metathesis initiating species.

2.2.1 From Free to Metal-Bound Carbenes

Carbenes are compounds that possess a neutral divalent sp^2 -hybridized (methylene) carbon atom with six electrons in its valence shell.⁴⁰ Two ground state carbenes exist: singlet and triplet, each having a different electronic structure at the methylene C-atom. Loss of small, stable molecules from precursors is often the driving force behind carbene formation: for instance, through α -elimination of HCl from chloroform,⁴¹ thermal decarboxylation of alkali trichloroacetates (CO_2),⁴² and via photolysis of the C–N bond in diazo compounds (liberating nitrogen gas, Scheme 3).⁴⁰

The singlet carbene has two valence electrons paired up in a nonbonding sp^2 -orbital; the remaining p-orbital remains empty and is available for π -overlap with lone-pairs on substituents (**a.**, Figure 1).^{40,41} This, and inductive electron withdrawal from the sp^2 -orbital by electronegative α -substituents, stabilize the singlet carbene; therefore, they are generally found when heteroatoms are present at the α -position, such as with $-\text{X}$, $-\text{OR}$, $-\text{SR}$, $-\text{SR}_3$, $-\text{NR}_2$, $-\text{PR}_2$, etc.⁴⁰ When the

Scheme 3: Example of carbene synthesis through photolysis or thermolysis of diazo compounds.



methylene carbon is, for instance, bearing α -alkyl or phenyl groups, the stabilization described above is greatly reduced, and a triplet carbene is obtained, with one electron located on a sp^2 -orbital and another on the p -orbital (**b.**, Figure 1).^{40,41}

Due to this biradical nature, the triplet carbene is much more reactive and difficult to isolate; in addition, larger $\text{R}-\text{C}-\text{R}$ bond angles ($130\text{--}150^\circ$) are observed when compared to singlet carbenes ($100\text{--}110^\circ$): repulsion of the α -substituents from a sp^2 -orbital filled with two electrons is larger than when the electrons are located on different orbitals; thus, the α -substituents are forced closer together in the former than in the latter.⁴¹ Furthermore, a difference in reactivity is observed when carbenes with different spin states are reacted with olefins: singlet carbenes react in a concerted fashion and propagate the alkene geometry into product cyclopropane (stereospecific reaction). However, $\text{C}-\text{C}$ bond rotation, in the two-step reaction observed with triplet carbenes, scrambles product stereochemistry.⁴¹

Most free carbenes are of relatively low stability: therefore, they readily react with organometallic compounds to form carbene complexes with $\text{L}_n\text{M}=\text{CR}_2$ as general formula.⁴³ Generally, coordinated carbenes tend to fall somewhere between two extreme types: the Fischer and Schrock carbene (**c.** and **d.** in Figure 1 respectively); even though these carbene complexes are different entities, there are analogies to free carbenes that can be used in describing the properties of their coordination chemistry.

The Fischer carbene, derived from the singlet carbene, is regarded as L-type ligand: the lone-pair in the sp^2 -orbital of the singlet carbene is an excellent neutral

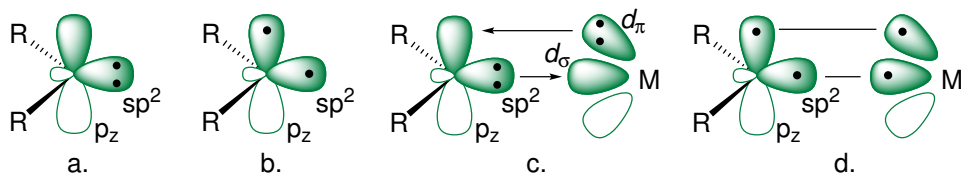


Figure 1: Electronic configuration of the singlet (**a.**), triplet (**b.**), Fischer (**c.**) and Schrock (**d.**) carbene.

two-electron σ -donor; in addition, the empty p-orbital is a π -acceptor which allows stabilization through π -donation from π -donor α -substituents ($-\text{OR}$, $-\text{NR}_2$, etc.) and through a small amount of $\text{M}(d\pi)\rightarrow\text{L}$ back-donation.⁴³ Since middle-to-late transition metals of low oxidation state are suitable for $\text{M}(d\pi)\rightarrow\text{L}$ back-donation, the Fischer carbene is generally found with $\text{Cr}(0)$, $\text{Mo}(0)$, $\text{W}(0)$, $\text{Mn}(0)$, $\text{Fe}(0)$, $\text{Co}(0)$, etc.; these metals are commonly associated with strong π -acceptor ligands, thus explaining why CO is very often found filling up the remaining coordination numbers in Fischer carbene complexes. In conclusion, the $\text{L}\rightarrow\text{M}(d\sigma)$ is much stronger than the $\text{M}(d\pi)\rightarrow\text{L}$. The electron depleted C-atom in the Fischer carbene is regarded as electrophilic.

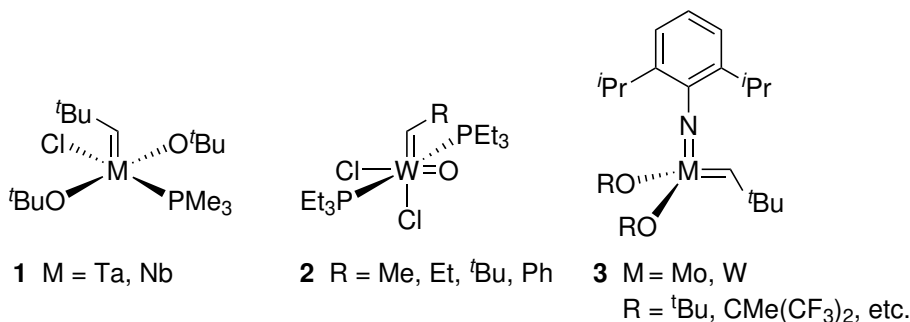
While the $\text{M}-\text{C}$ bond in the Fischer carbene is of a dative nature, that of the Schrock carbene is generally regarded as more covalent: the alkyl substituents on the α -position, analogue to the triplet carbene, are not capable of π -donation. Furthermore, the use of early transition metals with high oxidation states ($\text{Ta}(\text{V})$, $\text{W}(\text{VI})$, $\text{Ti}(\text{IV})$, etc.) in parallel with non- π -donor ligands, such as alkyl and cyclopentadienyl, polarizes the bonds towards the nucleophilic carbene carbon-atom. With the above in mind, the Schrock carbene is generally regarded as two X^- -ligands.

2.2.2 Schrock-Type Olefin Metathesis Catalysts

When Hérisson and Chauvin proposed the reaction mechanism in Scheme 2, only Fischer carbene complexes were known.³⁶ While some of these well-defined compounds show activity in olefin metathesis, the actual active species remained ill-defined;⁴⁴ other Fischer carbene complexes showed formation of cyclopropane derivatives instead of metathesis upon reaction with olefins.⁴⁵

The first Schrock carbene, a thermally stable neopentylidene complex of tantalum [$\text{Ta}(-\text{CH}_2^t\text{Bu})_3(=\text{CH}^t\text{Bu})$], does not readily catalyze olefin metathesis: to obtain an active catalyst, strong π -donors such as *tert*-butoxy or oxo ligands are required, making complexes such as **1** and **2** (Chart 1) the first well-defined olefin metathesis catalysts.^{46,47} Eventually, further development led to a large family of highly active molybdenum- and tungsten-based olefin metathesis catalysts (**3**).⁴⁸⁻⁵¹

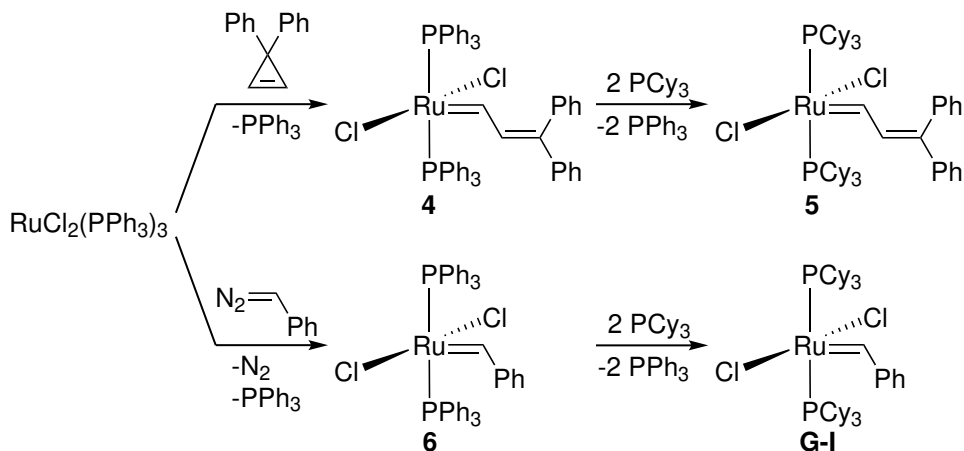
Especially the molybdenum-based catalysts are able to perform metathesis on olefins containing a wide range of functional groups, such as (thio)ethers, esters,

Chart 1: Olefin metathesis catalysts developed by Schrock.

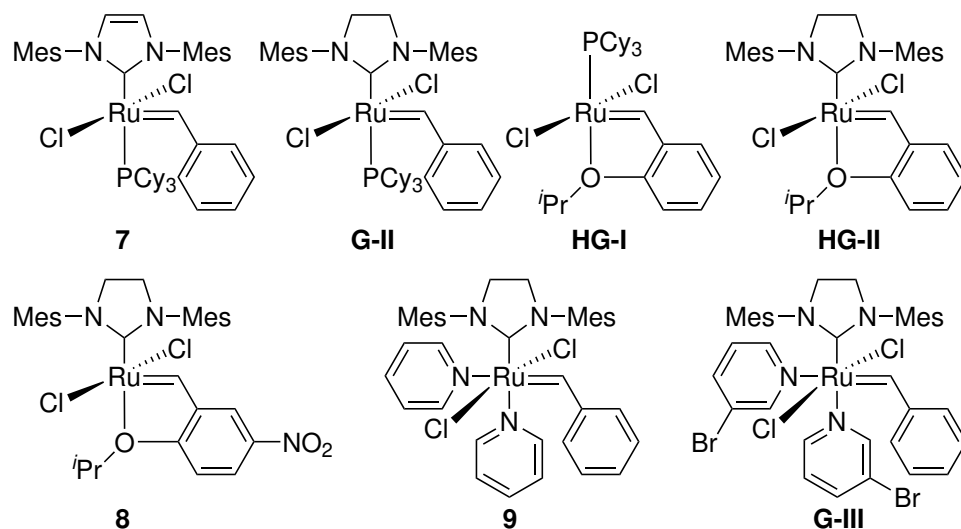
epoxides, acetals, lactams, lactones, nitriles, substituted silanes, carbamates, sulfides, disulfides, and phosphanes.⁵² In addition, free alcohols and tertiary amines can be used when the heteroatom is sufficiently shielded by the steric bulk of the substituents; other unsaturated alcohols, amines, and amides usually require a protecting group. Unfortunately, molybdenum and tungsten possess a very high oxophilicity, being early transition metals. Therefore, special techniques and equipment are required to be able to synthesize, manipulate and store these catalysts under inert atmosphere, excluding oxygen and moisture at any cost. Similarly, incompatibility towards olefins with functional groups such as aldehydes, carboxylic acids, (primary) amines, and most free alcohols often requires thorough purification of the substrate and solvent used.

2.2.3 Grubbs-Type Olefin Metathesis Catalysts

Experiments with ruthenium salts and complexes showed promising results in ROMP of highly strained substrates;^{53–57} moreover, *in situ* use of a carbene precursor enabled ROMP with less-strained substrates.⁵⁸ Isolable and well-defined ruthenium-based olefin metathesis catalysts **4** and **6** (Scheme 4) were obtained through addition of carbene precursors to RuCl₂(PPh₃)₃.^{59–62} Catalytic activity correlates with the basicity of the phosphine ligands (PPh₃ ≪ P^{*i*}Pr₃ < PCy₃): exchange of triphenylphosphine for the more basic tricyclohexylphosphine afforded much more active catalysts **5** and **G-I**. The latter, the most active catalyst from this family, is known for its stability in air and its tolerance to a large spectrum of functional groups, and is commercially available as Grubbs first-generation catalyst.

Scheme 4: Synthesis of well-defined ruthenium-based olefin metathesis catalysts.

Substitution of one or both phosphine ligands in **G-I** was anticipated to yield olefin metathesis catalysts with improved catalytic activity and stability; unfortunately, initial attempts resulted in compounds that decompose easily or lack sufficient catalytic activity.^{63–65} Soon, N-heterocyclic carbenes (NHC) were recognized as excellent candidates for the role as L-spectator ligand: the ability of inducing high electron-density on a metal, caused by strong σ -donation, resembles that of basic phosphine ligands.⁶⁶ However, while substitution of both phosphine moieties in **G-I** gives stable *bis*-NHC complexes, no significant improvement of the catalytic activity was observed.⁶⁷ Density functional theory (DFT) calculations indicated relatively high energies associated with dissociation of the NHC, hampering the formation of the catalytically active 14-electron species.⁶⁸ This was resolved through synthesis of heteroleptic NHC/phosphine ruthenium complexes: again the NHC remains tightly bound to the metal, while the phosphine ligand dissociates relatively easily.⁶⁸ Subsequently, clean phosphine-substitution products were obtained with 2,6-disubstituted aryl groups on the NHC's N-atom;⁶⁹ particularly, with 1,3-bis(2,4,6-trimethylphenyl)imidazol-2-ylidene (IMes) ligand, an active catalyst was obtained (**7**, Chart 2) that retained the stability of parent complex **G-I**.^{69–71} Lack of π -interactions in the saturated NHC-backbone gives the more basic carbene ligand 1,3-bis(2,4,6-trimethylphenyl)-4,5-dihydroimidazol-2-ylidene (SIMes), resulting in a catalyst that shows even higher activity than **7** and is currently commercially available as Grubbs second-generation catalyst (**G-II**).⁷²

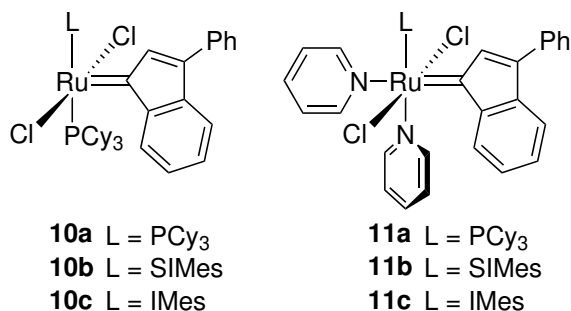
Chart 2: Selection of ruthenium alkylidene-based olefin metathesis catalysts.

Hoveyda–Grubbs first-generation catalyst (**HG-I**), which is easier to purify, recover and recycle, was discovered upon reaction of **G-I** with 2-isopropoxy-styrene.⁷³ In an analogue fashion, the phosphine-free Hoveyda–Grubbs second-generation catalyst **HG-II** is obtained from **G-II**.^{74,75} The chelating styrenyl ligand in these complexes opened up new possibilities in tuning the catalytic properties through variation in substituents on the phenyl group and oxygen-atom: for instance, addition of electron-withdrawing substituents, such as $-\text{NO}_2$ (**8**), on the isopropoxystyrene moiety lowers the electron density on the oxygen atom, weakening the Ru–O bond and reducing the chelating ability. This allowed Grela et al. to perform metathesis efficiently at temperatures as low as 0 °C.⁷⁶

Through reaction of **G-II** with an excess of pyridine, phosphine-free bis-pyridine ruthenium complex **9**, which initiates olefin metathesis much more rapidly than the parent compound, was obtained.⁷⁷ Modification through addition of bromine substituents on the pyridine ligands resulted in the fast-initiating Grubbs third-generation catalyst (**G-III**).⁷⁸

Olefin metathesis catalysts bearing an indenylidene moiety, as alternative to the traditional alkylidene ligand, are displayed in Chart 3. While synthesis of **G-I** and **G-II** requires dangerous and costly chemicals to “install” the alkylidene moiety, such as diazoalkane derivatives (Scheme 4), the cheap and easily available 1,1-diphenylpropargyl alcohol forms the basis for **10a–c** and **11a–c**. Reaction of

Chart 3: Selection of ruthenium indenylidene-based olefin metathesis catalysts.



this alcohol with RuCl₂(PPh₃)₃ was initially believed to give diphenylallenylidene complex RuCl₂(=C=C=CPh₂)(PPh₃)₂;⁷⁹ however, a thorough inspection of previously recorded spectroscopic data and X-ray crystallography showed that rearrangement to a cyclized vinyl carbene or indenylidene complex had taken place.^{23,80} Subsequently, a family of Ru-indenylidene complexes, analogue to first- (**10a**) and second-generation (**10b–c**) Grubbs catalysts, was obtained through substitution of PPh₃ with PCy₃ and various N-heterocyclic carbenes.^{23,80–83} Another motivation for the development of indenylidene-bearing olefin metathesis catalysts is the limited temperature stability of **G-I**, and to a lesser extent of **G-II**. With no signs of decomposition after 10 days of heating at 80 °C in toluene-*d*₈, **10a** and **10c** are indeed thermally much more stable than their benzylidene analogues.²³ Catalysts **10a–c** perform well in the synthesis of complex natural products^{80,82,84–89} and in RCM.^{83,90,91} In addition, **10c** mediates RCM leading to tetrasubstituted cyclic alkenes,^{90,92} which has not been possible with **G-I** and **G-II**. With these catalysts, the formation of trisubstituted alkenes through RCM already proceeds with difficulty.⁹²

In a similar strategy as with the Ru-alkylidene bearing catalysts,⁷⁸ substitution of the remaining phosphine ligand in **10a–c** with pyridine yields fast-initiating bipyridine complexes **11a–c**.^{93,94}

2.2.4 Mechanism of Ru-Catalyzed Olefin Metathesis

The Hérisson–Chauvin cycle in Scheme 2 depicts a simplified image of the mechanism that controls olefin metathesis: activation of the precatalyst, olefin binding, formation of the MCB, product release, etc. depend on the metal and of the lig-

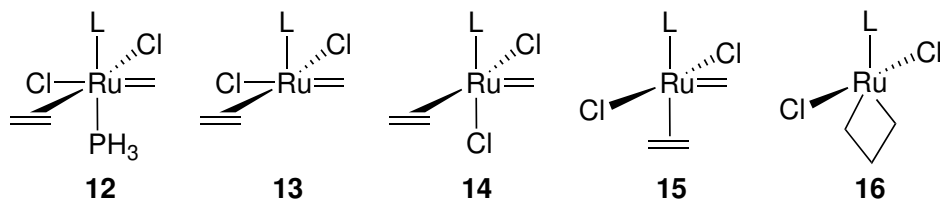
ands bound to it. An array of experimental and theoretical studies gives a good insight in the mechanism with ruthenium-based olefin metathesis catalysts.

Olefin metathesis initiates from the 16-electron precatalyst (Chart 2) through a dissociative pathway; that is, coordination of an olefin is preceded by dissociation of a L-type ligand, such as phosphine, pyridine, or alkoxy moiety, to form an active 14-electron Ru-alkylidene species. In fact, dissociation of the phosphine ligand in **G-I** and **G-II** is relatively facile ($\Delta G = 18\text{--}26 \text{ kcal}\cdot\text{mol}^{-1}$) and barrier-less;^{95–100} moreover, dissociation of the 3-bromopyridine in **G-III** has been shown to be even easier.⁷⁸ Direct coordination of an olefin to a precatalyst, i.e. an associative pathway, would lead to the formation of a hexacoordinate 18-electron complex (**12**, Chart 4); computational studies, performed on model catalysts resembling **G-I** and **G-II**, show that high entropic factors and steric hindrance around ruthenium lead to a very high barrier, making this a highly unlikely activation pathway.^{97,100–102}

Following the formation of a tetracoordinate 14-electron species, the olefin competes with the free L-type ligand to coordinate ruthenium. Coordination of an olefin can theoretically result into three geometrically different π -complexes: the olefin can be *cis* (**13** and **14**), or *trans* (**15**) with respect to the phosphine or NHC.¹⁰⁰ In **13** an unfavorable barrier is connected to *cis*-coordination;¹⁰⁰ the other proposed *cis* or side-bound complex (**14**),¹⁰³ with one of the chloride-ligand *trans* w.r.t. the phosphine or NHC, showed disagreement between the predicted and observed stereoselectivity.¹⁰⁴ The remaining *trans*-coordination (**15**) is barrier-less and thus forms the preferred pathway of olefin coordination.^{100,105}

After olefin binding, [2+2] cycloaddition leads to the formation of a ruthenacyclobutane (RCB). Initially this species was perceived to be a transition state;¹⁰⁶ however, this was rapidly disproven: computational¹⁰⁷ and experimental studies¹⁰⁸

Chart 4: Geometry of olefin complexes using a model catalyst.^a



^aL = PH₃ or imidazol-2-ylidene.

show that the RCB is a real intermediate. Furthermore, it was shown that the kite-shaped and flat RCB is, analogue to the coordinated olefin, located *trans* to the L-type ligand (**16**).¹⁰⁸

2.2.5 Activity of First- vs. Second-Generation Catalysts

For some time the higher catalytic activity observed with second-generation catalysts, compared to their first-generation counterparts, was attributed to the larger *trans*-effect of the stronger σ -donating NHC-ligand,⁹⁸ that is, phosphine dissociation in second-generation catalysts should be easier, leading to more ready formation of the catalytically active 14-electron complex. On the contrary, experimental studies show that phosphine dissociation is actually more facile in first-generation catalysts.⁹⁹ Computations show that steric hindrance of the two phosphines in **G-I** facilitates phosphine dissociation;¹⁰⁹ in addition, steric pressure, caused by the bulky mesitylene substituents of the NHC-ligand, destabilizes the dissociated 14-electron complex, making the second-generation catalysts slower-initiating.

However, rotation around the P–Ru bond at the RCB species, required to avoid unfavourable steric interactions with the two chlorine ligands, is associated with a relatively high barrier and constitutes the rate-limiting step with first-generation catalysts.¹¹⁰ Due to the twofold symmetry of the NHC, no such barrier exists with second-generation catalyst,¹¹⁰ thus offering a partial explanation why **G-II** possesses a higher overall metathesis activity compared to **G-I**.

In addition, the destabilized 14-electron complex, obtained after phosphine dissociation from **G-II**, actually promotes olefin coordination (an essentially irreversible step) and stabilizes the MCB; thus, the barrier of the rate-limiting step in the metathesis reaction is reduced, especially when compared to the huge phosphine rotation barrier associated with **G-I**.^{100,109}

Chapter 3

Selectivity in Olefin Metathesis

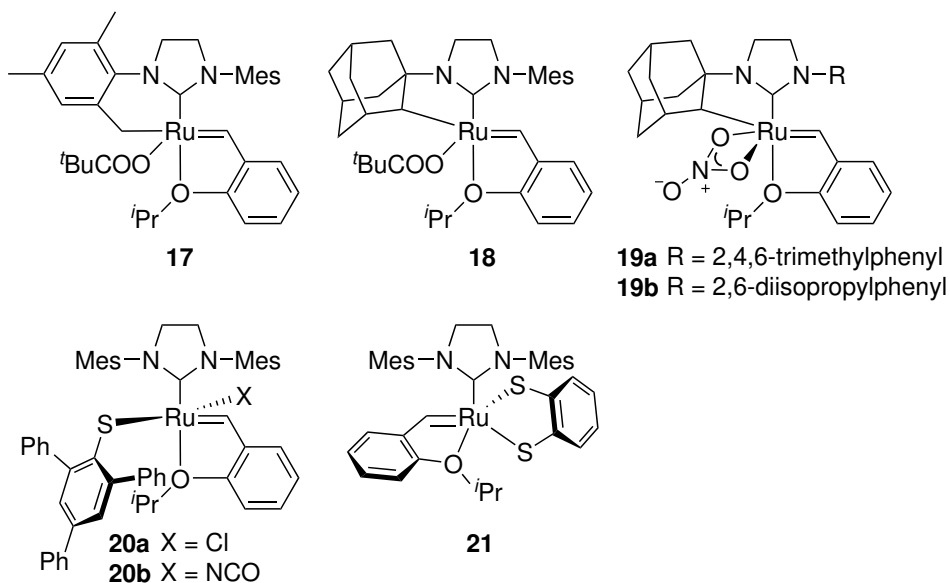
In general, olefin metathesis yields a mixture of two different product stereoisomers: the *E*- and *Z*-olefin. For instance, at conversions < 60% the *E/Z* ratio is ≈ 5 with first-generation catalysts compared to ≈ 3 with second-generation catalysts.^{111–114} Furthermore, at high conversion (> 60%) the *E/Z* ratio increases significantly (> 6). Reversibility of the metathesis reaction leads to a product composition that is time-dependent:¹¹⁵ close to the initiation, a product rich in *Z*-isomer is often observed. This initial “explosive” production of *Z*-product can be explained from kinetic control of the reaction under primary metathesis; that is, the barrier to RCB collapse is lower in the pathway leading to *Z*-product compared to that of the *E*-product.¹¹⁶ Although decoordination of the product olefin is the energetically most uneconomic step in the mechanism, release of the *E*-product is somewhat more facile than that of *Z*-product. Thus, any initially gained π -coordinated *Z*-olefin can, as a consequence of the principle of microscopic reversibility, easily re-enter the catalytic cycle.¹¹⁶ Similarly, re-entry occurs when, as the reaction proceeds and the substrate olefin becomes gradually more depleted, the products starts to compete with the substrate in binding the active catalytic species.¹¹⁷ Altogether, the thermodynamically more stable *E*-product is effectively “trapped” in a thermodynamic well and the reaction mixture will get richer in the *E*-product. Eventually an equilibrium is reached and the *E/Z*-ratio stabilizes at a value that depends roughly on the steric properties of the substrate and the difference in stability between the product isomers (thermodynamic control). Often a higher stability of the *E*-product explains why reaction mixtures are richer in this isomer. However, the difference in thermodynamic stability is often small, resulting in mixtures that are not very useful from a synthetic point

of view when only one of the two isomers is desired, mainly because separation of the two isomers is often quite difficult and costly.¹¹⁵

3.1 Enabling *Z*-Selectivity

Excellent molybdenum and tungsten based *Z*-selective catalysts (up to 98%) were obtained by introducing a significant difference in size between the imido- and aryloxy ligand.^{118–121} However, like their nonselective analogues, these systems show problems regarding tolerance to different functional groups, oxygen and water (Section 2.2.2). Since this is much less of an issue with ruthenium-based catalysts, such as **G-I** and **G-II**, making these systems *Z*-selective would allow for catalysis under less strict conditions and with substrates that are incompatible with tungsten and molybdenum.

Early attempts in preparing *Z*-selective ruthenium-based catalysts, albeit with modest results, involved asymmetric NHC-ligands,^{111,114,122–126} acyclic diamino-carbene ligands,¹²⁷ or substitution of a chloride ligand with a sulfonate or phosphate ligand.¹¹³ Similarly, Grubbs and co-workers exchanged both small chloride ligands of the Hoveyda–Grubbs catalyst with rather bulky pivalate moieties; while initially the expected substitution complex was obtained, at longer reaction times an intramolecular C–H bond activation at one of the *o*-methyl groups of the mesityl moiety on the NHC took place, forming the six-membered chelated complex **17** (Chart 5).¹²⁸ In a similar fashion the five-membered chelated complex **18** was obtained from the corresponding Hoveyda–Grubbs type catalyst with an asymmetric NHC-ligand bearing an adamantyl and mesityl moiety. Tests in CM show somewhat mediocre results with **17**; however, a *Z*-selectivity comparable to that of molybdenum and tungsten based catalysts was obtained using **18**, though at a relatively high reaction temperature (70 °C).¹²⁸ Optimization of the reaction conditions allowed, with retention of the high *Z*-selectivity, for comparable activities with turnover numbers (TONs) of 20–50 at lower temperatures.¹²⁹ Additionally, **18** is easily synthesized and stable in the presence of water.¹²⁸ Further investigations into the improvement of catalytic activity, robustness, and reduction of secondary metathesis yielded **19a**; here, the carboxylic ligand in **18** has been substituted by a nitrate moiety, giving much higher activity in CM/HC (TONs up to 1000) while keeping the parent compound’s key features;¹³⁰ moreover, high *Z*-selectivity in RCM was also reported.¹³¹ Finally, *Z*-selectivities of > 95%, with

Chart 5: Selection of ruthenium-based *Z*-selective olefin metathesis catalysts.

TONs up to 7400, were obtained through substitution of the remaining mesityl moiety on the NHC for a 2,6-diisopropyl group (**19b**).¹³²

Based on computational predictions by Jensen and co-workers the sterically demanding 2,4,6-triphenylbenzenethiolate was selected to replace one of the chloride anions in **HG-II**.^{19,20} Once synthesized, **20a** showed a *Z*-selectivity in HC up to 96% with allyltrimethylsilane and > 85% with linear unsubstituted alkenes, reaching TONs of up to 2000. Furthermore, this catalyst tolerates the presence of water and relatively strong bases, such as proton sponge; however, the presence of acid is deleterious. The stability of **20a** towards neutral substrates is comparable to that of other ruthenium-based catalyst and tolerance to oxygen was found similar to **19a**. Even though catalysis with **20a** was performed at elevated temperature (40–60 °C), the results are comparable to those of the adamantyl-chelate systems discussed above. Substitution of the remaining chloride ligand with isocyanate yields the highly *Z*-selective and very robust catalyst **20b**; this catalyst can be used in air, does not require any purification or degassing of substrates or solvents, and tolerates acids excellently.¹³³

Ruthenium-based olefin metathesis catalyst **21** was developed by Hoveyda and co-workers through substitution of the two chloride ligands of the **HG-II** with a catechothiolate ligand.¹³⁴ Initially **21** was described as *Z*-selective, yet, stereo-

or *Z*-retentive would be a better label: ROMP and ring-opening/cross-metathesis (ROCM) indeed give > 98% *Z*-product, even at > 90% conversion; however, it must be noted that the C=C bonds in the 3–8 membered cyclic alkenes used as substrate are already *Z*-disubstituted olefins.^{134,135} Similarly, in CM, with slightly modified analogues of **21**, at least one of the substrates used is a *Z*-disubstituted alkene.¹³⁶ Nevertheless, **21** and its analogues are, with TONs up to 43000, highly active catalysts, tolerate alcohols and are relatively easy to prepare and use.^{134,135}

3.2 The Origin of *Z*-Selectivity

With traditional nonselective olefin metathesis catalysts, the pathway in which incoming olefin and the ensuing RCB are bottom-bound (*trans* with respect to the phosphine or NHC-ligand) is generally preferred (Section 2.2.4). However, DFT calculations, performed on the *Z*-selective acetate-bearing analogue of **18**, show that unfavourable steric repulsions between the bulky chelating adamantyl group and alkylidene H-atoms destabilize the bottom-bound [2 + 2] cycloaddition and cycloreversion transition states (**a.**, Figure 2).¹³⁷ When cycloaddition and reversion take place under the relatively flat mesityl moiety of the NHC, via a side-bound pathway, such interactions do not exist (**c.**). Next to steric effects the bottom-side pathway is also disfavoured because of electronic reasons: while in the side-bound pathway the $d \rightarrow \pi^*$ back-donation to NHC and alkylidene is originating from two different Ru d-orbitals (**d.** and **e.**), the same Ru d-orbital is used for $d \rightarrow \pi^*$ back-donation to both alkylidene and NHC in the bottom-bound pathway (**b.**). As a consequence, the Ru–C_{NHC} bond is significantly elongated, which acts destabilizing.¹³⁷

Computational studies performed on **18** and **19a** revealed that *Z*-selectivity with the side-bound mechanism originates in the transition states leading to cycloreversion:^{138,139} in the *Z*-pathway (**TS1(Z)**, Figure 3) both substituent R¹ and R² point away from mesityl. However, an upwards pointing R² in the *E*-pathway suffers steric repulsion from the mesityl moiety located directly above (**TS1(E)**), thus destabilizing the transition state, making this pathway less preferable, and yielding a *Z*-selective catalyst.

Success with the side-bound mechanism inspired others in using a similar strategy to obtain *Z*-selective or retentive catalysts. Catalyst **21** was intentionally designed to have catechthiolate ligands bind to ruthenium with one Ru–S bond

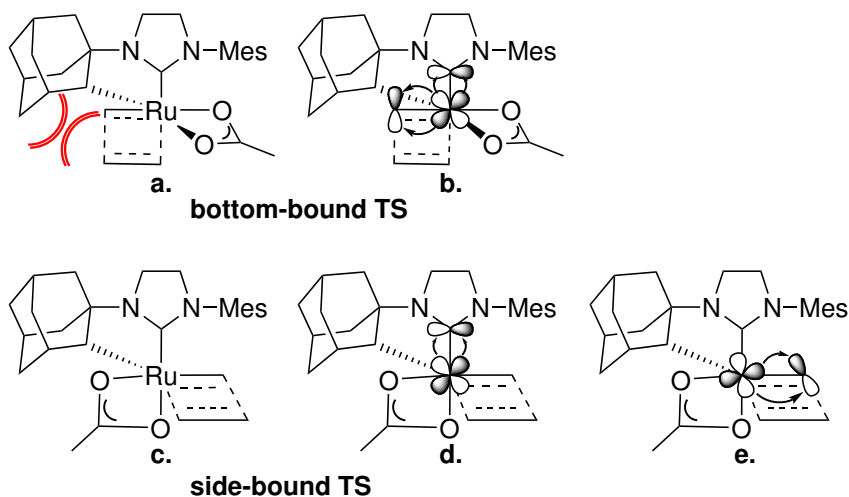


Figure 2: Steric and electronic differences between the bottom- and side-bound cycloaddition transition states with the acetate-bearing analogue of **18**. **a.** Unfavourable steric interaction between the RCB and adamantyl moiety in the bottom-bound pathway, **b.** $d \rightarrow \pi^*$ back-donation to NHC and alkyldiene originates from the same d-orbital in bottom-bound pathway, **c.** side-bound pathway with the RCB located under the mesityl group, **d.** and **e.** $d \rightarrow \pi^*$ back-donation to NHC and alkyldiene originating from different d-orbitals in the side-bound pathway.¹³⁷

equatorial and the other Ru–S bond meridional, effectively blocking the site *trans* w.r.t. SIMes.¹³⁴ DFT calculations on ROCM, with norbornene and styrene as substrates, show that, analogue with **18** and **19a**, the *Z*-selectivity originates from steric pressure between the mesityl moiety and RCB substituents in the cycloaddition transition states: in the *E*-pathway an unfavorable steric interaction between the bridging C-atom of norbornene and the mesityl moiety is observed (**TS2(E)**). This interaction is greatly reduced or not even present in the *Z*-pathway with norbornene bending away from mesityl in **TS2(Z)**; therefore, the overall barrier in the *Z*-pathway is 3.2 kcal·mol⁻¹ lower than in the *E*-pathway, leading to high *Z*-retentivity.¹³⁴

Interestingly, a catechol analogue of **21** is not *Z*-retentive at all.¹⁴⁰ Since the steric bulk of both catechol and catechthiolate are of similar size, it was envisaged that electronic effects must be causing the lack of stereoretention. For instance, the Ru–O bonds in the catechol complex could be weaker than the Ru–S bonds in **21**;¹⁴⁰ this would allow dissociation of the catechol ligand, followed by substitution with other donating species coming from the substrate, or even formation of a dichloride complex in chlorinated solvents. However, when

reaction conditions where set carefully and decomposition of the catechol complex was prevented, olefin metathesis was still not performed stereoretentively.¹⁴⁰ Subsequent DFT studies showed that not MCB formation (as with **21**), but olefin coordination is the rate determining barrier with the catechol complex. The coordinating olefin is located rather far away from the catechol moiety and experiences little steric pressure, explaining the poor *Z*-retentivity.¹⁴⁰

Different from the *Z*-selective/retentive systems described above, that were obtained through a combination of serendipity, chemical intuition and experimental trial-and-error, Jensen and co-workers designed *Z*-selective catalysts **20a** and **20b** completely *in silico* before they were actually synthesized.¹⁹ The underlying aim was modification of **HG-II** to obtain a *Z*-selective catalyst, while maintaining certain characteristics of the parent compound such as bottom-side binding of the olefin and formation of the MCB.

Application of a larger steric pressure on one side of the MCB, through substitution of a chloride ligand with another much larger anionic ligand, was envisaged

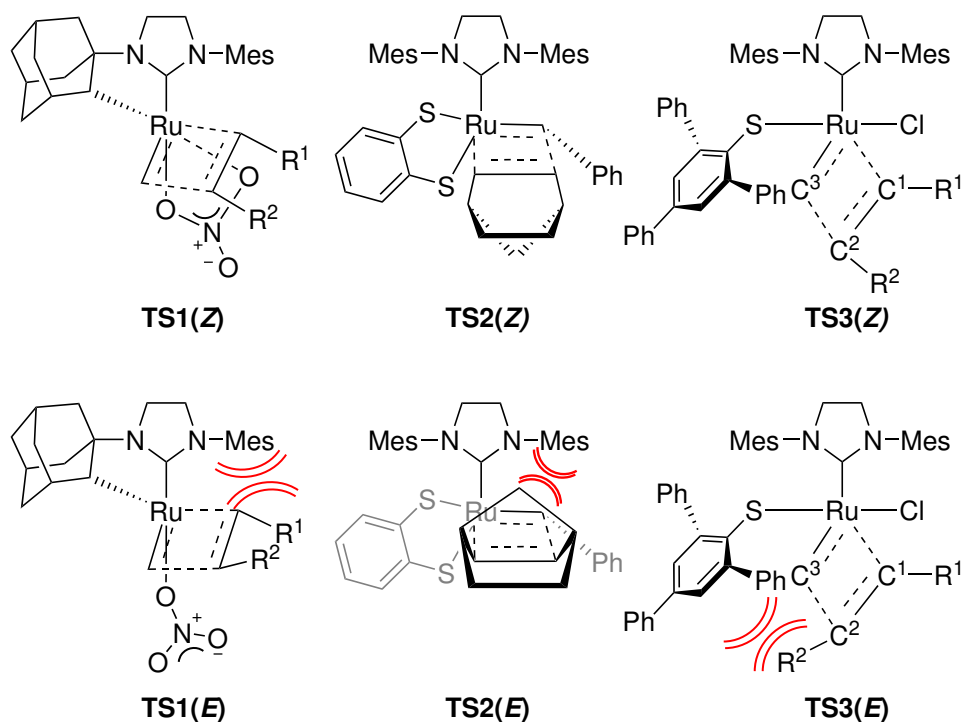


Figure 3: Transition states for cycloaddition or cycloreversion showing unfavorable steric interaction in the *E*-pathway, inducing *Z*-selectivity in catalysts **18–21**.

as a strategy to improve the *Z/E* ratio.¹⁹ Computations showed that the bulky 2,4,6-triphenylbenzenethiolate is well suitable for this job, since it exerts sufficient steric pressure near the MCB C²-atom (**TS3**); as a consequence, an increase of energy is obtained for the *E* transition state (**TS3(E)**) because of the R²-substituent pointing towards the thiolate moiety. Naturally, the steric pressure on the *Z*-MCB is much less pronounced, since the R¹- and R²-substituent are pointing away from the thiolate; this lowers the energy of transition state in the *Z*-pathway (**TS3(Z)**), inducing *Z*-selectivity.

Chapter 4

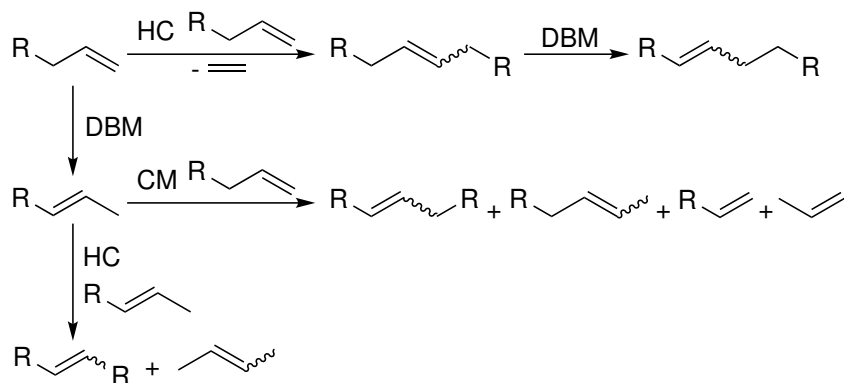
Catalyst decomposition

With olefin metathesis catalysts now being an important tool in organic synthesis and the growing use of olefin metathesis in industrial processes, identifying catalyst decomposition pathways has become crucial. Deactivation, caused by decomposition of the molecular catalyst into metathesis inactive species, leads to a reduction in catalytic activity.¹⁴¹ As a consequence, catalyst recycling becomes less useful and higher catalytic loads are required to obtain sufficient conversion. More problematic is the decomposition of olefin metathesis catalysts into ruthenium-based species that actively catalyze non-metathesis reactions. For instance, quite some ruthenium compounds are known as effective olefin isomerization catalysts.¹⁴²⁻¹⁴⁴ This results in the formation of undesired side-products, often at the cost of expensive substrates, that can be difficult and costly to separate from the desired compound.¹⁴⁵

4.1 Isomerization

Double-bond migration or isomerization affects the position of the double bond in olefins. Generally, a release in free energy, through formation of a thermodynamically more stable internal olefin, is the driving force behind the C=C bond wandering to the centre of the carbon chain. During an olefin metathesis experiment, competing double-bond migration converts the substrate into an isomerization product. Subsequently, when a substantial concentration has been reached, this product will start to compete with the intended substrate in olefin metathesis: CM of the isomerization product with the intended substrate and, after its depletion, HC between two equivalents of isomerization product produce a large range of different olefins. Eventually, even the products themselves are subject to double-bond migration. In addition, *Z/E*-isomerization destroys any obtained

Scheme 5: Example of the main products obtained through a combination of several subsequent double-bond migration and olefin metathesis reactions.^a

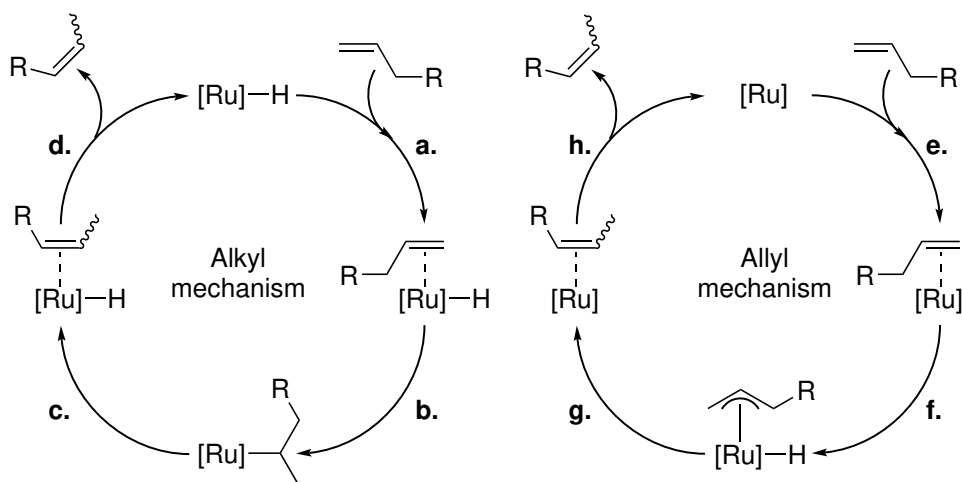


^aHC = homocoupling, DBM = double-bond migration, CM = cross-metathesis.

Z-selectivity, returning a mixture based on the thermodynamic stability of the stereoisomers. It is evident that a combination of several successive isomerization and olefin metathesis steps leads to a complex mixture of olefins. As an illustration, Scheme 5 shows the main products obtained from only a few competing olefin metathesis and isomerization steps of a simple alkene that has only one possible internal position.

Interestingly, experiments show that olefin metathesis carried out with second-generation catalysts generally leads to more isomerization than with their first-generation counterparts.^{21,22,145} In addition, substrates containing allylic amine, ether and aromatic groups are more susceptible to isomerization.²¹

The alkyl and aryl mechanism, shown in Scheme 6, are generally accepted mechanisms to double-bond migration:¹⁴⁶ in the former, a coordinatively unsaturated ruthenium hydride binds the olefin (**a.**). Following this, insertion of the now η^2 -bound olefin into the Ru–H bond results in the formation of a ruthenium-alkyl species (**b.**). Subsequently, β -hydride elimination, depending on the site of abstraction, either re-forms the species preceding step **b.**, or it generates the η^2 -bound product olefin (**c.**). Dissociation then releases the isomerized alkene and regenerates the initial ruthenium hydride (**d.**). In a similar fashion, the allyl mechanism begins with the association of an olefin to ruthenium (**e.**). However, the absence of a Ru–H bond renders hydride insertion impossible. Instead, one of the C–H bonds at the allylic position, sufficiently activated due to its vicinity to the metal, undergoes oxidative addition (**f.**). The η^3 -allyl ruthenium hydride thus formed suf-

Scheme 6: Alkyl and allyl mechanisms leading to double-bond migration.^a

^aAlkyl mechanism: **a.** association of an olefin to the ruthenium hydride, **b.** insertion of the η^2 -bound olefin into the Ru-H bond yields a ruthenium-alkyl compound, **c.** β -hydride elimination gives the η^2 -bound product olefin and **d.** dissociation regenerates the initial ruthenium hydride and releases the product olefin. Allyl mechanism: **e.** association of an olefin to a ruthenium species to obtain a η^2 -bound olefin, **f.** oxidative addition of the allylic C-H bond yields a η^3 -allyl ruthenium hydride, **g.** reductive elimination forms the η^2 -bound product olefin, **h.** dissociation regenerates the initial ruthenium compound and releases the product olefin.

fers reductive elimination, resulting in either re-formation of the species preceding step **f.** or the η^2 -bound product olefin (**g.**). Subsequent dissociation regenerates the initial ruthenium species and liberates the isomerized alkene (**h.**).

Crossover experiments with deuterium-labeled substrates can be used to differentiate between the two mechanisms. When a mixture of two olefins, one of them D-labeled, is subject to an isomerization catalyst operating through the alkyl mechanism, crossover of deuterium atoms into the unlabeled compound is observed. However, with the allyl mechanism, no crossover is seen since the 1,3-D shift takes place in an intramolecular fashion.

4.2 Ruthenium Hydrides

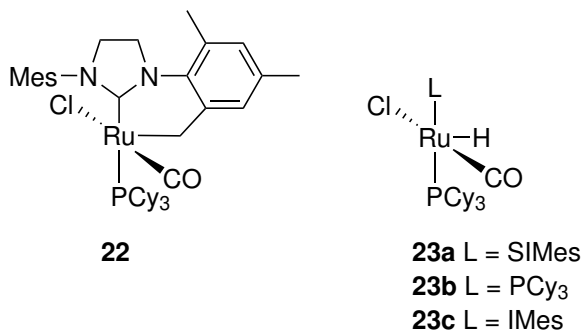
The alkyl mechanism suggests the possibility that ruthenium hydrides are important players in double-bond migration. During synthesis of some second-generation catalysts, a hydridic by-product is obtained, which was thought to be responsible for double-bond migration during catalysis.¹⁴⁷ Thereafter, several studies that

investigate the formation of ruthenium hydrides and their role in double-bond migration have been performed: for instance, when inert conditions are not sufficiently warranted, decomposition of **G-II** affords **22** (Chart 6), as a result of intramolecular C–H activation of the *o*-methyl groups on the NHC.¹⁴⁸ Although **22** is not a hydride itself, it is supposed to be the decomposition product of one. In addition, experiments with *o*-CD₃ groups on the NHC's aromatic rings did not yield the expected ruthenium deuteride complex either; however, proof of its existence and transient nature is found in the mixture of deuterated olefins that was obtained in catalysis.¹⁴⁹ However, the isomerization activity of decomposition mixtures containing **22** did not match the activities found during olefin metathesis; thus, this compound and its hydride precursors cannot completely explain double-bond migration. Moreover, its formation can easily be prevented when strict anoxic conditions are observed.

Hydrido-carbonyl-chloride complexes **23a–c** are obtained when protic solvents are present during the synthesis of Grubbs-type catalysts;¹⁴⁸ especially primary alcohols are reported to aid the formation of these complexes. Hence, rigorous purification of solvents, reagents and substrates affords a relatively easy way of eliminating this problem.

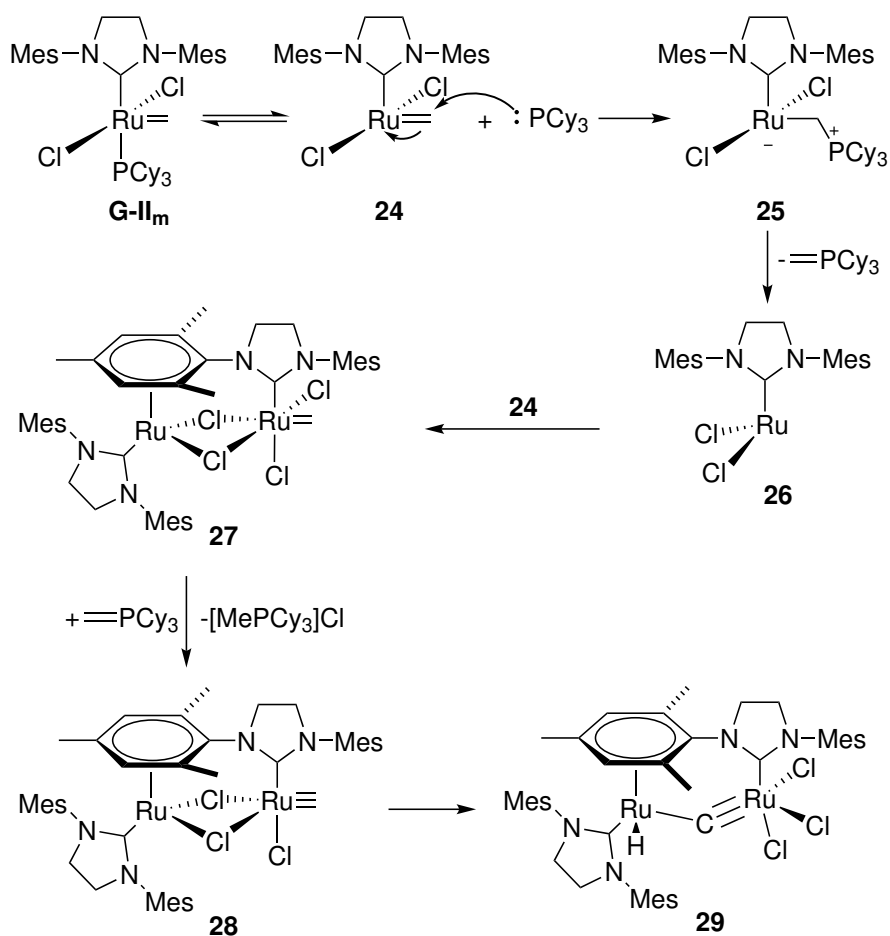
Other starting points for catalyst decomposition might originate in the catalytic cycle itself: for example, ruthenium methylidenes are known as unstable intermediates present during olefin metathesis.^{150,151} Indeed, through moderate heating of a solution of tricycloheptylphosphine-stabilized methyldene complex **G-II_m** (Scheme 7) in benzene, dinuclear ruthenium hydride **29** was obtained.¹⁵² Decomposition is proposed to begin with dissociation of the phosphine ligand that,

Chart 6: Ruthenium compounds from catalyst decomposition suspected of being active in double-bond migration.



in its free state, swiftly attacks the methylene C-atom in methylene complex **24**, forming σ -alkyl species **25**.^{150,152} Following this, elimination of a phosphine ylide leads to 12-electron complex **26** which dimerizes with another equivalent of **24** to dinuclear ruthenium complex **27**. Subsequently, HCl abstraction by the previously liberated ylide gives **28** and a phosphonium salt, followed by oxidative addition and migration of the two Cl-atoms to yield hydride **29**. Initially, only the presence of **29** and the phosphonium salt were detected.¹⁵² A later, more thorough study revealed that **27** is indeed observed in the decomposition pathway.¹⁵⁰ The detection and isolation of these intermediates greatly enhances the validity of this pathway.

Scheme 7: Proposed decomposition pathway of ruthenium methylene **24**.^{150,152}



In addition, Fogg and co-workers showed that pyridine-induced displacement of the phosphine ligand in methylenes complexes, followed by the free phosphine attacking the methylene C-atom, gives σ -alkyl species **25** and its first-generation analogue.^{153,154} In addition, the above is analogously observed with other amines, explaining the high isomerization observed with allylic amines (Section 4.1).¹⁵⁵

Catalytic tests performed with **29** show that this compound is active in olefin isomerization.¹⁵² However, a study in which **29** and the aforementioned hydrides **23a–c** are tested in olefin isomerization shows, after comparison to the isomerization obtained with the Grubbs second-generation catalyst, that their contribution to total isomerization activity is relatively small.²¹

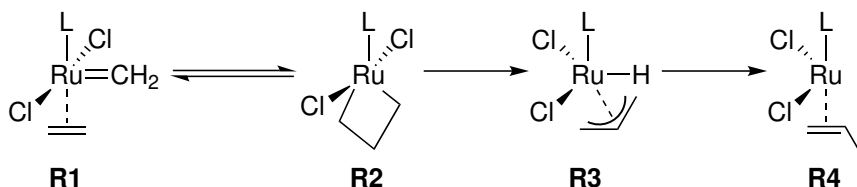
4.3 Ruthenium Nanoparticles

Fogg and co-workers identified ruthenium nanoparticles (RuNPs) as a major contributor to isomerization activity during olefin metathesis.²⁴ At first, it was thought that RuNPs present in commercially available precatalysts were responsible for the observed isomerization. However, careful purification of the precatalyst under inert conditions gave only minor reduction of isomerization. This shows that isomerization active ruthenium compounds are generated through catalyst decomposition during actual catalysis. A steady increase in RuNPs, detected during an initiation period leading to the onset of major isomerization activity, revealed that RuNPs are indeed possible decomposition products. Subsequent Hg-poisoning experiments show that RuNPs are responsible for approximately 50% yield on a total isomerization of 80%. The formation of RuNPs is, analogue to the decomposition into dinuclear ruthenium hydride **29** in the previous section, connected to the decomposition of unstable ruthenium methylenes. Although no exact pathway has been proposed, more or less all the ligands are envisaged to be ejected from **24** in several decomposition steps, leading to formation of RuNPs.²⁴

4.4 Substrate-Induced Decomposition

The catalyst decomposition described in the previous sections was caused by the presence of impurities during synthesis and through heating of catalytic intermediates. Janse van Rensburg suggested that β -hydride transfer from the ruthenacy-

Scheme 8: Substrate-induced decomposition through β -hydride transfer from the RCB.^a



^aL = PCy₃, IMes.

clobutane (RCB), an intermediate in the catalytic cycle, could be a starting point for substrate-induced decomposition of the olefin metathesis catalyst.^{156,157}

DFT calculations start from π -complex **R1** (Scheme 8), with ethene as substrate. From here, RCB **R2**, which is of relatively low-energy compared to the other intermediates, is obtained. Generally, this leads to normal olefin metathesis; however, a competing deviation was suggested: β -hydride abstraction from the RCB leads to allyl ruthenium hydride species **R3**. Subsequently, reductive elimination gives the η^2 -bound propene ruthenium complex **R4** that is supposed to be inactive in olefin metathesis, thus reducing the initial olefin metathesis activity.

The highest barrier of the RCB decomposition process is located between **R2** and **R3**, that is, on the transition state leading to β -hydride abstraction; furthermore, this barrier is not massively higher than that of metathesis. The barrier to reductive elimination between **R3** and **R4** was found to be so low that it is effectively barrier-less. Therefore, considering the above, it is not unlikely that this decomposition mechanism is competing with olefin metathesis.

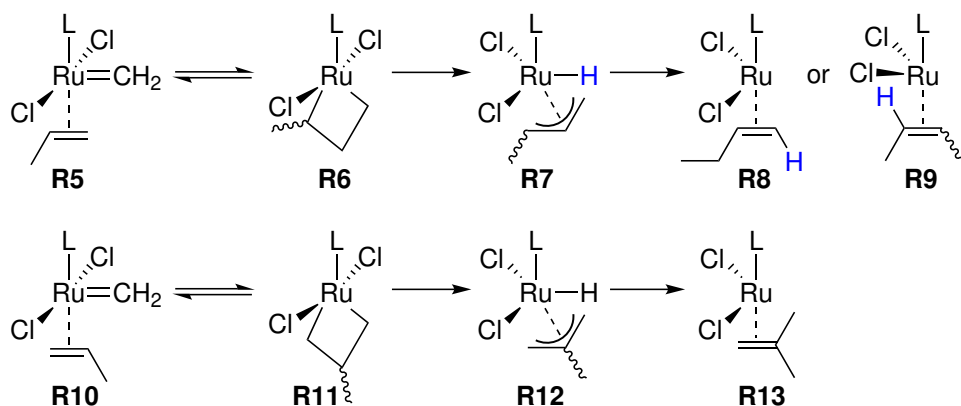
To verify the theoretical results, experiments were performed in which the methylidene analogue of the Grubbs catalysts, i.e. **G-II_m** (Scheme 7) and its first-generation analogue ((PCy₃)₂RuCl₂(=CH₂), **G-I_m**), are used to catalyze the metathesis of ethene. With such a simple olefin as substrate, the possibility of higher olefin formation through the metathesis process is absent; thus, such compounds will not obscure products obtained from the decomposition pathway. These experiments were performed by heating a solution of **G-I_m** or of **G-II_m** in ethene saturated benzene-*d*₆ for 16 hours at 40 °C. Analysis of the mixture obtained with **G-I_m** showed that significant amounts of propene, 1-butene and 2-butenes had formed. Furthermore, small amounts of cyclopropane and isobutene were detected as well. **G-II_m** showed a slightly different picture with propene as major product, with 1-butene and 2-butenes presenting the smaller fraction of products

and isobutene and 1,3-butadiene observed in trace amounts. In addition to the olefinic products, imidazolium salt [SIMesH]Cl, coming from the decooordination of the NHC from ruthenium in the second-generation complex, was detected.

It is clear that dissociation of **R4** in Scheme 8 affords propene. Moreover, the formation of the different butene isomers can also be easily explained: they are obtained via the same decomposition mechanism that yields propene from ethene. Coordination of propene to a ruthenium-methylidene complex gives either **R5** or **R10** depending on the orientation of the olefin (Scheme 9). From **R5** the RCB **R6**, with the methyl group located in the α -position, is obtained and subsequent β -hydride abstraction gives allylic ruthenium hydride **R7**. Here, the H-atom can be inserted on the allylic C1 (**R8**) or C3 (**R9**) position, resulting in 1-butene or 2-butenes respectively. Alternatively, it is possible for *cis*- and *trans*-2-butene to be obtained through HC of propene or via isomerization of 1-butene. From **R10**, however, β -methylruthenacyclobutane **R11** is obtained. Subsequent hydride insertion, whether it takes place at the allylic C1 or C3 position of **R12**, leads via **R13** to the formation of isobutene.

Interestingly, with **G-II_m** the yield in propene is 1.5 times in excess compared to the amount of decomposed catalyst. This suggests that a mechanisms leading to propene, other than β -hydride transfer, is functioning in parallel. Another explanation, explored in Chapter 9, could be that the the ruthenium-methylidene

Scheme 9: Formation of 1-butene, 2-butenes and isobutene through propene-induced olefin metathesis catalyst decomposition.^a



^aL = PCy₃, IMes.

species is somehow regenerated, after which it can be decomposed again, producing propene.

Chapter 5

Methods

Though a large share of the experimental results in **Paper I–Paper IV**, discussed in the next chapters, are obtained through use of standard laboratory techniques, sometimes special methods needed to be followed or developed. For instance, unlike standard organic synthesis, which can often be performed on the benchtop, organometallic chemistry often requires an inert atmosphere; see Section 5.1. Furthermore, Section 5.2 discusses which modifications are needed to turn a standard NMR experiment into one from which quantitative results can be obtained. In addition, an easy way to generate ethene is described in Section 5.3, and Section 5.4 gives a method to reduce the headspace in an NMR tube without causing loss of resolution.

5.1 Synthesis of Organometallic Compounds

Although Grubbs-style metathesis catalysts are generally air-stable in solid form, exposure to oxygen and moisture must be prevented when dissolved, for instance, during synthesis or catalytic testing. Moreover, the free phosphine ligands used in **Paper I** oxidize relatively easily due to the presence of alkyl groups on the P-atom; potassium thiolate salts react readily with moisture (**Paper I** and **Paper IV**); and the *p*-cymene protected 12-electron ruthenium species prepared in **Paper II**, the use of which extends to **Paper III**, is highly oxygen and moisture sensitive.

As a consequence, synthesis and manipulation of the compounds in this thesis required special techniques: for instance, double manifold vacuum/inert gas lines combined with special Schlenk glassware allows for relatively easy use in the synthesis of most sensitive compounds. However, when reactions involve multiple additions of reagents and intermediary product isolations, the risk of introducing

air increases with every step; here, success strongly depends on the skills of the chemist. For most of the experiments a glovebox was used; although much more expensive, it does not only offer a more user-friendly workspace, but also allows for more tight control of the oxygen and water content of the atmosphere in which experiments are performed and where products are stored: a blower continuously circulates the atmosphere inside a glovebox over a catalyst bed, where pallets of activated copper on diatomite and molecular sieves remove oxygen and moisture, respectively. In this way, typical concentrations below 0.1 ppm are maintained during normal operating conditions. While nitrogen-gas and argon are generally considered as suitable gasses for the Schlenk system and glovebox, the latter is generally preferred: nitrogen is not really inert and argon has the additional advantage of being more heavy than air, forming a protective blanket.

5.2 Quantitative NMR

In a simple pulse-acquisition NMR experiment, a pulse converts part or all (when a 90-deg pulse is applied) of the equilibrium z-magnetization into transverse (x, y) magnetization; subsequently, the free induction decay is recorded during the acquisition time (AQ), followed by a delay time (D1) to allow for relaxation of the excited nuclei, thus restoring equilibrium z-magnetization before the next pulse is applied. In routine experiments, after an AQ of several seconds and a short relaxation delay (D1 \approx 1 second), a pulse initiates the next experiment. Although this allows for a rapid collection of data, the combined AQ and D1 is too short for the transverse magnetization of nuclei with relatively large spin-lattice relaxation times (T_1) to convert back to equilibrium z-magnetization before the next pulse; this distorts the intensity of the integrated signal between nuclei with different chemical surroundings, making accurate quantification impossible. In quantitative NMR (qNMR) experiments, a D1 of at least five times the largest T_1 in the sample is recommended to obtain > 99% z-magnetization recovery, thus allowing for qNMR-analysis.^{158,159} In ^1H T_1 -values are generally of 1–15 seconds; therefore, a D1 interval of 60 seconds was used to obtain ^1H qNMR spectra in the catalytic experiments of **Paper III**.

5.3 Generation of Ethene

To exclude undesired decomposition of the oxygen sensitive *p*-cymene protected 12-electron ruthenium compound in **Paper III**, the ethene required for the experiments was synthesized directly inside a glovebox, instead of obtained from a gas cylinder externally. Homocoupling of 0.3 mL styrene using 15 mg Piers second-generation generally provided enough ethene to saturate the benzene- d_6 solutions. The apparatus in Figure 4 was used to generate and purify the gas: Styrene is injected from a syringe (3) into a 3 mL vial (1), containing the previously mentioned catalyst and a small stirring magnet. The evolved ethene rises via a cannula (4) through a septum (2) (that closes off the reaction vessel) into a glass tube (5) which is closed off at both sides with septa. Here possible impurities in the gas (such as vapors from styrene) are adsorbed on a layer of activated basic alumina (7), kept in place by two wads of quartz-wool (6). Subsequently, the purified gas flows through a long cannula (8) into the benzene- d_6 solution contained in a Shigemi NMR-tube (9) with J. Young valve. Closing off the NMR-tube with a septum (10) prevents loss of ethene. Another short cannula (11) is used to vent off excess gas. Analysis through NMR

The evolved ethene rises via a cannula (4) through a septum (2) (that closes off the reaction vessel) into a glass tube (5) which is closed off at both sides with septa. Here possible impurities in the gas (such as vapors from styrene) are adsorbed on a layer of activated basic alumina (7), kept in place by two wads of quartz-wool (6). Subsequently, the purified gas flows through a long cannula (8) into the benzene- d_6 solution contained in a Shigemi NMR-tube (9) with J. Young valve. Closing off the NMR-tube with a septum (10) prevents loss of ethene. Another short cannula (11) is used to vent off excess gas. Analysis through NMR

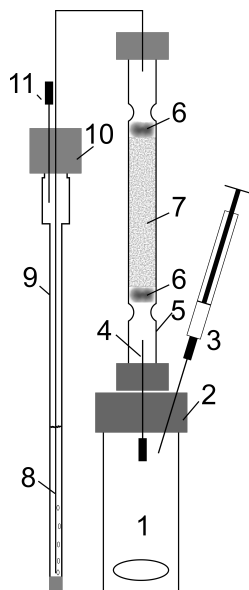


Figure 4: Apparatus used for the generation of ethene. 1. reaction vessel (3 mL vial), 2. septum, 3. syringe for the addition of styrene, 4. cannula, 5. glass tube, 6. quartz wool, 7. basic alumina, 8. long cannula, 9. NMR-tube, 10. septum, 11. cannula.

and gas chromatography (GC) shows that ethene obtained with the method above has a purity of $> 99.99\%$ (traces of propene were observed with GC).

5.4 Reduction of the NMR-Tube Headspace

The relatively large headspace volume of standard low-pressure/vacuum (LPV) NMR tubes (≈ 2 mL) allows a significant amount of dissolved gaseous compounds to be lost from solution, thus making the quantification that we wanted to achieve in **Paper III** more difficult, since compounds lost to the gas phase cannot be measured with conventional NMR spectroscopy. An additional problem is the relative unavailability to the dissolved catalyst of the gasses in the headspace. Although a reduction in headspace volume could have been achieved with a larger sample volume,^{157,160} this gives problems with magnetic field homogeneity in the NMR spectrometer, leading to a loss in resolution. Eventually, Shigemi NMR tubes with J. Young valves (Figure 5) were found to reduce the headspace volume significantly, to ≈ 0.5 mL: most of this volume is filled up by sliding a glass plunger and its attached PTFE holder into the tube. Two additional PTFE holders were added on top to fill the headspace even more.

Since the solubility of different gasses in benzene- d_6 might differ, NMR could show distorted ratios of the gasses in solution, even with a reduced headspace. Therefore, a previously obtained catalytic experiment was analysed through ^1H NMR and GC: the former gave the ratio of dissolved gasses; in the latter the whole sample was evaporated before measurement, thus giving the gas ratios for the complete sample. The molar ratios between the different gaseous compounds in solution and gas phase show a relative difference of no more than 6.6%.

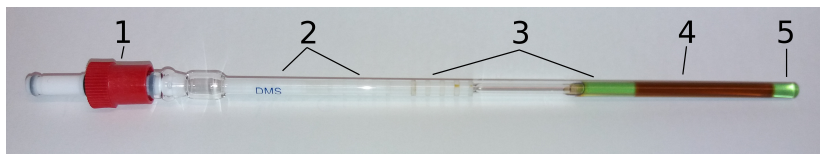


Figure 5: Experimental setup of using a LPV Shigemi tube set in combination with two additional PTFE holders to reduce headspace. 1. J. Young valve, 2. additional PTFE holders (2x), 3. PTFE holder with connected glass plunger, 4. reaction mixture, 5. glass tube-bottom.

Chapter 6

Z-Selective First-Generation Catalysts

The overview of *Z*-selective olefin metathesis catalysts in Section 3.1 shows that, prior to **Paper I**, they are all of the second-generation type. No significant attempts to develop *Z*-selective first-generation catalysts had been taken; remarkably, considering the fact that nonselective first-generation catalysts show less double-bond migration (Section 4.1), a property that is presumed to be easily transferred to *Z*-selective catalysts. Furthermore, Section 3.2 shows that **20a** and its isocyanate analogue **20b** are the only second-generation *Z*-selective catalysts that resemble the nonselective parent compound (**HG-II**): that is, they allow for olefin binding and MCB formation at the bottom side of the molecule, i.e. *trans* w.r.t. the NHC ligand.

To obtain first-generation *Z*-selective olefin metathesis catalysts of which the mechanism resembles that of the parent compound **HG-I**, the strategy used for **20a** is a good starting point. However, substitution of a chloride ligand in **HG-I** for a bulky thiolate is not expected to give *Z*-selectivities comparable to **20a**: distribution of steric bulk in complexes with tricyclohexylphosphine is different from those with SIMes; moreover, sufficient steric bulk from the L-ligand is expected to be required to keep the thiolate from bending away and releasing its *Z*-selectivity inducing steric pressure at the site of MCB formation (Section 3.2). However, since the exact effect of the L-ligand's size on the selectivity remains unexplored, clarification might aid further catalyst design.

6.1 Monodentate Phosphine Ligands

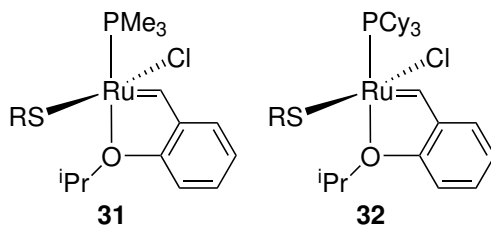
Compound **31** (Chart 7), containing the sterically nondemanding trimethylphosphine (PMe₃) and the bulky 2,4,6-triphenylbenzenethiolate, was selected as a good

base from which to start investigating the role of the L-ligand on stereoselectivity. After all, with a Tolman cone angle of only 118° ,^{161,162} PMe_3 is the smallest trialkylphosphine that exists; therefore, the relative minimum of steric pressure from the L-ligand is to be expected in **31**. As a consequence, *Z*-selectivity is most likely going to be very low. These expectations are mirrored by the results from DFT calculations: comparison of the absolute barrier in the pathway leading to respectively the *E*- and *Z*-product gives a relative indication of the selectivity ($\Delta\Delta G_{\text{Tol}}^\ddagger$, Table 1); thus, the high *Z*-selectivity obtained with second-generation catalyst **20a** is reflected in the relatively high energy found in entry 1. Consequently, the negative energy difference obtained with **31** ($\Delta\Delta G_{\text{Tol}}^\ddagger = -0.8 \text{ kcal}\cdot\text{mol}^{-1}$, entry 2) indicates that this catalyst is certainly not *Z*-selective and possibly even somewhat *E*-selective. Although not interesting from a selectivity point of view, a curiosity-driven attempt was made to synthesize **31**; however, substitution of PCy_3 in **32** with PMe_3 (from a 1 M sol. in tetrahydrofuran (THF)) remained fruitless.

Analysis of the P–Ru–S–C1 and Ru–S–C1–C2 torsion angles in the *E*-MCB rupture transition state **TS5(E)** (Figure 6, indicated with τ and ϕ , respectively) calculated for **31** (entry 2, Table 1) shows values that are far from the “ideal” angles necessary to obtain sufficient steric repulsion between the thiolate ligand and the R^2 -substituents; in other words, the *E*-pathway is not made unfavourable enough.

Augmentation of the Tolman cone angle from 118° to 170° ,¹⁶¹ through substitution of PMe_3 for the larger tricyclohexylphosphine (PCy_3) ligand (**32**), results in a reduction of 25° in twisting around the S–C_{Ar} bond and a more acute P–Ru–S–C1 torsion angle ($\Delta\tau = 37^\circ$, entry 3). As a consequence, the thiolate

Chart 7: Hoveyda–Grubbs-style catalyst bearing a monodentate trialkylphosphine and bulky 2,4,6-triphenylbenzenethiolate.^a



^aR = 2,4,6-triphenylphenyl.

is expected to exert more steric pressure at one face of the RCB, resulting in a higher *Z*-selectivity. Unfortunately, these improvements are not enough to obtain a significantly *Z*-selective catalyst, since the computed $\Delta\Delta G_{\text{Tot}}^{\ddagger}$ remains substantially lower than that of **20a** (0.9 vs. 3.1 kcal·mol⁻¹; entries 3 and 1, respectively). Additionally, with $\Delta G(Z)_{\text{Tot}}^{\ddagger} = 28.0$ kcal·mol⁻¹ in **32** compared to 18.8 kcal·mol⁻¹ in **20a**, the former is predicted to be much less catalytically active too. Despite the not-so-promising results, **32** was synthesized; via a relatively easy synthesis, this compound allows for verification of the computational results.

The synthesis of **32** is simple and straightforward, through reaction of the commercially available Hoveyda–Grubbs first-generation catalyst (**HG-I**) with potassium 2,4,6-triphenylbenzenethiolate in THF. Subsequently, dark red crystals of **32** suitable for X-ray structure analysis are readily obtained at low temperature (−30 °C) from a solution of **32** in THF/*n*-pentane. The molecular structure, together with relevant bond lengths and angles, is shown in Figure 7. The compound can be described as a slightly distorted square pyramid with the alkylidene ligand occupying the apical position. Of the remaining ligands, all occupying basal positions, the thiolate moiety is *trans* to the chloride ligand (C1) and the phosphine (P1) is *trans* to the oxygen atom of the isopropoxy ligand (O1). Bond lengths and angles of the moieties found in **32** are largely comparable to those found in **20a**.²⁰ However, a noticeable difference is the Ru1–S1–C1 angle being somewhat wider in **32** (117° vs. 113°). Furthermore, the angles around the arylthiolate are found to be in good agreement with geometries optimized using the ω B97XD functional. For instance, the calculated (experimental) P–Ru–S and Ru–S–C_{Ar} angles in **32** are 88° (88°) and 115° (117°) respectively; comparably, C_{NHC}–Ru–S = 92° (91°) and Ru–S–C_{Ar} = 112° (113°) are found in **20a**.

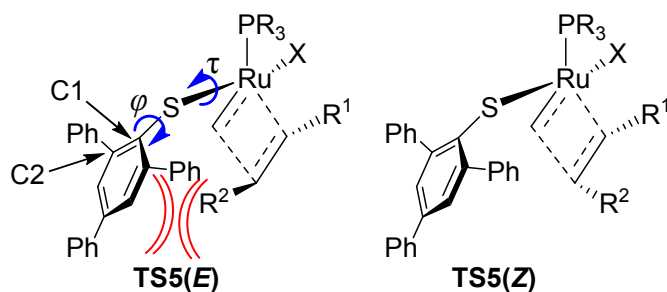


Figure 6: Rotation of the thiolate ligand, in **TS5(E)**, around Ru–S and S–C_{Ar} bonds with τ and ϕ as P–Ru–S–C1 and Ru–S–C1–C2 torsion angles respectively. Differences in steric pressure on the RCB in **TS5(E)** and **TS5(Z)** are shown.

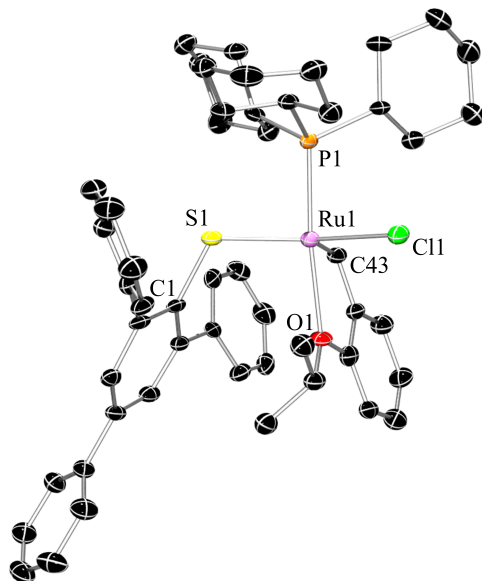


Figure 7: X-ray structure of **32** with displacement ellipsoids drawn at the 50% probability level. H-atoms and solvent molecule (*n*-pentane) are omitted for clarity. Selected geometrical parameters: Ru1–C43 = 1.840(8) Å, Ru1–P1 = 2.284(2) Å, Ru1–Cl1 = 2.358(2) Å, Ru1–O1 = 2.303(5) Å, Ru1–S1 = 2.276(2) Å, Ru1–S1–C1 = 117.0(3)°, P1–Ru1–S1 = 88.27(7)°, P1–Ru1–Cl1 = 90.21(7)°, S1–Ru1–Cl1 = 150.21(8)°, P1–Ru1–O1 = 174.4(1)°.

Testing of **32** in homocoupling of neat allylbenzene confirms the expectations and predictions made for this catalyst: lower *Z*-selectivity is obtained when compared with **20a** (entries 2 and 1, respectively, Table 2).

Because the calculated bond angles discussed above correspond well to those from the X-ray structure and the experimental results correlate positively to the calculated parameters, we can accept that the used computational method is valid. With validity established, further investigation into geometric aspects of the transition states that lead to RCB collapse can be performed. This shows that, while the transition states in the *E*-path show similar Ru–S–C_{Ar} angles (109°) for both **32** and **20a**, a sharper angle is obtained in the *Z*-pathway with the latter (115° vs. 116°), which is thought to be correlated with higher *Z*-selectivity. Relaxation of the Ru–S–C_{Ar} angle, observed in **TS5(Z)** (Figure 6) of **32**, is caused by a reduction of steric hindrance from the PCy₃ ligand. With **32** a Ru–P bond rotation of 13° is found between the **TS5(E)** and **TS5(Z)** transition states,

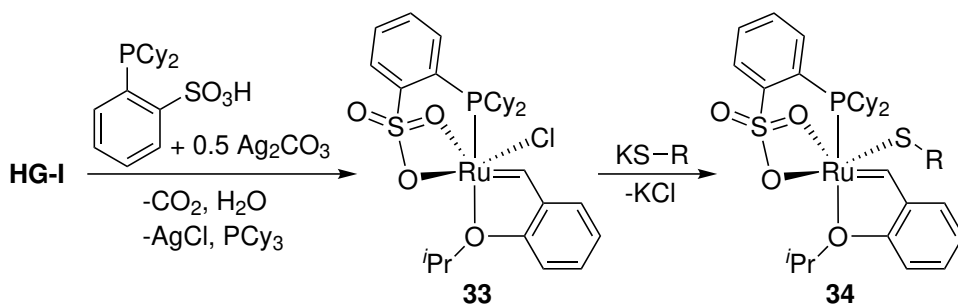
which is significantly more pronounced than the 1° Ru–C_{NHC} bond rotation in **20a**.

6.2 Restricting Phosphine Rotation

Bidentate LX-type ligands are anticipated to inhibit rotation around the Ru–P bond; with this in mind, chelating phosphine sulfonates, reported by Claverie and co-workers, were regarded as suitable candidates.¹⁶³ Indeed, the calculated Ru–P rotation between the RCB collapse transition states in the *E*- and *Z*-pathway is only 1° with compound **34** (Scheme 10); thus, this rotation is comparable to that observed with the NHC in **20a**. In addition to these hopeful results, the $\Delta\Delta G_{\text{Tot}}^\ddagger$ of 2.6 kcal·mol⁻¹ (entry 4, Table 1) predicts a *Z*-selectivity not much different from that of **20a**. Comparison of the $\Delta G(Z)_{\text{Tot}}^\ddagger$ shows that **34** is most likely somewhat less active than **20a**.

Compound **34** is easily prepared from **HG-I** in a two-step reaction: first *o*-(dicyclohexylphosphino)sulfonic acid was reacted with half an equivalent of Ag₂CO₃ in THF to produce the silver salt *in situ* (Scheme 10).¹⁶⁴ Following this, reaction with Hoveyda–Grubbs first-generation catalyst and subsequent purification yielded **33**, from which **34** was obtained through reaction with 2,4,6-triphenylbenzenethiolate. Dark green crystals, suitable for X-ray structure analysis, were obtained through diffusion of *n*-pentane in a concentrated solution of **34** in dichloromethane (DCM) at low temperature (-30°C); the molecular structure together with relevant bond lengths and angles is shown in Figure 8. Formally, **34** is an 18-electron compound, since the sulfonate moiety is bound in a $\kappa^2\text{O},\text{O}'$ fashion

Scheme 10: Two-step synthesis of compound **34**.^a



^aR = 2,4,6-triphenylphenyl.

to ruthenium. In this distorted octahedral structure, the two sulfonate oxygen atoms (O1, O2) are coordinated *trans* to the thiolate (S2) and *trans* to the alkylidene, respectively. The Ru1–O1 bond is significantly shorter than the Ru1–O2 bond (2.171 vs. 2.424 Å), which is caused by the stronger *trans*-influence of the alkylidene moiety; similarly, the S1–O1 bond (1.493 Å) is slightly longer than the S1–O2 (1.464 Å) bond. Furthermore, while the Ru1–O4 bond of the isopropoxy group is longer in **34** compared to **32** (2.345 vs. 2.304 Å), other bonds lengths are comparable between these complexes. Finally, the bond angle of ruthenium with the sulfur atom of the thiolate moiety (Ru1–S2–C19) is somewhat sharper in **34** than in **20a** (112° vs. 113°²⁰).

Despite the positive outcome of the computational predictions, **34** does not show any activity when tested in homocoupling of neat allylbenzene, neither at room temperature (RT) (entry 3, Table 2) nor at 40 °C (entry 4). This is some-

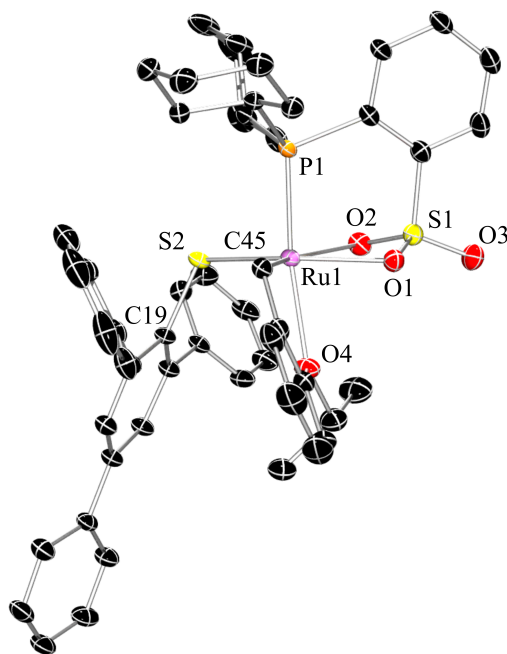


Figure 8: X-ray structure of **34** with displacement ellipsoids drawn at the 50% probability level. H-atoms and solvent molecule (DCM) are omitted for clarity. Selected geometrical parameters: Ru1–C45 = 1.8501(2) Å, Ru1–P1 = 2.2790(5) Å, Ru1–O1 = 2.1706(1) Å, Ru1–O2 = 2.4236(2) Å, Ru1–O4 = 2.3448(2) Å, Ru1–S2 = 2.2886(5) Å, S1–O1 = 1.4931(2) Å, S1–O2 = 1.4641(2) Å, S1–O3 = 1.4321(2) Å, Ru1–S2–C19 = 112.41(6)°, P1–Ru1–S2 = 89.138(2)°, P1–Ru1–O1 = 93.29(4)°, P1–Ru1–O2 = 83.25(4)°, P1–Ru1–O4 = 169.66(4)°, S2–Ru1–O1 = 157.44(4)°.

what remarkable, since compounds similar to precursor **33** are metathesis active catalysts.¹⁶³ Thus, it is likely that the presence of the additional steric pressure coming from the thiolate ligand in **34**, combined with steric and electronic effects of the $\kappa^2\text{O},\text{O}'$ -bound sulfonate moiety, hampers catalyst activation or olefin binding *trans* w.r.t. the P-atom, or creates another high barrier somewhere in the catalytic cycle.

Slightly higher barriers might be overcome at increased reaction temperatures; however, an increase to 60 °C gives only a very small amount of isomerization products (entry 5); in addition, the *E*-selective metathesis activity observed at 80 °C (entry 6) is most likely caused by decomposition of **34**. Attempts to activate the catalyst at RT through addition of two equivalents of phenylphosphoric acid (PPA) (i.e. replicating entry 3 with the acid) results again in *E*-selective metathesis, most likely due to catalyst decomposition.

A follow-up computational investigation showed barriers in the catalyst initiation pathway that are comparable or even lower than those in **20a**; thus, catalyst activation is certainly not the bottleneck. In addition, olefin coordination is more facile with **34** too. Furthermore, dissociation of the *Z*-selectivity-inducing thiolate is not a likely cause of the *E*-selective activity observed at higher temperatures. In conclusion, the inactivity of **34** remains unexplained.

6.3 Reducing the Size of the P–O Chelate

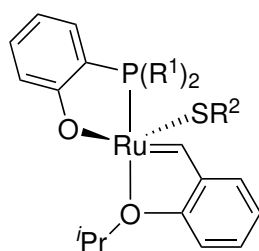
Even though no explanation for the inactivity of sulfonate complex **34** could be found, chemical intuition still regards the tridentate nature of the phosphine sulfonate as the main cause. As a consequence, the attention was shifted to chelating *o*-(dialkylphosphino)phenolate ligands.¹⁶⁵ With this family a five-membered ring ($\text{Ru}-\text{P}-\text{C}_{\text{Ar}}-\text{C}_{\text{Ar}}-\text{O}$) is formed; this is less sterically demanding than the six-membered ring ($\text{Ru}-\text{P}-\text{C}_{\text{Ar}}-\text{C}_{\text{Ar}}-\text{S}(=\text{O})_2-\text{O}$) of the sulfonate ligand in **34**. Moreover, the phenolate moiety can only bind ruthenium in a $\kappa^1\text{O}$ fashion; naturally this bidentate nature is enough to hamper rotation around the Ru–P bond. Finally, the fact that olefin metathesis catalysts highly active in co-polymerization of norbornene, producing co-polymers with increased *cis* content of the C=C bonds, were developed with these ligands sounded promising.^{166,167}

To design a catalyst that exerts optimal steric pressure towards the 2,4,6-triphenylbenzenethiolate, complexes using *o*-(dialkylphosphino)phenolate ligands with

different alkyl groups were computationally evaluated: for instance, sterically demanding *tert*-butyl groups in **37** (Figure 9) are compared with the somewhat smaller cyclohexyl groups (**38**) and the massive 1-adamantyl substituents (**39**). The consequence of using the smaller 2,4,6-trimethylbenzenethiolate in combination with *tert*-butyl groups on the phosphine (**36**) was investigated as well.

The calculated activities and selectivities of compound **36–39** (entries 5–8, Table 1) show that the catalyst bearing *o*-(di-*tert*-butylphosphino)phenolate (**37**, entry 6) is an interesting candidate: first, the $\Delta\Delta G_{\text{Tot}}^{\ddagger}$ of **37** is larger compared the values found with **32**, **36**, **38** and **39**, but lower than with **20a**, indicating that at least a decent *Z*-selectivity can be expected. Second, the absolute barrier to metathesis ($\Delta G(Z)_{\text{Tot}}^{\ddagger}$) of **37** is the lowest of the phenolate family but higher than that of **20a**; thus, the activity of **37** will be lower compared to **20a**. Surprisingly, the predicted *Z*-selectivity of **39** (entry 8) is nearly equal to that of **37**, while the former is equipped with sterically more demanding 1-adamantyl groups; this is caused by solvent corrections, as gas-phase calculations foresee a significantly higher *Z*-selectivity for **39**. The cyclohexyl groups in **38** (entry 7) are, analogue to those in monodentate **32**, unable to sufficiently prevent the thiolate from twisting, resulting in similarly low selectivity. Finally, the predictions show that a small thiolate in **36** manages to “escape” the steric bulk of the *tert*-butyl groups (entry 5).

The lower costs involving the preparation of the *o*-(di-*tert*-butylphosphino)phenolate ligand were decisive in choosing to synthesize **37** instead of **39**; in addition, with little extra effort and costs, **36** can be obtained, since both compounds are



36 $R^1 = \textit{tert}$ -butyl, $R^2 = 2,4,6$ -trimethylphenyl

37 $R^1 = \textit{tert}$ -butyl, $R^2 = 2,4,6$ -triphenylphenyl

38 $R^1 = \text{cyclohexyl}$, $R^2 = 2,4,6$ -triphenylphenyl

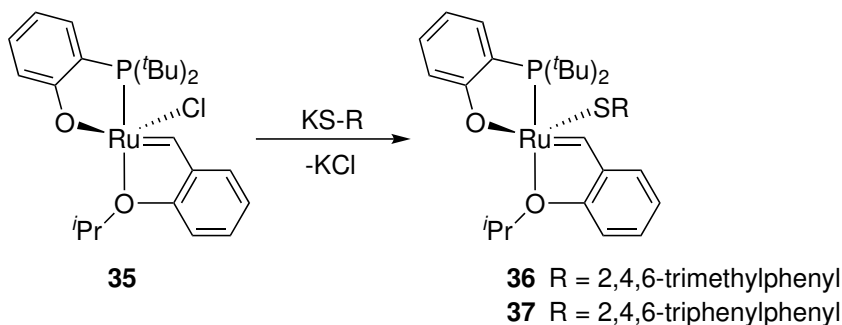
39 $R^1 = 1$ -adamantyl, $R^2 = 2,4,6$ -triphenylphenyl

Figure 9: Ruthenium *o*-(dialkylphosphino)phenolate compounds **36–39**.

made via the same precursor **35** (Scheme 11). The *o*-(di-*tert*-butylphosphino)-phenolate ligand and the aforementioned precursor synthesized with it were prepared according to literature procedures.^{167,168} Subsequent reaction of **35** with an equivalent of potassium 2,4,6-trimethylbenzenethiolate and potassium 2,4,6-triphenylbenzenethiolate in THF yielded **36** and **37**, respectively. Dark red crystals suitable for X-ray structure analysis were obtained through diffusion of *n*-pentane into a concentrated solution of **37** in DCM at low temperature ($-32\text{ }^{\circ}\text{C}$); the molecular structure together with relevant bond lengths and angles is shown in Figure 10. Compound **37** is a slightly distorted square pyramid with the alkylidene located at the apical position. Of the remaining ligands, which occupy basal positions, the thiolate moiety (S1) and the phosphine (P1) are located *trans* w.r.t. phenolate and alkoxy oxygen atoms (O2 and O1), respectively. Bond lengths are comparable to those found in **20a**,²⁰ **32** and **34**; however, the bond distance between ruthenium and the phenolate oxygen ($\text{Ru1-O2} = 2.025\text{ \AA}$) is distinctly shorter than those of the $\text{Ru-O}_{\text{sulfonate}}$ in **34** (2.171 and 2.424 \AA); in addition, with 84° the P1-Ru1-O2 angle is smaller than 90° , showing the distortion from true square pyramidal geometry. The bond angle around the sulfur atom of the thiolate ligand ($\text{Ru1-S1-C25} = 114^{\circ}$) is sharper than that of **32** (117°) but larger than that of **34** (112°).

Catalytic testing shows that with **36** in homocoupling of neat allylbenzene mainly by-products are obtained (entry 7, Table 2); the 2% yield in olefin metathesis products is obtained with relatively low *Z*-selectivity (50%), as predicted (entry 5, Table 1). Analysis of **TS5(E)** shows that angles τ and ϕ deviate significantly from the ideal values: actually, the deviation in **36** is the largest when compared to **37**, **38** and **39** (entries 5–8, Table 1); thus, the bulky *tert*-butyl groups

Scheme 11: Synthesis of compounds **36** and **37**.



on the phosphine do not provide enough steric pressure to prevent twisting of the relatively small 2,4,6-trimethylbenzenethiolate in **36**.

Compound **37** catalyzes homocoupling of neat allylbenzene with a *Z*-selectivity over 80% (entry 8, Table 2); this is the highest *Z*-selectivity obtained this far with phosphine-based first-generation-style catalysts. Furthermore, the yield of **37** is larger than that of **36** and **32**, which is in agreement with the lower calculated barrier to olefin metathesis ($\Delta G(Z)_{\text{Tol}}^{\ddagger}$) of **37**.

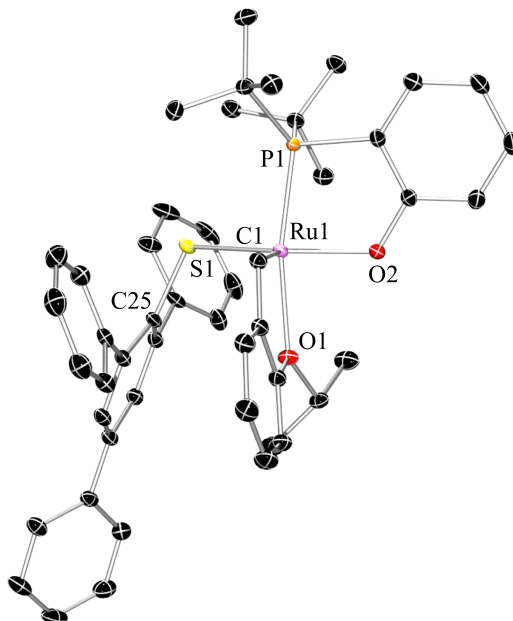


Figure 10: X-ray structure of **37** with displacement ellipsoids drawn at the 50% probability level. H-atoms and solvent molecule (DCM) are omitted for clarity. Selected geometrical parameters: Ru1–C1 = 1.846(2) Å, Ru1–P1 = 2.2653(5) Å, Ru1–O1 = 2.2531(2) Å, Ru1–O2 = 2.0246(2) Å, Ru1–S1 = 2.2846(6) Å, Ru1–S1–C25 = 114.21(7)°, P1–Ru1–S1 = 92.412(2)°, P1–Ru1–O1 = 168.79(5)°, P1–Ru1–O2 = 83.51(4)°, S1–Ru1–O2 = 152.11(5)°.

Table 1: Comparison of computed parameters of assessed complexes with **20a**.

entry	cat.	$\Delta\Delta G_{\text{Tol}}^{\ddagger}$ ^a (kcal·mol ⁻¹)	$\Delta G(Z)_{\text{Tol}}^{\ddagger}$ ^b (kcal·mol ⁻¹)	τ ^c (°)	ϕ ^c (°)
1	20a	3.1	18.8	n.a.	n.a.
2	31	-0.8	n.a.	-137	-115
3	32	0.9	28.0	-174	-90
4	34	2.6	22.0	n.a.	n.a.
5	36	0.3	26.3	-165	-99
6	37	1.6	24.8	-168	-94
7	38	0.8	26.7	-178	-88
8	39	1.5	n.a.	178	-85

^aThe relative energies represent a measure of *Z*-selectivity; $\Delta\Delta G_{\text{Tol}}^{\ddagger} = \Delta G(E)_{\text{Tol}}^{\ddagger} - \Delta G(Z)_{\text{Tol}}^{\ddagger}$. ^b $\Delta G(Z)_{\text{Tol}}^{\ddagger}$ is the absolute barrier to **TS5(Z)** with the precatalyst as reference. ^c Calculated torsion angles P–Ru–S–C1 (τ) and Ru–S–C1–C2 (ϕ) in the transition state leading to MCB rupture in the *E*-pathway; ideal torsion angles are $\tau = 180^\circ$ and $\phi = 90^\circ$ (see Figure 6).

Table 2: Comparison of synthesized complexes with **20a** in homocoupling of neat allylbenzene.

entry	cat. ^a	<i>T</i> (°C)	<i>t</i> (h)	conv. ^b (%)	yield ^b (%)	<i>Z</i> ^b (%)
1	20a ^c	20	1	7	5	85
2	32	20	1	1	0.2	n.d.
			16	10	1	61
3	34	20	1	0	0	n.a.
4	34	40	1	0	0	n.a.
5	34	60	1	1	0	n.a.
6	34	80	1	73	9	29
			24	100	7	29
7	36	20	1	60	2	50
8	37	20	1	21	13	81

^aCatalyst loading = 1 mol%. ^bDetermined by ¹H NMR analysis. Conversion is the amount of substrate converted, whereas yield refers to the amount of substrate converted into metathesis homocoupling products. The difference between conversion and yield corresponds to the amount of 1-alkene to 2-alkene isomerization of the substrate. ^cCatalyst loading = 0.1 mol%.

6.4 Different Reaction Conditions

A series of experiments, investigating the performance of **37** under variation in the reaction temperature, catalyst loading, solvent and substrate concentration (Table S1, SI of **Paper I**), yielded the following results:

- temperature increase promotes isomerization of the substrate, especially at high conversion (entries 1–3), possibly because isomerization-active decomposition products start to accumulate;
- higher catalyst loading gives only little improvement in *Z*-isomer yield (entries 1, 4 and 5). It is likely that even at the lowest used catalyst loading (1 mol%) saturation is obtained. Thus, other factors, such as diffusion to and from the catalyst, might determine the outcome of these experiments;
- in solvents, lower conversion and yields are observed compared to neat allylbenzene, most likely due to a lower concentration of reactants; between the various solvents only insignificant differences are observed (entries 6–8);
- reduction in the substrate concentration gives lower conversion and yield (entries 9–12).

In addition, the effects of different additives were studied:

- due to its ability to destruct hydrides or even block their formation, isomerization is effectively prevented with 2,6-dichloro-1,4-benzoquinone (QUI, entry 13).¹⁶⁹ Unfortunately, however, addition of QUI is, in this case, detrimental to *Z*-selectivity;
- phenylphosphoric acid (PPA, entry 14) is supposed to prevent isomerization in a similar fashion as QUI.¹⁷⁰ However, here low conversion and yield are obtained, with moderate *Z*-selectivity;
- tricyclohexylphosphine oxide (TCPO, entry 15) and water (entry 16) prevent isomerization of the *Z*-product in the *E*-product. As a consequence, high *Z*-selectivity is maintained at longer reaction times; however, with water as additive, progress of the reaction unfortunately stops at ca. 25% conversion due to inactivation or decomposition;

The discussion above leads to the general conclusion that at 20 °C, using 1 mol% catalyst in neat substrate with five equivalents of TCPO as additive, optimal results were obtained.

Building on these results, catalyst **36** and **37** were tested in several neat substrates, with the addition of TCPO when the substrate is susceptible to isomerization (Table 3). Addition of TCPO does neither improve the *Z*-selectivity nor the yield of **36** in allylbenzene (AB, entry 1). Using this catalyst, the highest *Z*-selectivity was obtained in allyltrimethylsilane (ATMS, entry 2), which is mainly caused by the steric effects of the large silyl groups; an attempt to improve selectivity through addition of TCPO resulted in a lack of activity (entry 3).

Catalyst **37** converts 1-octene (OCT) and allyl acetate (AAc) with high *Z*-selectivity and moderate yield (entries 4 and 5); in addition, only negligible isomerization of the substrate is observed. However, *Z*-selectivity in 2-allyloxyethanol (AOE) is low (entry 6); this was improved by addition of TCPO (entry 7). Furthermore, yield and *Z*-selectivity in 4-phenyl-1-butene (PB) are similar to those obtained with allylbenzene (entries 8 and 9). An important observation is that, in contrast to NHC-based catalysts, **37** gives only negligible or little *Z/E* isomerization of the product with increasing substrate conversion; this is possibly due to low secondary metathesis activity.

Table 3: Comparison of **36** and **37** in homocoupling with different substrates.

entry	cat. ^a	sub. ^b	additive ^c	<i>t</i> (h)	conv. ^d (%)	yield ^d (%)	<i>Z</i> ^d (%)
1	36	AB	TCPO	8	95	6	38
2	36	ATMS		1	1	0.5	88
3	36	ATMS	TCPO	1	0		
4	37	OCT		8	27	27	82
5	37	AAc		8	24	24	92
6	37	AOE		8	8	3	54
7	37	AOE	TCPO	8	8	4	74
8	37	PB		1	14	12	80
				8	77	36	71
9	37	PB	TCPO	8	43	34	79

A complete overview of the results obtained with **36** and **37** is found in Table 6 of **Paper I**. ^aCatalyst loading = 1 mol%, *T* = 20 °C. ^bAB = allylbenzene, ATMS = allyltrimethylsilane, OCT = 1-octene, AAc = allyl acetate, AOE = 2-allyloxyethanol, PB = 4-phenyl-1-butene. ^cTCPO = tricyclohexylphosphine oxide (5 equiv.) ^dDetermined by ¹H NMR analysis. iso = conv. – yield. For entries 1, 6, and 7, iso = DBM of 1-alkene to 2-alkene; for entry 2, iso = DBM of 1-alkene to 2-alkene (major) + CM of substrate and 2-alkene isomer (minor product);¹³⁷ for entries 8 and 9, iso = DBM of 1-alkene to 2-alkene (major) + CM of substrate and 2-alkene isomer (minor product) + DBM of the HC product (trace).

Furthermore, ROMP performed with **32**, **34**, **36** and **37** in neat *cis*-cyclooctene gave low activities and only moderate *Z*-selectivities. While higher than obtained with **HG-I**, these *Z*-selectivities were not much different from those obtained by Chen and co-workers.¹⁷¹

Chapter 7

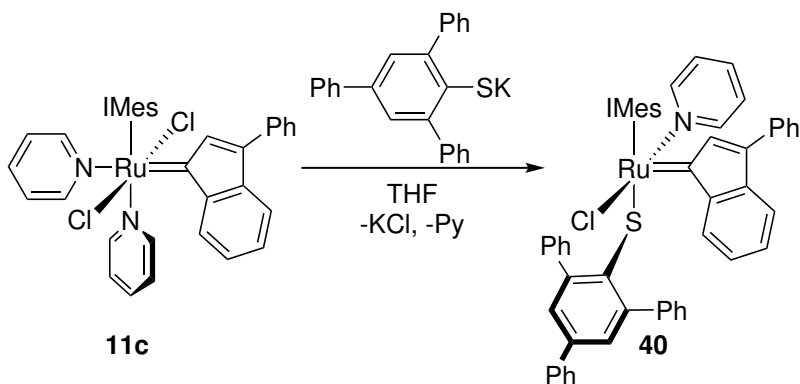
Z-Selective Ru-Indenylidene Catalysts

The previous chapter illustrates that the method used to obtain **20a** can easily be extended to yield first-generation *Z*-selective catalyst **37**. With the generality of this design established, an attempt was made to further improve this system; higher thermal stability of Ru-indenylidene catalysts, compared to those based on benzylidene (Section 2.2.3), was the prime motivation to turn towards these types of catalysts. Although it would be interesting to make *Z*-selective congeners of **10b** and **10c** (Chart 3), substitution of the chloride ligand for the large 2,4,6-triphenylbenzenethiolate is unlikely to succeed due to steric reasons: the steric bulk of the NHC and tricyclohexylphosphine is complemented with that of the indenylidene moiety and is significantly larger than with benzylidene.

Catalysts **11b** and **11c** offer a better starting point: the two much smaller pyridine moieties that replace the PCy₃ ligand are expected to dissociate easily. This creates space for the incoming thiolate during chloride substitution, after which one equivalent of pyridine will probably re-coordinate. Furthermore, the fast initiation obtained with nonselective Ru-bipyridine complexes can be transferred to *Z*-selective Ru-monothiolate catalysts.¹⁷² Therefore, it is likely that these properties will be maintained in *Z*-selective analogues of **11b** and **11c** as well. This chapter discusses the synthesis and properties of such catalysts, representing the work in **Paper IV**.

7.1 Catalyst Synthesis

Compound **40** was obtained by reacting **11c**⁹³ with one equivalent of potassium 2,4,6-triphenylbenzenethiolate in THF (Scheme 12). Dark red crystals, suitable for X-ray structure analysis, were obtained by slow diffusion of *n*-pentane into a

Scheme 12: Synthesis of compound **40**.

concentrated solution of **40** in DCM at low temperature ($-32\text{ }^\circ\text{C}$); the molecular structure, relevant bond lengths, and angles are shown in Figure 11.

Compound **40** adopts a slightly distorted square pyramidal geometry, with the indenylidene occupying the apical position, a configuration typical of pentacoordinate Grubbs catalyst precursors. Surprisingly, however, in the basal plane, the two ligands with the strongest *trans* influence, the thiolate ligand (S1) and IMes (C1),

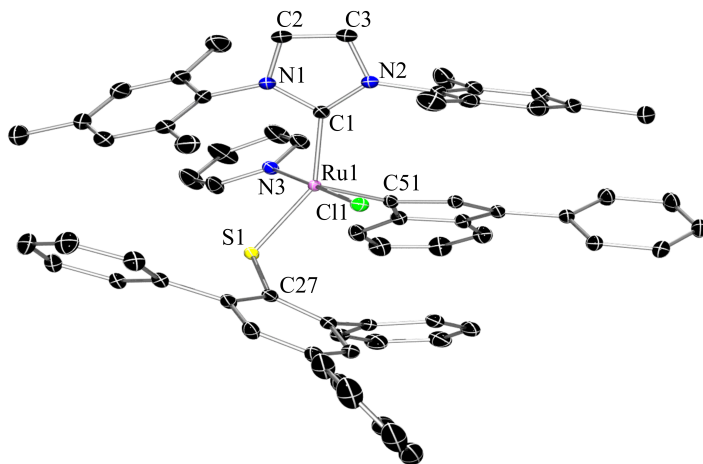
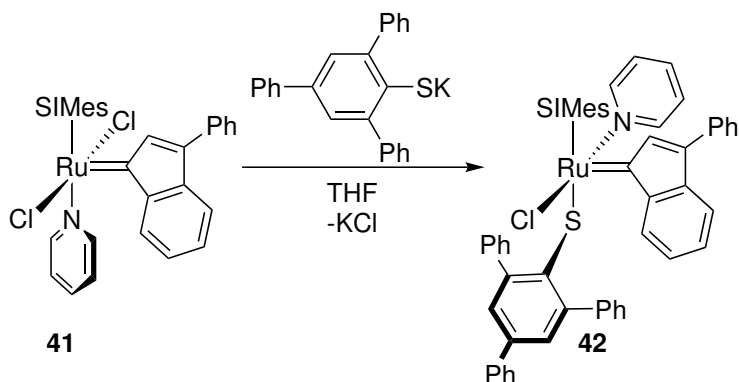


Figure 11: X-ray structure of **40** with displacement ellipsoids drawn at the 50% probability level. H-atoms and solvent molecules (DCM) are omitted for clarity. Selected geometrical parameters: Ru1–C1 = 2.0911(16) Å, Ru1–Cl1 = 2.3903(4) Å, Ru1–N3 = 2.1113(14) Å, Ru1–C51 = 1.8731(16) Å, Ru1–S1 = 2.3066(4) Å, C2–C3 = 1.346(3) Å, N1–C1–N2 = 103.24(14)°, C1–Ru1–Cl1 = 88.52(5)°, C1–Ru1–N3 = 89.71(6)°, C1–Ru1–C51 = 106.20(7)°, C1–Ru1–S1 = 145.78(5)°, C51–Ru1–Cl1 = 91.76(5)°, C51–Ru1–N3 = 93.03(6)°, C51–Ru1–S1 = 108.01(5)°, N3–Ru1–S1 = 88.53(4)°, Cl1–Ru1–S1 = 90.408(14)°, Ru1–S1–C27 = 114.26(5)°.

are positioned *trans* to each other ($\text{C1-Ru1-S1} = 146^\circ$). The total steric pressure, larger than usual due to the indenylidene ligand, prevents the *cis*-coordination observed in corresponding alkylidene monothiolate complexes (Section 3.1 and Chapter 6). It is likely that, to make room for the incoming bulky thiolate, pyridine dissociates during synthesis and subsequently re-coordinates *cis* to IMes. If this solid-state structure equals that of the precatalyst in solution, some problems may arise: the weak *trans* influence of Cl (Cl1) might not be able to warrant the rapid pyridine dissociation expected from fast-initiating catalysts. Furthermore, the incoming olefin and the RCB intermediate will experience a roughly equally distributed steric pressure from IMes and the thiolate, both located on opposite sites *cis* w.r.t. the ring. This, in contrast to the selectivity-inducing steric pressure towards a single face of the RCB seen with the other Ru-monothiolate catalysts (Section 3.2), is expected to have negative consequences for the *Z*-selectivity.

Reaction of $\text{RuCl}_2(\text{SIMes})(\text{py})(3\text{-phenylindenylidene})$ (**41**, Scheme 13), commercially available as Umicore M31, with one equivalent of potassium 2,4,6-triphenylbenzenethiolate in THF afforded, after purification, **42**, the SIMes analogue of **40**. Unfortunately, ^1H NMR spectra taken of the reaction mixture showed that conversions $> 70\%$ could not be reached; subsequently, addition of extra thiolate or extension of the reaction time (> 30 min) led to near complete decomposition of the product. Dark red crystals suitable for X-ray structure analysis were obtained through slow diffusion of *n*-pentane into a concentrated solution of **42** in DCM at low temperature (-32°C); the molecular structure, relevant bond lengths, and angles are shown in Figure 12.

Scheme 13: Synthesis of compound **42**.



Compound **42**, similar to **40**, adopts a slightly distorted square pyramidal geometry, with the indenylidene occupying the apical position, and with *trans*-positioning of the SIMes and the thiolate in the basal plane. The shorter Ru–C_{NHC} bond in **42** compared to that in **40** (Ru1–C1 = 2.080 vs. 2.091 Å) shows that SIMes is more strongly bound to ruthenium than IMes; this agrees with calculations on LCl₂R=CH₂ complexes that show slightly stronger L→Ru σ -donation and $d\pi\rightarrow L\pi$ back-donation with SIMes when compared to IMes.¹⁷³ Furthermore, the N1–C1–N2 angle is less sharp in **42** (107° vs. 103° in **40**); as a consequence, the ligands located *cis* w.r.t. the NHC are expected to experience a slightly higher steric pressure from the mesityl groups. The stronger L→Ru σ -donation and steric pressure of the more tightly bound SIMes moiety should translate in longer bond lengths for the other ligands. Indeed, the Ru=C_{Ind} and Ru–N_{Py} bonds are slightly larger in **42** (Ru1–C51 = 1.875 vs. 1.873 Å; Ru1–N3 = 2.113 vs. 2.111 Å); however, the Ru–Cl bond is shorter (Ru1–Cl1 = 2.388 vs. 2.390 Å) Finally, the larger *trans* effect of SIMes is demonstrated by the elongated Ru1–S1 bond in **42** (2.318 vs. 2.307 Å in **40**).

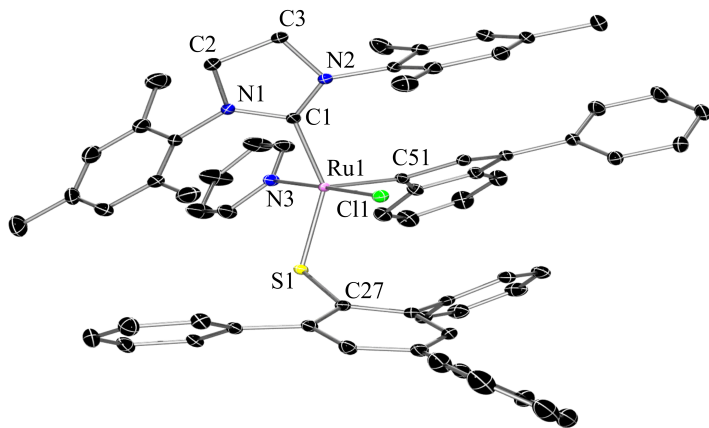


Figure 12: X-ray structure of **42** with displacement ellipsoids drawn at the 50% probability level. H-atoms and solvent molecules (DCM) are omitted for clarity. Selected geometrical parameters: Ru1–C1 = 2.0795(15) Å, Ru1–Cl1 = 2.3879(4) Å, Ru1–N3 = 2.1134(14) Å, Ru1–C51 = 1.8745(15) Å, Ru1–S1 = 2.3181(4) Å, C2–C3 = 1.520(2) Å, N1–C1–N2 = 106.56(14)°, C1–Ru1–Cl1 = 87.21(4)°, C1–Ru1–N3 = 91.37(6)°, C1–Ru1–C51 = 107.23(6)°, C1–Ru1–S1 = 145.07(4)°, C51–Ru1–Cl1 = 91.25(5)°, C51–Ru1–N3 = 93.03(6)°, C51–Ru1–S1 = 107.66(5)°, N3–Ru1–S1 = 88.48(4)°, Cl1–Ru1–S1 = 90.385(13)°, Ru1–S1–C27 = 113.73(5)°.

Additional attempts were made to synthesize analogues of **40** and **42** that bear the 2,4,6-tri(di-*m*-methylphenyl)benzenethiolate; unfortunately, the use of this even bulkier thiolate resulted in decomposition or gave yields that are too low to isolate.

^1H and ^{13}C NMR spectra recorded of **40** and **42** (see SI of **Paper IV**) show that the weak *trans* influence of Cl does not hamper pyridine dissociation, as was theorized above: the complexity of these spectra indicates that mixtures of **40** and **42** with their respective pyridine-free 14-electron complexes are readily established in solution. Furthermore, the fraction of dissociated pyridine quickly reaches > 90% when **40** is dissolved in chloroform-*d* and kept at 40 °C (SI of **Paper IV**); moreover, pyridine dissociation is shown to be irreversible.

7.2 Performance in Catalysis

Both **40** and **42** initiate metathesis rapidly (entries 1–10, Table 4); moreover, *Z*-selectivities up to and above 80% were obtained in HC of 1-alkenes, despite the unusual X-ray structures predicting negative consequences for the *Z*-selectivity. In addition, **42** is the most active catalyst, agreeing with the higher activity expected for SIMes-bearing catalysts (Section 2.2.3). The high conversion reached in entry 5 most likely explains the somewhat lower *Z*-selectivity. Entries 5, 6 and 9 show that only a small amount of double-bond migration products are formed with **42** in allylbenzene and 1-octene. However, with 4-phenyl-1-butene significant double-bond migration is observed, especially at high conversion (entries 7 and 8).

The results in Table 5 show the effect of pyridine on the catalytic performance: selectivity towards metathesis and the *Z*-product is reduced when pyridine is lost from the microcrystalline **40**. After **40** is freshly crystallized, slightly less pyridine than the stoichiometric amount is observed; batch B shows that 0.04 equivalents of pyridine, compared to the stoichiometric amount, were lost; after a subsequent recrystallization (batch A), pyridine was determined to be 0.08 equivalents less than the stoichiometric amount. Co-crystallization of **40** with the corresponding 14-electron complex, obtained after pyridine dissociation in solution, could explain this observation. When solid material from batch B was dried under vacuum, no loss of pyridine was observed.

Even though there is not much difference in the amount of pyridine between batches A and B (0.92 and 0.96 equivalents, respectively), significant differences

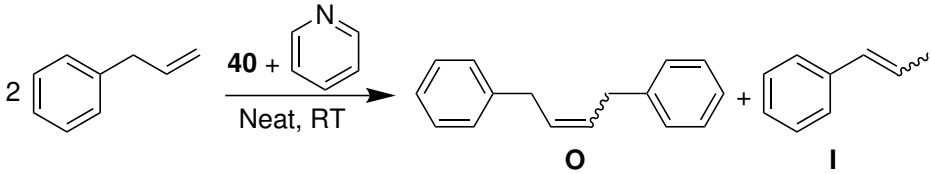
Table 4: Performance of complexes **40** and **42** in homocoupling of neat 1-alkenes.^a

$2 \text{ R-CH=CH}_2 \xrightarrow[\text{Neat, RT}]{\text{40 or 42}} \text{R-CH=CH-R (O)} + \text{R-CH=CH-R (I)}$

entry	cat.	cat. load. (mol%)	sub. ^b	<i>t</i> (min)	conv. ^c (%)	O/I ^{c, d}	<i>Z</i> ^c (%)
1	40 ^e	0.5	AB	5	8	13	80
2	40 ^e	0.5	PB	5	14	3	82
3	40 ^e	0.5	PB	15	34	4	82
4	40 ^e	0.1	OCT	15	4	9	85
5	42	0.5	AB	5	55	62	76
6	42 ^f	0.5	AB	30	19	28	83
7	42	0.5	PB	15	34	8	88
8	42	0.5	PB	60	72	4	83
9	42	0.1	OCT	15	5	36	87
10	42	0.01	OCT	240	22	10	84

^aR = phenyl, C₅H₁₁, or benzyl. ^bAB = allylbenzene, OCT = 1-octene, and PB = 4-phenyl-1-butene. ^cDetermined by ¹H NMR analysis using hexamethylbenzene as internal standard. ^dFraction of the homocoupling product (**O**) and the double-bond migration (isomerization) product (**I**) of allylbenzene. ^eBatch B +0.1 equiv. of pyridine. ^f+0.1 equiv. of pyridine.

in *Z*-selectivity were observed (entries 1 and 14; 2 and 15, Table 5). Furthermore, *Z*-selectivity and selectivity to olefin metathesis are increased, at the cost of a reduction in catalytic activity, when 0.1 equivalents of pyridine is added to the catalytic mixture (entries 3–6 and 16–19). At > 0.1 equivalents of pyridine, a further reduction of the initiation rate is observed without additional improvement of the *Z*-selectivity (entries 7–13). The most likely cause for the reduction in yield of *Z*-product with the loss of pyridine is the decomposition of the catalyst into isomerization-active species. Dissociation of pyridine from the 16-electron precatalysts yields the active species; these less stable 14-electron compounds are known to decompose into alkene isomerization catalysts (Chapter 4 and Chapter 8).

Table 5: Influence of pyridine on the catalytic properties of **40** in neat allylbenzene.


entry	batch of 40 ^a	equiv. pyridine	<i>T</i> (min)	conv. ^b (%)	O / I ^{b,c}	<i>Z</i> ^b (%)
1	A	0	5	14	10	61
2	A	0	15	24	7	40
3	A	0.1	5	5	14	82
4	A	0.1	15	12	11	80
5	A	0.1	60	28	12	71
6	A	0.1	120	62	8	46
7	A	0.2	5	2	5	83
8	A	0.2	15	10	6	81
9	A	0.2	60	24	13	78
10	A	0.2	120	38	11	75
11	A	1	5	0.2	n.d.	n.d.
12	A	1	15	1	3	82
13	A	1	60	6	12	80
14	B	0	5	12	6	72
15	B	0	15	23	7	58
16	B	0.1	5	8	13	80
17	B	0.1	15	18	17	78
18	B	0.1	60	32	11	71
19	B	0.1	120	44	9	69

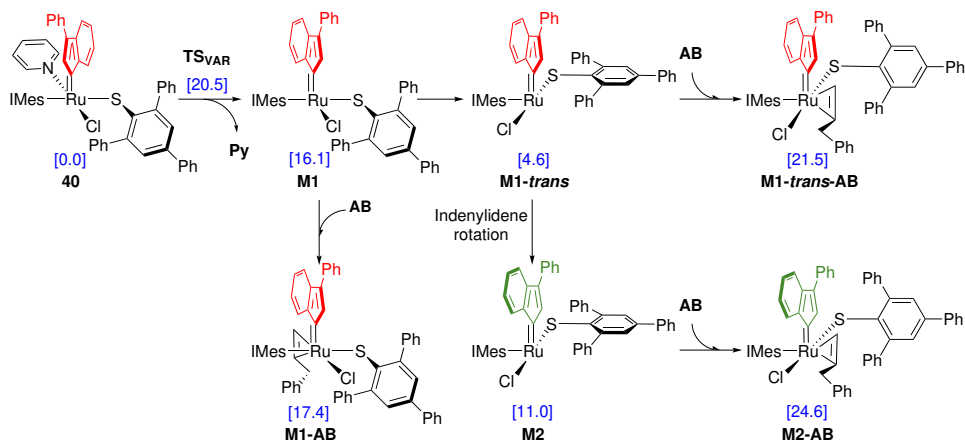
^aPyridine content in batches A and B determined with ¹H NMR to be 0.08 and 0.04 equiv. below the stoichiometric amount. Cat. load. = 0.5 mol%. ^bDetermined by ¹H NMR analysis using hexamethylbenzene as internal standard. ^cFraction of the homocoupling product (**O**) and the double-bond migration (isomerization) product (**I**) of allylbenzene.

7.3 Computational Investigation

A computational investigation into the unexpected activity and *Z*-selectivity observed with **40** and **42** was performed using DFT. Pyridine dissociation is, with a barrier of 20.5 kcal·mol⁻¹ in **40**, relatively facile; this is in line with what is expected of fast initiating catalysts. While olefin binding to the thus obtained 14-electron species (**M1**, Scheme 14) is not energetically costly, the subsequently formed π -complex **M1-AB**, with the olefin *cis* w.r.t. the NHC, does not have a configuration suitable for cycloaddition and metathesis.

Isomerization of **M1**, in which the thiolate moves to the position *trans* to Cl, affords the relatively stable **M1-*trans*** (4.6 kcal·mol⁻¹ w.r.t. **40**). The olefin binds this species *trans* w.r.t. the NHC, resulting in metathesis-potent π -complex **M1-*trans*-AB**. After one cycle the indenylidene moiety is replaced with 2-phenylethylidene and subsequent reaction leads to productive olefin metathesis. In this way, the configuration responsible for *Z*-selectivity in Ru-monothiolate catalysts such as **20a** is reproduced (Section 3.2). Alternatively, a 180°-rotation of the indenylidene ligand around the Ru=C_{Ind} bond in **M1-*trans***, which is surprisingly easy with a barrier of no more than 13 kcal·mol⁻¹, gives **M2**; subsequently, the metathesis cycle is entered after via π -complex **M2-AB**. Since the difference in stability between **M1-*trans*-AB** and **M2-AB** is merely 3.1 kcal·mol⁻¹, and **M2** is only 6.4 kcal·mol⁻¹ less stable than **M1-*trans***, it is likely that both pathways are active. Some other pathways were considered: isomerization of the indenylidene ligand to less sterically congested allenylidene (Section 2.2.3) was presumed to afford enough space for olefin binding; however, this species lies significantly higher on the potential energy surface. In addition, dissociation of the chloride is associated with high energetic costs as well.

Scheme 14: Activation of **40** through isomerization.^a



^aEnergies calculated in toluene at RT are given in kcal·mol⁻¹. AB = allylbenzene and Py = pyridine.

Chapter 8

Ru-Alkylidene Loss and Isomerization

The catalytic experiments in the previous two chapters show that double-bond migration (isomerization) virtually always runs in parallel with the olefin metathesis reaction. For instance, with the best first-generation *Z*-selective catalyst to date (**37**), only 62% of the converted allylbenzene is retrieved as olefin metathesis product (entry 8, Table 2); the remainder is the 2-alkene. Double-bond migration not only wastes precious substrates, but, combined with subsequent olefin metathesis reactions, it also produces a complex mixture, from which isolation of the desired product is difficult and costly (Section 4.1). Another important source of by-products is isomerization of the *Z*- into the *E*-isomer, especially in connection with what discussed in the previous two chapters. This process is detrimental to *Z*-selectivity and cancels the efforts of carefully designing *Z*-selective catalysts. As a matter of fact, Grubbs-type olefin metathesis catalysts, especially those that are *Z*-selective, should possess a higher stability to be viable in industrial processes.

Several ruthenium species originating from catalyst decomposition, such as ruthenium hydrides (Section 4.2) and nanoparticles (Section 4.3), were seen as possible culprits; however, they merely give a partial explanation to the observed double-bond migration: ruthenium hydrides show low isomerization activity and ruthenium nanoparticles seem at most to account for only 50% of total substrate isomerization; in addition, the formation of these RuNPs is not completely explained.

Paper II was conceived from the lack of a well established decomposition-isomerization pathway with clearly identified isomerization-active decomposition products that agree with the rate of isomerization observed during metathesis; the main results of this study are discussed in this chapter.

8.1 Evaluation of Known Mechanisms

Recalculation and re-evaluation of the ethene-assisted decomposition pathway postulated by Janse van Rensburg et al. (Section 4.4) shows that the barrier of β -hydrogen transfer ($\text{TS}_{\text{VR2/VR3}}$, Scheme 15), from the unsubstituted RCB (VR2) to form allyl ruthenium hydride VR3 , is only 1.3 kcal·mol⁻¹ higher than that of olefin metathesis (i.e. 23.5 kcal·mol⁻¹ w.r.t. HG-II). This indicates that the mechanism is likely contributing to catalyst decomposition. Furthermore, due to its relatively high stability (-3.4 kcal·mol⁻¹), VR2 acts as an energetic sink,¹⁷⁴ trapping “ruthenium” that would otherwise be available as OM5 , thus slowing down olefin metathesis.

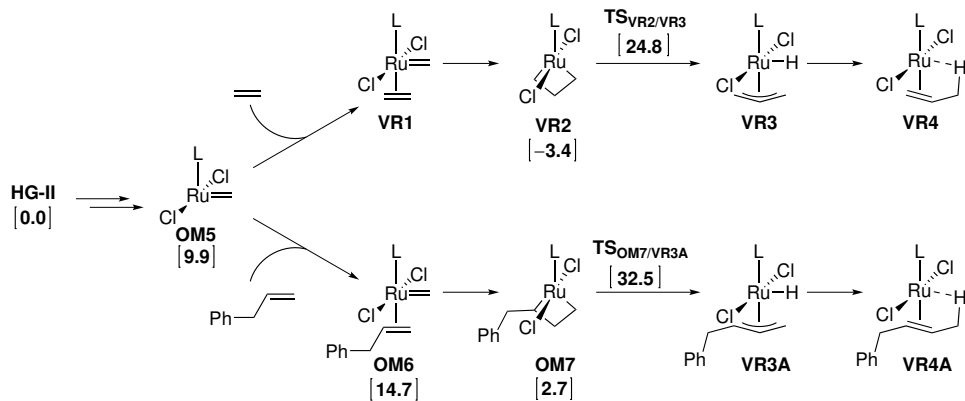
An excellent solution would be to completely disable the OM5-VR4 pathway through continuous removal of ethene from the reaction mixture. This is technically not difficult to achieve: application of a static vacuum or continuous degassing with argon removes all of the gas during catalysis. However, with these measures in place, combined with low catalyst loading to minimize the formation of isomerization-active dinuclear ruthenium complexes such as $\mathbf{29}$, isomerization and catalyst decomposition are far from eliminated.¹⁷⁵ This suggests that other mechanisms are at work; with all other options excluded, the main suspect is the substrate itself.

Repetition of the calculations with allylbenzene as substrate showed that substituted RCB OM7 (Scheme 15) does not act as an energetic sink ($\Delta G(\text{OM7}) = 2.7$ kcal·mol⁻¹). Moreover, the barrier of 32.5 kcal·mol⁻¹ to β -hydrogen transfer ($\text{TS}_{\text{OM7/VR3A}}$) shows that this mechanism is much less advantageous with allylbenzene than with ethene. On the other hand, the aforementioned barrier is only 9 kcal·mol⁻¹ higher than that leading to homocoupling of allylbenzene, and therefore it does afford a major pathway to catalyst decomposition. Nevertheless, other mechanisms that commence from the intermediates located before $\text{TS}_{\text{OM7/VR3A}}$ might offer lower barriers.

8.2 Decomposition via RCB Ring-Expansion

Relatively stable substituted RCB OM7 , readily obtained from allylbenzene and OM5 , forms a viable starting point for ring expansion. In literature, examples are found of repeated ethene insertion into a metallacycle. Increasing flexibility of

Scheme 15: Mechanism of RCB decomposition through β -hydrogen elimination postulated by Janse van Rensburg.^a



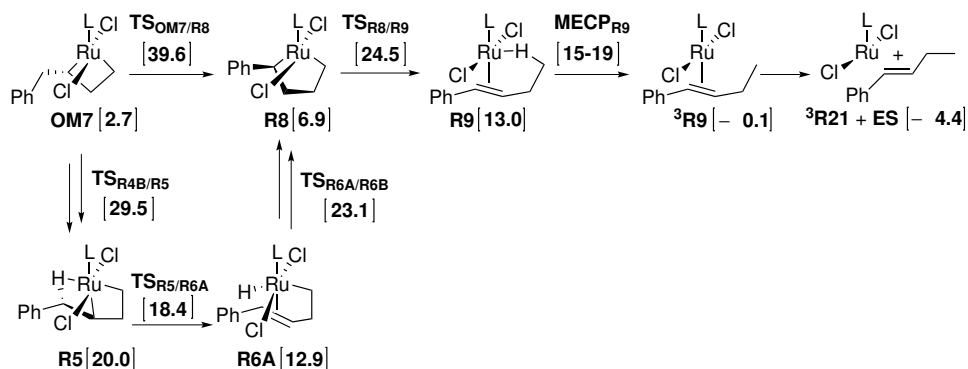
^aGibbs free energy, in square brackets, given in kcal·mol⁻¹ and relative to precatalyst **HG-II**. L = SIMes.

the expanding ring eventually allows relatively easy β -hydride abstraction, yielding trimers and tetramers of ethene.¹⁷⁶ Calculations show that such an expansion with **OM7** yields ruthenacyclopentane **R8** (Scheme 16). From here, π -complex **R9** is obtained from a 1,3-hydride shift that is relatively easy considering that the barrier **TS_{R8/R9}** is only 1 kcal·mol⁻¹ higher w.r.t. the metathesis barrier; subsequently, the 13.1 kcal·mol⁻¹ more stable triplet-state **³R9** is obtained effortlessly from singlet-state intermediate **R9**; finally, formation of 12-electron species **³R21** through olefin release is barrier-less.

Although **TS_{OM7/R8}** is associated with an energetically unfavorable barrier of 39.6 kcal·mol⁻¹, performing the conversion of **OM7** to **R8** in several separate consecutive steps, via **R5**, reduces this barrier significantly. Here, formation of the Ru–H agostic interaction in **R5** via transition state **TS_{R4B/R5}** forms the highest barrier (29.5 kcal·mol⁻¹), not only to the formation of **R8** but in the whole pathway. Moreover, this barrier is only 6 kcal·mol⁻¹ higher than that of olefin metathesis and 3 kcal·mol⁻¹ smaller than that of β -hydrogen abstraction (**TS_{OM7/VR3A}**); thus, ring-expansion is favored over the mechanism postulated by Janse van Rensburg.

8.3 Identifying a Key Isomerization Culprit

The triplet-state 12-electron species **³R21** is not only obtained via the ring expansion discussed in the previous section: olefin-decoordination from both **VR4** and

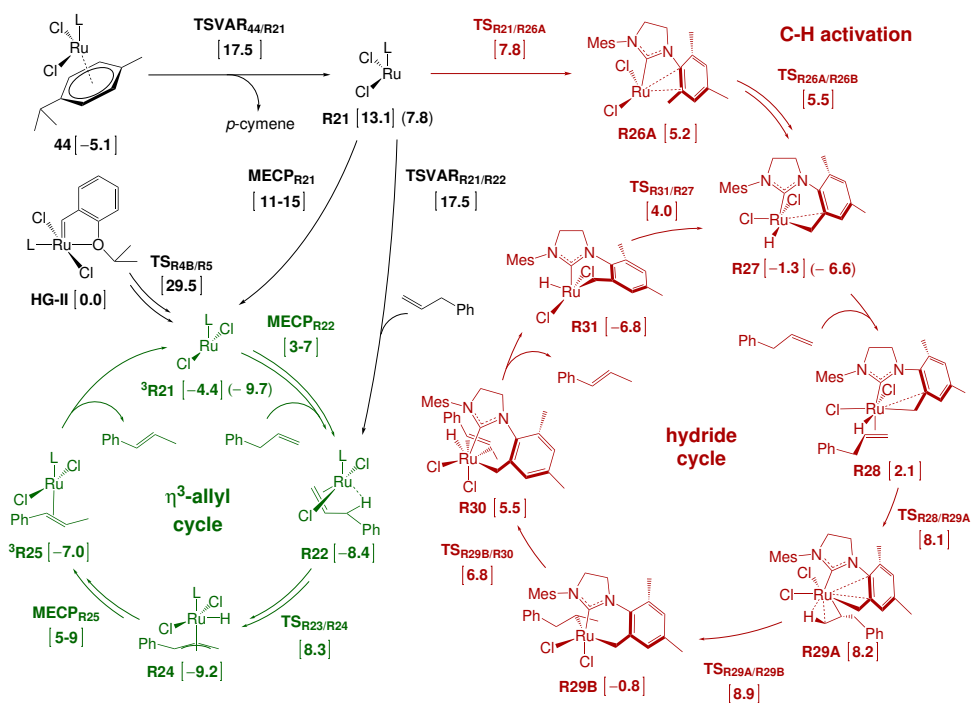
Scheme 16: 1-Alkene triggered decomposition pathways starting from **OM7**.^a

^aGibbs free energy, in square brackets, given in kcal·mol⁻¹ and relative to precatalyst **HG-II**. (L = SIMes, ES = ethyl styrene).

VR4A yields this species as well. Two of these three pathways, i.e. via **VR4A** and through ring expansion, proceed via metathesis homocoupling intermediate **OM7**. As noted in the previous section, the most favored one of those has a barrier ($\text{TS}_{\text{R4B/R5}}$) of only 6 kcal·mol⁻¹ higher than that of olefin metathesis. The fact that this route provides a major cause of catalyst decomposition becomes more clear when realizing that for every 1000 olefin metathesis turnovers one catalyst molecule is lost, since, according to transition state theory, decomposition to ${}^3\text{R21}$ is about three orders of magnitude slower than olefin metathesis.

8.3.1 The Allylic Isomerization Cycle

To investigate whether ${}^3\text{R21}$ has the capacity to catalyse double-bond migration, this species was “reacted” *in silico* with allylbenzene. This step gives access to the η^3 -allyl cycle (Scheme 17), which closely resembles the generally accepted allyl mechanism to double-bond migration in Scheme 6. Within a few steps, facile spin-crossover of a triplet-state intermediate gives singlet state π -complex **R22**. Subsequent hydride transfer to ruthenium is easy, but the succeeding rotation of the η^3 -allyl moiety is associated with a relatively high barrier of 8.3 kcal·mol⁻¹ connected to $\text{TS}_{\text{R23/R24}}$.¹⁷⁴ Following this, relatively stable (-9.2 kcal·mol⁻¹) η^3 -allyl hydride **R24** undergoes facile hydride transfer followed by spin-crossover, to obtain triplet-state π -complex ${}^3\text{R25}$. Dissociation of the isomerization product β -methylstyrene regenerates ${}^3\text{R21}$ at -9.7 kcal·mol⁻¹, which is 5.3 kcal·mol⁻¹ lower than at the beginning of the cycle, indicating the exergonicity of this reaction.

Scheme 17: Isomerization mechanisms originating from $^3\mathbf{R21}$ and $\mathbf{R21}$.^a

^aGibbs free energy, in square brackets, given in kcal·mol⁻¹ and relative to precatalyst **HG-II**. L = SIMes.

The singlet-state intermediates with a π -coordinated olefin, **R22** and **R24**, are low-energy species in the η^3 -allyl mechanism (at -8.4 and -9.2 kcal·mol⁻¹, respectively). Thus, considering these values and those of the relative barriers to hydride-abstraction via $\mathbf{TS}_{\mathbf{R}23/\mathbf{R}24}$ and spin-crossover ($\mathbf{MECP}_{\mathbf{R}25}$), absolute barriers between 16–17 kcal·mol⁻¹ are obtained for these steps. Therefore, both **R22** and **R24** are species that play an important role in determining the rate of olefin isomerization.

The turnover frequency (TOF) was estimated at 1–1.5 s⁻¹ using some assumptions: first, no deactivation takes place and no other competing pathways are active; second, an average value, lying in the middle of the range (5–9 kcal·mol⁻¹) for $\mathbf{MECP}_{\mathbf{R}25}$ was used. In addition, the estimated TOF is valid for substrate concentrations > 1 mM.

8.3.2 C-H Bond Activation and the Hydride Cycle

Instead of reacting with allylbenzene, $^3\mathbf{R21}$ can undergo spin pairing to reactive electron-deficient spin-singlet $\mathbf{R21}$, a step that is associated with a barrier of 11–15 kcal·mol⁻¹ ($\mathbf{MECP}_{\mathbf{R21}}$). Reaction of allylbenzene affords a pathway, via $\mathbf{TSVAR}_{\mathbf{R21}/\mathbf{R22}}$, directly back into the singlet-state part of the η^3 -allyl mechanism.

However, when the concentration of allylbenzene is low, the relatively unstable $\mathbf{R21}$ (13.1 kcal·mol⁻¹) is somewhat stabilized through η^2 -coordination of one of the mesityl rings on the NHC, yielding $\mathbf{R26A}$ at 5.2 kcal·mol⁻¹. Subsequently, intra-molecular activation of one of the *o*-methyl C–H bonds, followed by insertion of ruthenium via a relatively low barrier ($\mathbf{TS}_{\mathbf{R21}/\mathbf{R26A}}$), affords ruthenium-hydride $\mathbf{R27}$. This species forms the entry point for the hydride cycle, which resembles the generally accepted alkyl mechanism to double-bond migration (Scheme 6).

Double-bond migration of the substrate commences with a slightly endergonic coordination of allylbenzene. The obtained π -complex $\mathbf{R28}$ reacts further via insertion of the coordinated substrate into the Ru–H bond to give $\mathbf{R29A}$. This species, which is relatively high in energy (8.2 kcal·mol⁻¹), easily rearranges to $\mathbf{R29B}$, after which π -complex $\mathbf{R30}$ is obtained through β -hydride abstraction. Subsequently, dissociation of methylstyrene, exergonic by 12 kcal·mol⁻¹, gives hydride $\mathbf{R31}$ which then isomerizes to the species at the start of this cycle ($\mathbf{R27}$). When the hydride cycle is active in neat substrate, this isomerization step constitutes the rate determining step; at lower concentrations this shifts to the $\mathbf{TS}_{\mathbf{R21}/\mathbf{R26A}}$ barrier. Furthermore, now the rate is predicted to be dependent of concentration and the TOF is significantly higher (1300 s⁻¹ at 0.02 M) than those obtained with the allylic mechanism discussed in Section 8.3.1.

8.4 Experimental Verification of the Predictions

Experimental verification to test whether $^3\mathbf{R21}$ is indeed the key catalyst decomposition intermediate and promoter of double-bond migration requires synthesis of this species and an investigation into its catalytic behavior. However, while $^3\mathbf{R21}$ is of relatively low energy, the synthesis of such a coordinatively unsaturated triplet-state 12-electron Ru(II)-compound is very difficult, if not impossible. Therefore, the synthesis of a singlet-state precatalyst with an increased coordina-

tion number, containing one or more relatively weakly-bound protective ligands, was considered a more practical approach. Although, in that case, ligand dissociation will afford singlet-state 12-electron complex **R21** instead of the initially desired **³R21**, this is not seen as a problem, because there are at least three isomerization routes with low activation barriers that start at this high-energy intermediate: (i) triplet-state **³R21** is reached through spin-inversion; (ii) reaction of **R21** with one equivalent of substrate gives, via the relatively stable spin-singlet π -complex **R22**, access to the allylic-cycle; (iii) the hydride-cycle may be engaged through C–H bond activation of the mesityl groups on the NHC. The latter is effectively disfavored at high substrate concentrations because barrier-less formation of **R22** in neat substrate makes olefin binding to **R21** no longer depending on diffusion.

The aromatic *p*-cymene answers well to the characteristics desired of a protective ligand: even though this moiety will bind ruthenium in a η^6 -fashion, yielding 18-electron adduct (SIMes)(η^6 -*p*-cymene)RuCl₂ (**44**, Scheme 17), dissociation is expected to be facile enough ($\text{TSVAR}_{44/\text{R21}} = 17.5 \text{ kcal}\cdot\text{mol}^{-1}$) to obtain a sufficiently high concentration of **R21** in solution. Furthermore, free *p*-cymene is quite “inert” and unlikely to negatively interfere with the catalytic processes in these experiments.

However, a study of the available literature revealed that the synthesis of **44** was going to be challenging: while several (NHC)(η^6 -*p*-cymene)RuCl₂ complexes are known in literature,^{150,177–183} all isolated compounds of this type contain unsaturated NHC-ligands; in fact, **44** had only been prepared *in situ*.^{184–188} Furthermore, attempts to synthesize **44** through reaction of (η^6 -*p*-cymene)RuCl₂ dimer with two equivalents of SIMes, using the synthetic method for unsaturated NHC-bearing analogues, gave a mixture of undefined hydridic decomposition products.¹⁸⁰ Most likely, dissociation of the *p*-cymene moiety in **44** is more facile than with the unsaturated NHC-ligand analogues, allowing the thermodynamically unstable **R21** species to decompose, probably through formation of a hydride such as **R27**. The presence of an excess of *p*-cymene during synthesis was found to be a sufficient solution to this problem.

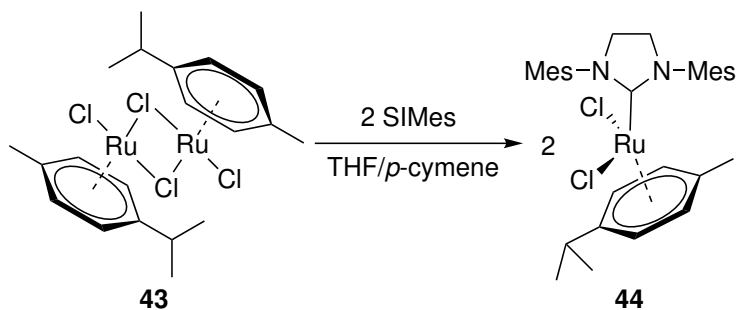
8.4.1 Synthesis of the Precatalyst

With the above in mind, the synthetic procedure was easily modified; compound **44** was readily obtained when a solution of SIMes in THF was slowly added to (η^6 -*p*-cymene)RuCl₂ dimer (**43**) suspended in a 1:1 mixture of THF and *p*-cymene (Scheme 18). After the reaction was completed, most of the THF was removed *in vacuo*; from the remaining reaction mixture, small red crystals that were suitable for synchrotron-radiation X-ray structure analysis were obtained at low temperature (-32 °C) (Figure 13). Compound **44** can be described as a distorted octahedral complex with the carbene located axially; the two chloride ligands are positioned equatorial and are *cis* w.r.t. each other, and the η^6 -bound *p*-cymene ligand is occupying distorted axial and equatorial positions. In general, the bond distances and angles are comparable to those of the IMes analogue of **44**;¹⁸⁹ however, the Ru–C_{NHC} bond is slightly shorter in **44** (2.113 vs. 2.142 Å), probably as a consequence of stronger back-donation observed with SIMes; in addition, the torsion angle Cl1–Ru1–C22–C28 = -35° in **44** is 101° in the IMes analogue, demonstrating a difference in the rotational conformation of the *p*-cymene ligand as well.

8.4.2 Experimental Evaluation in Allylbenzene

Initial catalytic experiments were performed in neat allylbenzene, at elevated temperature (80–100 °C) and with low loadings of **44** (1–100 ppm), to promote dissociation of the η^6 -bound *p*-cymene. A catalyst load of 1 ppm exclusively yields primary isomerization product β -methylstyrene (entry 1, Table 6); subsequently, increase in catalyst loading leads to a reduction in selectivity towards isomer-

Scheme 18: Synthesis of compound **44**, precatalyst to **R21**.



ization and development of metathesis activity (entries 1–4). In addition, with higher reaction temperature a higher selectivity towards isomerization is obtained (entries 4 and 5). It must be noted that, compared to **HG-II**, **44** shows higher isomerization selectivity when tested under similar circumstances (comparing entries 1 and 7; 4 and 8). In conclusion, the results described above prove that, as predicted computationally in the previous sections, **44** is mainly catalysing double bond migration.

Interestingly, at higher catalyst loadings significant olefin metathesis activity is observed. Alongside isomerization, this results in the formation of more complex reaction mixtures (Scheme 5); for instance, with 100 ppm of **44** the total yield in isomerization products (ISO) consists, next to β -methylstyrene, of a small amount of compounds resulting from secondary isomerization (entry 6; see Table S2, SI **Paper II** for details). Similarly, these products are also observed at longer reaction times, probably because the amount of olefin metathesis products is initially low and increases over time (entry 4).

Higher isomerization activity and selectivity were observed when **44** was preheated in toluene without substrate, before catalysis in neat allylbenzene was performed (entry 10). The origin of this higher activity stems from activation of the hydride-mechanism, which has a higher predicted activity compared to that

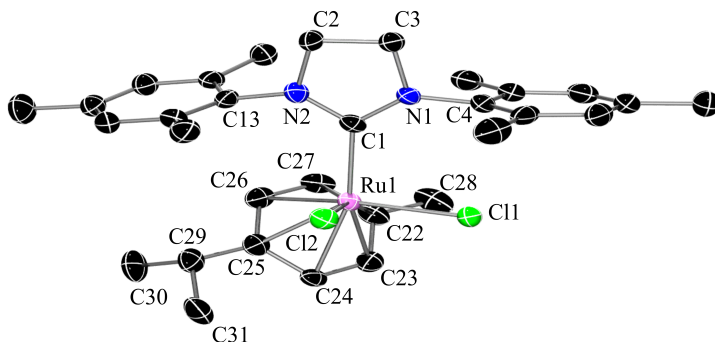


Figure 13: X-ray structure of **44** with displacement ellipsoids drawn at the 50% probability level. H-atoms are omitted for clarity. Selected geometrical parameters: Ru1–C1 = 2.113(4) Å, Ru1–Cl1 = 2.412(1) Å, Ru1–Cl2 = 2.405(1) Å, Ru1–C22 = 2.185(5) Å, Ru1–C23 = 2.204(4) Å, Ru1–C24 = 2.242(4) Å, Ru1–C25 = 2.233(4) Å, Ru1–C26 = 2.196(4) Å, Ru1–C27 = 2.164(4) Å, C2–C3 = 1.150(0) Å, C1–Ru1–Cl1 = 92.5(1)°, C1–Ru1–Cl2 = 81.7(1)°, C1–Ru1–C22 = 117.3(2)°, C1–Ru1–C23 = 153.7(2)°, C1–Ru1–C24 = 163.6(1)°, C1–Ru1–C25 = 126.5(1)°, C1–Ru1–C26 = 100.1(1)°, C1–Ru1–C27 = 95.9(2)°, Cl1–Ru1–Cl2 = 86.25(4)°, N1–C1–N2 = 106.1(3)°, C1–N1–C4 = 132.6(3)°, C1–N2–C13 = 130.4(3)°.

Table 6: Results of catalytic tests with **44** and **HG-II** in neat allylbenzene.

entry	cat.	cat. load. (ppm)	T ($^{\circ}\text{C}$)	t (h)	conv. ^a (%)	ISO ^b (%)
1	44	1	80	1	1	100 ^c
				20	4	100 ^c
2	44	3	80	1	3	73 ^c
3	44	5	80	1	4	67 ^c
4	44	10	80	1	8	63 ^c
				4	17	79 ^c
				24	39	93
5	44	10	100	162	48	94
				1	12	75 ^c
				4	28	86 ^c
6	44	100	80	1	47	51
7	HG-II	1	80	1	10	22 ^c
				4	11	32 ^c
8	HG-II	10	80	1	83	8
				4	93	14
9	44 +Hg(0)	10	100	1	33	84
10	44 ^d	10	100	1	28	86
11	44 ^d +Hg(0)	10	100	1	13	74

^aDetermined by ^1H NMR analysis of the reaction mixture. ^bCombined yield of the primary (β -methylstyrene) and secondary isomerization products compared to total yields (that includes HC products of allylbenzene) determined by ^1H NMR and GC analysis. ^cSolely β -methylstyrene was observed as isomerization product. ^dPre-treated by heating a solution of the catalyst in toluene at 100 $^{\circ}\text{C}$ for 1 hour in absence of substrate and used after removal of the solvent.

of the η^3 -allyl mechanism (Section 8.3.2): heating of **21** in absence of substrate results primarily in the formation of hydrides like **R27** because the pathway from **R21** to **R22** is cut off and formation of **³R21** is hampered by the relatively high **MCEP_{R21}** barrier. Entry into the hydride mechanism is supported by the fact that ^1H NMR spectra of **44** in benzene- d_6 at different temperatures showed the formation of a ruthenium hydride at increased temperature (Figure S2, SI of **Paper II**). However, it must be noted that mercury-poisoning experiments²⁴ show that some of the isomerization activity in this particular experiment comes from ruthenium nanoparticles (entry 11); in the regular catalytic tests (without preheating), ruthenium nanoparticles were not observed (entry 9).

Results of catalytic experiments with **44** performed at room temperature in different solvents, using allylbenzene as substrate, are found in Table 7. In a *n*-pentane/dichloromethane mixture (P/D) one hour of reaction time is enough to

reach near complete conversion of allylbenzene to primary isomerization product β -methylstyrene (entry 1). When this experiment is repeated under the same circumstances with **HG-II** (entry 2), only 33% selectivity to isomerization is obtained in 4 hours; this again shows that **44** is primarily catalyzing double-bond migration. In polar solvent THF similar results are found for **44** (entry 7), while **HG-II** shows a much higher selectivity towards isomerization than in the P/D mixture (entry 8).

A considerable difference is observed when toluene was used as solvent: with **44** not only a much lower conversion is obtained, but more importantly, most

Table 7: Conversion and selectivity toward isomerization (ISO) of allylbenzene at high substrate dilution and room temperature (22 °C).

entry	cat.	cat. load. (mol%)	solvent, S	[S] (mM)	<i>t</i> (h)	conv. ^a (%)	ISO ^b (%)
1	44	1	P/D ^c	20	1	96	100 ^d
					4	100	100 ^d
2	HG-II	1	P/D ^c	20	1	52	13
					4	63	33
3	44	1	P/D ^c	10	1	94	100 ^d
					4	100	100 ^d
4	44	1	P/D ^c	5	1	81	100 ^d
					4	100	100 ^d
5	44	1	P/D ^c	0.25	1	49	100 ^d
					4	93	100 ^d
6	44	0.1	P/D ^c	0.25	1	3	100 ^d
					4	9	100 ^d
					26	25	100 ^d
7	44	1	THF	20	1	91	100 ^d
					4	98	100 ^d
8	HG-II	1	THF	20	1	44	37
					4	83	64
9	44	1	C ₇ H ₈	20	1	51	22
					4	70	36
10	HG-II	1	C ₇ H ₈	20	1	52	13
					4	75	25

^aDetermined by GC analysis of the reaction mixture. ^bCombined yield of the primary (β -methylstyrene) and secondary isomerization products compared to total yields (that includes HC products of allylbenzene) determined by ¹H NMR and GC analysis. ^c*n*-Pentane/DCM (9:1); **44** has very low solubility in *n*-pentane, hence DCM was added as co-solvent. ^dSolely β -methylstyrene was observed as isomerization product.

allylbenzene is converted into olefin metathesis product (entry 9). **HG-II** shows results similar to those obtained in the P/D mixture (entry 10): selectivity towards metathesis is only slightly higher than with **44** in toluene. In conclusion, these experiments show that weakly coordinating and polar solvents exclusively give primary isomerization, while HC dominates in a coordinating solvent like toluene.

The TOFs and TONs stay effectively constant when the substrate concentration is lowered (entries 1, 3–5), even at concentrations comparable to that of common impurities¹⁹⁰ found in solvents (0.25 mM, entry 6), thus being consistent with computational predictions for both allyl and hydride cycle (Section 8.3.1 and Section 8.3.2).

Chapter 9

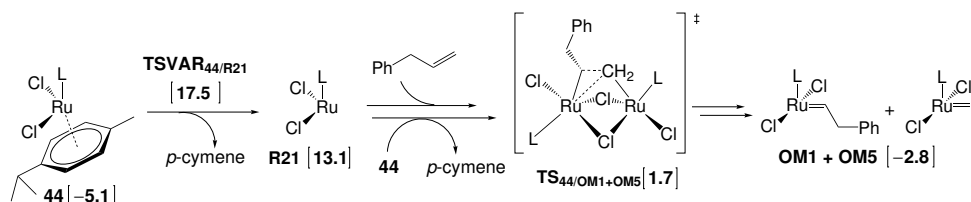
Ru-Alkylidene Regeneration

The previous chapter shows that **44** primarily catalyzes double-bond migration; however, under certain conditions a significant amount of olefin metathesis activity can be observed. Moreover, other arene-stabilized **R21** analogues are known olefin metathesis catalysts.^{177–179,181,182} This is remarkable, because a well-defined olefin metathesis catalyst contains an alkylidene-moiety (Section 2.2) that is absent in **44** and its congeners. Thus, to explain these results, *in situ* formation of a Ru-alkylidene species needs to be considered; this investigation is part of **Paper II** and forms a point of entry for the work in **Paper III**, which is discussed later in this chapter.

9.1 Dinuclear Ruthenium Alkene Activation

A previous computational study, investigating the formation of a ruthenium alkylidene species from *p*-cymene stabilized **R21** and functionalized norbornenes, showed that direct alkylidene formation from ruthenium-norbornene π -complexes is associated with a very high barrier ($> 40 \text{ kcal}\cdot\text{mol}^{-1}$).¹⁷⁸ Subsequently, turning to the isomerization mechanism in Scheme 17, two substrate-induced alkylidene-forming routes starting from the η^3 -allyl cycle were identified; however, the rate determining barriers ($26\text{--}27 \text{ kcal}\cdot\text{mol}^{-1}$ w.r.t. **R22**) are much higher than those leading to isomerization, rendering these pathways insignificant.

Further inspiration was found in a known decomposition reaction that involves loss of the alkylidene moiety after bimolecular coupling of the metathesis catalyst molecules;¹⁵¹ in reverse this reaction could afford a more favourable route to ruthenium alkylidene generation. For the decomposition pathway no molecular-level calculations have been reported and only few mechanistic details are known;

Scheme 19: Dinuclear ruthenium alkene activation mechanism.^a

^aGibbs free energy, in square brackets, given in kcal·mol⁻¹ and relative to **HG-II**. L = SIMes.

however, coupling of two alkylidenes to form an alkene molecule should be the key transition state. Thus, according to the principle of microscopic reversibility, the dinuclear ruthenium alkene activation should proceed through the same intermediate. DFT calculations show that this transition state (**TS**_{44/OM1+OM5}, Scheme 19) is of unexpectedly low energy (1.7 kcal·mol⁻¹ w.r.t. **HG-II**). Keeping in mind that no further computational investigations in this mechanism were performed, this low barrier provides us with an explanation for the metathesis activity observed with arene-stabilized **R21**.

The mechanism in Scheme 19 shows that the rate of Ru-alkylidene formation is second-order w.r.t. the concentration of **44**. However, due to the relatively high barrier (17.5 kcal·mol⁻¹, via **TSVAR**_{44/R21}), *p*-cymene dissociation forms the rate determining step. As a consequence, Ru-alkylidene formation must be first-order w.r.t. **44** at relatively high concentrations. This is consistent with the pattern of decreasing metathesis activity at lower loadings of **44** shown in Figure 14. Similarly, Figure 15 shows a decreasing olefin metathesis activity in time, thus the concentration of **44** decreases during the reaction.

The relatively high selectivity towards olefin metathesis observed with **44** in toluene (entry 9, Table 7), opposed to high selectivity for double-bond migration in THF and the P/D mixture (entries 1 and 7), is caused by the ability of apolar aromatic compounds to stabilize **R21** through η^6 -coordination to ruthenium.

9.2 Ethene-Triggered Ru-Alkylidene Formation

The computational and experimental results discussed in the previous section support the mechanism in Scheme 19 and show that species obtained from catalyst decomposition (**R21**) can be revived to olefin metathesis active catalysts. More importantly, the calculations show that Ru-alkylidenes can be generated *in situ*

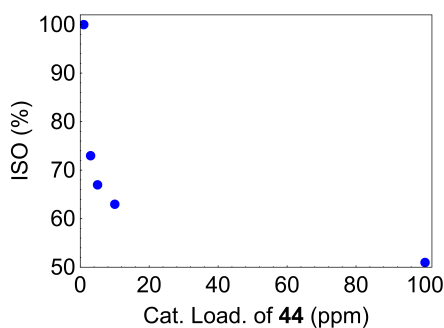


Figure 14: Isomerization of allylbenzene at different loads of **44** after 1 hour and at 80 °C (entry 1–4 and 6, Table 6).

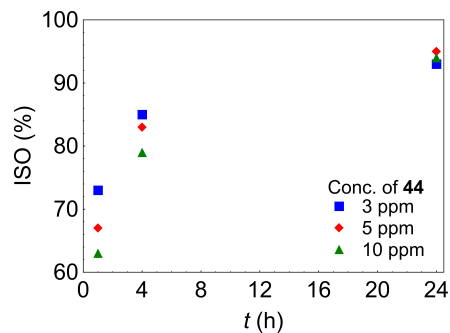


Figure 15: Isomerization of allylbenzene in time with different loads of **44** at 80 °C (entries 2–4, Table S2 in SI of **Paper II**).

from **44**, **R21**, and substrate, thus without the need for additional activators. This is particularly interesting, since decomposition of the olefin metathesis catalyst has always been regarded as irreversible.¹⁹¹ Therefore, more insight in regeneration of the olefin metathesis catalyst needed to be obtained, work that is represented by **Paper III** and that is discussed in the next sections.

While the previous section offers a theoretical explanation for catalyst regeneration, the explicit presence of Ru-alkylidene species was not proven experimentally. In order to gain insight into their formation, we planned to react **44** with an olefin while following the reaction using NMR. Although allylbenzene or another olefinic substrate could be used in these follow-up experiments, homocoupling reactions and isomerization via double-bond migration would yield a complex reaction mixture that is difficult to follow. This complexity was reduced by choosing ethene, the simplest alkene available, as substrate in these reactions. This is a remarkable turn because ethene is known to aid decomposition of **G-I** and **G-II** (Scheme 8). However, not only simplification of the reaction mixture, but also the observation that decomposition of **G-II_m** yields 1.5 times an excess of propene compared with the amount of decomposed catalyst (Section 4.4), stimulated the use of ethene.

9.2.1 Propene as Ru-Methylidene Indicator

Compound **44** was reacted with an excess of ethene in benzene-*d*₆ at 25 °C (Sections 5.3 and 5.4); a quantitative ¹H NMR spectrum was recorded every 30 minutes to follow the reaction (Section 5.2). The results of the ¹H NMR experiment is plotted in Figure 16 and shows the build-up of propene, butenes (1-butene, *cis*-,

and *trans*-2-butene), and ethane during the experiment. 1-Butene, which is most likely obtained through dimerization of ethene (Scheme 20), is the major product throughout the reaction. The rate of formation of 1-butenes shows an increase during the first 20–25 hours; after this time the rate starts to sink very slowly and continuously until termination of the experiment; this observation could indicate that per unit of time less 1-butene is produced, due to decomposition of **R21**. However, the TOF w.r.t. the total olefinic products remains constant throughout the reaction (Figure S4, SI of **Paper III**). Therefore, it is more likely that a fraction of the obtained 1-butene is consumed in a parallel reaction. The observation that *cis*- and *trans*-2-butene are obtained with a continuously increasing rate of formation indicates that primary product 1-butene is isomerized to 2-butenes (Scheme 20). This is not surprising; in the previous chapter the double-bond migration capacities of **44** are extensively discussed. In addition, it must be noted that ruthenium nanoparticles could be partly responsible for the observed isomerization; isolation of the imidazolium salt (32% w.r.t. **44**) from the reaction mixture after the experiment had finished, indicates at least partial decomposition of **44**.

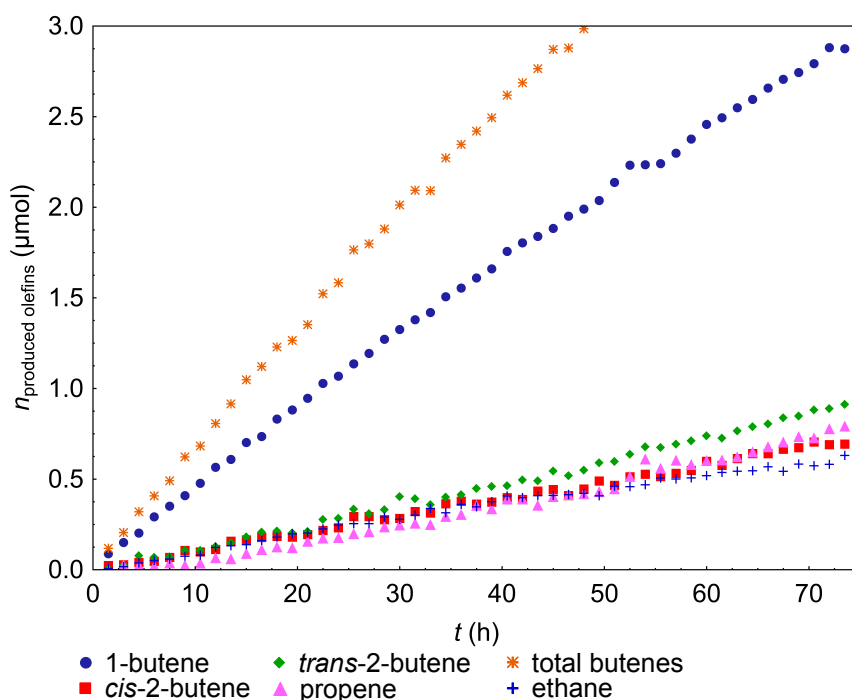
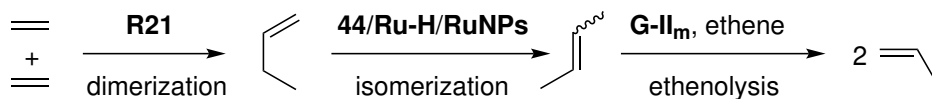


Figure 16: Amount of products obtained at 25 °C, with **44** (3.7 μmol) and ethene (92.0 μmol) in C_6D_6 , as determined by ^1H NMR (see Section 5.2).

Scheme 20: Proposed three-step conversion of ethene to propene.



Ru-H = ruthenium hydrides, **RuNPs** = ruthenium nanoparticles.

The *cis/trans* ratio is close to unity at an early stage of the reaction, indicating that formation of *cis* and *trans*-2-butene are kinetically similar. Further on, however, this ratio drops, most likely due to isomerization caused by an unidentified ruthenium hydride that starts to form after 48 hours. Altogether, a total production of butenes > 3.7 μmol (the amount of **44**) shows that the generation of these products is catalytic rather than stoichiometric.

Propene is thought to be obtained via two different pathways: first, through decomposition of an unsubstituted RCB (**VR2**, which is formed from a ruthenium methylidene and ethene); second, via ethenolysis of 2-butene,¹³ as proposed in Scheme 20. Both mechanisms explicitly involve a ruthenium methylidene; this makes the presence of propene an important indicator that this species must have formed. Unfortunately, in this experiment qualitative evidence was not obtained: free ruthenium alkylidenes are unstable and difficult, if not impossible, to detect in ^1H NMR.

Phosphine-coordinated analogues, such as **G-II_m**, are more stable and have characteristic NMR resonances that aid their detection; therefore, the experiment above was repeated, at the same temperature, in the presence of 0.6 equivalents of PCy_3 . The results from this catalytic experiment show that, similar to the phosphine-less experiment, alkylidene indicator propene was produced together with the other organic products seen before (Figure S7, SI of **Paper III**). Regrettably, PCy_3 -stabilized alkylidenes were not observed; most likely the rate of formation is too low at 25 $^\circ\text{C}$, thus keeping their concentration below the detection limit of NMR.

9.2.2 Ru-Alkylidene Formation at Higher Temperature

Replication of the experiment at higher temperature (50 $^\circ\text{C}$) yields more promising results: two hours into the experiment, the **G-II_m** methylidene resonance started to appear in the ^1H NMR spectra (18.42 ppm,¹⁹² Figure 17); furthermore,

first-generation methyldiene **G-I_m** (19.42 ppm)¹⁹² was observed transiently. In addition, the presence of (PCy₃)(η^6 -*p*-cymene)RuCl₂ (**45**) showed that PCy₃ may replace SIMes in **44**. Moreover, another ruthenium alkylidene species was observed transiently at 9.5–10 hours into the reaction; its resonance (19.00 ppm) agrees with that reported for the ethylidene or propylidene analogue of **G-II_m**.¹⁹³ In addition, two unidentified weak resonances were observed in the alkylidene region at 18.46 and 18.38 ppm, respectively. The total yield of C3 and C4 olefins (17.7 μ mol) corresponds to 4.3 catalytic turnovers, indicating that the conversion of ethene into these olefins proceeds via a catalytic process. Initially, 1-butene is produced at a relatively high rate and forms the dominating product during the first 10 hours of the reaction. However, between 5–15 hours the rate of 1-butene formation decreases and even becomes negative, indicating that this olefin is used up faster than it is being produced. Maximum 1-butene yield, obtained at 13 hours,

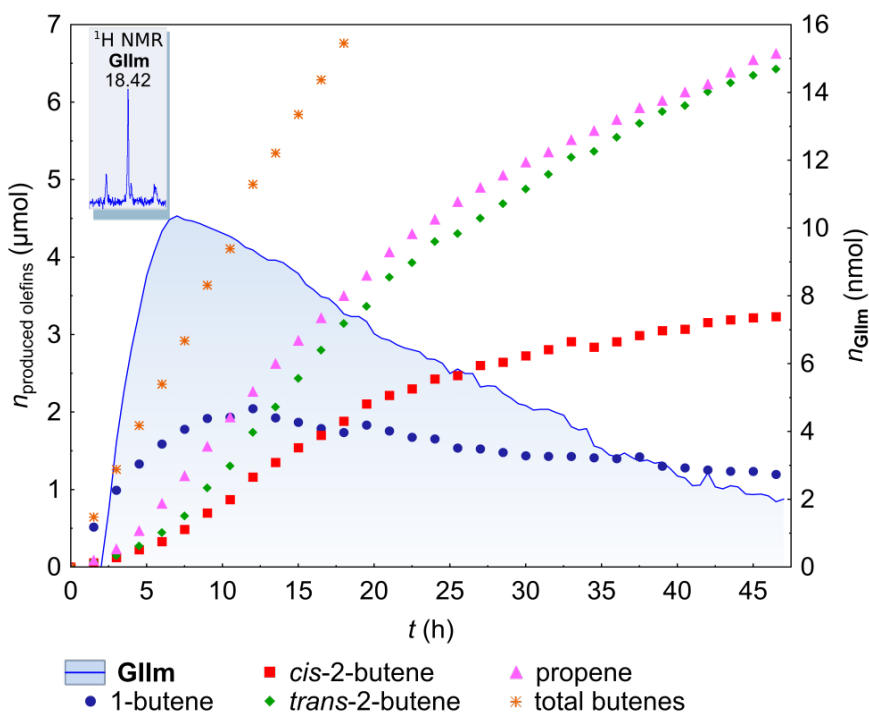


Figure 17: Amount of C3 and C4 olefins (left ordinate) and **GIIIm** (right ordinate) obtained at 50 °C, with **44** (4.1 μ mol), 0.58 equiv. of PCy₃ and ethene (78.5 μ mol) in C₆D₆, as determined by ¹H NMR (Section 5.2). The inset shows the ¹H NMR Ru methyldiene resonance recorded 7 hours into the experiment. Ethane has been omitted for clarity here, but is included in Figure S12 (SI of **Paper III**).

corresponds to a maximum in the rate of formation of 2-butene, suggesting that isomerization of 1-butene is responsible for the formation of 2-butene (Figure 18).

A rapid increase in the amount of **G-II_m** is observed a few hours into the experiment, which coincides with a rapid increase in the rate of propene formation after an initial induction period (Figure 19). Furthermore, the rate of propene production correlates with the amount of **G-II_m**. This indicates that ethenolysis of 2-butene with **G-II_m** is most likely the main contributor to propene formation. It is possible that propene is obtained via **G-II_m** decomposition (Scheme 15); however, the yield of **G-II_m** is orders of magnitude smaller than that of propene, making this pathway a minor contributor. The fairly constant formation rate of total butene products supports the assumption that the C3 and C4 products are most likely obtained via different active species.

Both 2-butene isomers initially form at approximately the same rate, even though *trans*-2-butene is more stable than *cis*-2-butene; however, during the experiment *cis/trans* isomerization of *cis*-2-butene gradually lowers the *cis/trans* ratio to 0.5. There is an indication that ruthenium hydrides could play a role in the observed isomerization: two resonances in the ¹H NMR spectrum, at -7.44

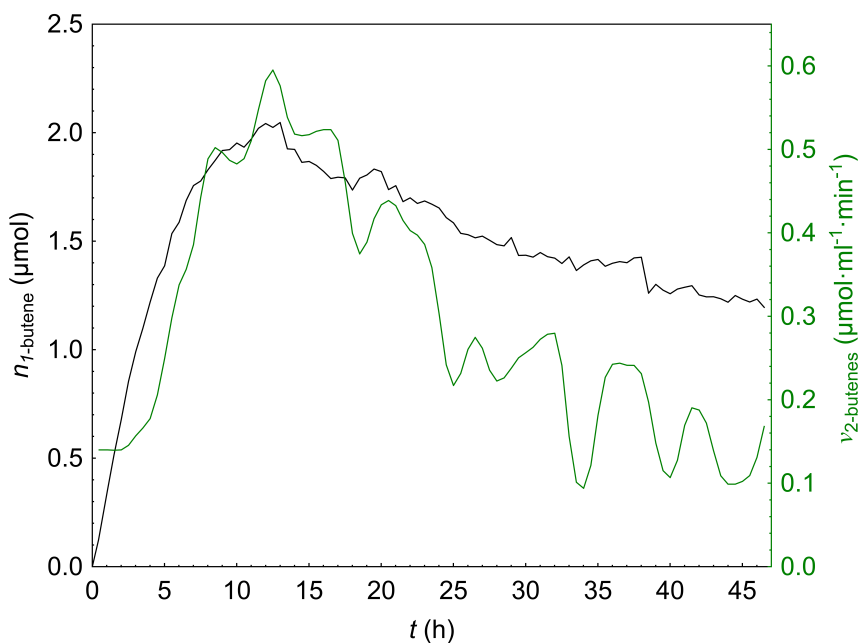


Figure 18: Correlation between the yield of 1-butene (black plot) and the generation rate of 2-butenes (green plot, smoothed using the T4253H smoothing function¹⁹⁴).

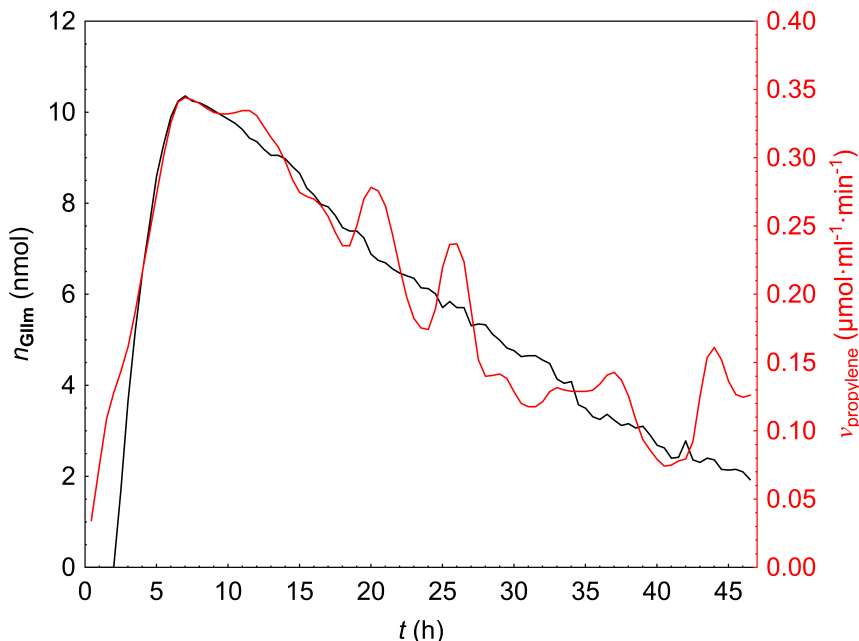


Figure 19: Correlation between the yield of **G-II_m** (left ordinate, black line) and the propene generation rate (right ordinate, red line, smoothed using the T4253H function¹⁹⁴).

and -7.50 ppm, appear after ca. 10 hours and reach maximum intensity after ca. 30 hours. Lastly, the declining TOFs (Figure S14, SI of **Paper III**) support the decomposition of both **G-II_m** (also observed in Figure 17) and the butene-producing species during the experiments at 50 °C. The origin of the ethane, observed in these experiments, is unknown.

9.2.3 Decomposition of **G-II_m**

It is remarkable that any **G-II_m** was observed at all given the excess of ethene, which acts as catalyst poison, and was used in experiments where decomposition of **G-II_m** by ethene was actually desired (Section 4.4).¹⁵⁷ In our experiment a maximum yield of 10.4 nmol (0.44%) **G-II_m** is obtained at 7 hours, followed by a steady decline due to decomposition at a rate of 39% in 16 hours (Figure 17). Initially, this might look similar to the decomposition of **G-II_m** observed by Janse van Rensburg et al. (38% in 16 hours);¹⁵⁷ however, their experiment was performed at lower temperature (40 °C). Furthermore, with a concentration of 0.17 M **G-II_m**

(compared to less than 0.017 mM in our experiment), they would have a much larger contribution from bimolecular decomposition pathways.^{151,160}

9.2.4 Notable Differences w.r.t. Temperature

The experiments at 25 °C are less influenced by catalyst decomposition. While the TOF (Figure S4, SI of **Paper III**) remains fairly constant without PCy₃, addition of PCy₃ causes the TOF to increase throughout the experiment (Figure S8, SI of **Paper III**): dissociation of *p*-cymene from **44**, which generates the presumed 1-butene-forming species (**R21**), is most likely facilitated by the addition of PCy₃. The dominating product throughout both the experiments with (Figure S7, SI of **Paper III**) and without PCy₃ (Figure 16) is 1-butene; furthermore, the 2-butene *cis/trans* ratio remains close to unity, which was not the case at 50 °C; thus, at 25 °C, decomposition of **44** results in much smaller amount of the highly active isomerization catalysts. Moreover, there is much less variation in the product formation rates at room temperature compared to the experiment at 50 °C, with the exception of propene, since its formation requires **OM5**, which is only generated after some time. The above suggests that **R21**, obtained through dissociation of *p*-cymene from **44**, is largely determining the reactivity at low temperature.

9.2.5 Regenerated Catalyst in Olefin Metathesis

The question remains if the small amount of **G-II_m** generated at 50 °C is capable of performing productive olefin metathesis on an observable scale. To test this, **44** was heated for 7 hours at 50 °C with an excess of ethene; after this, all gasses and the solvent were removed, the residue was redissolved, and diethyl diallylmalonate (DEDAM) was added. After 4 hours at 35 °C, 19% of DEDAM is converted into the RCM product (entry 2, Table 8). In comparison, without prior ethene-assisted

Table 8: Ring closing metathesis of diethyl diallylmalonate (DEDAM) with **44** and **44** after regeneration of the alkylidene.

entry	cat.	<i>T</i> (°C)	[DEDAM] (ppm)	<i>t</i> (h)	conv. ^b (%)	yield ^b (%)
1	44	35	0.1	4	1	1
2	44^a	35	0.1	4	19	19

^aPreheated at 50 °C for 7 hours with ethene (excess). ^bDetermined by ¹H NMR analysis using 2,2,3,3-tetramethylbutane as internal standard.

regeneration, thus using **44** directly, only 1% yield is obtained (entry 1).

Conclusions

The catalyst design employed in the development of NHC-bearing second-generation *Z*-selective olefin metathesis catalysts was successfully expanded to include first-generation and indenylidene-bearing third-generation catalysts. Based on maintaining the *trans*-binding of the incoming olefin observed in nonselective parent catalysts, this design employs a sterically demanding aryl thiolate as *Z*-selectivity inducing element.

Analysis of the geometry of phosphine-based catalysts, aided by DFT calculations, gave valuable insight into the selectivity-determining factors: experiments with smaller phosphine ligands show that the presence of the large 2,4,6-triphenylbenzenethiolate is not enough to obtain a highly *Z*-selective catalyst. It was shown that the steric bulk of the L-ligand plays an important role in creating the required phosphine-thiolate repulsion to push the thiolate towards the site where the MCB is formed, and induce *Z*-selectivity. An important factor was that, compared to the relative small rotation of the NHC around the Ru–C_{NHC} bond, monodentate phosphines rotate freely around the Ru–P bond; therefore, the use of chelating P–O-type ligands was required to prevent rotation.

Incorporating these modifications into the design, a bidentate, five-membered-ring-forming *o*-(di-*tert*-butylphosphino)phenolate ligand prevents rotation and exerts sufficient steric pressure on the thiolate. Catalytic tests of this newly designed catalyst (**37**) show appreciable *Z*-selectivity (70–95%) in homocoupling of several different terminal alkenes. These are the highest *Z*-selectivities reported for first-generation systems to date; the somewhat lower *Z*-selectivity and activity compared to second-generation catalysts was counterpoised by a lower tendency towards isomerization.

Through thiolate substitution, the first indenylidene bearing Ru-monothiolate catalysts were obtained (**40** and **42**). These complexes possess a remarkable structure: steric pressure from the large indenylidene moiety and the NHC forces the

thiolate ligand into a surprising and uncommon *trans*-position w.r.t. the NHC. Initially, this configuration was presumed to be incompatible with *Z*-selectivity, and a likely slow pyridine dissociation foresaw low catalytic activity. However, DFT calculations show that pyridine dissociation is compliant with what is expected of fast-initiating catalysts; moreover, these complexes relatively easily isomerize in solution to an active species that has the thiolate *trans* w.r.t. to chloride, thus honoring the desired design. Indeed, the synthesized indenylidene-bearing Ru-monothiolate catalysts not only show rapid initiation at room temperature, but they also reach up to 80% *Z*-selectivity in homocoupling of terminal alkenes; moreover, with TONs up to 2200 these catalysts are relatively long-lived.

Catalyst decomposition, double-bond migration, and *Z/E*-isomerization are detrimental to yield and *Z*-selectivity; however, a clear picture of the decomposition pathways to isomerization active Ru-compounds had never been fully established. Here, important progress is made in identifying isomerization-active species that originate in decomposition of second-generation catalysts: computational and experimental results indicate that 12-electron triplet-state Ru(II) species SIMes(Cl)₂Ru (**³R21**) is an important contributor to alkene isomerization. This species, which is obtained as a result of alkylidene loss, has been observed before in established decomposition pathways, such as bimolecular coupling and ethene-triggered breakdown of the unsubstituted metallacyclobutane (Chapter 4). In addition, a novel 1-alkene assisted decomposition pathway, via expansion of the metallacyclobutene ring, was found to contain an overall barrier only 6 kcal·mol⁻¹ higher to olefin metathesis of allylbenzene. This new pathway also explains why the presence of substrate is required to obtain sufficient isomerization activity.¹⁴⁹

Synthesis and testing of the *p*-cymene-stabilized **R21** (**44**) confirmed the isomerization capacity of **³R21** and its spin-singlet analogue **R21**: isomerization activity of **44** is especially high with conditions that promote dissociation of *p*-cymene and hinder the formation of dinuclear aggregates.

Depression of isomerization is observed in nonpolar solvents capable of η^6 -coordination, such as toluene; furthermore, **44** is under certain conditions also able to promote olefin metathesis with same qualitative trends in metathesis and isomerization selectivities as **HG-II**; therefore, both compounds share not just the catalytic isomerization and metathesis cycles, but also the whole calculated

reaction network that connects metathesis, alkylidene loss, isomerization and alkylidene regeneration.

Computational and experimental results indicated that regeneration of the ruthenium alkylidene may be accomplished through activation of an alkene by two alkylidene-free ruthenium complexes. The identification of ruthenium methylenes in reaction mixtures when **44** and ethene were reacted at 50 °C shows that loss of the alkylidene is not irreversible, as was previously thought. However, even more remarkable is the fact that regeneration of the olefin metathesis catalyst can be accomplished with ethene, a well-known catalyst poison. Interestingly, evidence from NMR indicates that the catalytically active propagating species obtained in these experiments is the same as that of **HG-II**, something that has been observed before with **45**, the phosphine-bearing analogue of **44**.¹⁹⁵

Moreover, a catalytic experiment with **44**, after treatment with ethene at 50 °C, showed that the small amount of regenerated catalyst produces reasonable olefin metathesis activity in RCM of diethyl diallylmalonate.

Major product 1-butene, obtained during the regeneration experiments, is most likely obtained via dimerization of ethene with **44**; subsequently, isomerization of this product yields 2-butene, from which propene is generated through ethenolysis. Although the origin of the relatively small amounts of ethane is unknown, hydride-mediated hydrogen transfer to ethene might be responsible for its steady generation during the experiments.

Outlook to the Future

The work represented by this thesis gives interesting new insights in ruthenium-based olefin metathesis. However, it also rises new questions, which could be answered with further work.

The *Z*-selectivity of phosphine-based catalyst **37** might be slightly improved by selecting a more bulky thiolate, such as 2,4,6-tri(di-*m*-methylphenyl)benzenethiolate. Furthermore, this large thiolate could be combined with the *o*-(di-(1-adamantyl)phosphino)phenolate ligand; this would give more or less the maximum repulsion between a thiolate and the alkyl groups on the P-atom. DFT calculations prior to synthesis might indicate whether it is worthwhile to synthesize these compounds. With this last suggestion, the capacity of the *o*-(di-alkylphosphino)phenolate family is exhausted and selecting other bidentate phosphine ligands will be required. Using instead P, P-disubstituted phosphinoacetic acids^{196,197} (R_2P-CH_2-COOH) with bulky alkyl substituents¹⁹⁷ might not directly offer an increase in *Z*-selectivity, but it might improve catalytic activity, due to the higher basicity of the trialkylphosphine.

Increasing the *Z*-selectivity of the Ru-indenylidene catalysts will most likely be rather difficult. Attempts to install the 2,4,6-tri(di-*m*-methylphenyl)benzenethiolate failed; perhaps isolable catalysts could be obtained with a smaller indenylidene ligand.

Understanding the pathways leading to decomposition of the olefin metathesis catalyst, double-bond migration, *Z/E* isomerization, and catalyst regeneration will, in the future, hopefully contribute to the development of better stereoselective catalysts. Furthermore, the report on the synthesis of (SIMes)(η^6 -*p*-cymene)RuCl₂ (**44**) has already opened up phosphine-free synthetic routes to traditional olefin metathesis catalysts.¹⁹⁸ However, the alkylidene moiety is still installed by using highly reactive and potentially explosive diazo compounds. As we showed that even catalyst poison ethene can regenerate the olefin metathesis catalyst, it must

be possible to develop a method to synthesize new catalysts purely by adding an alkene.

References

- (1) Hog, D. T.; Huber, F. M. E.; Mayer, P.; Trauner, D. *Angew. Chem. Int. Ed.* **2014**, *53*, 8513–8517.
- (2) Seetharamsingh, B.; Rajamohanam, P. R.; Reddy, D. S. *Org. Lett.* **2015**, *17*, 1652–1655.
- (3) Sulake, R. S.; Chen, C. *Org. Lett.* **2015**, *17*, 1138–1141.
- (4) Elacqua, E.; Weck, M. *Chem. Eur. J.* **2015**, *21*, 7151–7158.
- (5) Martinez, H.; Ren, N.; Matta, M. E.; Hillmyer, M. A. *Polym. Chem.* **2014**, *5*, 3507–3532.
- (6) Rybak, A.; Fokou, P. A.; Meier, M. A. R. *Eur. J. Lipid Sci. Technol.* **2008**, *110*, 797–804.
- (7) Herbert, M. B.; Marx, V. M.; Pederson, R. L.; Grubbs, R. H. *Angew. Chem. Int. Ed.* **2012**, *52*, 310–314.
- (8) Pesquet, A.; Othman, M. *Tetrahedron Lett.* **2013**, *54*, 5227–5231.
- (9) Kotha, S.; Ravikumar, O.; Sreevani, G. *Tetrahedron* **2016**, *72*, 6611–6615.
- (10) Cortez, G. A.; Baxter, C. A.; Schrock, R. R.; Hoveyda, A. H. *Org. Lett.* **2007**, *9*, 2871–2874.
- (11) Romulus, J.; Tan, L.; Weck, M.; Sampson, N. S. *ACS Macro Lett.* **2013**, *2*, 749–752.
- (12) Yang, K. S.; Jeong, D.-C.; Choi, E. J.; Ahn, T.-K.; Song, C. *Macromol. Res.* **2013**, *21*, 1159–1162.
- (13) Mol, J. C. *J. Mol. Catal. A: Chem.* **2004**, *213*, 39–45.
- (14) Daglar, O.; Durmaz, H.; Hizal, G.; Tunca, U. *J. Polym. Sci., Part A: Polym. Chem.* **2016**, *54*, 2593–2598.
- (15) Zhang, C.; Yu, C.; Long, H.; Denman, R. J.; Jin, Y.; Zhang, W. *Chem. Eur. J.* **2015**, *21*, 16935–16940.
- (16) Bauer, K. N.; Tee, H. T.; Lieberwirth, I.; Wurm, F. R. *Macromolecules* **2016**, *49*, 3761–3768.
- (17) Zhang, H.; Liu, F.; Cao, J.; Ling, L.; Sun, R.-F. *Chin. J. Polym. Sci.* **2016**, *34*, 242–252.
- (18) Gandi, V. R. *Tetrahedron* **2013**, *69*, 6507–6511.
- (19) Jensen, V. R.; Occhipinti, G.; Hansen, F. R. Novel olefin metathesis catalysts. European pat., WO2012032131, 2012.
- (20) Occhipinti, G.; Hansen, F. R.; Törnroos, K. W.; Jensen, V. R. *J. Am. Chem. Soc.* **2013**, *135*, 3331–3334.
- (21) Higman, C. S.; Plais, L.; Fogg, D. E. *ChemCatChem* **2013**, *5*, 3548–3551.
- (22) Lee, C. W.; Grubbs, R. H. *Org. Lett.* **2000**, *2*, 2145–2147.

- (23) Jafarpour, L.; Schanz, H.-J.; Stevens, E. D.; Nolan, S. P. *Organometallics* **1999**, *18*, 5416–5419.
- (24) Higman, C. S.; Lanterna, A. E.; Marin, M. L.; Scaiano, J. C.; Fogg, D. E. *ChemCatChem* **2016**, *8*, 2446–2449.
- (25) Banks, R. L.; Bailey, G. C. *Ind. Eng. Chem. Prod. Res. Dev.* **1964**, *3*, 170–173.
- (26) Eleuterio, H. S. Polymerization of Cyclic Olefins. US Patent, US 3074918, 1963.
- (27) Calderon, N.; Chen, H. Y.; Scott, K. W. *Tetrahedron Lett.* **1967**, *8*, 3327–3329.
- (28) Adams, C.; Brandenberger, S. G. *J. Catal.* **1969**, *13*, 360–363.
- (29) Crain, D. *J. Catal.* **1969**, *13*, 110–113.
- (30) Calderon, N.; Ofstead, E. A.; Ward, J. P.; Judy, W. A.; Scott, K. W. *J. Am. Chem. Soc.* **1968**, *90*, 4133–4140.
- (31) Mol, J.; Moulijn, J.; Boelhouwer, C. *J. Catal.* **1968**, *11*, 87–88.
- (32) Mol, J.; Visser, F.; Boelhouwer, C. *J. Catal.* **1970**, *17*, 114–116.
- (33) Lewandos, G. S.; Pettit, R. *J. Am. Chem. Soc.* **1971**, *93*, 7087–7088.
- (34) Hérisson, J.-L.; Chauvin, Y. *Makromol. Chem.* **1971**, *141*, 161–176.
- (35) Katz, T. J.; McGinnis, J. *J. Am. Chem. Soc.* **1975**, *97*, 1592–1594.
- (36) Fischer, E. O.; Maasböl, A. *Angew. Chem. Int. Ed.* **1964**, *3*, 580–581.
- (37) Natta, G.; Dall’Asta, G.; Mazzanti, G. *Angew. Chem. Int. Ed.* **1964**, *3*, 723–729.
- (38) Hlil, A. R.; Balogh, J.; Moncho, S.; Su, H.-L.; Tuba, R.; Brothers, E. N.; Al-Hashimi, M.; Bazzi, H. S. *J. Polym. Sci., Part A: Polym. Chem.* **2017**, *55*, 3137–3145.
- (39) Greenlee, W. S.; Faron, M. F. *Inorg. Chem.* **1976**, *15*, 2129–2134.
- (40) De Frémont, P.; Marion, N.; Nolan, S. P. *Coord. Chem. Rev.* **2009**, *253*, 862–892.
- (41) Clayden, J.; Greeves, N.; Warren, S., *Organic Chemistry*, 2nd edition; Oxford University Press Inc.: New York, 2012; Chapter 38.
- (42) Wagner, W. M.; Kloosterziel, H.; van der Ven, S. *Recl. Trav. Chim. Pays-Bas* **1961**, *80*, 740–746.
- (43) Crabtree, R. H., *The Organometallic Chemistry of the Transition Metals*, 6th ed.; John Wiley & Sons, Inc., Hoboken, New Jersey: 2014, pp 296–300.
- (44) Schrock, R. R.; Hoveyda, A. H. *Angew. Chem. Int. Ed.* **2003**, *42*, 4592–4633.
- (45) Dötz, K. H.; Fischer, E. O. *Chem. Ber.* **1972**, *105*, 1356–1367.
- (46) Schrock, R.; Rocklage, S.; Wengrovius, J.; Rupprecht, G.; Fellmann, J. *J. Mol. Catal.* **1980**, *8*, 73–83.
- (47) Wengrovius, J. H.; Schrock, R. R.; Churchill, M. R.; Missert, J. R.; Youngs, W. J. *J. Am. Chem. Soc.* **1980**, *102*, 4515–4516.
- (48) Bazan, G. C.; Khosravi, E.; Schrock, R. R.; Feast, W. J.; Gibson, V. C.; O’Regan, M. B.; Thomas, J. K.; Davis, W. M. *J. Am. Chem. Soc.* **1990**, *112*, 8378–8387.

- (49) Bazan, G. C.; Oskam, J. H.; Cho, H. N.; Park, L. Y.; Schrock, R. R. *J. Am. Chem. Soc.* **1991**, *113*, 6899–6907.
- (50) Schrock, R. R.; Murdzek, J. S.; Bazan, G. C.; Robbins, J.; DiMare, M.; O'Regan, M. *J. Am. Chem. Soc.* **1990**, *112*, 3875–3886.
- (51) Schrock, R. R.; DePue, R. T.; Feldman, J.; Schaverien, C. J.; Dewan, J. C.; Liu, A. H. *J. Am. Chem. Soc.* **1988**, *110*, 1423–1435.
- (52) Grela, K., *Olefin Metathesis: Theory and Practice*, 1st ed.; John Wiley & Sons, Incorporated: 2014.
- (53) Michelotti, F. W.; Keaveney, W. P. *J. Polym. Sci. Part A: Gen.* **1965**, *3*, 895–905.
- (54) Novak, B. M.; Grubbs, R. H. *J. Am. Chem. Soc.* **1988**, *110*, 960–961.
- (55) Rinehart, R. E.; Smith Homer, P. *J. Polym. Sci. Part B: Polym. Lett.* **1965**, *3*, 1049–1052.
- (56) Hillmyer, M. A.; Lepetit, C.; McGrath, D. V.; Novak, B. M.; Grubbs, R. H. *Macromolecules* **1992**, *25*, 3345–3350.
- (57) Novak, B. M.; Grubbs, R. H. *J. Am. Chem. Soc.* **1988**, *110*, 7542–7543.
- (58) France, M. B.; Paciello, R. A.; Grubbs, R. H. *Macromolecules* **1993**, *26*, 4739–4741.
- (59) Nguyen, S. T.; Grubbs, R. H.; Ziller, J. W. *J. Am. Chem. Soc.* **1993**, *115*, 9858–9859.
- (60) Nguyen, S. T.; Johnson, L. K.; Grubbs, R. H.; Ziller, J. W. *J. Am. Chem. Soc.* **1992**, *114*, 3974–3975.
- (61) Schwab, P.; France, M. B.; Ziller, J. W.; Grubbs, R. H. *Angew. Chem. Int. Ed.* **1995**, *34*, 2039–2041.
- (62) Schwab, P.; Grubbs, R. H.; Ziller, J. W. *J. Am. Chem. Soc.* **1996**, *118*, 100–110.
- (63) Chang, S.; Jones, L.; Wang, C.; Henling, L. M.; Grubbs, R. H. *Organometallics* **1998**, *17*, 3460–3465.
- (64) Dias, E. L.; Grubbs, R. H. *Organometallics* **1998**, *17*, 2758–2767.
- (65) Sanford, M. S.; Henling, L. M.; Grubbs, R. H. *Organometallics* **1998**, *17*, 5384–5389.
- (66) Herrmann, W. A.; Köcher, C. *Angew. Chem.* **1997**, *109*, 2256–2282.
- (67) Weskamp, T.; Schattenmann, W. C.; Spiegler, M.; Herrmann, W. A. *Angew. Chem. Int. Ed.* **1998**, *37*, 2490–2493.
- (68) Weskamp, T.; Kohl, F. J.; Hieringer, W.; Gleich, D.; Herrmann, W. A. *Angew. Chem. Int. Ed.* **1999**, *38*, 2416–2419.
- (69) Scholl, M.; Trnka, T. M.; Morgan, J. P.; Grubbs, R. H. *Tetrahedron Lett.* **1999**, *40*, 2247–2250.
- (70) Ackermann, L.; Fürstner, A.; Weskamp, T.; Kohl, F. J.; Herrmann, W. A. *Tetrahedron Lett.* **1999**, *40*, 4787–4790.
- (71) Huang, J.; Stevens, E. D.; Nolan, S. P.; Petersen, J. L. *J. Am. Chem. Soc.* **1999**, *121*, 2674–2678.
- (72) Scholl, M.; Ding, S.; Lee, C. W.; Grubbs, R. H. *Org. Lett.* **1999**, *1*, 953–956.

- (73) Kingsbury, J. S.; Harrity, J. P. A.; Bonitatebus, P. J.; Hoveyda, A. H. *J. Am. Chem. Soc.* **1999**, *121*, 791–799.
- (74) Garber, S. B.; Kingsbury, J. S.; Gray, B. L.; Hoveyda, A. H. *J. Am. Chem. Soc.* **2000**, *122*, 8168–8179.
- (75) Gessler, S.; Randl, S.; Blechert, S. *Tetrahedron Lett.* **2000**, *41*, 9973–9976.
- (76) Grela, K.; Harutyunyan, S.; Michrowska, A. *Angew. Chem. Int. Ed.* **2002**, *41*, 4038–4040.
- (77) Sanford, M. S.; Love, J. A.; Grubbs, R. H. *Organometallics* **2001**, *20*, 5314–5318.
- (78) Love, J. A.; Morgan, J. P.; Trnka, T. M.; Grubbs, R. H. *Angew. Chem. Int. Ed.* **2002**, *41*, 4035–4037.
- (79) Harlow, K. J.; Hill, A.; D. E. T. Wilton-Ely, J. *Dalton Trans.* **1999**, 285–292.
- (80) Fürstner, A.; Guth, O.; Düffels, A.; Seidel, G.; Liebl, M.; Gabor, B.; Mynott, R. *Chem. Eur. J.* **2001**, *7*, 4811–4820.
- (81) Boeda, F.; Clavier, H.; Nolan, S. P. *Chem. Commun.* **2008**, 2726–2740.
- (82) Fürstner, A.; Grabowski, J.; Lehmann, C. W. *J. Org. Chem.* **1999**, *64*, 8275–8280.
- (83) Fürstner, A.; Liebl, M.; Hill, A. F.; Wilton-Ely, J. D. E. T. *Chem. Commun.* **1999**, 601–602.
- (84) Fürstner, A.; Grabowski, J.; Lehmann, C. W.; Kataoka, T.; Nagai, K. *Chembiochem* **2001**, *2*, 60–68.
- (85) Fürstner, A.; Jeanjean, F.; Razon, P. *Angew. Chem. Int. Ed.* **2002**, *41*, 2097–2101.
- (86) Fürstner, A.; Radkowski, K.; Wirtz, C.; Goddard, R.; Lehmann, C. W.; Mynott, R. *J. Am. Chem. Soc.* **2002**, *124*, 7061–7069.
- (87) Fürstner, A.; Thiel, O. R. *J. Org. Chem.* **2000**, *65*, 1738–1742.
- (88) Lecourt, C.; Boinapally, S.; Dhambri, S.; Boissonnat, G.; Meyer, C.; Cossy, J.; Sautel, F.; Massiot, G.; Ardisson, J.; Sorin, G.; Lannou, M.-I. *J. Org. Chem.* **2016**, *81*, 12275–12290.
- (89) Scheiper, B.; Glorius, F.; Leitner, A.; Fürstner, A. *Proc. Natl. Acad. Sci. USA* **2004**, *101*, 11960–11965.
- (90) Fürstner, A.; Thiel, O. R.; Ackermann, L.; Schanz, H.-J.; Nolan, S. P. *J. Org. Chem.* **2000**, *65*, 2204–2207.
- (91) Schmidt, B.; Wildemann, H. *J. Chem. Soc., Perkin Trans. 1* **2000**, 2916–2925.
- (92) Dragutan, V.; Dragutan, I.; Verpoort, F. *Platinum Met. Rev.* **2005**, *49*, 33–40.
- (93) Clavier, H.; Nolan, S. P., *NATO Science Series, II: Mathematics, Physics and Chemistry*; Imamoglu, Y., Dragutan, V., Eds.; Springer: Dordrecht, the Netherlands, 2007; Vol. 243 (Metathesis Chemistry), pp 29–37.
- (94) Clavier, H.; Petersen, J. L.; Nolan, S. P. *J. Organomet. Chem.* **2006**, *691*, 5444–5447.
- (95) Ashworth, I. W.; Hillier, I. H.; Nelson, D. J.; Percy, J. M.; Vincent, M. A. *ACS Catal.* **2013**, *3*, 1929–1939.

- (96) Benitez, D.; Tkatchouk, E.; Goddard, W. A. *Organometallics* **2009**, *28*, 2643–2645.
- (97) Fomine, S.; Vargas, S. M.; Tlenkopatchev, M. A. *Organometallics* **2003**, *22*, 93–99.
- (98) Sanford, M. S.; Love, J. A.; Grubbs, R. H. *J. Am. Chem. Soc.* **2001**, *123*, 6543–6554.
- (99) Sanford, M. S.; Ulman, M.; Grubbs, R. H. *J. Am. Chem. Soc.* **2001**, *123*, 749–750.
- (100) Vyboishchikov, S. F.; Bühl, M.; Thiel, W. *Chem. Eur. J.* **2002**, *8*, 3962–3975.
- (101) Aagaard, O. M.; Meier, R. J.; Buda, F. *J. Am. Chem. Soc.* **1998**, *120*, 7174–7182.
- (102) Meier, R. J.; Aagaard, O. M.; Buda, F. *J. Mol. Catal. A: Chem.* **2000**, *160*, 189–197.
- (103) Seiders, T. J.; Ward, D. W.; Grubbs, R. H. *Org. Lett.* **2001**, *3*, 3225–3228.
- (104) Benitez, D.; Tkatchouk, E.; Goddard, W. A. *Chem. Commun.* **2008**, 6194–6196.
- (105) Piacenza, M.; Hyla-Kryspin, I.; Grimme, S. *J. Comput. Chem.* **2007**, *28*, 2275–2285.
- (106) Adlhart, C.; Hinderling, C.; Baumann, H.; Chen, P. *J. Am. Chem. Soc.* **2000**, *122*, 8204–8214.
- (107) Bernardi, F.; Bottoni, A.; Miscione, G. P. *Organometallics* **2003**, *22*, 940–947.
- (108) Romero, P. E.; Piers, W. E. *J. Am. Chem. Soc.* **2007**, *129*, 1698–1704.
- (109) Cavallo, L. *J. Am. Chem. Soc.* **2002**, *124*, 8965–8973.
- (110) Adlhart, C.; Chen, P. *Angew. Chem. Int. Ed.* **2002**, *41*, 4484–4487.
- (111) Anderson, D. R.; Ung, T.; Mkrtumyan, G.; Bertrand, G.; Grubbs, R. H.; Schrodi, Y. *Organometallics* **2008**, *27*, 563–566.
- (112) Ritter, T.; Hejl, A.; Wenzel, A. G.; Funk, T. W.; Grubbs, R. H. *Organometallics* **2006**, *25*, 5740–5745.
- (113) Teo, P.; Grubbs, R. H. *Organometallics* **2010**, *29*, 6045–6050.
- (114) Vehlow, K.; Maechling, S.; Blechert, S. *Organometallics* **2006**, *25*, 25–28.
- (115) Fürstner, A. *Science* **2013**, *341*, 1357.
- (116) Bahri-Laleh, N.; Credendino, R.; Cavallo, L. *Beilstein J. Org. Chem.* **2011**, *7*, 40–45.
- (117) Ulman, M.; Grubbs, R. H. *Organometallics* **1998**, *17*, 2484–2489.
- (118) Jiang, A. J.; Zhao, Y.; Schrock, R. R.; Hoveyda, A. H. *J. Am. Chem. Soc.* **2009**, *131*, 16630–16631.
- (119) Meek, S. J.; O'Brien, R. V.; Llaveria, J.; Schrock, R. R.; Hoveyda, A. H. *Nature* **2011**, *471*, 461–466.
- (120) Wang, C.; Yu, M.; Kyle, A. F.; Jakubec, P.; Dixon, D. J.; Schrock, R. R.; Hoveyda, A. H. *Chem. Eur. J.* **2013**, *19*, 2726–2740.
- (121) Yu, M.; Wang, C.; Kyle, A. F.; Jakubec, P.; Dixon, D. J.; Schrock, R. R.; Hoveyda, A. H. *Nature* **2011**, *479*, 88–93.

- (122) Ledoux, N.; Allaert, B.; Linden, A.; Van Der Voort, P.; Verpoort, F. *Organometallics* **2007**, *26*, 1052–1056.
- (123) Ledoux, N.; Linden, A.; Allaert, B.; Mierde, H. V.; Verpoort, F. *Adv. Synth. Catal.* **2007**, *349*, 1692–1700.
- (124) Van Veldhuizen, J. J.; Gillingham, D. G.; Garber, S. B.; Kataoka, O.; Hoveyda, A. H. *J. Am. Chem. Soc.* **2003**, *125*, 12502–12508.
- (125) Vougioukalakis, G. C.; Grubbs, R. H. *Organometallics* **2007**, *26*, 2469–2472.
- (126) Vougioukalakis, G. C.; Grubbs, R. H. *J. Am. Chem. Soc.* **2008**, *130*, 2234–2245.
- (127) Rosen, E. L.; Sung, D. H.; Chen, Z.; Lynch, V. M.; Bielawski, C. W. *Organometallics* **2010**, *29*, 250–256.
- (128) Endo, K.; Grubbs, R. H. *J. Am. Chem. Soc.* **2011**, *133*, 8525–8527.
- (129) Keitz, B. K.; Endo, K.; Herbert, M. B.; Grubbs, R. H. *J. Am. Chem. Soc.* **2011**, *133*, 9686–9688.
- (130) Keitz, B. K.; Endo, K.; Patel, P. R.; Herbert, M. B.; Grubbs, R. H. *J. Am. Chem. Soc.* **2012**, *134*, 693–699.
- (131) Marx, V. M.; Herbert, M. B.; Keitz, B. K.; Grubbs, R. H. *J. Am. Chem. Soc.* **2013**, *135*, 94–97.
- (132) Rosebrugh, L. E.; Herbert, M. B.; Marx, V. M.; Keitz, B. K.; Grubbs, R. H. *J. Am. Chem. Soc.* **2013**, *135*, 1276–1279.
- (133) Occhipinti, G.; Koudriavtsev, V.; Törnroos, K. W.; Jensen, V. R. *Dalton Trans.* **2014**, *43*, 11106–11117.
- (134) Khan, R. K. M.; Torker, S.; Hoveyda, A. H. *J. Am. Chem. Soc.* **2013**, *135*, 10258–10261.
- (135) Koh, M. J.; Khan, R. K. M.; Torker, S.; Hoveyda, A. H. *Angew. Chem. Int. Ed.* **2014**, *53*, 1968–1972.
- (136) Koh, M. J.; Khan, R. K. M.; Torker, S.; Yu, M.; Mikus, M. S.; Hoveyda, A. H. *Nature* **2015**, *517*, 181–186.
- (137) Liu, P.; Xu, X.; Dong, X.; Keitz, B. K.; Herbert, M. B.; Grubbs, R. H.; Houk, K. N. *J. Am. Chem. Soc.* **2012**, *134*, 1464–1467.
- (138) Dang, Y.; Wang, Z.-X.; Wang, X. *Organometallics* **2012**, *31*, 8654–8657.
- (139) Dang, Y.; Wang, Z.-X.; Wang, X. *Organometallics* **2012**, *31*, 7222–7234.
- (140) Khan, R. K. M.; Torker, S.; Hoveyda, A. H. *J. Am. Chem. Soc.* **2014**, *136*, 14337–14340.
- (141) Amoroso, D.; Yap, G. P. A.; Fogg, D. E. *Organometallics* **2002**, *21*, 3335–3343.
- (142) Salvini, A.; Frediani, P.; Piacenti, F. *J. Mol. Catal. A: Chem.* **2000**, *159*, 185–195.
- (143) Salvini, A.; Piacenti, F.; Frediani, P.; Devescovi, A.; Caporali, M. *J. Organomet. Chem.* **2001**, *625*, 255–267.
- (144) McGrath, D. V.; Grubbs, R. H. *Organometallics* **1994**, *13*, 224–235.
- (145) Bourgeois, D.; Pancrazi, A.; Nolan, S. P.; Prunet, J. *J. Organomet. Chem.* **2002**, *643-644*, 247–252.

- (146) Crabtree, R. H., *The Organometallic Chemistry of the Transition Metals*, 6th ed.; John Wiley & Sons, Inc., Hoboken, New Jersey: 2014, pp 231–233.
- (147) Fürstner, A.; Ackermann, L.; Gabor, B.; Goddard, R.; Lehmann, C. W.; Mynott, R.; Stelzer, F.; Thiel, O. R. *Chem. Eur. J.* **2001**, *7*, 3236–3253.
- (148) Trnka, T. M.; Morgan, J. P.; Sanford, M. S.; Wilhelm, T. E.; Scholl, M.; Choi, T.-L.; Ding, S.; Day, M. W.; Grubbs, R. H. *J. Am. Chem. Soc.* **2003**, *125*, 2546–2558.
- (149) Courchay, F. C.; Sworen, J. C.; Ghiviriga, I.; Abboud, K. A.; Wagener, K. B. *Organometallics* **2006**, *25*, 6074–6086.
- (150) Hong, S. H.; Wenzel, A. G.; Salguero, T. T.; Day, M. W.; Grubbs, R. H. *J. Am. Chem. Soc.* **2007**, *129*, 7961–7968.
- (151) Ulman, M.; Grubbs, R. H. *J. Org. Chem.* **1999**, *64*, 7202–7207.
- (152) Hong, S. H.; Day, M. W.; Grubbs, R. H. *J. Am. Chem. Soc.* **2004**, *126*, 7414–7415.
- (153) Lummiss, J. A. M.; McClennan, W. L.; McDonald, R.; Fogg, D. E. *Organometallics* **2014**, *33*, 6738–6741.
- (154) McClennan, W. L.; Rufh, S. A.; Lummiss, J. A. M.; Fogg, D. E. *J. Am. Chem. Soc.* **2016**, *138*, 14668–14677.
- (155) Lummiss, J. A. M.; Ireland, B. J.; Sommers, J. M.; Fogg, D. E. *Chem-CatChem* **2014**, *6*, 459–463.
- (156) Janse van Rensburg, W.; Steynberg, P. J.; Kirk, M. M.; Meyer, W. H.; Forman, G. S. *J. Organomet. Chem.* **2006**, *691*, 5312–5325.
- (157) Janse van Rensburg, W.; Steynberg, P. J.; Meyer, W. H.; Kirk, M. M.; Forman, G. S. *J. Am. Chem. Soc.* **2004**, *126*, 14332–14333.
- (158) Pauli, G. F.; Jaki, B. U.; Lankin, D. C. *J. Nat. Prod.* **2007**, *70*, 589–595.
- (159) Saito, T.; Nakaie, S.; Kinoshita, M.; Ihara, T.; Kinugasa, S.; Nomura, A.; Maeda, T. *Metrologia* **2004**, *41*, 213–218.
- (160) Bailey, G. A.; Foscatto, M.; Higman, C. S.; Day, C. S.; Jensen, V. R.; Fogg, D. E. *J. Am. Chem. Soc.* **2018**, *140*, 6931–6944.
- (161) Clavier, H.; Nolan, S. P. *Chem. Commun.* **2010**, *46*, 841–861.
- (162) Tolman, C. A. *J. Am. Chem. Soc.* **1970**, *92*, 2956–2965.
- (163) Bashir, O.; Piche, L.; Claverie, J. P. *Organometallics* **2014**, *33*, 3695–3701.
- (164) Occhipinti, G.; Bjørsvik, H.-R.; Törnroos, K. W.; Jensen, V. R. *Organometallics* **2007**, *26*, 5803–5814.
- (165) Rauchfuss, T. B. *Inorg. Chem.* **1977**, *16*, 2966–2968.
- (166) Bornand, M.; Torker, S.; Chen, P. *Organometallics* **2007**, *26*, 3585–3596.
- (167) Torker, S.; Müller, A.; Sigrist, R.; Chen, P. *Organometallics* **2010**, *29*, 2735–2751.
- (168) Torker, S.; Müller, A.; Chen, P. *Angew. Chem. Int. Ed.* **2010**, *49*, 3762–3766.
- (169) Hong, S. H.; Sanders, D. P.; Lee, C. W.; Grubbs, R. H. *J. Am. Chem. Soc.* **2005**, *127*, 17160–17161.
- (170) Gimeno, N.; Formentín, P.; Steinke, J. H. G.; Vilar, R. *Eur. J. Org. Chem.* **2007**, *2007*, 918–924.

- (171) Jovic, M. Structure–Reactivity Relationships in Novel Ruthenium and Rhodium Olefin Metathesis Catalysts., Ph.D. Thesis, ETH Zurich, 2014.
- (172) Occhipinti, G.; Törnroos, K. W.; Jensen, V. R. *Organometallics* **2017**, *36*, 3284–3292.
- (173) Occhipinti, G.; Bjørsvik, H. R.; Jensen, V. R. *J. Am. Chem. Soc.* **2006**, *128*, 6952–6964.
- (174) Ashworth, I. W.; Hillier, I. H.; Nelson, D. J.; Percy, J. M.; Vincent, M. A. *Eur. J. Org. Chem.* **2012**, *2012*, 5673–5677.
- (175) Kadyrov, R. *Chem. Eur. J.* **2013**, *19*, 1002–1012.
- (176) Van Leeuwen, P. W.; Clément, N. D.; Tschan, M. J.-L. *Coord. Chem. Rev.* **2011**, *255*, 1499–1517.
- (177) Lübbe, C.; Dumrath, A.; Neumann, H.; Beller, M.; Kadyrov, R. *ChemCatChem* **2019**, *6*, 105–108.
- (178) Buchmeiser, M. R.; Wang, D.; Zhang, Y.; Naumov, S.; Wurst, K. *Eur. J. Inorg. Chem.* **2007**, *2007*, 3988–4000.
- (179) Delaude, L.; Demonceau, A.; Noels, A. F. *Chem. Commun.* **2001**, 986–987.
- (180) Ledoux, N.; Allaert, B.; Verpoort, F. *Eur. J. Inorg. Chem.* **2007**, *2007*, 5578–5583.
- (181) Méret, M.; Maj, A. M.; Demonceau, A.; Delaude, L. *Monats. Chem.* **2015**, *146*, 1099–1105.
- (182) Simal, F.; Demonceau, A.; Noels, A. F.; Knowles, D.; O’Leary, S.; Maitlis, P. M.; Gusev, O. *J. Organomet. Chem.* **1998**, *558*, 163–170.
- (183) Zhang, Y.; Wang, D.; Lönnecke, P.; Scherzer, T.; Buchmeiser, M. R. *Macromol. Symp.* **2006**, *236*, 30–37.
- (184) Ackermann, L.; Bruneau, C.; Dixneuf, P. H. *Synlett* **2001**, 397–399.
- (185) Sémeril, D.; Bruneau, C.; Dixneuf, P. H. *Helv. Chim. Acta* **2001**, *84*, 3335–3341.
- (186) Sémeril, D.; Bruneau, C.; Dixneuf, P. H. *Adv. Synth. Catal.* **2002**, *344*, 585–595.
- (187) Sémeril, D.; Cléran, M.; Bruneau, C.; Dixneuf, P. H. *Adv. Synth. Catal.* **2001**, *343*, 184–187.
- (188) Tudose, A.; Demonceau, A.; Delaude, L. *J. Organomet. Chem.* **2006**, *691*, 5356–5365.
- (189) Lo, C.; Cariou, R.; Fischmeister, C.; Dixneuf, P. H. *Adv. Synth. Catal.* **2007**, *349*, 546–550.
- (190) Bowers, W. D.; Parsons, M. L.; Clement, R. E.; Eiceman, G. A.; Karasek, F. W. *J. Chromatogr.* **1981**, *206*, 279–288.
- (191) Schrodi, Y., *Handbook of Metathesis*; Grubbs, R. H., Wenzel, A. G., O’Leary, D. J., Khosravi, E., Eds.; Wiley-VCH: Weinheim, 2015; Vol. 1, pp 323–342.
- (192) Lummiss, J. A. M.; Beach, N. J.; Smith, J. C.; Fogg, D. E. *Catal. Sci. Technol.* **2012**, *2*, 1630–1632.
- (193) Williams, J. E.; Harner, M. J.; Sponsler, M. B. *Organometallics* **2005**, *24*, 2013–2015.
- (194) Velleman, P. F. *J. Am. Stat. Assoc.* **1980**, *75*, 609–615.

- (195) Ahr, M.; Thieuleux, C.; Copéret, C.; Fenet, B.; Basset, J.-M. *Adv. Synth. Catal.* **2007**, *349*, 1587–1591.
- (196) Issleib, K.; Thomas, G. *Chem. Ber.* **1960**, *93*, 803–808.
- (197) Wu, A.-H. Preparation of Phosphinoacetic Acids., US 5157153, 1992.
- (198) Day, C. S.; Fogg, D. E. *Organometallics* **2018**, *37*, 4551–4555.

Paper I

Phosphine-Based *Z*-Selective Ruthenium Olefin Metathesis Catalysts

Wietse Smit, Vitali Koudriavtsev, Giovanni Occhipinti,
Karl W. Törnroos, and Vidar R. Jensen

Organometallics **2016**, 35, 1825–1837

*Reprints were made with permission from the American Chemical Society.
Further permissions related to the material excerpted should be directed to the ACS.*

<https://pubs.acs.org/doi/10.1021/acs.organomet.6b00214>

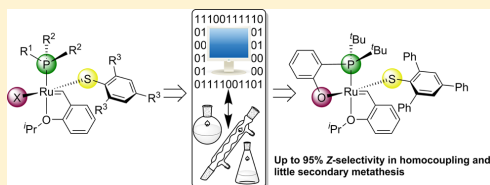
Phosphine-Based Z-Selective Ruthenium Olefin Metathesis Catalysts

Wietse Smit, Vitali Koudriavtsev, Giovanni Occhipinti,* Karl W. Törnroos, and Vidar R. Jensen*

Department of Chemistry, University of Bergen, Allégaten 41, N-5007 Bergen, Norway

Supporting Information

ABSTRACT: Whereas a number of highly Z-selective ruthenium-based olefin metathesis catalysts bearing N-heterocyclic carbene ligands have been reported in recent years, Z-selectivity has so far been difficult to achieve for phosphine-based catalysts. Guided by predictive density functional theory (DFT) calculations, we have developed phosphine-based ruthenium olefin metathesis catalysts giving 70–95% of the Z-isomer product in homocoupling of terminal alkenes such as allylbenzene, 1-octene, allyl acetate, and 2-allyloxyethanol. Starting from a moderately selective catalyst, $[P(\text{Cy})_3](-S-2,4,6\text{-Ph-C}_6\text{H}_3)\text{ClRu}(\text{=CH-O-}i\text{-PrC}_6\text{H}_4)$ (**4**, Cy = cyclohexyl, Pr = isopropyl), obtained by substituting a chloride of the Hoveyda–Grubbs first-generation catalyst with 2,4,6-triphenylbenzenethiolate, we moved on to replace Cl and PCy_3 by chelating, anionic phosphine ligands. Such ligands increase selectivity by limiting rotation around the P–Ru bond and by specifically directing the steric bulk of the phosphine substituents toward the selectivity-inducing thiolate ligand. In particular, DFT calculations predicted that *o*-(dialkylphosphino)phenolate ligands should improve selectivity and activity compared to **4**. The most promising of these compounds (**8b**), based on the *o*-(*tert*-butylphosphino)phenolate ligand, directs the two P-bonded *tert*-butyl substituents toward the 2,4,6-triphenylbenzenethiolate and has little steric hindrance *trans* to the thiolate. This compound metathesizes terminal olefins such as allylbenzene and 1-octene with Z-selectivities above 80% and allylacetate above 90%. Although these phosphine-based ruthenium monothiolate catalysts in general achieve somewhat lower activities and Z-selectivities than their second-generation counterparts, they also offer examples giving less substrate and product isomerization and thus higher yields.



INTRODUCTION

Olefin metathesis is an important carbon–carbon coupling method of the organic chemist’s toolbox. It is, for instance, used extensively in the synthesis of natural products^{1–3} and polymers^{4,5} and in oleochemistry⁶ and has found applications even in peptide and protein modifications.^{7–10} Metathesis of terminal olefins to give disubstituted olefins typically results in mixtures of the Z- and E-isomers, with the thermodynamically more stable E-isomer usually being the major product. Separating these isomers is costly and often challenging, which may hamper the assessment of their activity and the application of olefin metathesis in medicinal chemistry.^{11–13}

In recent years, several catalysts with enhanced Z-selectivity have been reported. The first highly Z-selective catalysts, based on molybdenum and tungsten, were developed by Schrock and Hoveyda.^{14–16} More recently, ruthenium-based counterparts, containing an N-heterocyclic carbene (NHC) chelated to the metal center via a Ru–C bond, were discovered by Grubbs and co-workers.^{17–19} Highly Z-selective ruthenium-based catalysts were also developed by Hoveyda and co-workers, by replacing the chloride ligands of the Hoveyda–Grubbs second-generation catalyst with a dithiolate ligand.^{20–22}

Computational studies of Grubbs-type catalysts show that the incoming olefin binds the metal center in the *trans*-position with respect to the bulky spectator ligand (e.g., alkyl phosphine or NHC),^{23–33} where also the metallocyclobutane (MCB) intermediate has been experimentally proven to form.^{34–39} In

contrast, the above-mentioned Z-selective ruthenium-based catalysts prefer a side-on or *cis*-bound olefin (see Figure 1).^{20,22,40} An alternative Z-selective catalyst, containing an aryl monothiolate ligand (**1**, Figure 1), was computationally designed and developed in our group, specifically to resemble the parent Grubbs catalysts and to maintain the *trans*-binding of the olefin.³⁸ This compound was obtained through simple substitution of one of the anionic chloride ligands of the Hoveyda–Grubbs second-generation catalyst by 2,4,6-triphenylbenzenethiolate.⁴¹

Upon exchange of the remaining anionic chloride ligand of **1** with isocyanate, catalyst **2** was obtained. This catalyst is surprisingly robust, and it can be used in air without the necessity of solvent and substrate purification.⁴² Furthermore, it tolerates acidic additives under an argon atmosphere while maintaining appreciable Z-selectivity. These conditions (air or acid) significantly reduce the isomerization of the substrate and product that accompanies many transformations.^{42,43} In contrast **1**, which displays a similar tendency to isomerize substrate and products, decomposes rapidly under the same conditions.⁴²

The Z-selectivity of our catalysts **1** and **2** is determined by steric repulsion between the bulky thiolate, effectively shielding one face of the molecule *trans* to the NHC, and the reacting

Received: March 17, 2016

Published: May 18, 2016

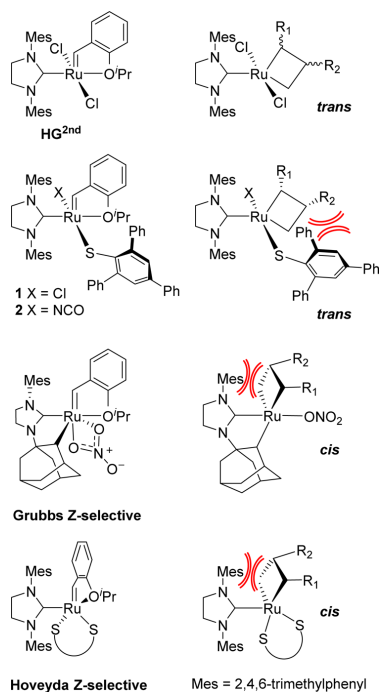


Figure 1. Positioning (*cis* or *trans* with respect to the NHC ligand) of the metallacyclobutane moiety in the catalytic cycle of the Hoveyda–Grubbs second-generation catalyst and of various *Z*-selective ruthenium-based catalysts.

metallacyclobutane moiety and its substituents, R¹ and R² (Figure 2). A sterically demanding thiolate thus gives higher

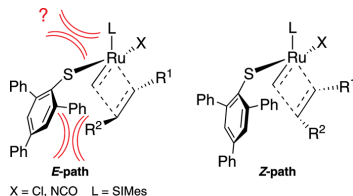


Figure 2. The *E*-path is destabilized with respect to the *Z*-path by the steric repulsion (shown in red) between the arylthiolate and the metallacyclobutane reacting moiety and possibly also by the interactions between the donor L-ligand and the thiolate. The importance of the latter interactions (indicated by a question mark) is studied in this work.

Z-selectivity than a small thiolate.³⁸ Also, as indicated in Figure 2, one may also speculate that these thiolate–metallacyclobutane interactions are influenced by the donor L-ligand, even if the latter is positioned *trans* to the metallacyclobutane. Clearly, a very small L-ligand would allow the thiolate to bend upward, away from the reacting moiety, resulting in complete loss of selectivity. However, the effect of the L-ligand on the *Z*-selectivity has so far not been systematically studied and is

poorly understood. It is not known how L-ligands with different steric requirements than the SIMes ligand of 1 and 2 would influence the selectivity.

Thus, in order to study the effect of the *trans*-positioned L-ligand on the selectivity, and also, more generally, to explore the generality of our catalyst design, we decided to investigate whether “first-generation” versions (i.e., based on phosphine instead of NHC ligands) of the *Z*-selective ruthenium-thiolate catalysts can be obtained and, if so, to what extent they are active and selective. Progress to this end could offer additional molecular “handles” to control and improve the selectivity and other properties of the *Z*-selective monothiolate catalysts.

Some effect of changing the L-ligand should be expected simply by considering the well-known fact that the nature of the remaining neutral donor ligand (e.g., NHC or phosphine) strongly influences the catalytic properties of Grubbs-type catalysts.^{44,45} Thus, a key motivation of this work was to investigate the influence of a different class of neutral donor ligands on the selectivity, activity, and stability of the ruthenium arylthiolates.

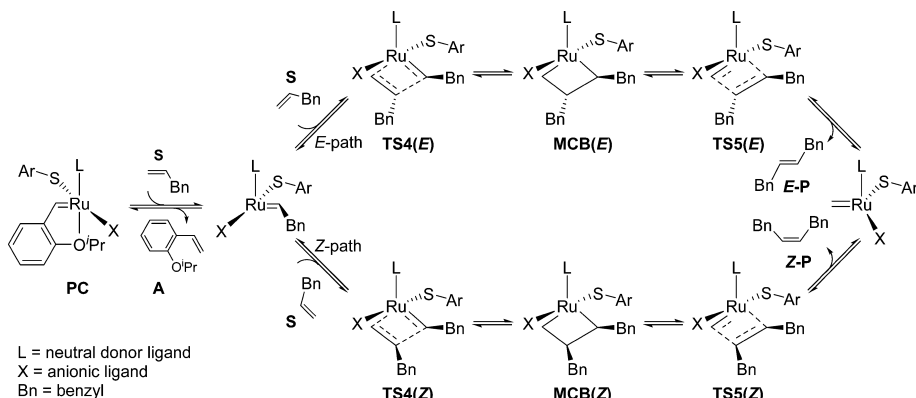
Although second-generation Grubbs catalysts are very active in general, first-generation catalysts are less prone to secondary metathesis reactions and double-bond migration.^{46,47} In addition, phosphine ligands have steric properties different from those of the NHCs, which could modify the thiolate–substituent interactions (Figure 2) and thus the selectivity compared to that of 1 and 2. A number of phosphine ligands with strongly varying steric properties are commercially available, making this class of ligands particularly tempting for exploration of *Z*-selectivity in combination with arylthiolates. Chen and co-workers have recently shown that the *Z*-selectivity of Ru-based catalysts containing a bidentate *o*-(alkylarylphosphino)phenolate ligand is influenced by the steric nature of the second anionic ligand.^{48,49} In particular, when the chloride was replaced by a sterically demanding thiosulfonate ligand, they observed an increased *cis*-content of the formed C–C double bonds. The same group has also investigated the replacement of chloride by several thiolate ligands, but they found lower *Z*-selectivities than with thiosulfonates.⁵⁰ Even if the best recorded *cis*-content was rather modest (<50%), these results demonstrate that it is possible to make *Z*-selective catalysts based on phosphine ligands and that prefer a bottom attack of the incoming olefin.

In general, the *Z*-selectivity and activity of new phosphine-based catalysts were first assessed computationally, using density functional theory (DFT), and next followed up by synthesis and catalytic tests.

RESULTS AND DISCUSSION

In the following we will try to arrive at improved *Z*-selective phosphine-based catalysts by using computational chemistry and experimental follow up in a sequence of prediction–realization iterations. Each iteration will start by molecular-level calculations to give insight and specific predictions to be followed up by synthesis and testing. The latter will, in turn, serve as feedback to the computational predictions of the next iteration.

The preferred pathways toward the formation of the *E*- and *Z*-olefin are shown in Scheme 1.^{38,39} A computational study of *Z*-selective propene metathesis using 1 shows that the MCB, obtained from cycloaddition via TS4, is less stable than the precatalyst (PC).³⁹ The rupture of the MCB via TS5 is energetically more demanding than its formation via TS4,³⁹

Scheme 1. Pathways Leading from Initiation to Product^a

^aPC = precatalyst, S = substrate, A = 2-isopropoxystyrene, TS4 = transition state for the cycloaddition, MCB = metallacyclobutane, and TS5(E) and TS5(Z) are the transition states for rupture of the MCB leading to the E (E-P) and Z (Z-P) product, respectively.

which makes TS5 the rate-limiting step. Therefore, the difference in calculated free energy at TS5 between the E- and Z-path, that is, the energy difference between TS5(E) and TS5(Z) ($\Delta\Delta G_{\text{Tol}}^{\ddagger} = \Delta G(E)_{\text{Tol}}^{\ddagger} - \Delta G(Z)_{\text{Tol}}^{\ddagger}$), is used as the computational measure of Z-selectivity.

The TS5(E) and TS5(Z) transition structures of Figure 2 are energetically favored with respect to the two alternative isomers where the R¹ substituent points toward the thiolate.^{38,39,42} Therefore, only the isomers with R¹ directed away from the thiolate were considered in this study, and steric interaction between R¹ and the thiolate is assumed to not contribute to selectivity differences between the catalysts studied in this work. The catalytic activity is approximated by the absolute barrier from the precatalyst (PC) to the most favorable route (TS5(Z)) via TSS. The calculations were performed using allylbenzene as substrate and toluene as solvent.

First-Generation Analogue of 1. In order to obtain initial insight into the role of the donor ligand (L) in controlling the stereoselectivity, we started with a computational evaluation of a variant of 1 bearing a very small L, trimethylphosphine, in combination with a bulky 2,4,6-triphenylbenzenethiolate (3, Figure 3).

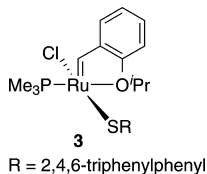


Figure 3. Hoveyda-style catalyst with sterically nondemanding phosphine ligand and bulky 2,4,6-triphenylbenzenethiolate.

A negative energy difference ($\Delta\Delta G_{\text{Tol}}^{\ddagger} = -0.8$ kcal/mol), computed for 3, shows preference for the E-path. That this complex should be E-selective may seem surprising given the presence of the large, presumably selectivity-inducing 2,4,6-triphenylbenzenethiolate ligand also found in 1. However, the small trimethylphosphine ligand allows the thiolate ligand to

twist around the Ru–S and S–Ar bonds. This causes a reduction in steric repulsion between the thiolate ligand and the substituent (R² in Figure 2) on the metallacyclobutane reacting moiety that is pointing toward the thiolate. In other words, the twisting allows for relaxation of the steric repulsion between the thiolate and the forming E-olefin, allowing the transition state of the E-path (TS5(E)), in spite of the fact that R² points toward the thiolate, to be lower in energy than the Z-counterpart. In order to destabilize the E-path, the steric repulsion between the thiolate and the forming olefin must be increased.

To achieve this repulsion, the L-ligand should be bulky enough so as to prevent the thiolate ligand from twisting around the Ru–S and S–Ar bonds. In other words, in the case of phosphine ligands, the P–Ru–S–Ar torsion angle (τ , Figure 4) should be as close to 180° as possible, whereas the Ru–S–C4–C5 torsion (φ , Figure 4) ideally should be 90°. Figure 4 shows that 4, an analogue of 3 equipped with the more bulky tricyclohexylphosphine ligand, reduces the twisting around the R–S bond by 37° ($\tau = -174^\circ$, compared to $\tau = -137^\circ$ in 3) and around the S–Ar bond by 25° ($\varphi = -90^\circ$, compared to $\varphi = -115^\circ$ in 3). This ensures Z-selectivity, but the predicted Z-selectivity for complex 4 ($\Delta\Delta G_{\text{Tol}}^{\ddagger} = 0.9$ kcal/mol) is still significantly lower than that of 1 ($\Delta\Delta G_{\text{Tol}}^{\ddagger} = 3.1$ kcal/mol). In addition, the tricyclohexylphosphine complex also has a much higher calculated absolute barrier (i.e., TS5(Z) calculated from PC) to olefin metathesis ($\Delta G(Z)_{\text{Tol}}^{\ddagger} = 28.0$ kcal/mol in 4 vs 18.8 kcal/mol in 1), suggesting that 4 should be a less active catalyst than 1.

Even though the calculated indicators of the first-generation analogue 4 were not very promising, we decided to proceed with the experimental work. The synthesis of 4 was expected to be straightforward, and this compound could thus offer a quick initial feedback on the accuracy of the calculations for the phosphine-based Z-selective catalysts. Indeed, the first-generation analogue 4 (Scheme 2) of 1 was easily prepared by reacting the commercially available Hoveyda–Grubbs first-generation catalyst with potassium 2,4,6-triphenylbenzenethiolate in tetrahydrofuran (THF) at room temperature.

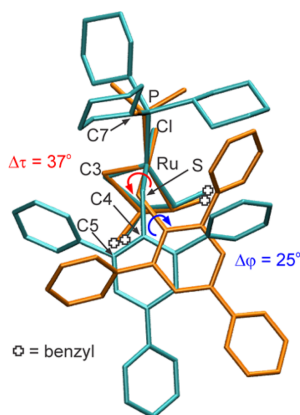
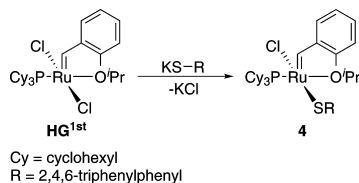


Figure 4. Comparison between the P–Ru–S–Ar (τ) and the Ru–S–C4–C5 (ϕ) torsion angles in **3** and **4**. The two structures have been fitted using the Quatfit program⁵¹ with the following weights: 10^8 for Ru, 10^7 for P, C3, and Cl. Only these four pairs of atoms were included in the fitting procedure.

Scheme 2. Synthesis of Compound **4**



Dark red crystals of **4** suitable for X-ray structure analysis were grown at low temperature ($-32\text{ }^{\circ}\text{C}$) from a THF/*n*-pentane solution. Its molecular structure and relevant bond lengths and angles are shown in **Figure 5**. The compound can be described as a slightly distorted square pyramid with the alkylidene ligand occupying the apical position. Of the remaining ligands occupying basal positions the thiolate moiety is *trans* to the chloride ligand (Cl1) and the phosphine (P1) is *trans* to the oxygen atom of the isopropoxy ligand (O1). Bond lengths and angles of the moieties found in both **1** and **4** are comparable, the most noticeable difference being the Ru1–S1–C1 angle, which is somewhat wider in **4** (117° vs $113^{\circ 41}$).

Catalytic tests of **4** and **1** in metathesis homocoupling reactions (**Table 1**) reveal lower activity and *Z*-selectivity compared to **1**. This is in qualitative agreement with the above calculated barriers.

As discussed above, the DFT calculations revealed that the tricyclohexylphosphine, in contrast to the smaller trimethylphosphine, ligand is able to orient the thiolate downward, enough to ensure moderate *Z*-selectivity. Here, we will analyze the geometries in more detail, to shed some light on the origin of the lower *Z*-selectivity of **4** with respect to **1**. First of all, as already seen in the validation against X-ray structures of ruthenium precatalysts,⁵² geometries optimized using the ω B97XD functional (applied here) compare well with the corresponding structures obtained from single-crystal X-ray diffraction. This is also true for the angles defining the position of the arylthiolate. For example, the calculated (experimental)

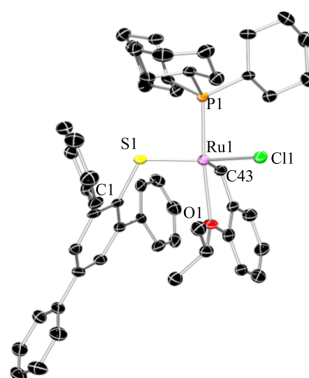


Figure 5. X-ray structure of **4** with displacement ellipsoids drawn at the 50% probability level. H atoms and solvent molecule (*n*-pentane) are omitted for clarity. Selected geometrical parameters: Ru1–C43 = 1.840(8) Å, Ru1–P1 = 2.284(2) Å, Ru1–Cl1 = 2.358(2) Å, Ru1–O1 = 2.303(5) Å, Ru1–S1 = 2.276(2) Å, Ru1–S1–C1 = $117.0(3)^{\circ}$, P1–Ru1–S1 = $88.27(7)^{\circ}$, P1–Ru1–Cl1 = $90.21(7)^{\circ}$, S1–Ru1–Cl1 = $150.21(8)^{\circ}$, P1–Ru1–O1 = $174.4(1)^{\circ}$.

Table 1. Comparison of **1** and **4** in Metathesis Homocoupling

entry	cat	sub ^a	t (h)	conv ^b (%)	yield ^b (%)	Z ^b (%)
1 ^c	1	ATMS	18	22	12	95
2 ^c	4	ATMS	68	3	2.5	87
3 ^d	1	AB	1	7	5	85
4 ^e	4	AB	1	1	0.2	n.d.
			16	9	1	61

^aATMS = allyltrimethylsilane, AB = allylbenzene. ^bDetermined by ¹H NMR analysis. Conversion is the amount of substrate converted, whereas yield refers to the amount of substrate converted into metathesis homocoupling products. For entries 3 and 4 the difference between conversion and yield corresponds to the amount of 1-alkene to 2-alkene isomerization of the substrate. For entries 1 and 2 the difference is due to the 1-alkene to 2-alkene isomerization of the substrate (major product) and to the cross metathesis products between the substrate and its 2-alkene isomer (minor product). ^cCatalyst loading = 0.25 mol %, 4 M in THF, $T = 60\text{ }^{\circ}\text{C}$. ^dCatalyst loading = 0.1 mol %, neat substrate, $T = 20\text{ }^{\circ}\text{C}$. ^eCatalyst loading = 1 mol %, neat substrate, $T = 20\text{ }^{\circ}\text{C}$.

P–Ru–S angle in the precatalyst of **4** is 88° (88°), while the Ru–S–C(Ar) angle is 115° (117°). In comparison, the NHC ligand of **1** is better at pushing the thiolate down toward the site to which the olefin binds, with the C(NHC)–Ru–S angle being 92° (91°) and the Ru–S–C(Ar) angle being 112° (113°). A more downward bent thiolate in **1** is also seen in the optimized selectivity-determining transition states (TS5), with a C(NHC)–Ru–S angle for the *E*-path (*Z*-path) equal to 89° (90°) and the Ru–S–C(Ar) angle being 115° (109°), compared to 85° (86°) and 116° (109°), respectively, for **4**.

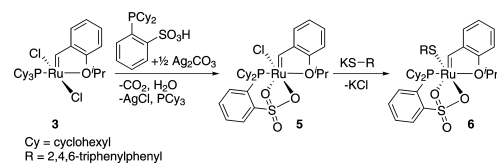
One might speculate that part of the lower selectivity of **4** compared to **1** could be due to relaxation of the *E*-olefin/thiolate steric repulsion via rotation of the tricyclohexyl ligand around the P–Ru bond. Indeed, the analysis of geometries of the optimized transition states TS5(*E*) and TS5(*Z*) for **4** shows that the phosphine ligand is rotated by 13° (as measured using the C3–Ru–P–C7 angle, **Figure 4**) around the Ru–P bond in

TSS(*E*) with respect to its orientation in TSS(*Z*). In comparison, the NHC ligand in **1** rotates much less (1°) between *E*- and *Z*-transition states.

Restricting Phosphine Rotation Using a P–O Chelate.

Claverie and co-workers recently reported olefin metathesis catalysts bearing chelating phosphine sulfonates.⁵³ Encouraged by these results, we performed DFT calculations showing promising *Z*-selectivity for a complex (**6**, Scheme 3) containing

Scheme 3. Two-Step Synthesis of Compound **6**



such a ligand. The measure of *Z*-selectivity, $\Delta\Delta G_{\text{Tot}}^\ddagger = 2.6$ kcal/mol, for this complex is not much lower than that of **1**. A phosphine rotation of only 1° is seen between the TSS *E*- and *Z*-transition states, confirming robustness against relaxation of phosphine–thiolate steric interactions. However, the slightly higher $\Delta G(Z)^\ddagger_{\text{Tot}}$ of **6** (22.0 kcal/mol) compared to **1** indicates that a somewhat lower catalytic activity can be expected.

Reaction of *o*-(dicyclohexylphosphino)sulfonic acid with half an equivalent of Ag_2CO_3 in THF produces the required silver salt *in situ* (Scheme 3).⁵⁴ Subsequent addition of the Hoveyda–Grubbs first-generation catalyst gives a mixture of the precursor compound **5** and the starting complex. The final product **6** was obtained after reaction of purified **5** with potassium 2,4,6-triphenylbenzenethiolate. Diffusion of *n*-pentane into a concentrated solution of **6** in dichloromethane at low temperature (-32°C) yielded dark green crystals suitable for X-ray structure analysis. The molecular structure and relevant bond lengths and angles are shown in Figure 6.

With the sulfonate moiety bound to ruthenium in a $\kappa^2\text{O},\text{O}'$ fashion, **6** is formally an 18-electron complex with a distorted octahedral structure. The two sulfonate oxygen atoms (O1, O2) are coordinated *trans* to the thiolate (S2) and *trans* to the alkylidene, respectively. In agreement with the expected stronger *trans*-influence of the alkylidene, the O1–Ru (2.171 Å) is significantly shorter than the O2–Ru (2.424 Å) bond. This, in turn gives a somewhat longer S1–O1 (1.493 Å) than S1–O2 (1.464 Å) bond. The other bond lengths are comparable to those of **4**, with the exception that the Ru1–O4 bond of the isopropoxy group is longer (2.345 vs 2.304 Å in **4**), presumably as a result of hexacoordination. The bond angle formed by the thiolate sulfur (Ru1–S2–C19 = 112°) is slightly sharper than that in **1** (113°).⁵¹

Surprisingly, and in spite of a relatively low calculated absolute barrier to olefin metathesis ($\Delta G(Z)^\ddagger_{\text{Tot}} = 22.0$ kcal/mol), compound **6** turned out to be completely inactive in homocoupling of allylbenzene at room temperature (entry 3, Table 2) and at 40°C (entry 4). Whereas only some isomerization of the substrate was observed at 60°C , further temperature increases led to olefin metathesis products, mainly of the *E*-isomer, presumably as a result of decomposition of **6** into catalytically active species (entry 6). Similarly, it is also possible to activate **6** using acid to give a catalyst that is not *Z*-selective. An experiment similar to entry 3 except for the use of

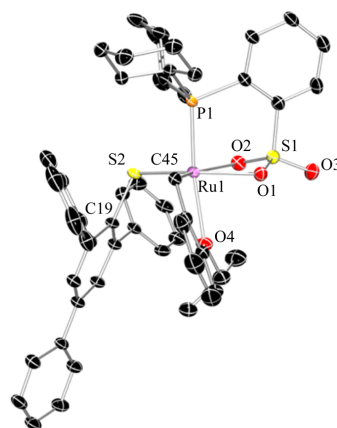


Figure 6. X-ray structure of **6** with displacement ellipsoids drawn at the 50% probability level. H atoms and solvent molecule (dichloromethane) are omitted for clarity. Selected geometrical parameters: Ru1–C45 = 1.8501(2) Å, Ru1–P1 = 2.2790(5) Å, Ru1–O1 = 2.1706(1) Å, Ru1–O2 = 2.4236(2) Å, Ru1–O4 = 2.3448(2) Å, Ru1–S2 = 2.2886(5) Å, S1–O1 = 1.4931(2) Å, S1–O2 = 1.4641(2) Å, S1–O3 = 1.4321(2) Å, Ru1–S2–C19 = $112.41(6)^\circ$, P1–Ru1–S2 = $89.138(2)^\circ$, P1–Ru1–O1 = $93.29(4)^\circ$, P1–Ru1–O2 = $83.25(4)^\circ$, P1–Ru1–O4 = $169.66(4)^\circ$, S2–Ru1–O1 = $157.44(4)^\circ$.

Table 2. Homocoupling of Neat Allylbenzene

entry	cat ^a	T (°C)	t (h)	conv ^b (%)	yield ^b (%)	Z ^b (%)
1	1 ^c	20	1	7	5	85
2	4	20	1	1	0.2	n.d.
			16	10	1	61
3	6	20	1	0	0	
4	6	40	1	0	0	
5	6	60	1	1	0	
6	6	80	1	73	9	29
			24	100	7	29
7	8a	20	1	60	2	50
8	8b	20	1	21	13	81

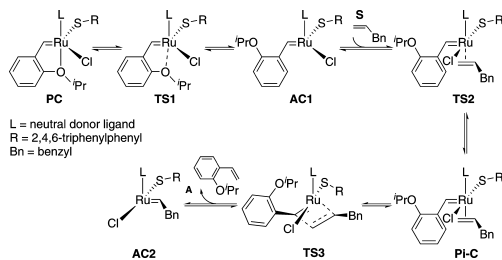
^aCatalyst loading = 1 mol %. ^bDetermined by ¹H NMR analysis. Conversion is the amount of substrate converted, whereas yield refers to the amount of substrate converted into metathesis homocoupling products. The difference between conversion and yield corresponds to the amount of 1-alkene to 2-alkene isomerization of the substrate. ^cCatalyst loading = 0.1 mol %.

2 equiv of phenylphosphoric acid gave 22% conversion, 21% yield, and 21% *Z*.

In addition to the fact that the $\kappa^2\text{O},\text{O}'$ -binding of the sulfonate provides electronic saturation (with an electron count of 18) and adds steric congestion around ruthenium, the bulky thiolate ligand, forming an even sharper angle (Ru1–S2–C19 = 112°) with ruthenium than in **1**, projects significant steric pressure toward the site located *trans* with respect to the phosphorus atom, seemingly shielding the catalytic site. Thus, at least at first glance, the electronic saturation and steric congestion together are consistent with low or no activity for **6**, whereas less sterically congested compounds (similar to precursor **5**) containing chelating phosphine sulfonate ligands are in fact active in olefin metathesis.⁵³

In order to possibly shed some light on the reasons for the inactivity of **6**, additional DFT calculations were performed on both **1** and **6**. One potential cause for the lack of activity could be a prohibitively high barrier to initiation. Whereas a computational study of propene metathesis using **1** showed **TS5** to be the selectivity-determining barrier of the regular catalytic cycle, the transition state for formation of the MCB intermediate during the initiation stage (**TS3**, Scheme 4) was

Scheme 4. Pathway from Precursor to Active Catalyst^{4f}



^{4f}PC = pre-catalyst, **TS1** = transition state for Ru–O'Pr bond rupture, **AC1** = first active complex, **S** = substrate, **TS2** = transition state for olefin coordination, **Pi-C** = π -complex, **TS3** = transition state for MCB formation, **A** = 2-isopropoxystyrene, **AC2** = second active complex. The MCB and the transition state for rupture of the MCB, located between **TS3** and **AC2**, have been omitted for clarity.

found to be the overall highest barrier.³⁹ However, formation of the MCB during initiation seems to be easy for **6**, with a lower barrier for **TS3** (calculated with substituents on the same side of the metallacyclobutane, as previously shown to be the most stable isomer of **TS3**)³⁹ than that calculated for **1** (entries 1, 2, Table 3), implying that **TS3** of the initiation cannot explain the

Table 3. Key Stationary Points along the Initiation Path^{4f}

entry	cat.	TS1	AC1	TS2	Pi-C	TS3
1	1	12.0	8.0	22.9	23.9	28.7
2	6	10.0	8.4	21.5	20.0	22.8

^{4f}Gibbs free energy [kcal/mol] in toluene.

lack of activity. We thus continued by checking whether the other elementary steps of the initiation (Scheme 4) could be associated with prohibitively high barriers. The first of these involves the rupture of the Ru–O'Pr bond (**TS1**) according to a dissociative mechanism, but also this barrier is lower for **6** than for **1** (entries 1, 2, Table 3). An alternative interchange mechanism, in which the isopropoxy dissociation is promoted by the incoming olefin, is reported to be competitive for the Hoveyda–Grubbs dichloride catalysts.⁵⁵ However, the bulky arylthiolate ligand of **6** effectively blocks coordination of the olefin prior to isopropoxy dissociation.³⁹

One might think that the next step, the coordination of the olefin, could be hindered by the combination of the bulky groups, the arylthiolate and the sulfonate, enveloping the metal center. However, also this reaction appears to be more facile, with less energy required to reach **TS2** for **6** than for **1**.

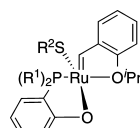
Since both the initiation phase and the catalytic cycle of **6** appear to be relatively facile, the explanation for the lack of activity must be sought elsewhere. The activity combined with lack of selectivity observed at higher temperatures (Table 2)

suggests that, under catalytic conditions, **6** may undergo structural changes, or decomposition, to give catalytically active but unselective species. Of course, it is hard to guess which species or decomposition reactions that are involved. However, we have previously observed that the thiolate ligand weakens the *trans*-positioned Ru–Cl bond in **1**,⁴² and one candidate structural modification thus could be dissociation of the sulfonate ligand of **6**. In other words, if dissociation of the sulfonate is more facile than dissociation of the O'Pr moiety to form the active complex (**AC**), then the resulting zwitterionic species could be responsible for the catalytic activity observed at higher temperatures. However, the calculated free energy of the zwitterionic species is 22.0 kcal/mol above that of the pre-catalyst and thus also 12.0 kcal/mol above **TS1**. With also this alternative determined to be unlikely, we can only conclude that the computational mechanistic exploration offered no explanation for the lack of activity and selectivity of **6**.

Reducing the Size of the P–O Chelate. Since the *o*-(dicyclohexylphosphino)sulfonate ligand did not lead to appreciable activity and selectivity, we turned to an alternative class of bidentate phosphine ligands, based on an *o*-(dialkylphosphino)phenolate chelating moiety.⁵⁶ Chen and co-workers have recently used this kind of ligand to develop a new family of highly active ruthenium–alkylidene olefin metathesis catalysts for copolymerization of norbornene and cyclooctene.^{48,49} They have also shown that a sterically demanding second anionic ligand (in combination with the chelating phosphino phenolate) leads to increased *cis*-content of C–C double bonds in the resulting copolymer.

Encouraged by the *Z*-selectivity and activity observed by Chen and co-workers, and still with the goal to hinder rotation of the phosphine and improve upon the design of complex **6**, we decided to explore the *o*-(dialkylphosphino)phenolate ligand. Also encouraging is the fact that the five-membered ring formed by an *o*-(dialkylphosphino)phenolate with ruthenium (Ru–P–aryl–O) represents a less sterically demanding second anionic ligand, to be used in combination with a large arylthiolate, than the six-membered Ru–P–aryl–SO₃ ring in **6**. Even if the reasons for the lack of activity and selectivity of the latter catalyst could not be determined, it is intuitively promising that the phenolate moiety can be expected to bind ruthenium in κ^1 O fashion only and thus avoid formation of an 18-electron complex as in **6**.

In combination with the relatively compact Ru–P–aryl–O chelating moiety, we opted to equip the phosphorus atom with sterically demanding *tert*-butyl substituents to help push the arylthiolate down toward the olefin-binding site (**8b**, Figure 7), cf. the mechanism of Figure 2. To help evaluate this expected selectivity-boosting phosphine–thiolate repulsion, we also



- 8a** R¹ = *tert*-butyl, R² = 2,4,6-trimethylphenyl
8b R¹ = *tert*-butyl, R² = 2,4,6-triphenylphenyl
9 R¹ = cyclohexyl, R² = 2,4,6-triphenylphenyl
10 R¹ = 1-adamantyl, R² = 2,4,6-triphenylphenyl

Figure 7. Compounds **8**–**10**, bearing *o*-(dialkylphosphino)phenolate ligands.

included the smaller 2,4,6-trimethylbenzenethiolate ligand (**8a**) and two variants of **8b**, one with somewhat less sterically demanding alkyl groups (cyclohexyl) on phosphorus (**9**) and one with somewhat more sterically demanding alkyl groups (1-adamantyl) on phosphorus (**10**).

The calculated activities and selectivities of compounds **8a**, **8b**, **9**, and **10** are given in Table 4. The catalyst with *o*-(di-*tert*-

Table 4. Comparison of Computed Parameters of the OM Catalysts with **1**

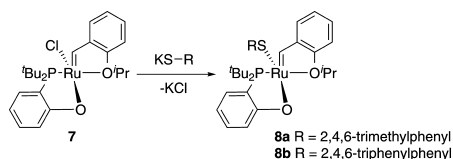
entry	cat	$\Delta\Delta G_{\text{Tot}}^{\ddagger}$ ^a	$\Delta G(Z)_{\text{Tot}}^{\ddagger}$ ^b
1	1	3.1	18.8
2	3	-0.8	n.a.
3	4	0.9	28.0
4	6	2.6	22.0
5	8a	0.3	26.3
6	8b	1.6	24.8
7	9	0.8	26.7
8	10	1.5	n.a.

^aThe relative energies [kcal/mol] are a measure of *Z*-selectivity; $\Delta\Delta G_{\text{Tot}}^{\ddagger} = \Delta G(E)_{\text{Tot}}^{\ddagger} - \Delta G(Z)_{\text{Tot}}^{\ddagger}$. ^b $\Delta G(Z)_{\text{Tot}}^{\ddagger}$ is the absolute barrier to **TSS**(*Z*) with the precatalyst **PC** as the reference.

butylphosphino)phenolate (**8b**, entry 6) appears to be a promising candidate. Although the measure of selectivity ($\Delta\Delta G_{\text{Tot}}^{\ddagger}$) is only about half that of **1**, it is higher than that obtained for **4**, **8a**, **9**, and **10** (entries 5, 7 and 8, Table 4). Furthermore, the absolute barrier ($\Delta G(Z)_{\text{Tot}}^{\ddagger}$) calculated for **8b** is lower than for the other catalysts (except **1**), suggesting that this compound could be a reasonably active catalyst. Surprisingly, in spite of the adamantyl groups of **10** presumably being even more sterically demanding than the *tert*-butyl groups of **8b**, the calculated selectivity of **10** is essentially the same as that of **8b**. This, the unexpectedly low $\Delta\Delta G_{\text{Tot}}^{\ddagger}$ of **10**, results from the solvent corrections (see the Supporting Information for tabulated relative energies and enthalpies and the various thermochemical and solvent corrections), which favor the *E*-path. In other words, the intramolecularly induced selectivity of **10**, reflected in the gas-phase-calculated $\Delta\Delta G^{\ddagger}$ (= 2.1 kcal/mol), is, as expected, higher than that of **8b** (1.2 kcal/mol).

As seen above, in solution **8b** and **10** are predicted to be equally selective, which means that other factors must count when selecting which compound to synthesize. Due to the lower cost of preparing the *o*-(di-*tert*-butylphosphino)phenolate ligand, we decided to synthesize **8b**. For comparison, the closely related **8a** was also selected for experimental follow up since the thiol is commercially available and the synthesis was not expected to require much extra work. Precursor **7** (Scheme 5) and the *o*-(di-*tert*-butylphosphino)phenolate ligand necessary to synthesize **7** were prepared according to literature procedures.^{49,57} The final products were obtained after reaction

Scheme 5. Synthesis of Compounds **8a** and **8b**



of **7** with potassium 2,4,6-trimethylbenzenethiolate (**8a**) and potassium 2,4,6-triphenylbenzenethiolate (**8b**), respectively.

Diffusion of *n*-pentane into a concentrated solution of **8b** in dichloromethane at low temperature (-32 °C) yielded dark red crystals suitable for X-ray structure analysis. Its molecular structure and relevant bond lengths and angles are shown in Figure 8. Compound **8b** can be described as a slightly distorted

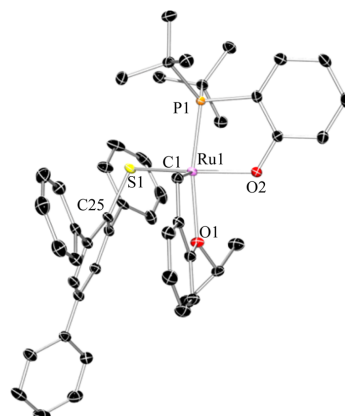


Figure 8. X-ray structure of **8b** with displacement ellipsoids drawn at the 50% probability level. H atoms and solvent molecule (dichloromethane) are omitted for clarity. Selected geometrical parameters: Ru1-C1 = 1.846(2) Å, Ru1-P1 = 2.2653(5) Å, Ru1-O1 = 2.2531(2) Å, Ru1-O2 = 2.0246(2) Å, Ru1-S1 = 2.2846(6) Å, Ru1-S1-C25 = 114.21(7)°, P1-Ru1-S1 = 92.412(2)°, P1-Ru1-O1 = 168.79(5)°, P1-Ru1-O2 = 83.51(4)°, S1-Ru1-O2 = 152.11(5)°.

square pyramid with the alkylidene occupying the apical position. Of the remaining ligands occupying basal positions the thiolate moiety is *trans* to the phenoxylate oxygen (O2) and the phosphine (P1) is *trans* to the alkoxy oxygen atom (O1). Bond lengths are comparable to those of **4**, **6**, and **1**.⁴¹ However, the bond distance between ruthenium and the phenolate oxygen (Ru-O2 = 2.025 Å) is clearly shorter than the corresponding Ru-O_{sulfonate} bond distances (2.304 and 2.345 Å) of complex **6**. Furthermore, the angle between phosphorus and the phenolate oxygen atom (O2) of the sulfonate moiety (P1-Ru1-O2 = 83.51°) is smaller than 90°. The bond angle around the sulfur atom of the thiolate ligand (Ru1-S1-C25 = 114°) is larger than that of **6** (112°) but sharper than that of **4** (117°).

Catalyst **8a** rapidly converts allylbenzene at room temperature (entry 7, Table 2). However, even though 60% of the allylbenzene was converted after 1 h, only 2% metathesis product was obtained and with only modest *Z*-selectivity (50%). Even though the conversion of **8b** (entry 8) is somewhat lower compared to **8a**, its olefin metathesis yield is much higher than that of both **4** and **8a**, in agreement with the fact that the computational barrier to olefin metathesis, $\Delta G(Z)_{\text{Tot}}^{\ddagger}$ is lower for **8b** than for **8a** and **4**. Perhaps more important, we found that **8b** gave a *Z*-selectivity above 80% in homocoupling of allylbenzene, to our knowledge the highest *Z*-selectivity so far obtained with phosphine-based, first-generation-style catalysts.

Table 5. Homocoupling of Allylbenzene with 8b under Different Reaction Conditions

entry	cat load (mol %)	additive ^a	solvent	[sub] (M)	T (°C)	t (h)	conv ^b (%)	yield ^b (%)	Z ^b (%)
1	1			neat	20	0.5	10	6	83
						1	21	13	81
						4	69	26	73
2	1			neat	40	4	99	17	26
3	1			neat	60	0.5	97	19	45
4	2			neat	20	1	32	18	82
5	4			neat	20	1	35	19	82
6	1		toluene	4	20	1	9	5	81
7	1		THF	4	20	1	9	3	81
8	1		<i>p</i> -cymene	4	20	1	6	3	82
9	1		toluene	1	20	1	6	1	81
10	1		toluene	2	20	1	6	2	80
11	1		toluene	3	20	1	9	4	81
12	1		toluene	4	40	1	19	11	77
13	1	QUI		neat	20	4	29	28	49
14	1	PPA		neat	20	4	9	4	63
15	1	TCPO		neat	20	4	37	25	81
16	1	H ₂ O		neat	20	4	25	12	81

^aQUI = 2,6-dichloro-1,4-benzoquinone (1 equiv with respect to the cat), PPA = phenyl phosphoric acid (1 equiv with respect to the cat), TCPO = tricyclohexylphosphine oxide (5 equiv with respect to the cat), 1 drop H₂O. ^bDetermined by ¹H NMR analysis. Conversion is the amount of substrate converted, whereas yield refers to the amount of substrate converted into metathesis homocoupling products. The difference between conversion and yield corresponds to the amount of 1-alkene to 2-alkene isomerization of the substrate.

The low *Z*-selectivity obtained with the small thiolate ligand (**8a**) is as predicted (entry 5, Table 4) and shows that the *o*-(*di*-*tert*-butylphosphine)phenolate, even with its bulky *tert*-butyl groups facing the thiolate, does not induce much selectivity by itself. As expected, the small trimethylbenzene in **8a** allows for relaxation of the steric interaction between the thiolate and the R² substituent (Figure 2) via thiolate twisting around the Ru–S (τ) and S–Ar (φ) bonds as defined in Figure 4. Indeed, TSS(*E*) of **8a** shows the largest departure from the ideal, nontwisted case ($\tau = 180^\circ$ and $\varphi = -90^\circ$) for both Ru–S ($\tau = -165^\circ$ vs $\tau = -168^\circ$ in **8b**, $\tau = -178^\circ$ in **9**, and $\tau = 178^\circ$ in **10**) and S–Ar ($\varphi = -99^\circ$ vs $\varphi = -94^\circ$ in **8b**, $\varphi = -88^\circ$ in **9**, and $\varphi = -85^\circ$ in **10**) among the complexes with *o*-(dialkylphosphino)phenolate chelating moieties. This twisting allows **8a** to have a wide P–Ru–S angle (95° vs 94° in **8b**, 90° in **9**, and 95° in **10**) and a sharp Ru–S–C(Ar) angle (113° vs 114° in **8b**, 113° in **9**, and 113° in **10**) without this being reflected in high selectivity.

From the above we can conclude that the small thiolate allows for relaxation of the metallacyclobutane–thiolate repulsion, which decreases *Z*-selectivity. Therefore, increasing the size of the thiolate, by introducing phenyl substituents on the benzene ring as in **8b**, seems to be the key selectivity-inducing element.

Catalysis Using 8b under Different Reaction Conditions. A series of experiments with varying catalyst loading, solvent, substrate concentration, reaction temperature, and additives were performed using **8b**. Whereas a complete overview of these results is given in Table S1 of the Supporting Information, a summary is included in Table 5. The best conditions seem to be a temperature of 20 °C, with 1 mol % catalyst in neat substrate using 5 equiv of tricyclohexylphosphine oxide (TCPO) as additive. Further conclusions from these experiments are described in the following:

- Isomerization of the substrate is promoted by increasing temperature, especially at high substrate conversion (entries 1–3).

- Increasing the catalyst loading leads to only slight improvement in *Z*-isomer yield (i.e., the product of the yield and percentage of *Z*-isomeric product, entries 1, 4, 5).

- Using solvents (entries 6–8) invariably results in lower conversion and yield than catalysis in neat allylbenzene (entry 1). Only insignificant differences between the various solvents are observed.

- Reduced substrate concentration leads to lower conversion and yield (entries 9–12).

Several additives were tested: 2,6-dichloro-1,4-benzoquinone effectively prevents isomerization (entry 13), but unfortunately at the expense of a sharp decline in *Z*-selectivity. Phenylphosphoric acid gives low conversion and yield and only moderate *Z*-selectivity (entry 14). Tricyclohexylphosphine oxide and water (entries 15, 16) prevent isomerization of the *Z*-product in the *E*-product, resulting in persistent, high *Z*-selectivity at longer reaction times. Unfortunately, when using water as additive, the progress of the reaction stops at ca. 25% substrate conversion, indicating inactivation or decomposition of the catalyst.

Catalysis Using Different Substrates. Catalysts **8a** and **8b** were tested in several neat substrates other than allylbenzene to determine tolerance toward different functional groups (Table 6). For substrates particularly prone to isomerization, TCPO was added to attempt to maintain *Z*-selectivity and yield as described above for allylbenzene (Table S1). For **8a**, yield and *Z*-selectivity remained low, as expected, and addition of TCPO did not improve the *Z*-selectivity but to some extent suppressed isomerization of the substrate (entries 3, 4). For allyltrimethylsilane (entry 6), addition of TCPO led to complete lack of catalytic activity.

Interestingly, high *Z*-selectivity, moderate yield, and only negligible isomerization of the substrate were obtained with **8b** in 1-octene and allyl acetate (entries 7 and 8). In contrast, the corresponding *Z*-selectivity in 2-allyloxyethanol (entry 9) is low and comparable to that obtained with **8a**, presumably due to

Table 6. Homocoupling of Various Neat Substrates

entry	cat ^a	sub ^b	additive ^c	t (h)	conv ^d (%)	yield ^d (%)	Z ^d (%)
1	8a	AB	TCPO	8	95	6	38
2	8a	AAc		1	5	5	34
3	8a	AOE		1	12	2	65
4	8a	AOE	TCPO	1	1.4	0.8	66
				48	98	4	44
5	8a	ATMS		1	1	0.5	88
6	8a	ATMS	TCPO	1	0	0	
				48	0		
7	8b	OCT		1	4	4	82
				4	10	10	82
				8	27	27	82
8	8b	AAc		1	6	6	95
				4	16	16	93
				8	24	24	92
9	8b	AOE		1	3	2	54
				4	6	3	54
				8	8	3	54
10	8b	AOE	TCPO	8	8	4	74
				48	19	8	74
11	8b	PB		1	14	12	80
				4	45	30	77
				8	77	36	71
12	8b	PB	TCPO	8	43	34	79
				24	71	47	74

^aCatalyst loading = 1 mol %, $T = 20\text{ }^{\circ}\text{C}$. ^bAB = allylbenzene, OCT = 1-octene, AAc = allyl acetate, AOE = 2-allyloxyethanol, ATMS = allyltrimethylsilane, PB = 4-phenyl-1-butene. ^cTCPO = tricyclohexylphosphine oxide (5 equiv). ^dDetermined by ¹H NMR analysis. Conversion is the amount of substrate converted, whereas yield refers to the amount of substrate converted into metathesis homocoupling products. For entries 1, 3, 4, 9, and 10 the difference between conversion and yield corresponds to the amount of 1-alkene to 2-alkene isomerization of the substrate. For entry 5 the difference is due to the 1-alkene to 2-alkene isomerization of the substrate (major product) and to the cross metathesis products between the substrate and its 2-alkene isomer (minor product).⁴⁰ For entries 11 and 12 the difference is mainly due to the 1-alkene to 2-alkene isomerization of the substrate. In addition, small amounts of cross metathesis products between the substrate and its 2-alkene isomer as well as of compounds resulting from double-bond migration in the target homocoupling product were detected.

isomerization. Addition of TCPO improved the Z-selectivity (entry 10). The yield and Z-selectivity obtained with **8b** in 4-phenyl-1-butene (entries 11, 12) are comparable to those observed above with allylbenzene.

Importantly, and in contrast to results for NHC-based catalysts, only negligible or little Z-E isomerization of the product is observed with **8b** with increasing substrate conversion. The sustained Z-selectivity is probably due to low activity in secondary metathesis, since this trend is observed also when the Z-selectivity is moderate (e.g., entries 8 and 9).

Ring-Opening Metathesis Polymerization (ROMP). In addition to the above-described homocoupling reactions, our catalysts were tested in ROMP of neat *cis*-cyclooctene (Table 7). The conditions optimal for homocoupling of terminal olefins were applied also in ROMP. In general, the resulting activities were low and the Z-selectivities only moderate, even though the latter were still clearly higher than that of the Hoveyda-Gubbs first-generation catalyst (entry 1) and comparable to, or slightly higher than, those of related

Table 7. ROMP of *cis*-Cyclooctene at 20 °C

entry	cat	cat load (mol %)	t (h)	yield ^a (%)	Z ^a (%)
1	HC ^{first}	1	16	100	24
2	4	1	16	6	47
3	6	1	16	1	47
4	8a	1	16	0.5	67
5	8b	1	16	13	54

^aDetermined by ¹H NMR analysis.

complexes based on a chelating *o*-(alkylarylphosphino)-phenolate and a sterically demanding thiosulfonate ligand reported by Chen and co-workers.⁵⁰ The lower selectivity of the latter catalysts may in part be caused by the fact that one of the phosphine substituents, a phenyl, is less sterically demanding than the *tert*-butyl groups of **8a** and **8b**.

The highest yield was obtained for **8b**, in combination with rather low Z-selectivity. **6** and **8a** were hardly active in ROMP, but the 1% yield obtained with **6** is still an interesting observation given the fact that this compound was completely inactive in homocoupling at low temperatures.

CONCLUSIONS

We have synthesized and tested phosphine-based ruthenium olefin metathesis catalysts with appreciable Z-selectivity, giving 70–95% of the Z-isomer product in homocoupling of terminal alkenes such as allylbenzene, 1-octene, allyl acetate, and 2-allyloxyethanol, in combination with low to moderate (up to ca. 50%) yields. The Z-selectivity of these catalysts is induced by the presence of a sterically demanding monodentate arylthiolate. They may thus be termed first-generation analogues of our previously reported NHC-based Z-selective ruthenium catalysts bearing monodentate arylthiolate ligands,^{38,41,42} often achieving somewhat lower activities and Z-selectivities than their second-generation counterparts, but also offering examples giving less substrate and product isomerization and thus higher yields.

Both the first- and second-generation versions of the Z-selective ruthenium-based catalysts may be obtained via one or two ligand exchange reactions starting from the corresponding first- or second-generation Hoveyda–Grubbs ruthenium dichloride olefin metathesis catalyst, and they also resemble the “parent” unselective ruthenium catalysts by binding the substrate olefin to form the metallacyclobutane *trans* to the phosphine or NHC donor ligand, L.

Geometrical analysis and DFT calculations show that the steric bulk of the L-ligand is important, and surprisingly, a large thiolate is not enough to achieve high Z-selectivity. For example, the small trimethylphosphine ligand results in an E-selective catalyst even when combined with the bulky 2,4,6-triphenylbenzenethiolate. With increasing phosphine steric bulk, phosphine–thiolate repulsion will push the thiolate down toward the site of the metallacyclobutane formation and thus induce Z-selectivity.

Lack of phosphine steric bulk allows the thiolate to bend (via the Ru–S–Ar and P–Ru–S angles) upward, toward the phosphine, and, more importantly, to twist around the Ru–S and S–Ar bonds so as to minimize steric repulsion against the metallacyclobutane moiety. Phosphines, in contrast to NHC ligands, are also seen to relax steric repulsion against the thiolate ligand by rotation around the Ru–P bond. A chelating P–O-type ligand prevents this rotation. The most catalytically active and Z-isomer-yielding catalyst obtained here (**8b**)

contains a bidentate, five-membered-ring-forming *o*-(di-*tert*-butylphosphino)phenolate ligand that prevents rotation, directs bulky *tert*-butyl substituents toward the thiolate, and has little steric hindrance *trans* to the thiolate.

COMPUTATIONAL DETAILS

Geometry Optimization. All geometry optimizations were performed using the hybrid range-separated functional including empirical atom–atom dispersion, ω B97XD, as implemented in Gaussian 09.⁵⁸ The ω B97XD^{59–61} functional was chosen due to its excellent performance in reproducing X-ray geometries of ruthenium-based olefin metathesis catalysts and other functional transition metal compounds.⁵² Input geometries were constructed using the Spartan software package⁶² by modifying the available X-ray structures⁶³ or previously DFT-D-optimized geometries and by performing conformational searches at the MMFF⁶⁴ force-field level. The standard procedure consisted of selecting a few of the conformations of lowest MMFF energy for evaluation at the DFT level. The thus obtained conformation with the lowest Gibbs free energy in toluene was used. Tight geometry optimization, corresponding to a maximum force of 1.5×10^{-5} au and the accordingly scaled maximum displacement, was used (keyword opt = (Tight)). Numerical integrations were performed using the “superfine” grid (pruned, 150 radial shells and 974 angular points per shell for the first two rows of the periodic table, 225 shells and 974 angular points per shell for later elements) of Gaussian 09. The SCF density-based convergence criterion was tightened 100-fold compared to the default, to 10^{-10} (keyword SCF = (Conver = 10)). This tightening was necessary to ensure geometry convergence. All stationary points were characterized by the eigenvalues of the analytically calculated Hessian matrix.

The Stuttgart 28-electron relativistic effective core potential (ECP28MDF) in conjunction with the accompanying correlation consistent valence triple- ζ plus polarization (cc-pVTZ-PP) basis set, with the *g* function removed, was used for the Ru atom,⁶⁵ which implies a (41s37p25d2f)/[5s5p4d2f] contraction. The rest of the atoms were treated as follows: All atoms which, at some point in the reaction, are directly bonded (here termed a “nearest neighbor”, via a covalent or donor–acceptor bond) to ruthenium (e.g., the sp^2 carbon atoms of the substrate alkene) were described by correlation consistent valence triple- ζ plus polarization (cc-pVTZ)^{66,67} basis sets, obtained from the EMSL basis set exchange Web site,⁶⁸ in which, in each case, the highest angular momentum functions were removed. Moreover, the same triple- ζ basis sets were used also for the entire sulfonate group in 6 due to highly delocalized electrons and indistinguishable O atoms. The resulting contractions were C, N, O (18s5p2d)/[4s3p2d]; Cl, S (41s16p2d)/[5s4p2d]. All other atoms were described by the standard correlation consistent valence double- ζ plus polarization (cc-pVDZ)^{66,67} basis sets.

Thermochemistry. Translational, rotational, and vibrational partition functions for thermal corrections to give total enthalpies and Gibbs free energies were computed within the ideal-gas, rigid-rotor, and harmonic oscillator approximations following standard procedures, with a minor adjustment for the entropy corrections. To reduce the well-known problems (fluctuations in free energy corrections due to vibrational entropy divergence for low frequencies)^{69,70} caused by the harmonic-approximation low-frequency modes upon calculation of thermochemical corrections,^{69,71–73} we used the quasi-harmonic treatment of Truhlar and co-workers,^{72,73} consisting of shifting all frequencies below 100 cm^{-1} to 100 cm^{-1} , when calculating entropies. The temperature used in the calculation of thermochemical corrections was set to 298.15 K.

Single-Point Calculations (SP). The reported energies were obtained in SP calculations on optimized geometries using the gradient-corrected PBE^{74,75} functional in combination with the D3 version of Grimme’s empirical dispersion with Becke–Johnson damping,⁷⁶ termed PBE-D3(BJ), as implemented in Gaussian 09.⁵⁸ The PBE-D3(BJ) functional was chosen due to its excellent agreement with experimental relative gas-phase energies of ruthenium-mediated olefin metathesis.⁷⁷ Numerical integrations were performed using the

“ultrafine” grid of Gaussian 09. The SP SCF convergence criterion was set to 10^{-5} .

The Stuttgart 28-electron relativistic effective core potential (ECP28MDF) in conjunction with the accompanying correlation consistent valence quadruple- ζ plus polarization (cc-pVQZ-PP) basis set was used for the Ru atom.⁶⁵ The C and H atoms were treated with the correlation consistent valence quadruple- ζ plus polarization (cc-pVQZ)^{66,67} basis sets obtained from the EMSL basis set exchange Web site.⁶⁸ All other atoms were treated with an extended cc-pVQZ basis set obtained by adding diffuse functions from the “aug-cc-pVQZ Diffuse” set,^{67,78} resulting in the following contractions for the modified basis sets: O, N (22s7p4d3f2g)/[6s5p4d3f2g]; Cl, S (43s20p4d3f2g)/[7s6p4d3f2g].

Electrostatic and nonelectrostatic solvent effects were accounted for implicitly using the SMD solvation method, a polarizable continuum model (PCM) that includes alternative cavitation, dispersion, and solute structure reorganization terms and also uses a particular set of atomic radii that modifies the electrostatic contribution compared to regular PCM.⁷⁹ The SMD calculations were performed using Gaussian 09, with default settings.

Free energies were obtained using a standard state corresponding to a 1 M infinitely diluted solution and a temperature of 298.15 K, as $G_{\text{Tol}} = G_{\text{Gas}} + \Delta G_{\text{solvation}} + \Delta G^{\text{atm} \rightarrow 1\text{M}}$, where $\Delta G^{\text{atm} \rightarrow 1\text{M}} = 1.89 \text{ kcal/mol}$ and accounts for the change in standard state from 1 atm to 1 M.⁷⁷ $\Delta G_{\text{solvation}}$ is the solvation free energy and is the difference between the SMD and the gas-phase SCF energies. G_{Gas} is the Gibbs free energy in the gas phase calculated by adding the thermal correction (G_{corr}) to the single-point SCF energy; see the Supporting Information.

EXPERIMENTAL SECTION

Reactions were performed under a dry argon atmosphere using Schlenk techniques or in a glovebox, unless otherwise stated. Tetrahydrofuran, toluene, and dichloromethane were dried using an MBraun solvent purification system (“Grubbs column”) and degassed before use. Anhydrous *n*-pentane was purchased from Sigma-Aldrich and used as received. Allyl acetate, allylbenzene, 4-phenyl-1-butene, allyltrimethylsilane, 1-octene, 2-allyloxyethanol, *p*-cymene, and *cis*-cyclooctene were purchased from Sigma-Aldrich and degassed before use. Potassium 2,4,6-trimethylbenzenethiolate,⁴¹ potassium 2,4,6-triphenylbenzenethiolate,⁴² and $[P(-6-O-C_6H_4)(t-Bu)_2]ClRu(=CH-O-PrC_6H_4)$ ^{49,57} were prepared according to literature procedures. All the other chemicals were purchased from commercial suppliers and used as received.

NMR spectra were recorded on Bruker Biospin AV500 and AV600 spectrometers. The chemical shifts are reported relative to the residual solvent peaks.⁸⁰ Phosphorus resonance spectra were calibrated using a sealed ampule containing 85% aqueous H_3PO_4 , submerged in an NMR tube filled with D_2O , as external standard.⁸¹

HRMS DART and ESI mass spectra were recorded by means of respectively a DART-100 ion source from IonSense Inc. (Saugus, MA, USA) or an orthogonal electron spray ionization ion source (ESI) interfaced to a JMS-T100LC AccuTOF mass spectrometer from JEOL USA, Inc. (Peabody, MA, USA). The ions were transported into the orthogonal accelerating time-of-flight (TOF) single-stage reflectron mass analyzer by a high-frequency and high-voltage quadrupole ion guide. Detection was achieved with a dual microchannel plate detector. Elemental analyses were performed using an Elementar Vario EL III analyzer.

Suitable crystals for diffraction experiments were immersed in Paratone-N (Hampton Research) in a nylon loop. Data collection was done on a Bruker AXS TXS rotating anode system with an APEXII Pt¹³⁵ CCD detector using graphite-monochromated Mo $K\alpha$ radiation ($\lambda = 0.710 \text{ \AA}$). Data collection and data processing were done using APEX2,⁸² SAINT,⁸³ and SADABS⁸⁴ version 2008/1, or TWINABS,⁸⁵ whereas structure solution and final model refinement were done using SHELXS⁸⁶ version 2013/1 or SHELXT⁸⁷ version 2014/4 and SHELXL⁸⁸ version 2014/7.

$[P(Cy)_3](-S-2,4,6-Ph-C_6H_2)ClRu(=CH-O-PrC_6H_4)$, **4**. Under an inert atmosphere Hoveyda–Grubbs first-generation catalyst (120.9

mg, 0.20 mmol) and potassium 2,4,6-triphenylbenzenethiolate (80.3 mg, 0.21 mmol) were suspended in 10 mL of THF. After being stirred at room temperature for 24 h most of the solvent was removed *in vacuo*. Dark red crystals of **4** (126 mg, 0.14 mmol, 70%) were grown after addition of *n*-pentane at low temperature ($-32\text{ }^{\circ}\text{C}$). ^1H NMR (500.13 MHz, CD_2Cl_2): δ 14.6 (d, $^3J_{\text{HP}} = 5.3\text{ Hz}$, 1H), 7.78–7.64 (m, 2H), 7.62–7.54 (m, 2H), 7.50 (t, $^3J_{\text{HH}} = 7.7\text{ Hz}$, 2H), 7.45 (d, $^3J_{\text{HH}} = 2.2\text{ Hz}$, 1H), 7.44–7.27 (m, 5H), 7.22 (d, $^3J_{\text{HH}} = 2.3\text{ Hz}$, 1H), 7.05–6.72 (m, 8H), 4.74 (sep, $^3J_{\text{HH}} = 6.3\text{ Hz}$, 1H), 2.21 (q, $^3J_{\text{HH}} = 11.9\text{ Hz}$, 3H), 2.02–1.41 (m, 21H), 1.37 (d, $^3J_{\text{HH}} = 6.3\text{ Hz}$, 3H), 1.31–1.11 (m, 9H), 1.08 (d, $^3J_{\text{HH}} = 6.3\text{ Hz}$, 3H). $^{13}\text{C}\{^1\text{H}\}$ NMR (125.76 MHz, CD_2Cl_2): δ 252.84, 252.74, 153.43, 148.51, 147.39, 144.38, 144.27, 142.20, 141.60, 141.02, 138.46, 131.18, 129.39, 129.14, 128.63, 128.07, 127.95, 127.57, 127.53, 127.28, 127.12, 126.99, 125.64, 123.79, 122.67, 114.28, 77.33, 36.17, 35.98, 30.46, 29.74, 29.28, 28.51, 28.43, 28.40, 28.32, 26.79, 22.61, 21.32. ^{31}P NMR (202.46 MHz, CD_2Cl_2): δ 58.62. Anal. Calcd (%) for $\text{C}_{32}\text{H}_{38}\text{ClO}_2\text{PrRuS}$: C 69.19, H 6.92. Found: C 69.23, H 6.94. HRMS (DART) found (calcd): m/z 900.30661 (900.30851) [$\text{C}_{32}\text{H}_{38}\text{ClO}_2\text{PrRuS} + \text{H}^+$].

[P(–6–SO₃–C₆H₄)(Cy)₂]ClRu(=CH–o–O[–]PrC₆H₄), **5**. Under an inert atmosphere 2-(dicyclohexylphosphino)benzenesulfonic acid (202.7 mg, 0.571 mmol) and silver carbonate (83.3 mg, 0.302 mmol) were suspended in 20 mL of THF. After 1 h the solution was filtered followed by the addition of Hoveyda–Grubbs first-generation catalyst (123.3 mg, 0.205 mmol), and the mixture was stirred at room temperature for 24 h. The solvent was removed under reduced pressure, and the residue was passed through a silica gel column using *n*-hexane/diethyl ether (1:3) as eluent. Following this, the solvent of the collected brown fraction was removed *in vacuo*, and the product was dissolved in a little THF. Precipitation with *n*-pentane yielded 40 mg (yield = 30%) of complex **5**. ^1H NMR (500.13 MHz, CD_2Cl_2): δ 18.35 (d, $^3J_{\text{HP}} = 6.1\text{ Hz}$, 1H), 8.05–8.03 (m, 1H), 7.80–7.58 (m, 5H), 7.26 (d, $^3J_{\text{HH}} = 8.4\text{ Hz}$, 1H), 7.20 (t, $^3J_{\text{HH}} = 7.4\text{ Hz}$, 1H), 5.42 (sep, d, $^3J_{\text{HH}} = 6.4, 2.1\text{ Hz}$, 1H), 3.12–3.05 (m, 1H), 2.77–2.69 (m, 1H), 2.37–2.28 (br, 1H), 2.04–1.59 (br, 17H), 1.88 (d, $^3J_{\text{HH}} = 6.3\text{ Hz}$, 3H), 1.71 (d, $^3J_{\text{HH}} = 6.4\text{ Hz}$, 3H), 1.52–1.09 (m, 8H). $^{13}\text{C}\{^1\text{H}\}$ NMR (125.76 MHz, CD_2Cl_2): δ 305.68, 305.57, 155.66, 155.65, 145.87, 145.80, 132.29, 132.19, 132.15, 132.09, 131.25, 131.24, 128.03, 127.99, 126.65, 126.39, 124.67, 123.51, 114.34, 78.53, 35.30, 35.07, 35.01, 34.79, 30.12, 27.69, 27.61, 27.50, 27.44, 27.41, 27.35, 27.24, 27.16, 27.10, 26.66, 26.15, 26.04, 26.02, 22.08, 21.89. ^{31}P NMR (202.46 MHz, CD_2Cl_2): δ 52.19. Anal. Calcd (%) for $\text{C}_{28}\text{H}_{38}\text{ClO}_4\text{PrRuS}$: 0.13 THF·0.13 *n*-pentane: C 53.33, H 6.23. Found: C 53.69, H 6.39. HRMS (ESI⁺) found (calcd): m/z 661.08644 (661.08581) [$\text{C}_{28}\text{H}_{38}\text{ClO}_4\text{PrRuS} + \text{Na}^+$].

[P(–6–SO₃–C₆H₄)(Cy)₂](–S–2,4,6–Ph–C₆H₂)Ru(=CH–o–O[–]PrC₆H₄), **6**. In a glovebox, complex **5** [$\text{P(–6–SO}_3\text{–C}_6\text{H}_4\text{)(Cy)}_2\text{]ClRu(=CH–o–O}^{\text{–}}\text{PrC}_6\text{H}_4\text{)}$] (64.5 mg, 0.101 mmol) and potassium 2,4,6-triphenylbenzenethiolate (41.3 mg, 0.110 mmol) were suspended in THF (5 mL), and the mixture was stirred at room temperature for 12 h. The dark green solution was filtered, and the solvent removed *in vacuo*. Dark green crystals of **6** (82 mg, 0.0839 mmol, 84%) were grown by layering a solution of the crude product in dichloromethane with *n*-pentane at low temperature ($-32\text{ }^{\circ}\text{C}$). ^1H NMR (600.17 MHz, CD_2Cl_2): δ 15.61 (d, $^3J_{\text{HP}} = 6.0\text{ Hz}$, 1H), 7.88–7.84 (m, 1H), 7.82 (br d, $^3J_{\text{HH}} = 7.0\text{ Hz}$, 1H), 7.60–7.55 (m, 2H), 7.55–7.43 (m, 7H), 7.40 (tt, $^3J_{\text{HH}} = 7.7, 1.7\text{ Hz}$, 2H), 7.35 (br t, $^3J_{\text{HH}} = 6.9\text{ Hz}$, 1H), 7.31 (tt, $^3J_{\text{HH}} = 7.3, 1.3\text{ Hz}$, 1H), 7.18 (br s, 1H), 7.10 (br t, $^3J_{\text{HH}} = 6.6\text{ Hz}$, 1H), 7.05–6.87 (m, 7H), 4.94 (sep, $^3J_{\text{HH}} = 6.6\text{ Hz}$, 1H), 2.70–2.57 (m, 2H), 2.56–2.46 (br m, 1H), 2.11–2.01 (br m, 1H), 1.96–1.71 (br m, 7H), 1.67–1.22 (m, 12H), 1.38 (d, $^3J_{\text{HH}} = 6.6\text{ Hz}$, 3H), 1.17 (d, $^3J_{\text{HH}} = 6.6\text{ Hz}$, 3H), 1.10–0.90 (m, 2H), 0.56–0.43 (m, 1H). $^{13}\text{C}\{^1\text{H}\}$ NMR (150.91 MHz, CD_2Cl_2): δ 275.44, 275.36, 152.97, 149.55, 147.25, 147.19, 147.11, 145.41, 143.77, 141.59, 141.21, 140.98, 138.70, 131.82, 131.27, 130.90, 130.86, 130.75, 129.14, 129.04, 128.61, 128.56, 128.14, 127.87, 127.59, 127.49, 127.08, 126.89, 126.55, 126.33, 125.97, 124.48, 123.08, 115.39, 79.83, 34.33, 34.16, 34.01, 33.83, 28.48, 27.70, 27.62, 27.55, 27.40, 27.35, 27.33, 27.27, 27.11, 27.07, 26.77, 26.49, 26.43, 26.20, 26.18, 21.95, 20.70. ^{31}P NMR (202.46 MHz, CD_2Cl_2): δ 48.68. Anal. Calcd (%) for $\text{C}_{52}\text{H}_{55}\text{O}_4\text{PrRuS}_2$ ·0.36 *n*-pentane·0.19 THF: C

66.88, H 6.26. Found: C 66.59, H 6.43. HRMS (ESI⁺) found (calcd): m/z 963.22366 (963.22205) [$\text{C}_{52}\text{H}_{55}\text{O}_4\text{PrRuS}_2 + \text{Na}^+$].

[P(–6–O–C₆H₄)(Bu)₂](–S–2,4,6–Me–C₆H₂)Ru(=CH–o–O[–]PrC₆H₄) (**8a**). In a glovebox [$\text{P(–6–O–C}_6\text{H}_4\text{)(t-Bu)}_2\text{]ClRu(=CH–o–O}^{\text{–}}\text{PrC}_6\text{H}_4\text{)}$] (103.2 mg, 0.198 mmol) and potassium 2,4,6-trimethylbenzenethiolate (43.1 mg, 0.226 mmol) were suspended in THF (8 mL), and the mixture was stirred at room temperature for 12 h. The solvent was removed *in vacuo*. The residual was dissolved in *n*-pentane and filtered over Celite. After the solvent was removed *in vacuo* a red powder of **8a** was obtained (116 mg, 0.182 mmol, 92%). ^1H NMR (500.13 MHz, CD_2Cl_2): δ 14.83 (d, $^3J_{\text{HP}} = 5.2\text{ Hz}$, 1H), 7.46–7.37 (m, 2H), 7.36–7.31 (m, 1H), 7.05 (ddt, $^3J_{\text{HH}} = 8.4, 7.0, 1.4\text{ Hz}$, 1H), 6.98 (dt, $^3J_{\text{HH}} = 7.4, 1.0\text{ Hz}$, 1H), 6.89–6.00 (br, 5H), 6.65–6.55 (m, 3H), 4.50 (sep, d, $^3J_{\text{HH}} = 6.2, 1.4\text{ Hz}$, 1H), 2.96–2.05 (br, 6H), 2.16 (s, 3H), 1.75 (d, $^3J_{\text{HH}} = 13.8\text{ Hz}$, 9H), 1.56 (d, $^3J_{\text{HH}} = 13.4, 9\text{H}$), 1.42 (s, 1H), 1.30 (m, 8H). $^{13}\text{C}\{^1\text{H}\}$ NMR (125.76 MHz, CD_2Cl_2): δ 245.87, 245.78, 177.55, 177.45, 152.34, 152.33, 144.51, 139.06, 134.38, 132.72, 131.92, 131.91, 127.98, 126.74, 123.34, 122.71, 121.22, 120.91, 118.44, 118.36, 116.07, 116.02, 114.74, 76.43, 40.23, 40.06, 35.10, 34.93, 32.13, 32.11, 30.52, 28.56, 26.74, 21.13, 21.02, 20.99. ^{31}P NMR (202.46 MHz, CD_2Cl_2): δ 93.07. Anal. Calcd (%) for $\text{C}_{33}\text{H}_{45}\text{O}_2\text{PrRuS}$ ·0.25 *n*-pentane: C 62.72, H 7.38. Found: C 63.14, H 7.09. HRMS (ESI⁺) found (calcd): m/z 639.20112 (639.19996) [$\text{C}_{33}\text{H}_{45}\text{O}_2\text{PrRuS} + \text{H}^+$].

[P(–6–O–C₆H₄)(Bu)₂](–S–2,4,6–Ph–C₆H₂)Ru(=CH–o–O[–]PrC₆H₄) (**8b**). In a glovebox [$\text{P(–6–O–C}_6\text{H}_4\text{)(t-Bu)}_2\text{]ClRu(=CH–o–O}^{\text{–}}\text{PrC}_6\text{H}_4\text{)}$] (108.8 mg, 0.208 mmol) and potassium 2,4,6-triphenylbenzenethiolate (82.3 mg, 0.219 mmol) were suspended in THF (6 mL), and the mixture was stirred at room temperature for 12 h. The solution was filtered, and the solvent removed *in vacuo*. The residual was dissolved in *n*-pentane and filtered. After the solvent was removed *in vacuo* the remaining crude product was dissolved in a minimum amount of dichloromethane. Dark red crystals of **8b** (63 mg, 0.076 mmol, 37%) were grown upon layering the solution with *n*-pentane at low temperature ($-32\text{ }^{\circ}\text{C}$). ^1H NMR (500.13 MHz, CD_2Cl_2): δ 13.97 (d, $^3J_{\text{HP}} = 5.4, 1\text{H}$), 7.82–7.76 (m, 2H), 7.62–7.57 (m, 2H), 7.50 (d, $^3J_{\text{HH}} = 2.2\text{ Hz}$, 1H), 7.47–7.37 (m, 4H), 7.37–7.27 (m, 3H), 7.25–7.16 (m, 2H), 7.09–7.04 (m, 2H), 7.01 (tt, $^3J_{\text{HH}} = 7.4, 1.2\text{ Hz}$, 1H), 6.94–6.87 (m, 2H), 6.87–6.75 (m, 4H), 6.47–6.41 (m, 1H), 6.41–6.34 (m, 1H), 4.71 (sep, d, $^3J_{\text{HH}} = 6.2, 0.7\text{ Hz}$, 1H), 1.59 (d, $^3J_{\text{HH}} = 13.8\text{ Hz}$, 9H), 1.38 (d, $^3J_{\text{HH}} = 6.2\text{ Hz}$, 3H), 1.18 (br d, $^3J_{\text{HH}} = 12.1\text{ Hz}$, 9H), 0.98 (d, $^3J_{\text{HH}} = 6.2\text{ Hz}$, 3H). $^{13}\text{C}\{^1\text{H}\}$ NMR (125.76 MHz, CD_2Cl_2): δ 247.95, 247.84, 1.77.43, 177.33, 153.46, 153.45, 148.95, 147.47, 144.44, 143.80, 143.63, 141.60, 141.29, 138.11, 132.69, 131.63, 131.50, 129.13, 128.78, 127.83, 127.49, 127.45, 127.25, 127.15, 126.71, 126.69, 125.74, 123.25, 122.93, 121.04, 120.73, 118.17, 118.10, 115.64, 115.59, 113.27, 76.87, 40.13, 39.96, 35.09, 34.93, 31.90, 31.88, 28.15, 21.87, 20.67. ^{31}P NMR (202.46 MHz, CD_2Cl_2): δ 90.25. Anal. Calcd (%) for $\text{C}_{48}\text{H}_{51}\text{O}_2\text{PrRuS}$ ·0.2 *n*-pentane·0.6 DCM: C 66.98, H 6.19. Found: C 66.71, H 5.96. HRMS (ESI⁺) found (calcd): m/z 824.24873 (824.24814) [$\text{C}_{48}\text{H}_{51}\text{O}_2\text{PrRuS} + \text{H}^+$].

■ ASSOCIATED CONTENT

Supporting Information

The Supporting Information is available free of charge on the ACS Publications website at DOI: 10.1021/acs.organomet.6b00214.

Spectral (^1H , ^{13}C , and ^{31}P NMR) and X-ray refinement data for new compounds, calculated electronic energies and thermochemical and solvent corrections, and sample input files (PDF)

Computed molecular Cartesian coordinates in a format convenient for visualization (XYZ)

X-ray crystallographic data for **4** (CCDC-1458097) (CIF)

X-ray crystallographic data for **6** (CCDC-1458098) (CIF)

X-ray crystallographic data for **8b** (CCDC-1458099) (CIF)

AUTHOR INFORMATION

Corresponding Authors

*E-mail: Giovanni.Occhipinti@uib.no.

*E-mail: Vidar.Jensen@uib.no.

Notes

The authors declare no competing financial interest.

ACKNOWLEDGMENTS

The authors gratefully acknowledge the Research Council of Norway for financial support via the FORNY2020 (grant number 203379 and 239288) and GASSMAKS (208335) programs and for CPU and storage resources granted through the NOTUR (NN2506K) and NORSTORE (NS2506K) supercomputing programs. W.S. acknowledges the University of Bergen for a doctoral fellowship. Dr. Bjarte Holmelid is thanked for assistance with the HRMS (DART and ESI⁺) analyses.

REFERENCES

- Hog, D. T.; Huber, F. M. E.; Mayer, P.; Trauner, D. *Angew. Chem., Int. Ed.* **2014**, *53*, 8513–8517.
- Seetharamsingh, B.; Rajamohanam, P. R.; Reddy, D. S. *Org. Lett.* **2015**, *17*, 1652–1655.
- Sulake, R. S.; Chen, C. *Org. Lett.* **2015**, *17*, 1138–1141.
- Elacqua, E.; Weck, M. *Chem. - Eur. J.* **2015**, *21*, 7151–7158.
- Martinez, H.; Ren, N.; Matta, M. E.; Hillmyer, M. A. *Polym. Chem.* **2014**, *5*, 3507–3532.
- Rybak, A.; Fokou, P. A.; Meier, M. A. R. *Eur. J. Lipid Sci. Technol.* **2008**, *110*, 797–804.
- Kim, Y.-W.; Grossmann, T. N.; Verdine, G. L. *Nat. Protoc.* **2011**, *6*, 761–771.
- Walensky, L. D.; Bird, G. H. *J. Med. Chem.* **2014**, *57*, 6275–6288.
- Chhabra, S.; Belgi, A.; Bartels, P.; van Lierop, B. J.; Robinson, S. D.; Kompella, S. N.; Hung, A.; Callaghan, B. P.; Adams, D. J.; Robinson, A. J.; Norton, R. S. *J. Med. Chem.* **2014**, *57*, 9933–9944.
- Lin, Y. A.; Chalker, J. M.; Davis, B. G. *ChemBioChem* **2009**, *10*, 959–969.
- Mangold, S. L.; O'Leary, D. J.; Grubbs, R. H. *J. Am. Chem. Soc.* **2014**, *136*, 12469–12478.
- Feuillastre, S.; Piva, O. *Synlett* **2014**, *25*, 2883–2886.
- Yu, M.; Wang, C.; Kyle, A. F.; Jakubec, P.; Dixon, D. J.; Schrock, R. R.; Hoveyda, A. H. *Nature* **2011**, *479*, 88–93.
- Flook, M. M.; Jiang, A. J.; Schrock, R. R.; Müller, P.; Hoveyda, A. H. *J. Am. Chem. Soc.* **2009**, *131*, 7962–7963.
- Jiang, A. J.; Zhao, Y.; Schrock, R. R.; Hoveyda, A. H. *J. Am. Chem. Soc.* **2009**, *131*, 16630–16631.
- Marinescu, S. C.; Schrock, R. R.; Müller, P.; Takase, M. K.; Hoveyda, A. H. *Organometallics* **2011**, *30*, 1780–1782.
- Keitz, B. K.; Endo, K.; Herbert, M. B.; Grubbs, R. H. *J. Am. Chem. Soc.* **2011**, *133*, 9686–9688.
- Keitz, B. K.; Endo, K.; Patel, P. R.; Herbert, M. B.; Grubbs, R. H. *J. Am. Chem. Soc.* **2012**, *134*, 693–699.
- Endo, K.; Grubbs, R. H. *J. Am. Chem. Soc.* **2011**, *133*, 8525–8527.
- Khan, R. K. M.; Torker, S.; Hoveyda, A. H. *J. Am. Chem. Soc.* **2013**, *135*, 10258–10261.
- Khan, R. K. M.; Torker, S.; Hoveyda, A. H. *J. Am. Chem. Soc.* **2014**, *136*, 14337–14340.
- Koh, M. J.; Khan, R. K. M.; Torker, S.; Hoveyda, A. H. *Angew. Chem., Int. Ed.* **2014**, *53*, 1968–1972.
- Vyboishchikov, S. F.; Bühl, M.; Thiel, W. *Chem. - Eur. J.* **2002**, *8*, 3962–3975.
- Adlhart, C.; Chen, P. *J. Am. Chem. Soc.* **2004**, *126*, 3496–3510.
- Ashworth, I. W.; Hillier, I. H.; Nelson, D. J.; Percy, J. M.; Vincent, M. A. *ACS Catal.* **2013**, *3*, 1929–1939.
- Benitez, D.; Tkatchouk, E.; Goddard, W. A., III. *Chem. Commun.* **2008**, 6194–6196.
- Cavallo, L. *J. Am. Chem. Soc.* **2002**, *124*, 8965–8973.
- Fomine, S.; Vargas, S. M.; Tlenkopatchev, M. A. *Organometallics* **2003**, *22*, 93–99.
- Lippstreu, J. J.; Straub, B. F. *J. Am. Chem. Soc.* **2005**, *127*, 7444–7457.
- Nunez-Zarur, F.; Solans-Monfort, X.; Rodriguez-Santiago, L.; Pleixats, R.; Sodupe, M. *Chem. - Eur. J.* **2011**, *17*, 7506–7520.
- Nunez-Zarur, F.; Solans-Monfort, X.; Rodriguez-Santiago, L.; Sodupe, M. *Organometallics* **2012**, *31*, 4203–4215.
- Piacenza, M.; Hyla-Kryspin, I.; Grimme, S. *J. Comput. Chem.* **2007**, *28*, 2275–2285.
- Webster, C. E. *J. Am. Chem. Soc.* **2007**, *129*, 7490–7491.
- Romero, P. E.; Piers, W. E. *J. Am. Chem. Soc.* **2005**, *127*, 5032–5033.
- Romero, P. E.; Piers, W. E. *J. Am. Chem. Soc.* **2007**, *129*, 1698–1704.
- van der Eide, E. F.; Romero, P. E.; Piers, W. E. *J. Am. Chem. Soc.* **2008**, *130*, 4485–4491.
- Wenzel, A. G.; Grubbs, R. H. *J. Am. Chem. Soc.* **2006**, *128*, 16048–16049.
- Jensen, V. R.; Occhipinti, G.; Hansen, F. R. *Novel Olefin Metathesis Catalysts*. Patent WO2012032131, 2012.
- Nelson, J. W.; Grundy, L. M.; Dang, Y.; Wang, Z.-X.; Wang, X. *Organometallics* **2014**, *33*, 4290–4294.
- Liu, P.; Xu, X.; Dong, X.; Keitz, B. K.; Herbert, M. B.; Grubbs, R. H.; Houk, K. N. *J. Am. Chem. Soc.* **2012**, *134*, 1464–1467.
- Occhipinti, G.; Hansen, F. R.; Törnroos, K. W.; Jensen, V. R. *J. Am. Chem. Soc.* **2013**, *135*, 3331–3334.
- Occhipinti, G.; Koudriavtsev, V.; Törnroos, K. W.; Jensen, V. R. *Dalton Trans.* **2014**, *43*, 11106–11117.
- Gimeno, N.; Formentin, P.; Steink, J. H. G.; Vilar, R. *Eur. J. Org. Chem.* **2007**, *2007*, 918–924.
- Occhipinti, G.; Bjørsvik, H. R.; Jensen, V. R. *J. Am. Chem. Soc.* **2006**, *128*, 6952–6964.
- Trnka, T. M.; Grubbs, R. H. *Acc. Chem. Res.* **2001**, *34*, 18–29.
- Higman, C. S.; Plais, L.; Fogg, D. E. *ChemCatChem* **2013**, *5*, 3548–3551.
- Lee, C. W.; Grubbs, R. H. *Org. Lett.* **2000**, *2*, 2145–2147.
- Bornand, M.; Torker, S.; Chen, P. *Organometallics* **2007**, *26*, 3585–3596.
- Torker, S.; Muller, A.; Sigrist, R.; Chen, P. *Organometallics* **2010**, *29*, 2735–2751.
- Jovic, M. *Structure - Reactivity Relationships in Novel Ruthenium and Rhenium Olefin Metathesis Catalysts*. Ph.D. Thesis, ETH Zurich, Zurich, 2014.
- Heisterberg, D. J. *The Quatfit Program*; The CCL Archive, 1990.
- Minenkov, Y.; Singstad, Å.; Occhipinti, G.; Jensen, V. R. *Dalton Trans.* **2012**, *41*, 5526–5541.
- Bashir, O.; Piche, L.; Claverie, J. P. *Organometallics* **2014**, *33*, 3695–3701.
- Occhipinti, G.; Bjørsvik, H.-R.; Törnroos, K. W.; Jensen, V. R. *Organometallics* **2007**, *26*, 5803–5814.
- Thiel, V.; Hendann, M.; Wannowius, K.-J.; Plenio, H. *J. Am. Chem. Soc.* **2012**, *134*, 1104–1114.
- Rauchfuss, T. B. *Inorg. Chem.* **1977**, *16*, 2966–2968.
- Torker, S.; Mueller, A.; Chen, P. *Angew. Chem., Int. Ed.* **2010**, *49*, S3762/1–S3762/47.
- Frisch, M. J.; Trucks, G. W.; Schlegel, H. B.; Scuseria, G. E.; Robb, M. A.; Cheeseman, J. R.; Scalmani, G.; Barone, V.; Mennucci, B.; Petersson, G. A.; Nakatsuji, H.; Caricato, M.; Li, X.; Hratchian, H. P.; Izmaylov, A. F.; Bloino, J.; Zheng, G.; Sonnenberg, J. L.; Hada, M.; Ehara, M.; Toyota, K.; Fukuda, R.; Hasegawa, J.; Ishida, M.; Nakajima, T.; Honda, Y.; Kitao, O.; Nakai, H.; Vreven, T.; Montgomery, J. A., Jr.; Peralta, J. E.; Ogliaro, F.; Bearpark, M.; Heyd, J. J.; Brothers, E.; Kudin, K. N.; Staroverov, V. N.; Keith, T.; Kobayashi, R.; Normand, J.;

- Raghavachari, K.; Rendell, A.; Burant, J. C.; Iyengar, S. S.; Tomasi, J.; Cossi, M.; Rega, N.; Millam, J. M.; Klene, M.; Knox, J. E.; Cross, J. B.; Bakken, V.; Adamo, C.; Jaramillo, J.; Gomperts, R.; Stratmann, R. E.; Yazyev, O.; Austin, A. J.; Cammi, R.; Pomelli, C.; Ochterski, J. W.; Martin, R. L.; Morokuma, K.; Zakrzewski, V. G.; Voth, G. A.; Salvador, P.; Dannenberg, J. J.; Dapprich, S.; Daniels, A. D.; Farkas, Ö.; Foresman, J. B.; Ortiz, J. V.; Cioslowski, J.; Fox, D. J. *Gaussian 09*, Revision D.01; Gaussian, Inc.: Wallingford, CT, 2013.
- (59) Becke, A. D. *J. Chem. Phys.* **1997**, *107*, 8554–8560.
- (60) Chai, J. D.; Head-Gordon, M. *Phys. Chem. Chem. Phys.* **2008**, *10*, 6615–6620.
- (61) Wu, Q.; Yang, W. T. *J. Chem. Phys.* **2002**, *116*, 515–524.
- (62) *Spartan '08*; Wavefunction, Inc.: Irvine, CA, 2008.
- (63) Allen, F. H. *Acta Crystallogr., Sect. B: Struct. Sci.* **2002**, *58*, 380–388.
- (64) Halgren, T. A. *J. Comput. Chem.* **1996**, *17*, 490–519.
- (65) Peterson, K. A.; Figgen, D.; Dolg, M.; Stoll, H. *J. Chem. Phys.* **2007**, *126*, 126.
- (66) Dunning, T. H. *J. Chem. Phys.* **1989**, *90*, 1007–1023.
- (67) Woon, D. E.; Dunning, T. H. *J. Chem. Phys.* **1993**, *98*, 1358–1371.
- (68) Feller, D. *J. Comput. Chem.* **1996**, *17*, 1571–1586.
- (69) Grimme, S. *Chem. - Eur. J.* **2012**, *18*, 9955–9964.
- (70) Scott, A. P.; Radom, L. *J. Phys. Chem.* **1996**, *100*, 16502–16513.
- (71) Katzer, G.; Sax, A. F. *J. Comput. Chem.* **2005**, *26*, 1438–1451.
- (72) Zhao, Y.; Truhlar, D. G. *Phys. Chem. Chem. Phys.* **2008**, *10*, 2813–2818.
- (73) Ribeiro, R. F.; Marenich, A. V.; Cramer, C. J.; Truhlar, D. G. *J. Phys. Chem. B* **2011**, *115*, 14556–14562.
- (74) Perdew, J. P.; Burke, K.; Ernzerhof, M. *Phys. Rev. Lett.* **1996**, *77*, 3865–3868.
- (75) Perdew, J. P.; Burke, K.; Ernzerhof, M. *Phys. Rev. Lett.* **1997**, *78*, 1396–1396.
- (76) Grimme, S.; Ehrlich, S.; Goerigk, L. *J. Comput. Chem.* **2011**, *32*, 1456–1465.
- (77) Minenkov, Y.; Occhipinti, G.; Jensen, V. R. *Organometallics* **2013**, *32*, 2099–2111.
- (78) Kendall, R. A.; Dunning, T. H.; Harrison, R. J. *J. Chem. Phys.* **1992**, *96*, 6796–6806.
- (79) Marenich, A. V.; Cramer, C. J.; Truhlar, D. G. *J. Phys. Chem. B* **2009**, *113*, 6378–6396.
- (80) Fulmer, G. R.; Miller, A. J. M.; Sherden, N. H.; Gottlieb, H. E.; Nudelman, A.; Stoltz, B. M.; Bercaw, J. E.; Goldberg, K. I. *Organometallics* **2010**, *29*, 2176–2179.
- (81) Kühn, O. *Phosphorus-31 NMR Spectroscopy*. Springer-Verlag: Heidelberg, 2008.
- (82) APEX2, Version 2014.11-0; Bruker-AXS: Madison, WI, USA, 2014.
- (83) SAINT, Version 7.68A; Bruker-AXS: Madison, WI, USA, 2010.
- (84) Krause, L.; Herbst-Irmer, R.; Sheldrick, G. M.; Stalke, D. *J. Appl. Crystallogr.* **2015**, *48*, 3–10.
- (85) Sheldrick, G. M. *TWINABS*, Version 2012/1; Georg-August-Universität Göttingen: Göttingen, Germany, 2012.
- (86) Sheldrick, G. M. *XS*, Version 2013/1; Georg-August-Universität Göttingen: Göttingen, Germany, 2013.
- (87) Sheldrick, G. *Acta Crystallogr., Sect. A: Found. Adv.* **2015**, *71*, 3–8.
- (88) Sheldrick, G. *Acta Crystallogr., Sect. C: Struct. Chem.* **2015**, *71*, 3–8.

Paper II

Loss and Reformation of Ruthenium Alkylidene: Connecting Olefin Metathesis, Catalyst Deactivation, Regeneration, and Isomerization

Julien Engel, Wietse Smit, Marco Foscatto, Giovanni Occhipinti, Karl W. Törnroos, and Vidar R. Jensen

J. Am. Chem. Soc. **2017**, 139, 16609–16619

*Reprints were made with permission from the American Chemical Society.
Further permissions related to the material excerpted should be directed to the ACS.*

<https://pubs.acs.org/doi/10.1021/jacs.7b07694>

Loss and Reformation of Ruthenium Alkylidene: Connecting Olefin Metathesis, Catalyst Deactivation, Regeneration, and Isomerization

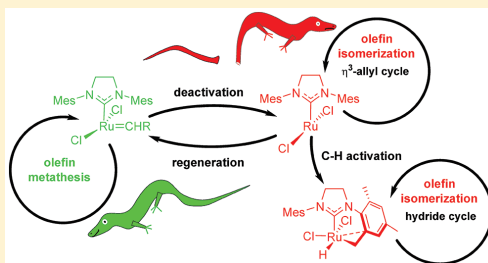
Julien Engel,^{†,§,||} Wietse Smit,^{‡,||} Marco Foscato,^{‡,||} Giovanni Occhipinti,^{*,‡,||} Karl W. Törnroos,^{‡,||} and Vidar R. Jensen^{*,‡,||}

[†]Institute of Organic Chemistry, RWTH Aachen University, Landoltweg 1, D-52074 Aachen, Germany

[‡]Department of Chemistry, University of Bergen, Allégaten 41, N-5007 Bergen, Norway

Supporting Information

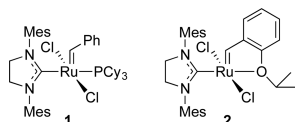
ABSTRACT: Ruthenium-based olefin metathesis catalysts are used in laboratory-scale organic synthesis across chemistry, largely thanks to their ease of handling and functional group tolerance. In spite of this robustness, these catalysts readily decompose, via little-understood pathways, to species that promote double-bond migration (isomerization) in both the 1-alkene reagents and the internal-alkene products. We have studied, using density functional theory (DFT), the reactivity of the Hoveyda–Grubbs second-generation catalyst **2** with allylbenzene, and discovered a facile new decomposition pathway. In this pathway, the alkylidene ligand is lost, via ring expansion of the metallacyclobutane intermediate, leading to the spin-triplet 12-electron complex (SIMes)RuCl₂ (³R21, SIMes = 1,3-bis(2,4,6-trimethylphenyl)-4,5-dihydroimidazol-2-ylidene). DFT calculations predict ³R21 to be a very active alkene isomerization initiator, either operating as a catalyst itself, via a η^3 -allyl mechanism, or, after spin inversion to give R21 and formation of a cyclometalated Ru-hydride complex, via a hydride mechanism. The calculations also suggest that the alkylidene-free ruthenium complexes may regenerate alkylidene via dinuclear ruthenium activation of alkene. The predicted capacity to initiate isomerization is confirmed in catalytic tests using *p*-cymene-stabilized R21 (**5**), which promotes isomerization in particular under conditions favoring dissociation of *p*-cymene and disfavoring formation of aggregates of **5**. The same qualitative trends in the relative metathesis and isomerization selectivities are observed in identical tests of **2**, indicating that **5** and **2** share the same catalytic cycles for both metathesis and isomerization, consistent with the calculated reaction network covering metathesis, alkylidene loss, isomerization, and alkylidene regeneration.



INTRODUCTION

Olefin metathesis is the most versatile tool known for the formation of carbon–carbon double bonds.¹ In particular, the ruthenium-based catalysts, such as the Grubbs second generation catalyst **1** (Chart 1)² and its phosphine-free congener known as the Hoveyda–Grubbs second generation catalyst **2**,³ have become widely used in organic synthesis¹ and are to an increasing extent being adopted in industrial

Chart 1. Grubbs Second Generation 1 and Hoveyda–Grubbs Second Generation 2 Catalysts



Mes = 2,4,6-trimethylphenyl
Cy = cyclohexyl

valorization of renewable feedstocks and production of natural products and pharmaceuticals.^{4,5}

These developments are striking in view of the low productivities of the ruthenium catalysts. Even if exceptional turnover numbers (TONs, several hundred thousand) have been reported with some highly reactive substrates and under solvent free conditions,⁶ ruthenium metathesis catalysts typically deactivate after only a few thousand turnovers,^{5,7} as compared to TONs typically in the range of 1–10 million for industrial processes.⁸ Even after 20 years of effort in academia and industry, these catalysts are possibly the least productive of any class of commercial, industrially used catalysts. The high catalyst loadings consequently required are the most important factor limiting further industrial uptake. Loadings of several mole percent are common in natural products synthesis⁹ and can approach stoichiometric amounts for peptide modification reactions such as stapling.¹⁰ High catalyst loadings are costly, unsustainable given the scarcity of ruthenium, and a critical

Received: July 23, 2017

Published: October 20, 2017

concern in pharma, where metal residues in drugs are strictly limited.

In addition to the need for high catalyst loadings, catalyst decomposition leads to species that promote olefin isomerization in the form of double-bond migration. In some cases, isomerization may compete with, or even dominate over, metathesis and thus seriously compromise both selectivity and yield.^{11,12} Even if metathesis-related isomerization may sometimes be exploited for synthetic purposes,¹³ this side reaction is a symptom of catalyst decomposition and is usually an unwanted companion to metathesis.

Unfortunately, rational design of more stable catalysts has so far been hampered by poor insight into the mechanism of decomposition. Valuable insight could come from identification of isomerization-active species, but the nature of these decomposition products still remains elusive. Ruthenium hydrides are widely thought to be responsible, but none of the known metathesis-related hydrides^{12,14} appear to be sufficiently isomerization active,¹⁵ or to form fast enough,¹⁶ to explain the quantities of isomerization observed during metathesis.¹⁵ Instead, in a recent contribution from Fogg and co-workers, metathesis has been shown to lead to formation of ruthenium nanoparticles estimated to account for ca. 50% of the substrate isomerization.¹⁷ The identification of the involvement of nanoparticles is an important step forward. However, decomposition reactions leading to both the isomerization-active molecular species and the nanoparticles are still unknown, which makes it difficult to prevent catalyst decomposition and isomerization.

Three guidelines may help guide the search for candidate decomposition reactions: *First*, the relatively low TONs for common metathesis catalysts^{5,7} imply that decomposition typically should be 3–4 orders of magnitude slower than metathesis, which (according to transition state theory) translates into a difference in rate-determining barriers amounting to ca. 5–7 kcal/mol. *Second*, isomerization is a symptom of catalyst decomposition, and a candidate decomposition pathway should lead to highly active olefin isomerization catalysts. A good portion of the decomposition must therefore be substrate-triggered, as absence of 1-alkene substrate leads to decomposition products mediating isomerization with too low rates.¹⁸ *Third*, these catalysts should operate with a mechanism consistent with the experimental observations, in particular the information derived from the deuterium labeling study of Wagener and co-workers.¹⁸ Addition of deuterated allyl ethers to **1** led to both 1,2- and 1,3-deuterium shifts. Whereas 1,2-shifts are inconsistent with a mechanism involving an allyl-hydride generated by oxidative addition of the substrate, both shifts are possible with a mechanism involving a preformed ruthenium hydride. Indications as to the nature of the ruthenium hydrides involved were obtained by using an analogue of **1** bearing deuterated *o*-methyl groups on the aromatic rings of the NHC ligand (**3**, Chart S1). Deuterium from **3** was observed in the isomerization products, suggesting that an unknown, active Ru-D species is formed via C–D activation of the CD₃ groups.¹⁸ Activation of N-heterocyclic carbene (NHC) aryl C–H bonds of ruthenium olefin metathesis catalysts is indeed a well-known catalyst deactivation reaction,^{19,20} but so far, no such C–H activation products, hydride or other, with appreciable isomerization activity have been identified.

Identifying such isomerization-active decomposition products and establishing a decomposition–isomerization reaction

sequence consistent with the above three guidelines was the goal of this work. In particular, when looking for substrate-triggered decomposition reactions (following *Guideline 2*), we hypothesized that 1-alkenes might induce a 1,2-hydride shift that leads to catalyst decomposition. In fact, a 1,2-hydride shift is part of the only known and well-understood substrate-triggered decomposition mechanism. The latter mechanism involves breakdown of the unsubstituted metallacyclobutane generated by cycloaddition of ethylene to ruthenium methylidene, and proceeds via an allyl hydride to liberate propene.^{21–24}

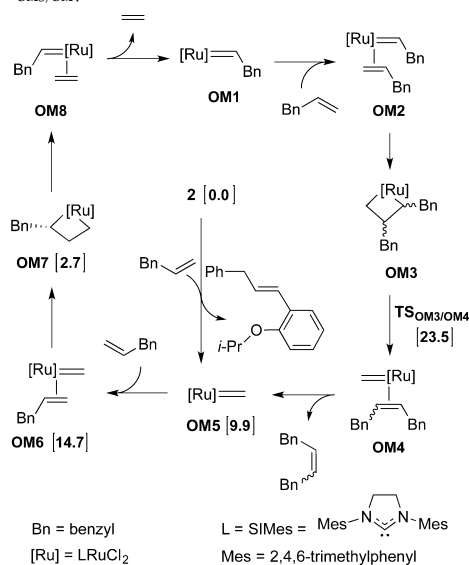
Indeed, using allylbenzene as a model 1-alkene substrate in density functional theory (DFT) explorations of decomposition mechanisms, we discovered a surprisingly facile (consistent with *Guideline 1*), stepwise 1,2-shift leading to a breakdown of the metallacyclobutane and loss of methylidene analogous to that triggered by ethylene. The alkylidene-free ruthenium complex is predicted to be a highly efficient initiator for olefin isomerization (*Guideline 2*), including via a hydride-based mechanism (*Guideline 3*). Finally, the isomerization activity of the alkylidene-free complex was confirmed by synthesizing and testing a donor-stabilized version of this compound.

RESULTS AND DISCUSSION

In the first subsection below, we establish, using DFT, a reference free energy and a corresponding overall barrier to olefin metathesis. In subsequent subsections, we compare this barrier to those of decomposition reactions, before we move on to study substrate isomerization.

The Olefin Metathesis Reference Reaction. The reference state against which all free energies will be calculated, unless otherwise stated, is that of catalyst precursor **2**. From **2**, homocoupling of a given substrate requires three metathesis events: the first to initiate the catalyst by replacing the precursor alkylidene and another two to complete the productive coupling between two substrate molecules. The rate of isomerization seems to be independent of the initiation rate,²⁷ and only the barrier to productive metathesis is considered here in comparison with barriers of candidate decomposition reactions. Consistent with findings of computational mechanistic studies,²⁸ the transition state of cycloreversion (TS_{OM3/OM4}, Scheme 1) has been taken to be rate determining for metathesis in the present work. This means that, for our model substrate allylbenzene, an olefin known to be prone to isomerization,²⁹ the barrier to metathesis is determined by $\Delta G^\ddagger = G(\text{TS}_{\text{OM3/OM4}}) - G(\mathbf{2}) = 23.5 \text{ kcal mol}^{-1}$. This and other barriers calculated relative to **2** will, in general, not be kinetically relevant absolute barriers. However, differences between such barriers should translate into differences in rate constants.

The Allyl-Hydride Ruthenacyclobutane Decomposition. A summary of the computational checks as to whether the η^3 -allyl mechanism might compete with olefin metathesis is given in the following; see the [Supporting Information](#) for details. We first recalculated, using the current computational model, the ethylene-triggered, η^3 -allyl route to loss of methylidene, proposed by van Rensburg and co-workers,^{22,24} (Scheme S2), and found the key transition state for β -hydride transfer in the unsubstituted ruthenacyclobutane to form the more stable allyl-hydride to be of only 1.3 kcal mol⁻¹ higher free energy than that of self-metathesis of allylbenzene (Scheme 1). This confirms the detrimental effects of ethylene.^{22,24}

Scheme 1. Mechanism of Metathesis Homocoupling of Allylbenzene and the Rate-Determining Transition State, TS_{OM3/OM4}^a


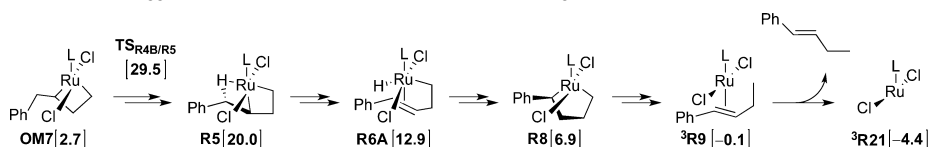
^aGibbs free energy, in kcal/mol, relative to precursor 2. After initiation (to reach OM5), alkene binding and dissociation reactions are assumed to occur with low or no barrier on the potential energy surface (PES),²⁵ and are unlikely to influence the kinetics significantly.²⁶

However, not even careful removal of ethylene during metathesis and low catalyst loading to minimize decomposition via dinuclear ruthenium complexes^{14,30,31} are enough to stop catalyst decomposition.³² When searching for alternative culprits, the fact that decomposition products generated in the absence of an olefinic substrate are not isomerization-active enough¹⁸ should be guiding. This is corroborated by our failed attempts at finding facile pathways, without involvement of a substrate, to ruthenium hydrides via activation of C–H bonds of NHC mesityl methyl groups in both catalyst precursor 2 and the corresponding methylidene analogue; see the [Supporting Information](#).

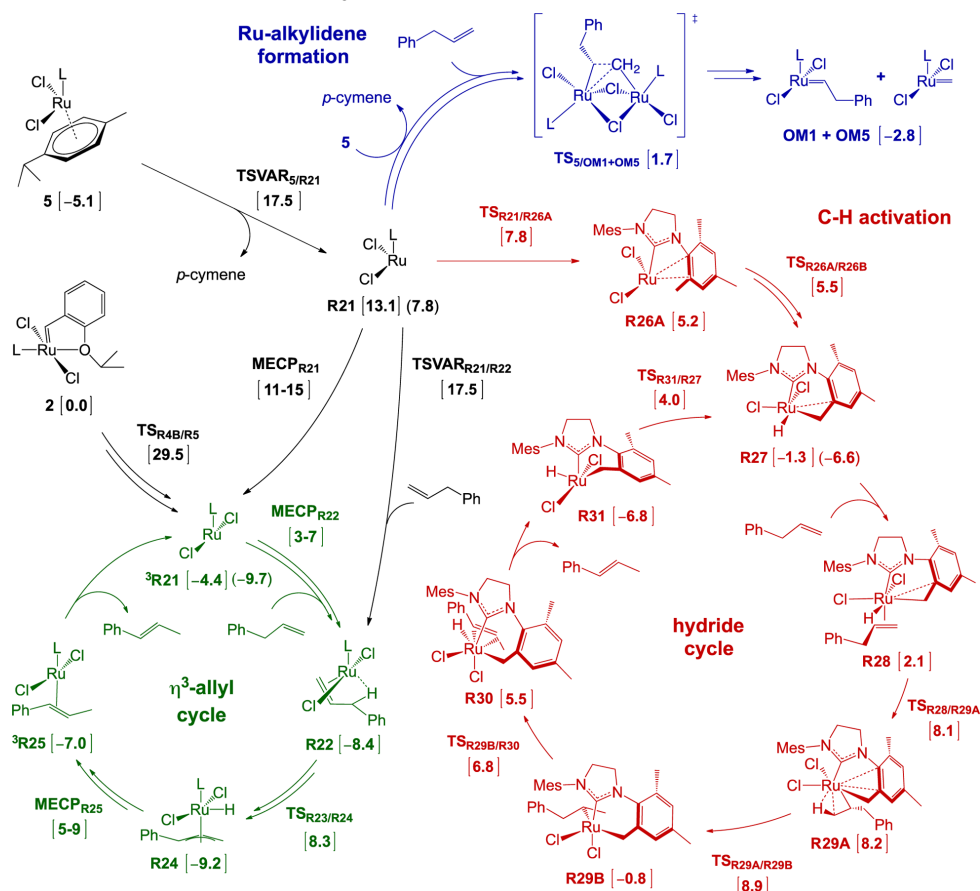
Instead, the above-described facile ethylene-triggered η^3 -allyl-hydride decomposition mechanism led us to hypothesize that 1-alkenes may trigger a similar loss of methylidene. To follow the hypothesis, we used allylbenzene as the substrate in the van Rensburg mechanism (Scheme S2) and found the overall barrier to decomposition, via TS_{OM7/VR3A'}, to be 9.0 kcal mol⁻¹ higher than the barrier to self-metathesis. This difference in barriers is not far from the range (5–7 kcal mol⁻¹; see the [Introduction](#)) required for candidate decomposition routes, suggesting that this is a catalyst decomposition pathway worth pursuing. The higher barrier to allylbenzene-triggered decomposition is reflected in a relatively late transition state for β -hydride transfer (Ru–H _{β} = 1.63 Å compared to Ru–H _{β} = 1.79 Å for ethylene). To reach the allylbenzene-triggered transition state, a stronger Ru–H _{β} bond must be formed to compensate for the weaker Ru–C _{α} interactions (Ru–C _{α} = 2.20 Å compared to Ru–C _{α} = 2.13 Å for ethylene) formed by the primary carbon atom compared to the more symmetric and η^3 -allyl-like transition state of the ethylene-triggered reaction. The question is whether 1-alkenes still can trigger methylidene loss by following a different route for the 1,2-shift.

Alternative 1-Alkene-Triggered Route to Methylidene Loss. To build on the above-mentioned, established ethylene-triggered decomposition of the unsubstituted ruthenacyclobutane, the exploration of new pathways for 1-alkene-triggered decomposition will assume substrate binding and cycloaddition to the 14-electron ruthenium methylidene OM5 (Scheme 1). This intermediate is not produced in metathesis of internal alkenes, for which catalyst decomposition is much less pronounced than for 1-alkenes,³³ and it is generally assumed that methylidene intermediate OM5 is implicated in catalyst decomposition, while the catalyst precursor plays, if any, a very minor role.^{14,18,30}

As shown in the complete 1-alkene-triggered decomposition pathway of Scheme S5 (see Scheme 2 for a summary), coordination of the substrate allylbenzene to OM5 gives the π -complex OM6 (14.7 kcal mol⁻¹), from which cycloaddition leads to the metallacyclobutane OM7 (2.7 kcal mol⁻¹). Looking for alternatives to a direct 1,2-hydride shift in OM7, we noted that ethylene trimerization and tetramerization catalysts achieve excellent selectivity by expanding metallacycles (via insertion of ethylene) until the rings reach sufficient flexibility so as to undergo the 1-alkene-releasing β -hydride transfer.³⁴ We thus wondered whether expansion of the four-membered ring of OM7 (Scheme 2) might facilitate the hydride shifts leading to loss of methylidene. Indeed, from the trigonal bipyramidal metallacyclopentane R8, which is less stable, by 4.2 kcal mol⁻¹,

Scheme 2. 1-Alkene-Triggered Metathesis Catalyst Decomposition Starting from Metallacyclobutane OM7^a


^aGibbs free energies (geometry optimization, ω B97XD/cc-pVDZ; single-point energies, PBE-D3BJ/cc-pVQZ; see the [Supporting Information](#) for details), in kcal mol⁻¹ relative to Hoveyda–Grubbs second-generation catalyst 2 (L = SIMes, see Scheme 1), are given in square brackets. See Scheme 1 for the metathesis steps leading to the metallacyclobutane intermediate OM7 from 2, and see Scheme S5 for additional intermediates and transition states. The Gibbs free energy of minimum energy crossing points (MECPs) has been estimated as described in ref 35. After catalyst initiation, the alkene binding and dissociation reactions are assumed to involve low or no barrier on the PES,²⁵ and are unlikely to influence the kinetics significantly.²⁶

Scheme 3. Isomerization and Alkylidene Regeneration Initiated by $^3R_{21}$ and R_{21}^{4a} 

^{4a}Gibbs free energies (geometry optimization, ω B97XD/cc-pVDZ; single-point energies, PBE-D3BJ/cc-pVQZ; see the Supporting Information for details), in kcal mol⁻¹ relative to precursor 2 and allylbenzene, are given in square brackets (L = SIMes, see Scheme 1). Each allylbenzene isomerization cycle is exergonic by 5.3 kcal mol⁻¹. The exergonicity is indicated by the relative free energies, given in parentheses, for the species to which allylbenzene is coordinated to initiate a new isomerization turnover. These energies thus reflect that one isomerization cycle has been completed. See Scheme S6 for additional intermediates, transition states, and disfavored reaction pathways. The Gibbs free energy of minimum energy crossing points (MECPs) has been estimated as described in ref 35. The Gibbs free energy of variational transition states (TSVAR) of diffusion-limited bimolecular reactions lacking transition states on the PES has been estimated as described in ref 26.

than OM7, a 1,3-shift to the former methyldiene moiety, along with scission of the ruthenium–carbon bonds, leads to a π -complex, R9 (13.0 kcal mol⁻¹), with an agostic bond between the terminal methyl group of β -ethylstyrene (ES) and ruthenium. The reductive elimination via TS_{R8/R9} (24.5 kcal mol⁻¹, Scheme S5) is only 1.0 kcal/mol more costly (relative to 2) than productive self-metathesis (Scheme 1).

The question is thus whether the starting point of this facile reductive elimination, the metallacyclopentane R8, can be reached from the metallacyclobutane OM7. A direct 1,2-hydrogen shift, via TS_{OM7/R8}, has a prohibitively high barrier (39.6 kcal mol⁻¹) relative to 2 (Scheme S5). Remarkably, however, the barrier can be reduced to below 30 kcal mol⁻¹ by performing the 1,2-shift in a stepwise manner. The rate-

determining of these steps is the formation of the agostic R5 via TS_{R4B/R5} (29.5 kcal mol⁻¹, optimized geometry in Figure S18). In comparison, the subsequent formation of hydride complexes R6A and R6B and completion of the 1,2-shift to reach R8 involve relatively facile steps. In other words, ring expansion of the metallacyclobutane intermediate OM7 gives the metallacyclopentane R8 with an overall barrier, via TS_{R4B/R5} (29.5 kcal mol⁻¹), only 6.0 kcal mol⁻¹ higher than that of the rate-determining step of metathesis homocoupling of allylbenzene (Scheme 1).

The subsequent rupture of the five-membered ring of R8 to form R9 (Scheme S5) is comparably fast, which means that allylbenzene-induced methyldiene loss from OM5 may occur with an overall barrier in agreement with Guideline 1 (5–7 kcal

mol^{-1}) of the Introduction. Alternative pathways exist (see the Supporting Information), but none can compete with that of ring expansion to **R8** and rupture to give **R9**, which is favored by 3 kcal mol^{-1} compared to the barrier defined by $\text{TS}_{\text{OM7/VR3A}}$ of the van Rensburg mechanism (Scheme S2). This energy difference is small but confirmed using two different density functionals (PBE-D3BJ and M06; see Table S8).

Finally, liberation of β -ethylstyrene from **R9** is thermodynamically favored and proceeds via a facile change of spin state³⁵ to the spin-triplet ³**R9**, which is 13.1 kcal mol^{-1} more stable than the singlet, followed by the alkene dissociation, which can be assumed to occur without a barrier on the potential energy surface (PES).^{25,26} The resulting ruthenium species is the three-coordinate, 12-electron dichloride ³**R21** that would also result from dissociation of the alkene ligand from the final complex of the van Rensburg mechanism (**VR4** and **VR4A** in Scheme S2). In other words, three distinct and relatively facile routes lead to the 12-electron intermediate. Two of these routes proceed via **OM7**, which is a key intermediate of metathesis homocoupling. The most favored of the latter two pathways requires only 6.0 kcal mol^{-1} more activation (via $\text{TS}_{\text{R4B/R5}}$ at 29.5 kcal mol^{-1} relative to **2**) than metathesis.

This implies (from transition state theory) that decomposition to form ³**R21** is 3 orders of magnitude slower than metathesis, and that one catalyst molecule is lost for every 1000 metathesis turnovers or so, suggesting that our calculated route to ³**R21** could be a significant cause of metathesis catalyst decomposition. In fact, pyridine adducts (with three coordinated pyridine molecules, presumably a spin-singlet complex) of this 12-electron compound have been isolated as metathesis catalyst decomposition products.²⁰

In comparison, ³**R21** itself is only a short-lived intermediate. Still, it is, in fact, more stable than the 14-electron methylidene **OM5**, as judged from the lower calculated free energy of ³**R21**. The latter, even if being a 12-electron complex, increases its stability by occupying the same number (seven) of molecular orbitals as **OM5**.

The Allylic Isomerization Cycle. Allylbenzene binding to ³**R21** leads, via ³**R22** (3.9 kcal mol^{-1} , Scheme S6) and facile spin crossover,³⁵ to the singlet **R22**, at -8.4 kcal mol^{-1} . From **R22**, hydride transfer to ruthenium to reach the η^3 -allyl complex **R23** is facile. The subsequent rotation of the substrate via $\text{TS}_{\text{R23/R24}}$ is, consistent with earlier studies,³⁶ associated with a comparably high free energy (8.3 kcal mol^{-1}) and results in the relatively stable η^3 -allyl hydride **R24**.

From **R24**, a facile second hydride transfer generates the isomerized β -methylstyrene coordinated to ruthenium, **R25**. A second spin crossover brings the system back to the spin-triplet PES but at an overall cost ($5-9$ kcal mol^{-1})³⁵ likely to contribute to determining the efficiency of the allylic isomerization cycle. Finally, ³**R25** liberates the β -methylstyrene isomerization product and regenerates ³**R21**, at -9.7 kcal mol^{-1} and thus 5.3 kcal mol^{-1} lower than at the start of the cycle, reflecting the reaction exergonicity (see Scheme 3).

A similar η^3 -allyl hydride isomerization mechanism, albeit without consideration of spin crossover, was originally suggested as a catalyst decomposition pathway²² but has also been explored computationally in isomerization of propene.^{24,36}

The efficiency of the allylic mechanism is largely determined by the two relatively stable intermediates with π -coordinated olefin (**R22**) or allyl (**R24**). The effective barriers to allyl formation from **R22** (**R22** \rightarrow $\text{TS}_{\text{R23/R24}}$) and to spin inversion

in the product internal olefin complex from **R24** (**R24** \rightarrow MECP_{R25}) are in the same range ($16-17$ kcal mol^{-1}), and both can be expected to contribute to determining the rate of isomerization for most relevant substrate concentrations; see the energetic span models³⁷ of the Supporting Information. Assuming no competing reactions or deactivation from the allylic cycle and a spin-change barrier for MECP_{R25} in the middle of the range ($5-9$ kcal mol^{-1}), the turnover frequency (TOF) is estimated to be in the range $1-1.5$ s^{-1} and to fall below 1 s^{-1} only for very low substrate concentrations (<1 mM), for which the olefin-free ³**R21** takes over from **R22** as a rate-relevant intermediate.

C-H Activation and Hydride-Mechanism Isomerization. In addition to mediating the above η^3 -allyl-type isomerization, the 12-electron spin-triplet ³**R21** may initiate intramolecular C-H activation and hydride-mechanism isomerization. However, this requires spin pairing, which costs $11-15$ kcal mol^{-1} relative to **2**. The resulting spin-singlet **R21** is electron deficient, very reactive, and may insert into a NHC σ -methyl C-H bond to form the ruthenium hydride **R27** without activation barriers.³⁸ Coordination of allylbenzene to **R27** is slightly endergonic and results in π -complex **R28** (2.1 kcal mol^{-1}), from which the substrate inserts into the ruthenium hydride bond. The hydride formed initially (**R29A**) rearranges to the more stable **R29B**, from which a β -hydrogen may be eliminated with a barrier (via $\text{TS}_{\text{R29B/R30}}$) 7.6 kcal mol^{-1} above **R29B**. From the resulting π -complex hydride **R30**, the subsequent β -methylstyrene dissociation is exergonic by more than 12 kcal mol^{-1} , and the alkene-free hydride (**R31**) may isomerize to **R27**, from which another isomerization cycle may begin.

In neat allylbenzene, the rearrangement **R31** \rightarrow $\text{TS}_{\text{R31/R27}}$ (10.8 kcal mol^{-1} under standard-state conditions; see the Supporting Information) is to a large extent rate-determining, while the corresponding energy span **R31** \rightarrow $\text{TS}_{\text{R29A/R29B}}$ (10.4 kcal mol^{-1}) is the most important for lower substrate concentrations. The latter barrier envelopes allylbenzene coordination, and the rate is therefore predicted to be dependent on the substrate concentration but with a TOF significantly higher (e.g., 1300 s^{-1} at a allylbenzene concentration of 0.02 M; see the Supporting Information) than that of the above allylic cycle for all relevant concentrations.

Regeneration of Ruthenium Alkylidene. Arene-stabilized **R21** and analogues thereof are known as olefin metathesis catalysts,^{39,40} and should therefore be expected to form ruthenium alkylidene *in situ*. Using DFT, Buchmeiser and co-workers investigated alkylidene formation from *p*-cymene-stabilized **R21** and functionalized norbornene substrates.⁴⁰ Their results indicate that the energy differences between the most stable ruthenium-norbornene π -complexes and the transition state for the alkylidene-forming hydrogen shift between the two carbon atoms of the alkene bond are very high (>40 kcal mol^{-1}). Instead, inspired by the relatively stable olefin and η^3 -allyl complexes of the allylic mechanism, we have studied two other substrate-induced routes to alkylidene, the details of which are given in the Supporting Information.

The first of these pathways is essentially the reverse of the alkylidene-loss reaction of van Rensburg (Scheme S2) and starts from allyl hydride **R23**. The second starts by oxidative addition of two substrate molecules followed by ring contraction. Both involve rate-determining transition states with a free energy $26-27$ kcal mol^{-1} above that of **R22**, the

most stable prebarrier intermediate. These barriers are much higher than that of isomerization itself, and the two alkylidene-formation pathways starting from the η^3 -allyl cycle cannot be expected to be very efficient.

In the search for a more favorable pathway, we noted that bimolecular coupling of metathesis catalyst molecules leading to loss of alkylidene is a known decomposition reaction.^{23,41} Although no molecular-level calculations have been reported for this reaction and few mechanistic details are known, the key transition state of bond-breaking and formation should be that of coupling of two alkylidenes to form an alkene molecule. The reverse reaction, here termed alkylidene formation via dinuclear ruthenium alkene activation, should proceed via the same transition state. This transition state ($TS_{S/OMI+OMS}$, Scheme 3) is of remarkably low energy (1.7 kcal mol⁻¹ relative to **2**). Thus, the facile interconversion between alkylidene and alkene implied by the energy of $TS_{S/OMI+OMS}$ strongly suggests that the metathesis activity observed for arene-stabilized **R21** and analogues thereof^{39,40} is due to dinuclear ruthenium alkene activation. The detailed reaction mechanism leading to this transition state via coupling of ruthenium complexes and binding of alkene is the subject of a future study. However, the much higher barrier (at 17.5 kcal mol⁻¹, via $TS_{VAR_S/R21}$) for dissociation of *p*-cymene from **5** compared to that of the alkene scission to give alkylidene ($TS_{S/OMI+OMS}$) makes *p*-cymene dissociation stand out as the most likely rate-determining step of the alkylidene formation from **5**.

Predicted Overall Reactivity of the 12-Electron Compound and Its 18-Electron Adducts. DFT calculations predict ³**R21** to be a key catalyst decomposition intermediate that reacts readily with alkene substrates. In particular, according to the calculations, this intermediate can initiate efficient double-bond migration via two different mechanisms. To validate the predicted isomerization activity, one should ideally test the catalytic properties of ³**R21** itself, but preparing and testing a 12-electron Ru(II) compound is very challenging. Thus, as will be detailed below, the synthetic target for experimental follow-up is complex **5**, which is stabilized by a *p*-cymene molecule (Scheme 3). Dissociation of *p*-cymene generates the 12-electron compound. However, unlike the 12-electron compound, which has a spin-triplet ground state, the 18-electron *p*-cymene adduct has a spin-singlet ground state, with the triplet being more than 15 kcal mol⁻¹ less stable and requiring a costly spin inversion if it is to be generated from **5**. Thus, instead of reaching the 12-electron compound via the triplet ³**5**, *p*-cymene is predicted to dissociate from **5** to give the bent (Cl–Ru–Cl = 124.7°), spin-singlet **R21**. At high concentrations of *p*-cymene, little **R21** will be liberated. In fact, a similar effect should be expected for other arenes, such as benzene and toluene. The latter has a calculated binding free energy (16.3 kcal mol⁻¹) to **R21** only 2 kcal mol⁻¹ lower than that of *p*-cymene. In other words, the observed isomerization activity of **5** as well as **2** and other metathesis catalysts should be higher in solvents that do not contain η^6 -coordinating arenes or other groups able to saturate **R21**.

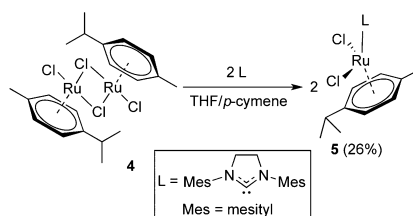
From the high-energy **R21**, at least three different routes require little or no activation: (i) the complex may undergo spin inversion to reach ³**R21**, (ii) it may form a relatively stable spin-singlet olefin adduct **R22** and thus enter the allylic isomerization cycle, and (iii) the electron-deficient ruthenium atom may insert into a methyl C–H bond of the mesityl and thus enter the hydride isomerization cycle. As the C–H activation step depends on the unsaturated ruthenium center,

entrance into the hydride cycle (iii) will be disfavored by high concentration of the alkene substrate. In neat substrate, substrate binding to reach **R22** will not be limited by diffusion²⁶ and will be barrierless. The resulting **R22** and other complexes of the allylic cycle are thermodynamically more stable than the hydride-cycle counterparts, which will limit the population of the latter. However, even under conditions favoring species of the allylic cycle, the hydride cycle will contribute to isomerization, as it is much more efficient. In general, both cycles will thus be responsible for the observed isomerization, and it may be difficult to establish their relative importance.

In addition to the above three facile pathways (i–iii) starting from **R21**, alkylidene formation via dinuclear ruthenium alkene activation also appears to be possible and involves dissociation of *p*-cymene from **5** and coupling of two different ruthenium complexes and a substrate, although the mechanistic details will have to be left for a future study.

Synthesis of the Predicted Isomerization Catalyst Precursor. 18-Electron adducts such as the *p*-cymene-stabilized complex **5** (Scheme 4) are known.^{30,35,40,42,43} In

Scheme 4. Synthesis of Compound **5**



fact, **5** and analogues based on unsaturated NHC ligands (e.g., IMes = 1,3-bis(2,4,6-trimethylphenyl)imidazol-2-ylidene and IDipp = 1,3-bis(2,6-diisopropylphenyl)imidazol-2-ylidene) have been studied as olefin metathesis catalysts.^{39,40} Thus, complex **5** is a realistic synthetic target and will generate the isomerization-active 12-electron compound on dissociation of the *p*-cymene ligand. Still, **5** itself has so far only been synthesized *in situ*.⁴⁴ For example, whereas (IMes)(η^6 -*p*-cymene)RuCl₂ was easily prepared by reacting (*p*-cymene)RuCl₂ dimer **4** with 2 equiv of IMes, corresponding attempts at reaching **5** mainly gave undefined hydridic decomposition products.⁴² Modifying these procedures to ensure excess *p*-cymene by performing the reaction in a mixture of THF and *p*-cymene resulted in a simple protocol for the synthesis of **5**; see Scheme 4.

After the reaction, most of the THF was removed *in vacuo*, and at low temperature (–32 °C), small red crystals suitable for synchrotron-radiation X-ray structure analysis (Figure S6) were obtained from the resulting concentrated solution. Compound **5** can be described as a distorted octahedral complex with an axial carbene ligand (SIMes), two *cis*-positioned equatorial chloride ligands, and the η^6 -bound *p*-cymene ligand occupying distorted axial and equatorial positions. The bond distances and angles are comparable to those of the IMes-coordinated analogue of **5**.⁴⁵

Complex **5 as an Isomerization Catalyst.** Initially, **5** was tested in neat allylbenzene, using elevated temperatures (80–100 °C) and low catalyst loadings (1–100 ppm) to promote

dissociation of the η^6 -bound *p*-cymene; see Scheme 5 and Table 1.

Scheme 5. Conversion of Allylbenzene into Metathesis and Isomerization Products with 2 and 5

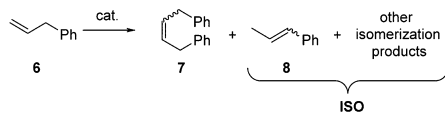


Table 1. Conversion of Neat Allylbenzene and Selectivity toward the Isomerization Products (ISO)

entry	cat.	cat. load. (ppm)	T (°C)	t (h)	conv. ^a (%)	ISO ^b (%)
1	5	1	80	1	1	100 ^c
				20	4	100 ^c
2	5	3	80	1	3	73 ^c
3	5	5	80	1	4	67 ^c
4	5	10	80	1	8	63 ^c
				4	17	79 ^c
5	5	10	100	1	12	75 ^c
				4	28	86 ^c
6	5	100	80	1	47	51
7	2	1	80	1	10	22 ^c
				4	11	32 ^c
8	2	10	80	1	83	8
				4	93	14
9			80	4	0	

^aDetermined by ¹H NMR analysis of the reaction mixture. ^bCombined yields of the primary (8) and secondary isomerization products (together labeled ISO)⁴⁶ compared to total yields also including the self-metathesis product 7, as determined by ¹H NMR and GC analysis. ^cCompound 8 was the only observed isomerization product.

First, consistent with computational prediction, 5 predominantly catalyzes alkene double-bond migration. Although the isomerization is usually accompanied by olefin metathesis, 5 has a much higher selectivity for isomerization than the Hoveyda–Grubbs second generation catalyst 2 under similar conditions; see entries 1 and 7, and 4 and 8 in Table 1. It should be noted that, when olefin metathesis operates along with double-bond migration, in addition to self-metathesis (7) and isomerization (8) of the substrate, other, secondary isomerization products may be generated from the transformation of the latter compounds.⁴⁶ Thus, to evaluate the selectivities of the catalyst toward isomerization, the combined yields of the primary (8) and secondary isomerization products (together labeled ISO) have been compared to the total yields that also include the self-metathesis product 7;⁴⁷ see Scheme 5 and the Supporting Information.

The selectivity toward isomerization increases with decreasing catalyst loading (Figure 1 and entries 1–4 and 6), with 8 being the sole product detected when using only 1 ppm of complex 5 (entry 1), and high temperature also favors isomerization (entries 4 and 5). This suggests that alkylidene formation via dinuclear ruthenium alkene activation (Scheme 3) may compete with isomerization. Since dissociation of *p*-cymene appears to be rate limiting (see above), the rate of the dinuclear ruthenium alkene activation to give alkylidene is expected to be first order in 5 at elevated catalyst concentrations but should approach the second order at very low concentrations of 5. Accordingly, the rate of alkylidene

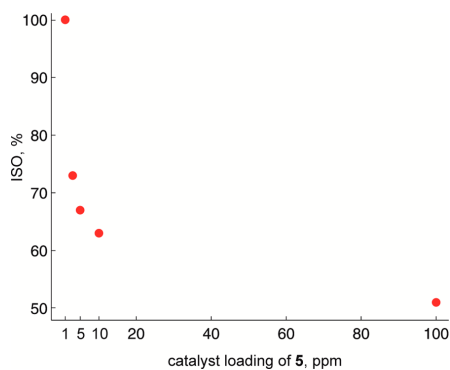


Figure 1. Percentage of isomerization products (ISO (%)) in the converted allylbenzene at increasing loading of 5, after 1 h and at 80 °C. See Table 1, entries 1–4 and 6.

formation should be at its maximum at the start of the experiment, and should fall as the concentration of 5 drops. This is consistent with the observed falling metathesis activity with the progress of the reaction (Figure 2) and at lower loading of 5 (Figure 1).

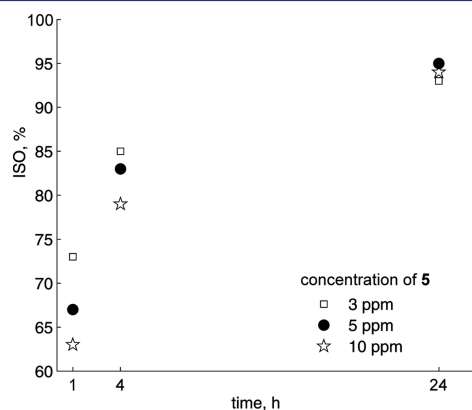


Figure 2. Percentage of isomerization products (ISO (%)) with time during conversion of neat allylbenzene with 5 at 80 °C. See entries 2–4 of Table S2 in the Supporting Information.

The above-described barrierless entry, via route iii, into the hydride-mechanism isomerization cycle suggests that hydrides such as R27 might form in the absence of alkene. Indeed, higher isomerization activity and selectivity were observed in experiments in which 5 was preheated in toluene in the absence of substrate; see Table S2. Variable-temperature ¹H NMR studies indicate that this additional isomerization, at least partly, could be caused by a ruthenium hydride; see Figure S2. However, mercury-poisoning experiments¹⁷ indicate that heating 5 in the absence of substrate also generates isomerization-active ruthenium nanoparticles; see Table S2. Similar signs of ruthenium nanoparticles are not observed in ordinary catalytic tests without preheating of 5.

The above considerations and observations suggest that more weakly coordinating solvents, without the possibility to stabilize **R21** by η^6 -coordination, in combination with low catalyst and substrate concentrations should promote generation of ruthenium hydrides and thus isomerization. In addition, polar solvents are expected to disfavor formation of the dinuclear ruthenium complexes of the alkylidene formation pathway (Scheme 3). This means that nonpolar and η^6 -coordinating solvents like toluene and *p*-cymene should favor olefin metathesis, while noncoordinating and more polar solvents such as tetrahydrofuran and dichloromethane should promote olefin isomerization. Indeed, tests of **5** in a solution of allylbenzene in pentane, including 10% of dichloromethane (here termed a P/D mixture) to fully dissolve the complex, confirm the isomerization-boosting effect; see Table 2. For

Table 2. Conversion and Selectivity toward Isomerization (ISO) of Allylbenzene at High Substrate Dilution and Room Temperature (22 °C)

entry	cat.	cat. load. (mol %)	solvent, S	[S] (mM)	t (h)	conv. ^a (%)	ISO ^b (%)
1	5	1	P/D ^c	20	1	96	100 ^d
					4	100	100 ^d
2	2	1	P/D ^c	20	1	52	13
					4	63	33
3	5	1	P/D ^c	10	1	94	100 ^d
					4	100	100 ^d
4	5	1	P/D ^c	5	1	81	100 ^d
					4	100	100 ^d
5	5	1	P/D ^c	0.25	1	49	100 ^d
					4	93	100 ^d
6	5	0.1	P/D ^c	0.25	1	3	100 ^d
					4	9	100 ^d
7	5	1	THF	20	1	91	100 ^d
					4	98	100 ^d
8	2	1	THF	20	1	44	37
					4	83	64
9	5	1	C ₇ H ₈	20	1	51	22
					4	70	36
10	2	1	C ₇ H ₈	20	1	52	13
					4	75	25

^aDetermined by GC analysis of the reaction mixture. ^bCombined yields of the primary (**8**) and secondary isomerization products (together labeled ISO)⁴⁶ compared to total yields also including the self-metathesis product **7**, as determined by ¹H NMR and GC analysis. ^c*n*-Pentane/dichloromethane (9:1). ^dCompound **8** was the only observed product.

example, at room temperature, almost all of the allylbenzene is converted to the isomerization product **8** in just 1 h (entry 1), which is very different from that obtained in toluene solution (entry 9). The catalytic potency of **5** is perhaps best illustrated by the fact that, in the P/D mixture, turnover frequencies (TOFs) and numbers (TONs) essentially stay intact even in dilution (0.25 μ M, entry 6) typical of solvent impurities.⁴⁸ And remarkably, not even traces of the self-metathesis product **7** or other secondary isomerization products could be detected in any of the catalytic tests of **5** in weakly coordinating solvents (P/D mixture or THF) in Table 2. In other words, the proposed catalyst decomposition product ³R21/R21, which here is liberated upon dissociation of *p*-cymene from **5**, may affect the outcome of metathesis experiments even when

present in tiny concentrations. Moreover, the catalytic activity of **5** only decreases moderately with the substrate dilution (Figure 3), consistent with the computational predictions for both the allyl and the hydride cycle.

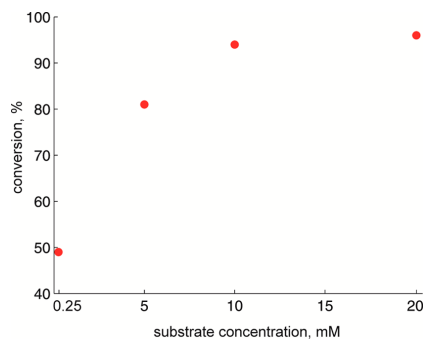


Figure 3. Conversion of allylbenzene to **8** at different substrate concentrations in 1 h, using 1 mol % of **5** in P/D solvent mixture at room temperature. See entries 1 and 3–5 of Table 2.

In striking contrast with the above perfect selectivity for isomerization, self-metathesis dominates in identical concentrations of **5** in toluene (entry 9). This is expected from the above-discussed thermodynamic stability of 18-electron toluene analogues of **5** under such conditions, and the suggested tendency of such complexes to form alkylidene via dinuclear ruthenium alkene activation. In fact, similar results, albeit with a somewhat higher selectivity for olefin metathesis, were recorded under identical conditions using the Hoveyda–Grubbs second-generation catalyst **2** (entry 10), suggesting that, under these conditions, **5** is partly converted to alkylidene at the start of the experiment.

The above considerations can also help explain the catalytic outcome when using the Hoveyda–Grubbs second-generation catalyst **2** in different solvents. Early in the experiment, the P/D mixture (entry 2) and toluene (entry 10) give similar efficiencies for the self-metathesis reaction, but the metathesis efficiency drops faster with time in P/D than in toluene, and is accompanied by more isomerization. This is consistent with the fact that the P/D solvent mixture promotes isomerization when using **5**, while toluene lowers the observed isomerization rate and instead seems to promote formation of alkylidene from **5**. In other words, ³R21 generated by decomposition of **2** will tend to form 18-electron analogues of **5** in toluene, leading to dinuclear ruthenium reformation of metathesis-active alkylidenes. In contrast, ³R21 generated by catalyst decomposition in weakly coordinating and more polar solvents such as P/D will to a larger extent enter the allyl and hydride isomerization cycles of Scheme 3 and thereby reduce the metathesis efficiency.

CONCLUSIONS

Our computational and experimental results point at the spin-triplet 12-electron compound SIMes(Cl)₂Ru (³R21) as an important contributor to alkene isomerization when using second-generation catalysts such as **2** in olefin metathesis, adding to known sources of metathesis-related isomerization, such as ruthenium nanoparticles.¹⁷ Except for some computa-

tional exploration,^{24,36} the capacity of compounds such as SIMes(Cl)₂Ru to initiate isomerization appears to have been overlooked so far. Still, these electron-deficient compounds are likely to result from a range of different routes to loss of alkylidene, among them established ones such as bimolecular coupling^{23,41} and ethylene-triggered breakdown of unsubstituted metallocyclobutane.^{21–24}

Here, molecular-level calculations have shown how alkylidene loss may be triggered from within the regular olefin metathesis cycles of **2** (and thus also any other ruthenium-based catalyst sharing the active species and olefin metathesis mechanism with **2**), either by ethylene via a known mechanism^{21–24} or by 1-alkenes via a novel mechanism involving expansion of the ruthenacyclobutane ring (Scheme 2). The overall barrier associated with this decomposition, located in the ring-expansion step, is only 6 kcal mol⁻¹ above that of allylbenzene self-metathesis, consistent with *Guideline 1* of the *Introduction*.

Importantly, the new catalyst decomposition pathway explains why the presence of substrate is required to reach compounds of sufficient isomerization activity,¹⁸ thereby fulfilling *Guideline 2*. ³R21 may initiate either allylic-mechanism isomerization or, after formation of a cyclometalated Ru-hydride complex, hydride-mechanism isomerization (Scheme 3). The latter mechanism offers the first explanation for the deuterium of a labeled catalyst (**3**) being found in isomerization products,¹⁸ thereby fulfilling *Guideline 3*.

Whereas the spin crossover at the end of the catalyst decomposition, to give the alkene complex ³R9 before liberating ³R21, is facile compared to the rate-determining ring expansion, change of spin state is predicted to be part of the bottleneck of the allylic isomerization cycle. In contrast, spin inversion is not part of the hydride cycle. However, to enter this, the isomerization cycle predicted to be the most efficient, a spin state change from ³R21 to R21 is necessary.

The calculations also suggest that two alkylidene-free ruthenium complexes may regenerate alkylidene by activating an alkene, the reverse of the known bimolecular loss of alkylidene.^{23,41}

The computationally predicted isomerization-initiating capacity of ³R21 and its spin-singlet congener R21 was confirmed by synthesizing and testing the *p*-cymene-stabilized R21 (**5**). The isomerization activity of **5** is particularly high under conditions favoring liberation of R21 by dissociation of *p*-cymene at the same time as hampering the formation of dinuclear aggregates, whereas a nonpolar solvent capable of η⁶-coordination (toluene) dampens isomerization.

Identical catalytic tests of **2** show the same isomerization-dampening effect of toluene, indicating that **5** and **2** share catalytic isomerization cycles. As **2**, **5** can, under the right conditions, also promote olefin metathesis, and the two compounds display the same qualitative trends in the relative metathesis and isomerization selectivities. This suggests that **5** and **2** also share the catalytic metathesis cycle, consistent with a calculated reaction network that connects metathesis, alkylidene loss, isomerization, and alkylidene regeneration.

■ ASSOCIATED CONTENT

Ⓢ Supporting Information

The Supporting Information is available free of charge on the ACS Publications website at DOI: 10.1021/jacs.7b07694.

Experimental and computational methods, additional results from catalytic tests, NMR spectra, X-ray refinement data for compound **5**, geometry-optimized structures, results from reaction pathway calculations, and additional material from DFT calculations (PDF) X-ray crystallographic data for **5** (CCDC-1515796) (CIF)

A file containing 3D rotatable images of all geometry-optimized structures (XYZ)

■ AUTHOR INFORMATION

Corresponding Authors

*Giovanni.Occhipinti@uib.no

*Vidar.Jensen@uib.no

ORCID

Giovanni Occhipinti: 0000-0002-7279-6322

Karl W. Törnroos: 0000-0001-6140-5915

Vidar R. Jensen: 0000-0003-2444-3220

Present Address

§J.E.: School of Chemistry, Cardiff University, Main Building, Park Place, Cardiff CF10 3AT, United Kingdom.

Author Contributions

||J.E., W.S., M.F.: These authors contributed equally.

Notes

The authors declare no competing financial interest.

■ ACKNOWLEDGMENTS

The authors gratefully acknowledge the Research Council of Norway (RCN) for financial support via the FORNY2020 (grant number 203379 and 239288), GASSMAKS (208335), and FRINATEK (262370) programs and for CPU and storage resources granted through the NOTUR (NN2506K) and NORSTORE (NS2506K) supercomputing programs. J.E. is grateful for the support of the German Academic Exchange Service (DAAD) through a short-term scholarship for doctoral students. W.S. acknowledges the University of Bergen for a doctoral fellowship. Dr. Bjarte Holmelid is thanked for assistance with the HRMS (DART) analyses. We are grateful to the Swiss-Norwegian beamlines at the ESRF, Grenoble, France, and to Dr. D. Chernyshov for assistance on beamline BM1A.

■ REFERENCES

- (1) Grubbs, R. H.; Wenzel, A. G.; O'Leary, D. J.; Khosravi, E., Eds. *Handbook of metathesis*, 2nd ed.; Wiley-VCH: Weinheim, Germany, 2015; Vols. 1–3.
- (2) Scholl, M.; Ding, S.; Lee, C. W.; Grubbs, R. H. *Org. Lett.* **1999**, *1*, 953–56.
- (3) Gessler, S.; Randl, S.; Blechert, S. *Tetrahedron Lett.* **2000**, *41*, 9973–76. Garber, S. B.; Kingsbury, J. S.; Gray, B. L.; Hoveyda, A. H. *J. Am. Chem. Soc.* **2000**, *122*, 8168–79.
- (4) Farina, V.; Horváth, A. In *Handbook of Metathesis*, 2nd ed.; Grubbs, R. H., Wenzel, A. G., O'Leary, D. J., Khosravi, E., Eds.; Wiley-VCH: Weinheim, Germany, 2015; Vol. 2, pp 633–58. Stoianova, D.; Johns, A.; Pederson, R. In *Handbook of Metathesis*; 2nd ed.; Grubbs, R. H., Wenzel, A. G., O'Leary, D. J., Khosravi, E., Eds.; Wiley-VCH: Weinheim, Germany, 2015; Vol. 2, pp 699–726.
- (5) Higman, C. S.; Lummiss, J. A. M.; Fogg, D. E. *Angew. Chem., Int. Ed.* **2016**, *55*, 3552–65.
- (6) Dinger, M. B.; Mol, J. C. *Adv. Synth. Catal.* **2002**, *344*, 671–77. Marx, V. M.; Sullivan, A. H.; Melaimi, M.; Virgil, S. C.; Keitz, B. K.; Weinberger, D. S.; Bertrand, G.; Grubbs, R. H. *Angew. Chem., Int. Ed.* **2015**, *54*, 1919–23. Nickel, A.; Ung, T.; Mkrtumyan, G.; Uy, J.; Lee,

- C. W.; Stoianova, D.; Papazian, J.; Wei, W. H.; Mallari, A.; Schrodi, Y.; Pederson, R. L. *Top. Catal.* **2012**, *55*, 518–23. Patel, J.; Mujcinovic, S.; Jackson, W. R.; Robinson, A. J.; Serelis, A. K.; Such, C. *Green Chem.* **2006**, *8*, 450–54.
- (7) Maechling, S.; Zaja, M.; Blechert, S. *Adv. Synth. Catal.* **2005**, *347*, 1413–22. Conrad, J. C.; Fogg, D. E. *Curr. Org. Chem.* **2006**, *10*, 185–202. du Toit, J. L.; van der Gryp, P.; Looock, M. M.; Tole, T. T.; Marx, S.; Jordaan, J. H. L.; Vosloo, H. C. M. *Catal. Today* **2016**, *275*, 191–200. Schrodi, Y.; Ung, T.; Vargas, A.; Mkrumyan, G.; Lee, C. W.; Champagne, T. M.; Pederson, R. L.; Hong, S. H. *Clean. Soil, Air, Water* **2008**, *36*, 669–73.
- (8) Hagen, J. *Industrial Catalysis: A Practical Approach*, 3rd ed.; Wiley-VCH: Weinheim, Germany, 2015.
- (9) Arisawa, M.; Nishida, A.; Nakagawa, M. *J. Organomet. Chem.* **2006**, *691*, 5109–21. Deiters, A.; Martin, S. F. *Chem. Rev.* **2004**, *104*, 2199–238. Hoveyda, A. H.; Malcolmson, S. J.; Meek, S. J.; Zhugralin, A. R. *Angew. Chem., Int. Ed.* **2010**, *49*, 34–44. Meek, S. J.; O'Brien, R. V.; Llaveria, J.; Schrock, R. R.; Hoveyda, A. H. *Nature* **2011**, *471*, 461–66. Prunet, J. *Eur. J. Org. Chem.* **2011**, *2011*, 3634–47.
- (10) Chhabra, S.; Belgi, A.; Bartels, P.; van Lierop, B. J.; Robinson, S. D.; Kompella, S. N.; Hung, A.; Callaghan, B. P.; Adams, D. J.; Robinson, A. J.; Norton, R. S. *J. Med. Chem.* **2014**, *57*, 9933–44. Gleeson, E. C.; Wang, Z. J.; Robinson, S. D.; Chhabra, S.; MacRaid, C. A.; Jackson, W. R.; Norton, R. S.; Robinson, A. J. *Chem. Commun.* **2016**, *52*, 4446–49.
- (11) Lehman, S. E., Jr; Schwendeman, J. E.; O'Donnell, P. M.; Wagener, K. B. *Inorg. Chim. Acta* **2003**, *345*, 190–98. Bourgeois, D.; Pancrazi, A.; Nolan, S. P.; Prunet, J. *J. Organomet. Chem.* **2002**, *643–644*, 247–52. Fokou, P. A.; Meier, M. A. R. *Macromol. Rapid Commun.* **2010**, *31*, 368–73. Kinderman, S. S.; van Maarseveen, J. H.; Schoemaker, H. E.; Hiemstra, H.; Rutjes, F. *Org. Lett.* **2001**, *3*, 2045–48. Schmidt, B. *Eur. J. Org. Chem.* **2004**, *2004*, 1865–80.
- (12) Hong, S. H.; Sanders, D. P.; Lee, C. W.; Grubbs, R. H. *J. Am. Chem. Soc.* **2005**, *127*, 17160–61.
- (13) Donohoe, T. J.; O'Riordan, T. J. C.; Rosa, C. P. *Angew. Chem., Int. Ed.* **2009**, *48*, 1014–17. Alcaide, B.; Almendros, P.; Luna, A. *Chem. Rev.* **2009**, *109*, 3817–58. Arisawa, M.; Terada, Y.; Nakagawa, M.; Nishida, A. *Angew. Chem.* **2002**, *114*, 4926–28. Schmidt, B. *Eur. J. Org. Chem.* **2003**, *2003*, 816–19. Schmidt, B. *J. Org. Chem.* **2004**, *69*, 7672–87. Arisawa, M.; Terada, Y.; Takahashi, K.; Nakagawa, M.; Nishida, A. *Chem. Rec.* **2007**, *7*, 238–53.
- (14) Hong, S. H.; Day, M. W.; Grubbs, R. H. *J. Am. Chem. Soc.* **2004**, *126*, 7414–15.
- (15) Higman, C. S.; Plais, L.; Fogg, D. E. *ChemCatChem* **2013**, *5*, 3548–51.
- (16) Young, A.; Vincent, M. A.; Hillier, I. H.; Percy, J. M.; Tuttle, T. *Dalton Trans.* **2014**, *43*, 8493–98.
- (17) Higman, C. S.; Lanterna, A. E.; Marin, M. L.; Scaiano, J. C.; Fogg, D. E. *ChemCatChem* **2016**, *8*, 2446–49.
- (18) Courchay, F. C.; Sworen, J. C.; Ghiviriga, I.; Abboud, K. A.; Wagener, K. B. *Organometallics* **2006**, *25*, 6074–86.
- (19) Mathew, J.; Koga, N.; Suresh, C. H. *Organometallics* **2008**, *27*, 4666–70. Poater, A.; Bahri-Laleh, N.; Cavallo, L. *Chem. Commun.* **2011**, *47*, 6674–76. Poater, A.; Ragone, F.; Correa, A.; Szadkowska, A.; Barbasiewicz, M.; Grela, K.; Cavallo, L. *Chem. - Eur. J.* **2010**, *16*, 14354–64. Vehlou, K.; Gessler, S.; Blechert, S. *Angew. Chem., Int. Ed.* **2007**, *46*, 8082–85. Trnka, T. M.; Morgan, J. P.; Sanford, M. S.; Wilhelm, T. E.; Scholl, M.; Choi, T. L.; Ding, S.; Day, M. W.; Grubbs, R. H. *J. Am. Chem. Soc.* **2003**, *125*, 2546–58.
- (20) Hong, S. H.; Chlenov, A.; Day, M. W.; Grubbs, R. H. *Angew. Chem., Int. Ed.* **2007**, *46*, 5148–51.
- (21) Tsang, W. C. P.; Schrock, R. R.; Hoveyda, A. H. *Organometallics* **2001**, *20*, 5658–69. Romero, P. E.; Piers, W. E. *J. Am. Chem. Soc.* **2007**, *129*, 1698–704.
- (22) Janse van Rensburg, W. J.; Steynberg, P. J.; Meyer, W. H.; Kirk, M. M.; Forman, G. S. *J. Am. Chem. Soc.* **2004**, *126*, 14332–33.
- (23) Schrodi, Y. In *Handbook of Metathesis*; Grubbs, R. H.; Wenzel, A. G., O'Leary, D. J., Khosravi, E., Eds.; Wiley-VCH: Weinheim, Germany, 2015; Vol. 1, pp 323–42.
- (24) van Rensburg, W. J.; Steynberg, P. J.; Kirk, M. M.; Meyer, W. H.; Forman, G. S. *J. Organomet. Chem.* **2006**, *691*, 5312–25.
- (25) Whereas the combination of sterically demanding alkenes and alkylidenes may lead to substantial barriers to dissociation and association of olefins (Nuñez-Zarur, F.; Solans-Monfort, X.; Rodríguez-Santiago, L.; Sodupe, M. *Organometallics* **2012**, *31*, 4203), the opposite is true for small alkylidenes, or alkylidene-free complexes, as found in the present work. See the [Supporting Information](#) for more information.
- (26) Some of the present addition and dissociation reactions do not have barriers on the PES above those defined by complete separation of the two molecules and can be expected to proceed close to the diffusion limit. The corresponding estimate of the Eyring-derived free energy barrier of these addition reactions is 4.4 kcal mol⁻¹. See the [Supporting Information](#) for more information.
- (27) Nelson, D. J.; Percy, J. M. *Dalton Trans.* **2014**, *43*, 4674–79.
- (28) Fomine, S.; Tlenkopatchev, M. A. *Organometallics* **2007**, *26*, 4491–97. Sliwa, P.; Kurleto, K.; Handzlik, J.; Rogalski, S.; Zak, P.; Wyrzykiewicz, B.; Pietraszuk, C. *Organometallics* **2016**, *35*, 621–28.
- (29) Hassam, M.; Taher, A.; Arnott, G. E.; Green, I. R.; van Otterlo, W. A. L. *Chem. Rev.* **2015**, *115*, 5462–569. Keitz, B. K.; Endo, K.; Patel, P. R.; Herbert, M. B.; Grubbs, R. H. *J. Am. Chem. Soc.* **2012**, *134*, 693–99. Occhipinti, G.; Hansen, F. R.; Törnroos, K. W.; Jensen, V. R. *J. Am. Chem. Soc.* **2013**, *135*, 3331–34. Occhipinti, G.; Koudriavtsev, V.; Törnroos, K. W.; Jensen, V. R. *Dalton Trans.* **2014**, *43*, 11106–17.
- (30) Hong, S. H.; Wenzel, A. G.; Salguero, T. T.; Day, M. W.; Grubbs, R. H. *J. Am. Chem. Soc.* **2007**, *129*, 7961–68.
- (31) Higman, C. S.; Rufin, S. A.; McDonald, R.; Fogg, D. E. *J. Organomet. Chem.* **2017**, *847*, 162–66.
- (32) Kadyrov, R. *Chem. - Eur. J.* **2013**, *19*, 1002–12.
- (33) Vancompennolle, T.; Vignon, P.; Trivelli, X.; Mortreux, A.; Gauvin, R. M. *Catal. Commun.* **2016**, *77*, 75–78.
- (34) van Leeuwen, P.; Clement, N. D.; Tschan, M. J. L. *Coord. Chem. Rev.* **2011**, *255*, 1499–517.
- (35) Whereas the enthalpic cost of spin inversion is associated with reaching the seam of intersection between the two spin surfaces and is represented by the minimum energy crossing point (MECP), the probability that the system will cross from one PES to the other can be thought of as contributing to the activation entropy of the spin-forbidden reaction. Since the spin-crossing probability is lower than unity, the effective activation free energy resulting from adding such an entropic contribution will be higher than that for an analogous spin-allowed reaction. See: Harvey, J. N. *Phys. Chem. Chem. Phys.* **2007**, *9*, 331 and Harvey, J. N. *WIREs Comput. Mol. Sci.* **2014**, *4*, 1. In the present work, following the approach described in Schiwiek, C.; Meiners, J.; Forster, M.; Wurtele, C.; Diefenbach, M.; Holthausen, M. C.; Schneider, S. *Angew. Chem., Int. Ed.* **2015**, *54*, 15271 a spin-crossing-related addition of 1–5 kcal/mol has been used, while the regular thermochemical contributions to give free energies of the MECPs have been obtained as averages for the two spin states of the minimum close to the crossing point.
- (36) Ashworth, I. W.; Hillier, I. H.; Nelson, D. J.; Percy, J. M.; Vincent, M. A. *Eur. J. Org. Chem.* **2012**, *2012*, 5673–77.
- (37) Kozuch, S. *Wiley Interdiscip. Rev. Comput. Mol. Sci.* **2012**, *2*, 795–815. Kozuch, S.; Shaik, S. *Acc. Chem. Res.* **2011**, *44*, 101–10. Uhe, A.; Kozuch, S.; Shaik, S. *J. Comput. Chem.* **2011**, *32*, 978–85.
- (38) At the geometry optimization level, a transition state exists on the PES. With larger basis sets and thermochemical and solvent corrections, the final free energy surface is barrierless.
- (39) Delaude, L.; Demonceau, A.; Noels, A. F. *Chem. Commun.* **2001**, 986–87. Lübke, C.; Dumrath, A.; Neumann, H.; Beller, M.; Kadyrov, R. *ChemCatChem* **2014**, *6*, 105–08. Méret, M.; Maj, A. M.; Demonceau, A.; Delaude, L. *Monatsh. Chem.* **2015**, *146*, 1099–105. Simal, F.; Demonceau, A.; Noels, A. F.; Knowles, D. R. T.; O'Leary, S.; Maitlis, P. M.; Gusev, O. *J. Organomet. Chem.* **1998**, *558*, 163–70.
- (40) Buchmeiser, M. R.; Wang, D.; Zhang, Y.; Naumov, S.; Wurst, K. *Eur. J. Inorg. Chem.* **2007**, *2007*, 3988–4000.
- (41) Ulman, M.; Grubbs, R. H. *J. Org. Chem.* **1999**, *64*, 7202–07.

(42) Ledoux, N.; Allaert, B.; Verpoort, F. *Eur. J. Inorg. Chem.* **2007**, *2007*, 5578–83.

(43) Zhang, Y.; Wang, D.; Lönnecke, P.; Scherzer, T.; Buchmeiser, M. R. *Macromol. Symp.* **2006**, *236*, 30–37.

(44) Ackermann, L.; Bruneau, C.; Dixneuf, P. H. *Synlett* **2001**, *2001*, 0397–99. Sémeril, D.; Bruneau, C.; Dixneuf, P. H. *Helv. Chim. Acta* **2001**, *84*, 3335–41. Sémeril, D.; Cléran, M.; Bruneau, C.; Dixneuf, P. H. *Adv. Synth. Catal.* **2001**, *343*, 184–87. Sémeril, D.; Bruneau, C.; Dixneuf, P. H. *Adv. Synth. Catal.* **2002**, *344*, 585–95. Tudose, A.; Demonceau, A.; Delaude, L. *J. Organomet. Chem.* **2006**, *691*, 5356–65.

(45) Lo, C.; Cariou, R.; Fischmeister, C.; Dixneuf, P. H. *Adv. Synth. Catal.* **2007**, *349*, 546–50.

(46) A possible sequence of reactions could, for example, start by isomerization of the self-metathesis product, followed by ethenolysis of the resulting isomerization products, and cross-metathesis of the new olefins with the substrate; see the [Supporting Information](#) for more details.

(47) The formation of these secondary compounds is expected to be minimal when one of the two catalytic processes dominates, while it should be important when the rates of metathesis and isomerization are comparable. Moreover, since secondary products are formed from the primary products **7** and **8**, their importance will grow with the progress of the reaction. In the majority of the experiments of [Table 1](#), the conversion of the substrate was below 50%, and the amount of secondary isomerization products was low. The only exceptions are entry **6**, where the rates of isomerization and metathesis are comparable, and entry **8**, where the conversion is high.

(48) Bowers, W. D.; Parsons, M. L.; Clement, R. E.; Eiceman, G. A.; Karasek, F. W. *J. Chromatogr.* **1981**, *206*, 279–88.



Paper I: Supporting Information

Phosphine-Based *Z*-Selective Ruthenium Olefin Metathesis Catalysts

Wietse Smit, Vitali Koudriavtsev, Giovanni Occhipinti,
Karl W. Törnroos, and Vidar R. Jensen

Organometallics **2016**, 35, 1825–1837

SI-I

Pages S19–S174 have been omitted.

*Reprints were made with permission from the American Chemical Society.
Further permissions related to the material excerpted should be directed to the ACS.*

<https://pubs.acs.org/doi/10.1021/acs.organomet.6b00214>

SI-I

Supplementary information for:

Phosphine-Based Z-selective Ruthenium Olefin Metathesis Catalysts

Wietse Smit, Vitali Koudriavtsev, Giovanni Occhipinti*, Karl W. Törnroos and Vidar R. Jensen*
Department of Chemistry, University of Bergen, Allégaten 41, N-5007 Bergen, Norway

Table of contents	
Supplementary results from catalytic tests.....	S2
Table S1: Homocoupling of allylbenzene with 8b under different reaction conditions.....	S2
Procedure catalytic testing	S3
Analytical data	S3
Figure S1: ¹ H NMR spectrum of compound 4 in CD ₂ Cl ₂	S4
Figure S2: ¹³ C{ ¹ H} NMR spectrum of compound 4 in CD ₂ Cl ₂ . (a) Full spectrum. (b) Expanded region between 132 and 122 ppm. (c) Expanded region between 31 and 21 ppm.....	S5
Figure S3: ³¹ P NMR spectrum of compound 4 in CD ₂ Cl ₂	S5
Figure S4: ¹ H NMR spectrum of compound 5 in CD ₂ Cl ₂	S6
Figure S5: ¹ H NMR spectrum of compound 5 in CDCl ₃ with solvate signals.....	S6
Figure S6: ¹³ C{ ¹ H} NMR spectrum of compound 5 in CD ₂ Cl ₂ . (a) Full spectrum. (b) Expanded region between 133 and 123 ppm. (c) Expanded region between 35 and 21 ppm.....	S7
Figure S7: ³¹ P NMR spectrum of compound 5 in CD ₂ Cl ₂	S8
Figure S8: ¹ H NMR spectrum of compound 6 in CD ₂ Cl ₂ . (a) Full spectrum. (b) Expanded region between 7.7 and 6.9 ppm. (c) Expanded region between 2.1 and 0.9 ppm.....	S9
Figure S9: ¹ H NMR spectrum of compound 6 in CDCl ₃ with solvate signals.....	S9
Figure S10: ¹³ C{ ¹ H} NMR spectrum of compound 6 in CD ₂ Cl ₂	S10
Figure S11: ³¹ P NMR spectrum of compound 6 in CD ₂ Cl ₂	S10
Figure S12: ¹ H NMR spectrum of compound 8a in CD ₂ Cl ₂	S11
Figure S13: ¹ H NMR spectrum of compound 8a in CDCl ₃ with solvate signals.....	S11
Figure S14: ¹³ C{ ¹ H} NMR spectrum of compound 8a in CD ₂ Cl ₂ . (a) Full spectrum. (b) Expanded region between 135 and 112 ppm. (c) Expanded region between 41 and 17 ppm.....	S12
Figure S15: ³¹ P NMR spectrum of compound 8a in CD ₂ Cl ₂	S13
Figure S16: ¹ H NMR spectrum of compound 8b in CD ₂ Cl ₂	S13
Figure S17: ¹ H NMR spectrum of compound 8b in CDCl ₃ with solvate signals.....	S14
Figure S18: ¹³ C{ ¹ H} NMR spectrum of compound 8b in CD ₂ Cl ₂ . (a) Full spectrum. (b) Expanded region between 155 and 112 ppm.....	S15
Figure S19: ³¹ P NMR spectrum of compound 8b in CD ₂ Cl ₂	S15
Crystallographic data.....	S16
Table S2: Crystal and structure refinement data for 4 , 6 and 8b	S16
Computational results.....	S17
Table S3: Comparison of calculated selectivity.....	S17
Table S4: Single point energies in gas phase and in solution (PBE-D3(BJ), a.u.), thermal corrections to enthalpy and Gibbs free energy (ωB97XD, a.u.), of the investigated structures.....	S18
Input file examples.....	S19

Supplementary results from catalytic tests

Table S1: Homocoupling of allylbenzene with **8b** under different reaction conditions.

entry	cat load (mol %)	additive ^a	solvent	[sub] (M)	<i>T</i> (°C)	<i>t</i> (h)	conv ^b (%)	yield ^c (%)	<i>Z</i> ^b (%)
1	1			neat	20	0.5	10	6	83
						1	21	13	81
						4	69	26	73
						8	98	32	52
2	1			neat	40	0.5	24	16	79
						1	49	24	76
						4	99	17	26
3	1			neat	60	0.5	97	19	45
						1	100	11	28
4	2			neat	20	0.5	19	11	83
						1	32	18	82
						4	85	31	68
						8	100	20	26
5	4			neat	20	0.5	24	12	83
						1	35	19	82
						4	87	32	71
						8	100	24	40
6	1		toluene	4	20	0.5	6	2	82
						1	9	5	81
						4	25	15	80
						8	59	21	76
						16	97	19	54
						16	97	19	54
7	1		THF	4	20	1	9	3	81
						4	30	9	83
						8	56	13	80
						16	94	12	65
						16	94	12	65
8	1		<i>p</i> -cymene	4	20	1	6	3	82
						4	19	11	80
						8	43	18	77
						16	89	19	62
						16	89	19	62
9	1		toluene	1	20	1	6	1	81
						4	14	5	78
						8	29	8	75
						16	71	10 (9)	68
						16	71	10 (9)	68

10	1		toluene	2	20	1	6	2	80
						4	16	8	78
						8	41	12	75
						16	90	13	61
11	1		toluene	3	20	1	9	4	81
						4	32	11	79
						8	67	14	72
						16	99	11	46
12	1		toluene	4	40	0.5	10	6	78
						1	19	11	77
						4	88	18	59
13	1	QUI	neat	20		4	29	28	49
						8	42	41	47
14	1	PPA	neat	20		4	9	4	63
						8	12	5	62
15	1	TCPO	neat	20		4	37	25	81
						8	55	36	81
						24	94	36	69
16	1	H ₂ O	neat	20		4	25	12	81
						8	25	12	82

^aQUI = 2,6-dichloro-1,4-benzoquinone (1 equiv with respect to the cat), PPA = phenylphosphoric acid (1 equiv with respect to the cat), TCPO = tricyclohexylphosphine oxide (5 equiv with respect to the cat), 1 drop H₂O. ^bDetermined by ¹H NMR analysis. ^c¹H NMR yields (values in parentheses are isolated yields).

Procedure catalytic testing

Under inert atmosphere (Ar), in a glove box, a vial (3 ml) was charged with 3-5 mg of catalyst after which the additive, solvent and substrate were weighed into the vial to obtain the desired concentration, mol% of catalyst and additive concentration. After capping the vial, the reaction mixture was heated in an aluminum block placed on a standard laboratory heater and attached to a thermostat, a small stirring magnet ensured continuous agitation. At timed intervals a small amount of reaction mixture was taken, transferred in an NMR tube and diluted up to 0.7 ml with CDCl₃. The ¹H NMR analysis of the samples was carried out as explained in *J. Am. Chem. Soc.* **2013**, *135*, 3331-3334.

Analytical data

NMR-spectra of compounds **4**, **5**, **6**, **8a** and **8b**

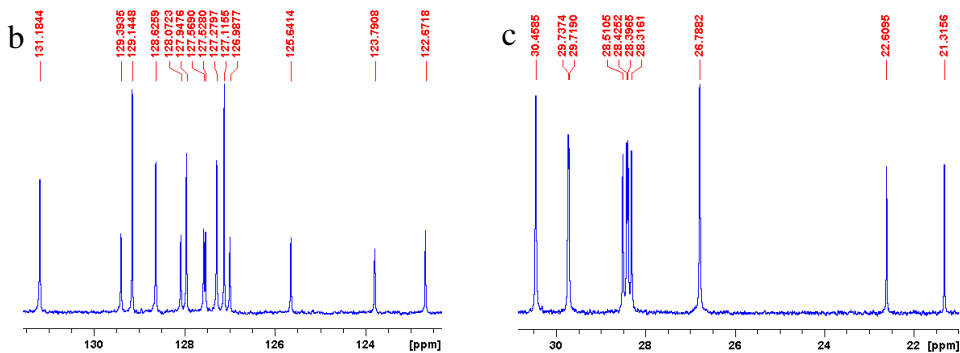


Figure S2: $^{13}\text{C}\{^1\text{H}\}$ NMR spectrum of compound **4** in CD_2Cl_2 . (a) Full spectrum. (b) Expanded region between 132 and 122 ppm. (c) Expanded region between 31 and 21 ppm.

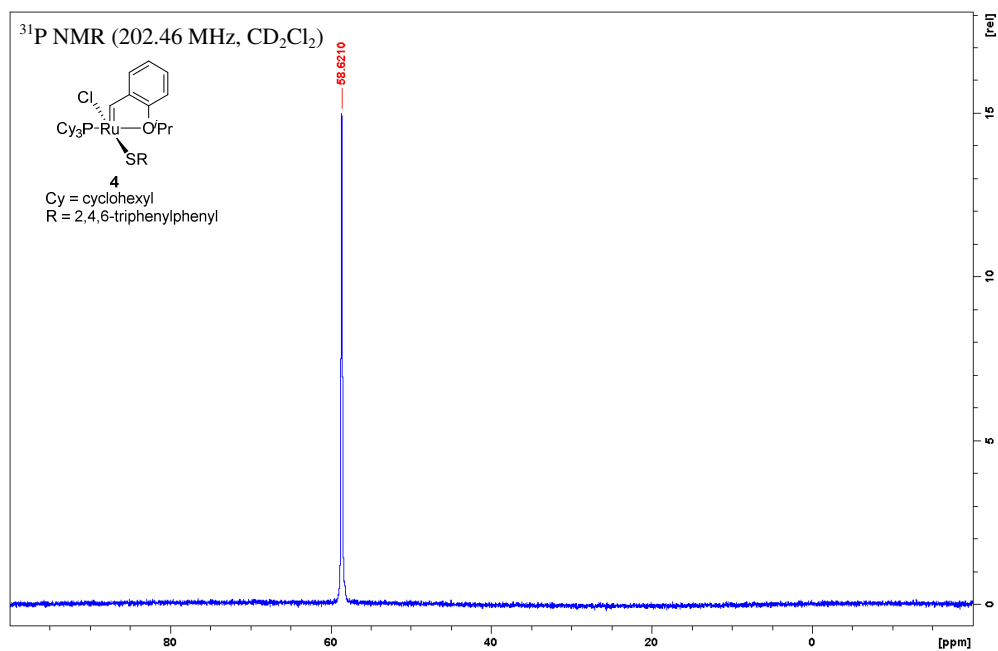


Figure S3: ^{31}P NMR spectrum of compound **4** in CD_2Cl_2 .

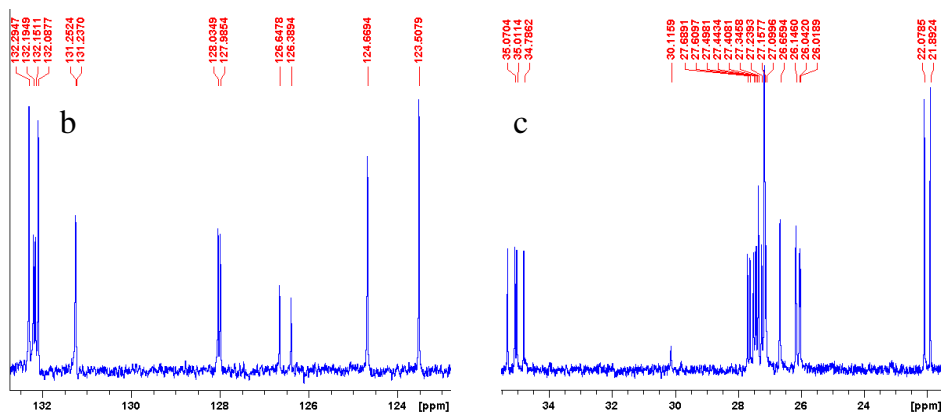
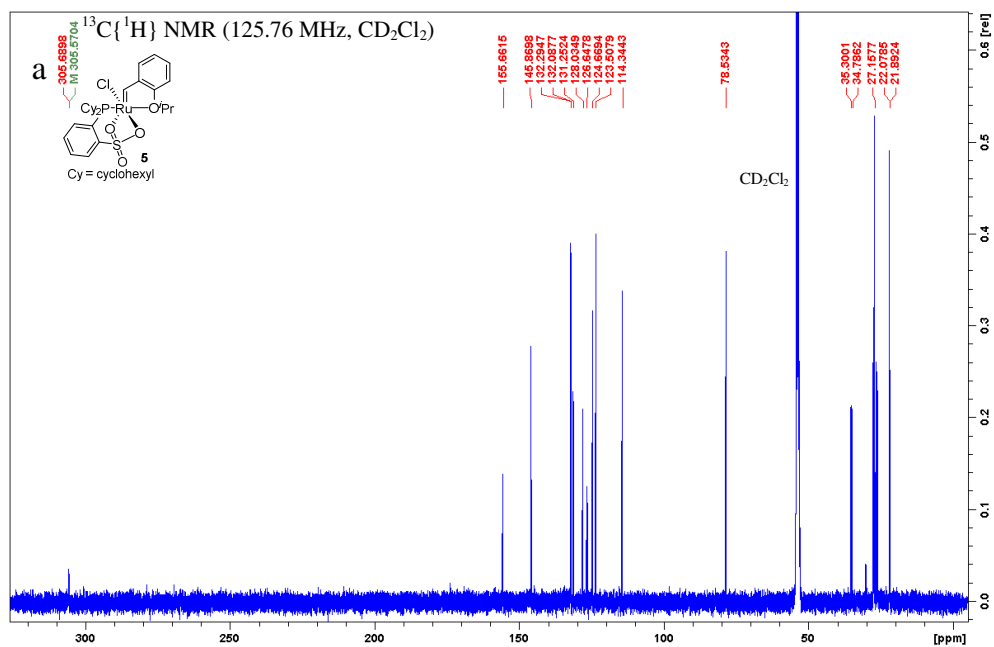
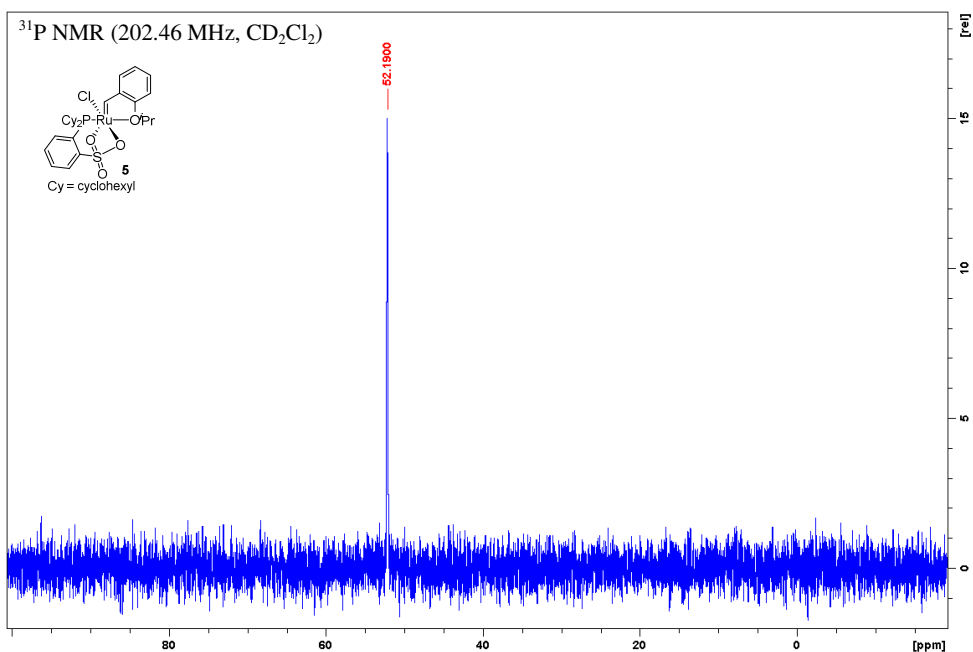
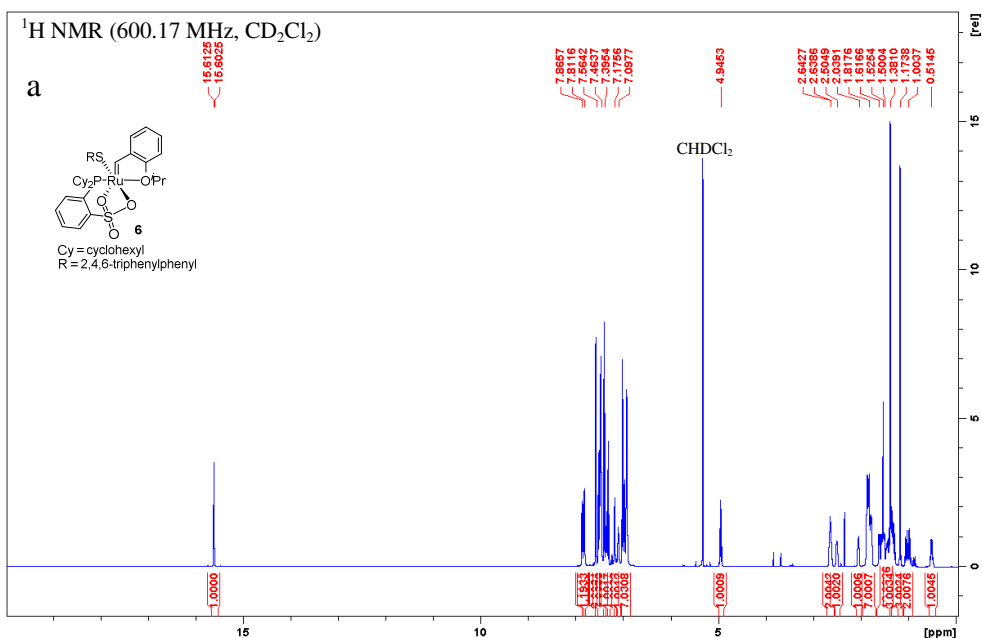


Figure S6: $^{13}\text{C}\{^1\text{H}\}$ NMR spectrum of compound **5** in CD_2Cl_2 . (a) Full spectrum. (b) Expanded region between 133 and 123 ppm. (c) Expanded region between 35 and 21 ppm.

Figure S7: ³¹P NMR spectrum of compound **5** in CD₂Cl₂.

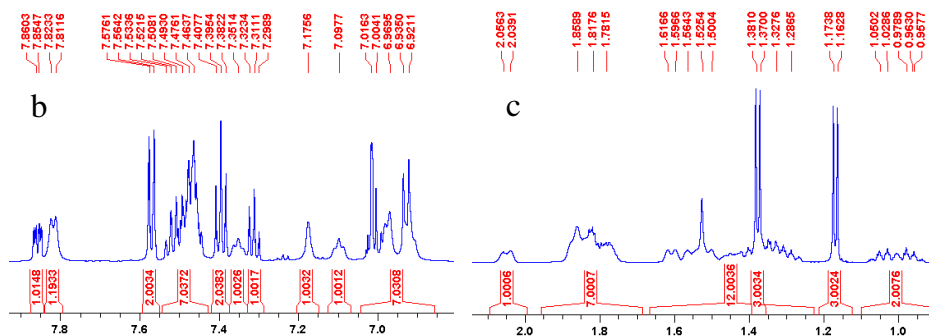


Figure S8: ^1H NMR spectrum of compound **6** in CD_2Cl_2 . (a) Full spectrum. (b) Expanded region between 7.7 and 6.9 ppm. (c) Expanded region between 2.1 and 0.9 ppm.

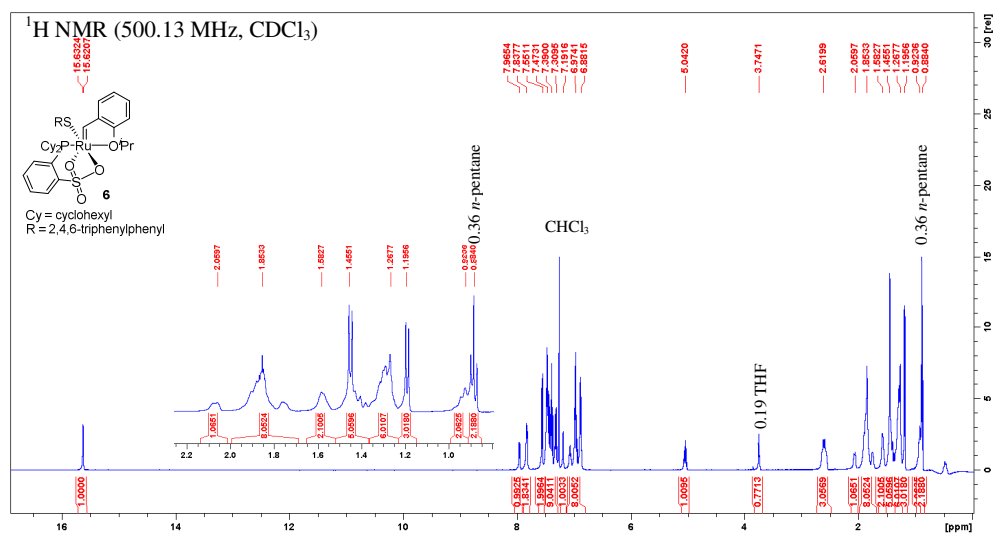
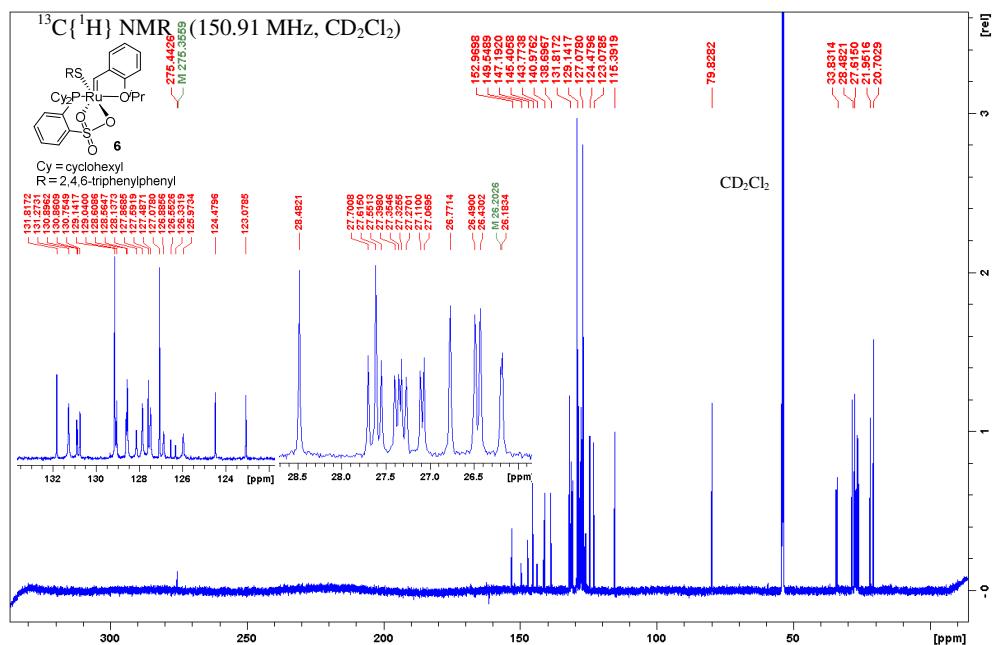
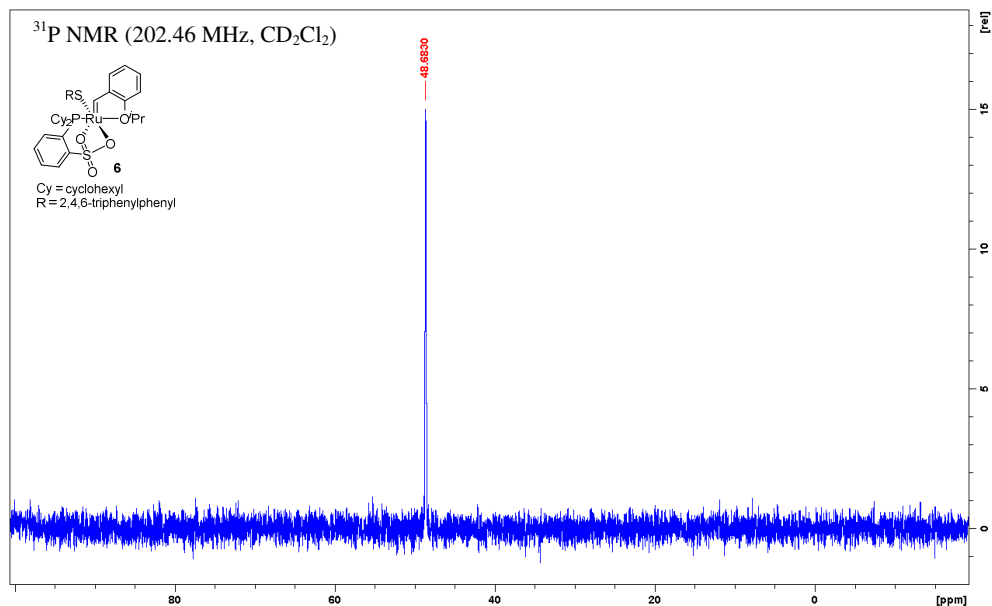
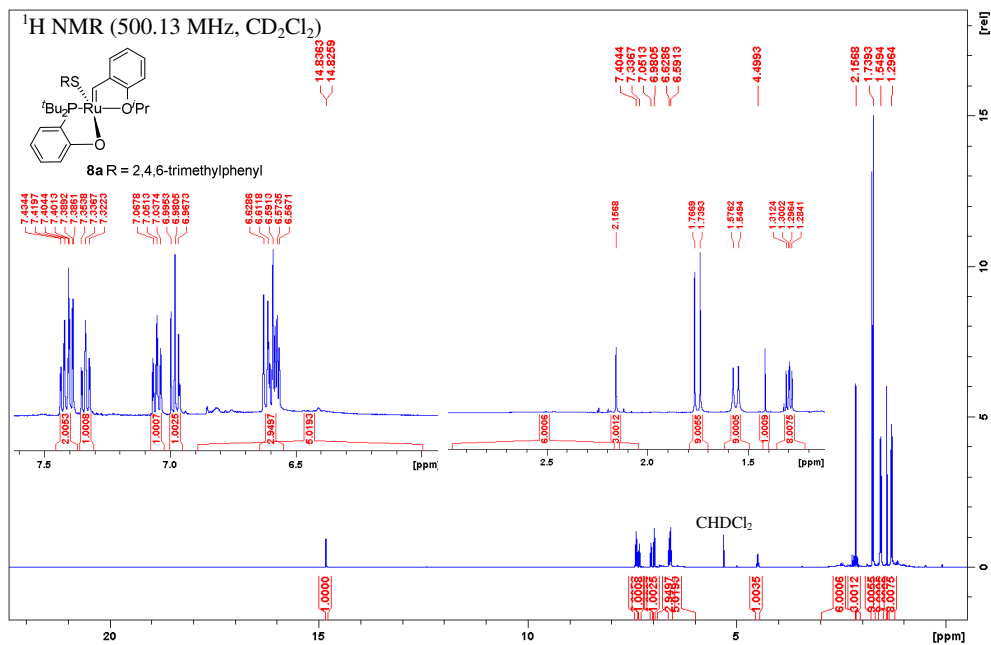
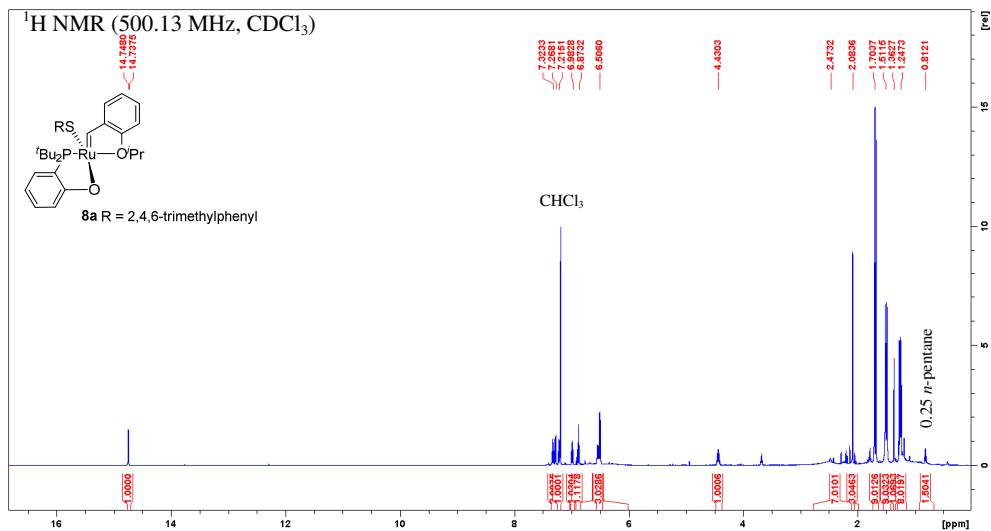


Figure S9: ^1H NMR spectrum of compound **6** in CDCl_3 with solvate signals.

Figure S10: $^{13}\text{C}\{^1\text{H}\}$ NMR spectrum of compound **6** in CD_2Cl_2 .Figure S11: ^{31}P NMR spectrum of compound **6** in CD_2Cl_2 .

Figure 12: ¹H NMR spectrum of compound **8a** in CD₂Cl₂.Figure 13: ¹H NMR spectrum of compound **8a** in CDCl₃ with solvate signals.

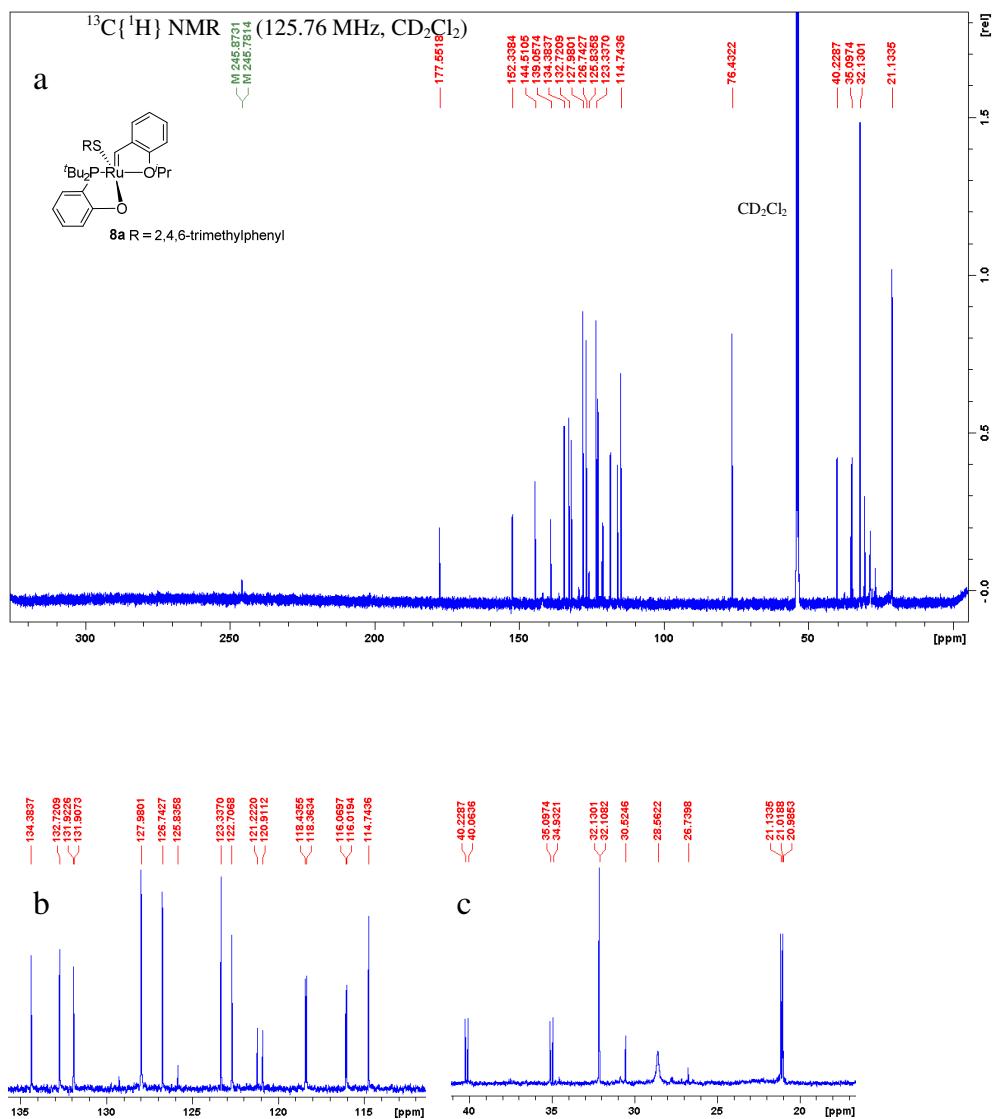
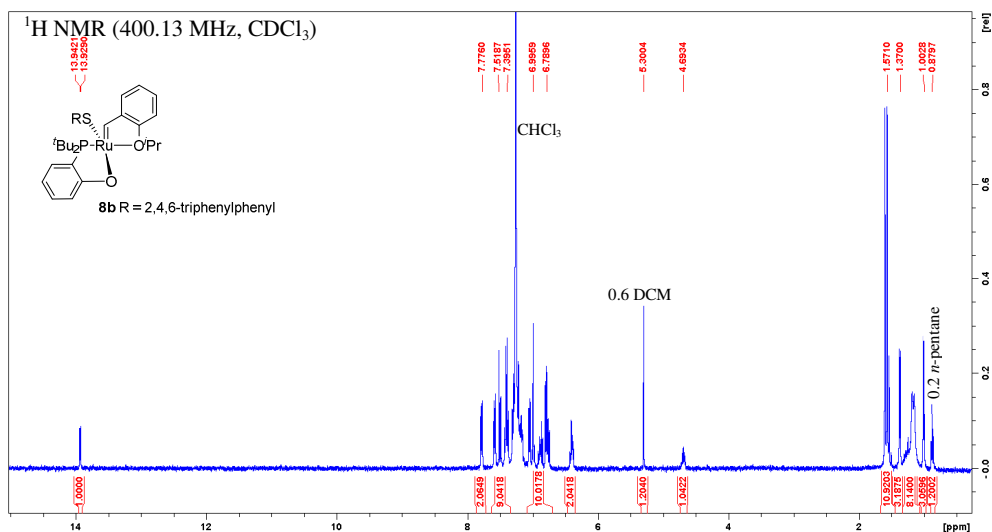
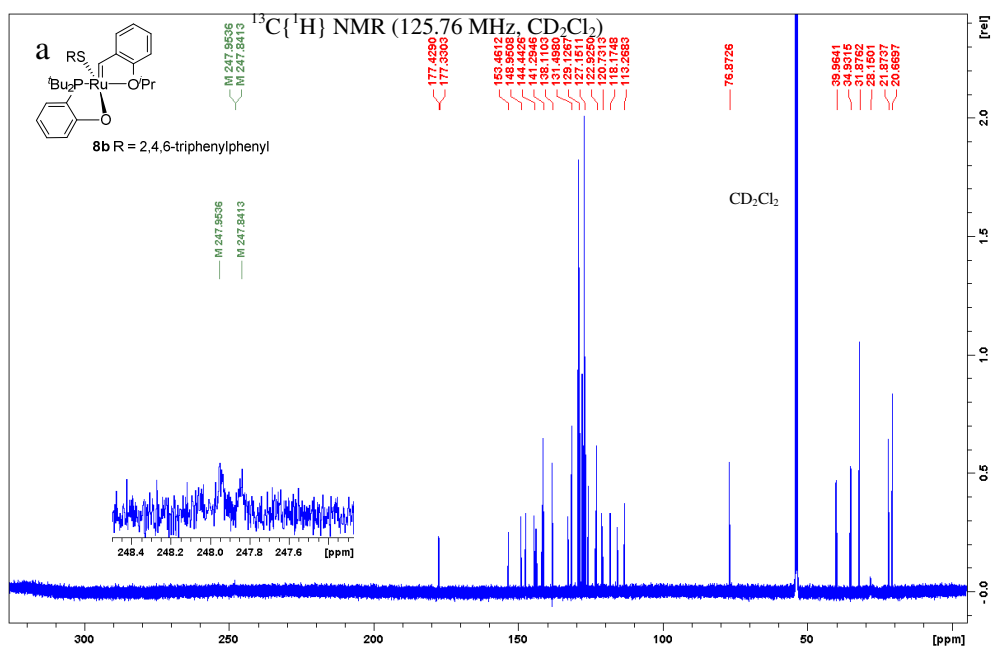


Figure S14: $^{13}\text{C}\{^1\text{H}\}$ NMR spectrum of compound **8a** in CD_2Cl_2 . (a) Full spectrum. (b) Expanded region between 135 and 112 ppm. (c) Expanded region between 41 and 17 ppm.

Figure S17: ¹H NMR spectrum of compound **8b** in CDCl₃ with solvate signals.

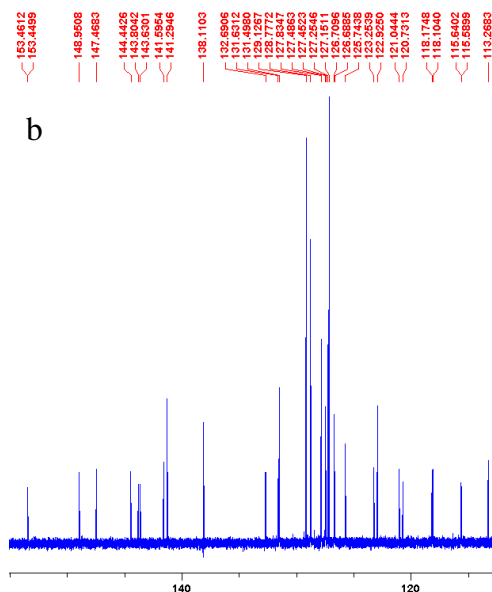


Figure S18: $^{13}\text{C}\{^1\text{H}\}$ NMR spectrum of compound **8b** in CD_2Cl_2 . (a) Full spectrum. (b) Expanded region between 155 and 112 ppm.

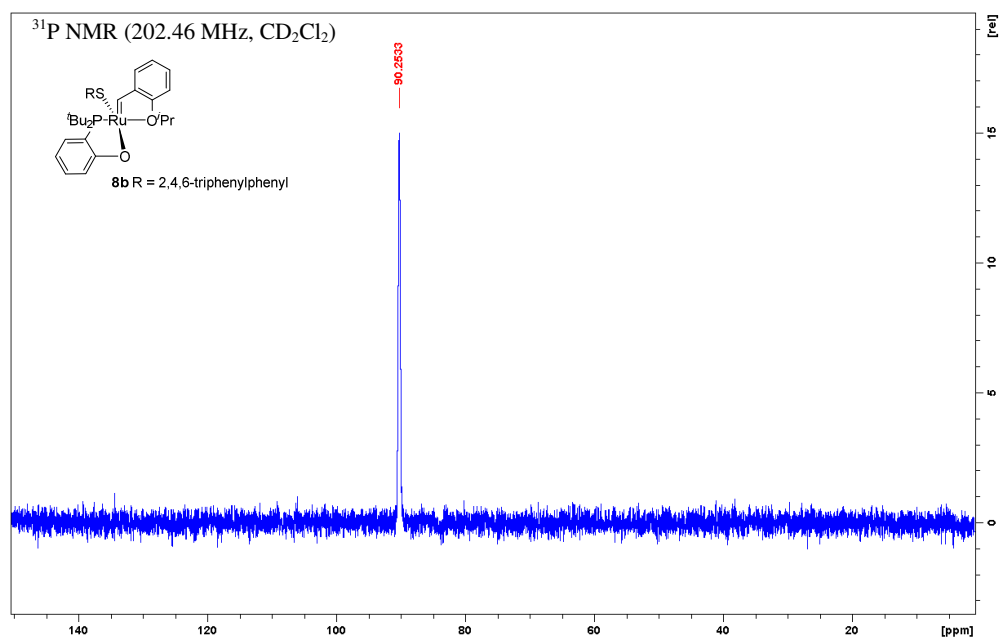


Figure S19: ^{31}P NMR spectrum of compound **8b** in CD_2Cl_2 .

Crystallographic data

Table S2: Crystal and structure refinement data for **4**, **6** and **8b**.

Compound	4	6	8b
<i>Crystal data</i>			
Chemical formula	C ₅₂ H ₆₂ ClOPRuS·C ₅ H ₁₂	C ₅₂ H ₅₅ O ₄ PRuS ₂ ·CH ₂ Cl ₂	C ₄₈ H ₅₁ O ₂ PRuS·CH ₂ Cl ₂
M_r	974.71	1025.04	908.91
Crystal system,	Monoclinic	Monoclinic	Monoclinic
Space group	$P2_1/n$	$P2_1/n$	$P2_1/n$
Temperature (K)	103	103	103
a, b, c (Å)	12.419 (3), 15.046 (3), 27.038 (6)	13.0441 (10), 23.8002 (18), 15.4295 (12)	12.8196 (5), 17.0380 (6), 20.3621 (7)
β (°)	97.968 (3)	94.932 (1)	105.436 (1)
V (Å ³)	5003.5 (17)	4772.4 (6)	4287.1 (3)
Z	4	4	4
$F(000)$	2064	2128	1888
D_x (Mg/m ³)	1.294	1.427	1.408
Radiation type	Mo $K\alpha$, $\lambda = 0.71073$ Å	Mo $K\alpha$, $\lambda = 0.71073$ Å	Mo $K\alpha$, $\lambda = 0.71073$ Å
No. cell param. reflections	9968	9753	9886
θ (°)	2.5–24.9	2.3–31.0	2.4–30.0°
μ (mm ⁻¹)	0.48	0.61	0.62
Crystal size (mm)	0.34 × 0.23 × 0.11	0.31 × 0.28 × 0.11	0.18 × 0.08 × 0.04
Appearance	Irr. Prism, dark purple	Irr. Prism, purple-brown	Irr. Prism, purple
<i>Data collection</i>			
No. meas. reflections	52714	84499	71691
No. indep. reflections	9135	15193	12539
No. refl. with $I > 2\sigma(I)$	6492	13180	10038
R_{int}	0.136	0.035	0.077
$\theta_{max}, \theta_{min}$ (°)	25.4, 1.7	31.0, 1.7	30.1, 2.0
$(\sin \theta/\lambda)_{max}$ (Å ⁻¹)	0.603	0.725	0.705
h	-14→14	-18→18	-18→18
k	-18→18	-34→34	-24→23
l	-32→32	-22→22	-28→28
<i>Refinement</i>			
Method	Full-matrix least squares on F^2	Full-matrix least squares on F^2	Full-matrix least squares on F^2
$R[F^2 > 2\sigma(F^2)]$	0.098	0.041	0.041
$wR(F^2)$	0.200	0.109	0.106
S	1.16	1.06	1.06
No. reflections	9135	15193	12539
No. parameters	563	570	513
No. restraints	504	0	0
$(\Delta/\sigma)_{max}$	0.001	0.002	0.001
$\Delta\rho_{max}, \Delta\rho_{min}$ (e.Å ⁻³)	2.39, -1.33	1.37, -0.94	2.97, -0.79

Computational results

Table S3: Comparison of calculated selectivity

Cat.	$\Delta\Delta E_{\text{Gas}}^{\ddagger a}$	$\Delta\Delta H_{\text{Gas}}^{\ddagger a}$	$\Delta\Delta G_{\text{Gas}}^{\ddagger a}$	$\Delta\Delta G_{\text{Tol}}^{\ddagger a}$
1	3.4	3.6	3.4	3.1
3	0.2	0.1	-0.2	-0.8
4	1.3	1.4	1.2	0.9
6	3.0	3.1	3.0	2.4
8a	0.3	0.2	-0.1	0.3
8b	0.9	1.2	1.2	1.6
9	0.5	0.7	0.5	0.8
10	2.3	2.4	2.1	1.5

^aThe relative energies [kcal/mol] are a measure of Z-selectivity, $\Delta\Delta G_{\text{Tol/Gas}}^{\ddagger} = \Delta G(E)_{\text{Tol/Gas}}^{\ddagger} - \Delta G(Z)_{\text{Tol/Gas}}^{\ddagger}$. The conformations that minimize Gibbs free energy in toluene were used.

Table S4: Single point energies in gas phase and in solution (PBE-D3(BJ), a.u.), thermal corrections to enthalpy and Gibbs free energy (ω B97XD, a.u.), of the investigated structures

Cat.	E_{Gas}^a	E_{Tol}^a	H_{corr}^b	G_{corr}^c
PC, 1	-3264.69418115	-3264.73999768	1.021759	0.882935
TS4(E), 1	-3459.59085972	-3459.64325498	1.130475	0.982125
TS4(Z), 1	-3459.59633281	-3459.64815053	1.130159	0.982137
TS4(E), 3	-2995.80411710	-2995.84629565	0.802577	0.685537
TS4(Z), 3	-2995.80446161	-2995.84557808	0.802748	0.686132
PC, 4	-3386.47917539	-3386.52464587	1.081138	0.950014
TS4(E), 4	-3581.36584113	-3581.41693038	1.189376	1.049338
TS4(Z), 4	-3581.36785955	-3581.41845007	1.189165	1.049411
PC, 6	-3545.82292906	-3545.86965579	1.014532	0.883592
TS4(E), 6	-3740.71637229	-3740.76863359	1.122446	0.982818
TS4(Z), 6	-3740.72117159	-3740.77288098	1.122313	0.982874
TS1, 1	-3264.66940309	-3264.71785757	1.019800	0.879939
TS1, 6	-3545.80741206	-3545.8537404	1.013325	0.883553
AC1, 1	-3264.67566255	-3264.72370127	1.020615	0.879364
AC1, 6	-3545.80769757	-3545.85344439	1.013386	0.880767
TS2, 1	-3613.32945336	-3613.38187534	1.194623	1.037868
TS2, 6	-3894.45919775	-3894.51312622	1.186971	1.037868
Pi-C, 1	-3613.33101661	-3613.38285135	1.196041	1.040535
Pi-C, 6	-3894.46440687	-3894.51743728	1.188527	1.039872
TS3, 1	-3613.32326093	-3613.3751295	1.195107	1.040461
TS3, 6	-3894.46137844	-3894.51469808	1.187985	1.041592
Dissociated sulfonate, 6	-3545.77626772	-3545.83133119	1.013079	0.880360
PC, 8a	-2267.91672243	-2267.94283179	0.749629	0.641895
TS4(E), 8a	-2462.80493386	-2462.83815602	0.857111	0.740639
TS4(Z), 8a	-2462.80534495	-2462.8393378	0.857148	0.741285
PC, 8b	-2842.67602801	-2842.71400848	0.929171	0.796732
TS4(E), 8b	-3037.56503359	-3037.610056	1.028371	0.896004
TS4(Z), 8b	-3037.56648443	-3037.61218787	1.027930	0.895552
PC, 9	-2997.40640113	-2997.45068568	0.998941	0.872775
TS4(E), 9	-3192.29382266	-3192.34485661	1.106910	0.971843
TS4(Z), 9	-3192.2946278	-3192.34616449	1.106584	0.971847
TS4(E), 10	-3501.72675097	-3501.77984765	1.257687	1.118423
TS4(Z), 10	-3501.73042881	-3501.78265547	1.257535	1.118811
S	-348.646582766	-348.656469867	0.171612	0.130063
A	-502.385841095	-502.397149269	0.236094	0.186306

^aSCF energies in gas phase and toluene. ^bThermal correction to enthalpy. ^cThermal correction to Gibbs free energy. **S** = substrate (allylbenzene), **A** = 2-isopropoxystyrene

Paper II: Supporting Information

Loss and Reformation of Ruthenium Alkylidene: Connecting Olefin Metathesis, Catalyst Deactivation, Regeneration, and Isomerization

Julien Engel, Wietse Smit, Marco Foscatto, Giovanni Occhipinti, Karl W. Törnroos, and Vidar R. Jensen

J. Am. Chem. Soc. **2017**, 139, 16609–16619

SI-II

Pages S45–S68 and S74–S96 have been omitted.

*Reprints were made with permission from the American Chemical Society.
Further permissions related to the material excerpted should be directed to the ACS.*

<https://pubs.acs.org/doi/10.1021/jacs.7b07694>

Supporting Information:

Loss and Reformation of Ruthenium Alkylidene: Connecting Olefin Metathesis, Catalyst Deactivation, Regeneration, and Isomerization

Julien Engel,^{†*} Wietse Smit,[‡] Marco Foscato,[‡] Giovanni Occhipinti,^{**} Karl W. Törnroos[‡] and Vidar R. Jensen^{**}

[†]Institute of Organic Chemistry RWTH Aachen University Landoltweg 1, D-52074 Aachen, Germany

[‡]Department of Chemistry, University of Bergen, Allégaten 41, N-5007 Bergen, Norway

Table of contents

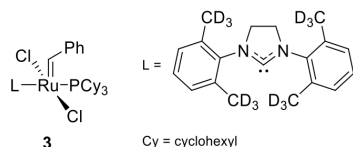
Background	S3
Catalyst used in deuterium labeling study	S3
Experimental part	S3
Experimental methods	S3
Procedure for catalytic testing: self-metathesis and isomerization of allylbenzene	S4
GC settings	S6
Detailed results of catalytic tests	S7
¹ H-NMR-spectra of 5 at different temperatures	S10
Analytical data	S12
Crystallographic data	S14
Computational part	S27
Computational methods	S27
Geometry optimizations	S27
Single-point energy calculations	S27
Minimum energy crossing points and the probability of spin crossing	S28
Association and dissociation of olefins and arenes	S29
Calculation of kinetic parameters	S29
Calculation of thermochemical corrections for R21	S29
Assessment of known decomposition mechanisms	S34
New decomposition pathways explored but not discussed in the main part of the paper	S38
Additional intermediates and transition states of the 1-alkene-triggered decomposition pathway	S39
Additional mechanistic details of the olefin isomerization cycles	S41
Additional mechanistic details of the alkylidene regeneration pathways	S43

Graphical representations of optimized molecular structures	S45
Decomposition of 2 (OM7-R9).....	S45
η^3 -allyl isomerization pathway (R21-R25).....	S52
Hydride isomerization pathway (R26-R31).....	S55
IRC calculations	S61
OM7 to R4B	S61
R4B to R5	S62
R5 to R6A	S63
R6A to R6B	S64
R6B to R8	S65
R8 to R9	S66
R21 to R26A	S67
R26A to R26	S68
Calculated absolute and relative energies.....	S69
Examples of Gaussian 09 input files	S74
Geometry optimization of OM7	S74
Single-point calculation of OM7	S83
Results from energetic span models	S97
η^3 -allyl pathway	S97
η^3 -allyl pathway with deactivation <i>via</i> MECP_{R21}	S98
η^3 -allyl pathway with deactivation <i>via</i> TS_{R36/R37}	S99
η^3 -allyl pathway with deactivation <i>via</i> TS_{R23/R39}	S100
Hydride pathway	S102
Hydride pathway with deactivation <i>via</i> MECP_{R21}	S102
References	S104

Background

Catalyst used in deuterium labeling study

Chart S1. The deuterium-labeled catalyst of Wagener and co-workers.¹



Experimental part

Experimental methods

Unless otherwise stated, all chemicals were obtained from Sigma-Aldrich of which [(*p*-cymene)RuCl₂]₂ and 1,3-bis(2,4,6-trimethylphenyl)-imidazolium chloride were used as received. *n*-Pentane, *p*-cymene, benzene-*d*₆ and inhibitor-free tetrahydrofuran (THF) were degassed, dried over calcium hydride (CaH₂), and subsequently filtered over basic alumina (Brockmann I, activated three days at 220 °C *in vacuo*) before use. Toluene and dichloromethane were purified using an MBraun solvent purification system (“Grubbs’ column”) and treated further as the solvent mentioned above. Chloroform-*d* was dried over CaH₂ and distilled trap-to-trap. The carbene 1,3-bis(2,4,6-trimethylphenyl)-4,5-dihydroimidazol-2-ylidene (SIMes) was synthesized from 1,3-bis(2,4,6-trimethylphenyl)-imidazolium chloride according to literature procedure.²

Allylbenzene of high purity is needed to reproduce the experiments shown in Table S2 and S3. All the allylbenzene used here was dried over CaH₂, distilled under vacuum (40 °C, 13 mbar), degassed, and filtered over basic alumina before use and stored in the glovebox at –32°C. The kind of impurities present in different batches of allylbenzene depends both on the supplier and on the lot number. Two different lots, from two different suppliers, were used in the present work. For the first of these (98%, Sigma-Aldrich, A29402, Lot No. SHBF0568V), a purity >99.9% (determined by gas chromatography (GC)) could be achieved by following the above-described purification procedure. This allylbenzene was used for most of the experiments. For a handful of experiments (entries 10–15 in Table S2), a second lot of allylbenzene (98%, Acros Organics, 102890250, Lot No. A0361159), purified to 99.8% following the above-described procedure, was used. The two purified lots gave comparable results in catalytic experiments. A few other lots were also tested. In some of these we discovered unidentified impurities, present even after purification. These impurities affected the catalytic performance of both **5** and **2** and hindered direct comparison of individual catalytic results between lots, in particular in combination with low catalyst loadings. Nonetheless, our experience is that the general trends reflected by the experiments presented here are always reproduced, regardless which allylbenzene lot is used.

NMR spectra were recorded on Bruker Biospin AV500 and AV600 spectrometers. Chemical shifts are reported relative to the residual solvent peaks.³ The HRMS DART mass spectrum was recorded by means of a DART-100 ion source from IonSense Inc. (Saugus, MA, USA) interfaced to a JMS-T100LC AccuTOF™ mass spectrometer from JEOL USA, Inc. (Peabody, MA, USA). The ions were transported into the orthogonal accelerating time of flight (TOF) single stage reflectron mass analyzer by a high

frequency and high voltage quadrupole ion guide. Detection was achieved with a dual micro channel plate detector. Elemental analysis was performed using an Elementar Vario EL III analyzer.

Gas chromatography (GC) analyses were performed on an Agilent technologies 7890A instrument equipped with a 7693 auto sampler, split/splitless injection port, Agilent technologies DB-WAX (30 m x 200 μm x 0.2 μm) column, and FID detector. In general, area percentages were reported. However, if metathesis products were present in the sample, the area percentages of the substrate, isomerization products and metathesis products were corrected according to their respective effective carbon numbers (ECN).⁴ Details about the temperature programs and the settings used can be found in Table S1.

Suitable crystals for diffraction experiments were immersed in Paratone-N (Hampton Research). The crystal specimen was mounted inside a MiTiGen MicroLoop and single crystal Bragg diffraction data were collected at 103 K using an Oxford Cryosystems, Cryostream 700 Plus N₂ open flow blower, on the PILATUS@SNBL diffractometer⁵ at the BM01A station of the Swiss–Norwegian Beamlines at the ESRF (Grenoble, France). The wavelength of the synchrotron radiation was set to $E = 17.71$ keV (0.6999 Å). The data were collected by way of three ϕ scans of 60 minutes each, with an angular step of 0.1° in a shutter-free mode with the PILATUS2M detector. The resulting 5400 frames were binned three times to give 1800 frames, and finally binned ten times to produce 180, 1.0 degree frames.

The raw data were processed with the *SNBL Toolbox*.⁵ The integrated intensities were extracted from the frames, scaled, and corrected for absorption with the *CrysAlisPro* software.⁶ The crystal structure was solved with *SHELXT*⁷ and refined with *SHELXL* version 2016/6.⁸

(SIMes)(η^6 -*p*-cymene)RuCl₂ (5**):** In an argon-filled glovebox, a solution of SIMes (153.8 mg, 0.502 mmol) in 4 ml of THF was very slowly (dropwise, 15 min) added to a suspension of [(*p*-cymene)RuCl₂]₂ (143.0 mg, 0.234 mmol) in 6 ml of *p*-cymene/THF (1:1). The reaction was followed with ¹H NMR. When complete conversion into the desired product was reached, most of the THF was removed from the reaction mixture *in vacuo*. Dark red-brown crystals of **5** were obtained from this solution at low temperature (−32 °C). After washing the crystals with *p*-cymene (2 × 0.5 ml) followed by *n*-pentane (2 × 0.5 ml) and drying *in vacuo* a light-brown powder of **5** (75.0 mg, 0.122 mmol, 26.0%) was obtained. ¹H NMR (600.17 MHz, C₆D₆): δ 6.77 (s, 4H), 4.87 (d, ³J_{HH} = 6.1 Hz, 2H), 4.39 (d, ³J_{HH} = 5.9 Hz, 2H), 3.20 (s, 4H), 2.52–2.44 (m, 13H), 2.13 (s, 6H), 1.72 (s, 3H), 1.06 (d, ³J_{HH} = 7.0 Hz, 6H). ¹³C{¹H} NMR (150.91 MHz, C₆D₆): δ 202.60, 140.15, 137.41, 136.86, 129.39, 102.00, 96.39, 87.24, 86.87, 52.64, 30.87, 22.93, 21.04, 19.65, 18.12. Anal. Calcd (%) for C₃₁H₄₀Cl₂N₂Ru·0.17C₁₀H₁₄(*p*-cymene): C 61.79 H 6.72 N 4.41 Found: C 63.40 H 6.57 N 4.14. Although the lack of stability of this compound gives results that are outside the range viewed as establishing analytical purity, they are provided to illustrate the best values obtained to date. HRMS (DART) found (calcd): m/z 576.19344 (576.19358) [C₃₁H₄₀ClN₂¹⁰¹Ru]⁺.

Procedure for catalytic testing: self-metathesis and isomerization of allylbenzene

Experiments in neat substrate. Under inert atmosphere (Ar), in a glove box, stock solutions of **5** (MW: 612.65) and **2** (MW: 626.62) were obtained by dissolving 1.4 mg of the compound in 5 g of toluene. Aliquots (0.9, 2.7, 4.6, 9.2 and 92.6 mg) of the stock solution were loaded into vials (4 ml), followed by the removal of the solvent *in vacuo* and addition of 50 mg of allylbenzene, to obtain catalyst loadings of 1, 3, 5, 10 and 100 ppm, respectively. After capping the vial, the reaction mixture was heated in an aluminum block placed on a standard laboratory heater and attached to a thermostat. A small stirring

magnet ensured continuous agitation. At timed intervals about 10 μL of reaction mixture was taken, transferred in an NMR tube, diluted up to 0.7 ml with CDCl_3 , and a ^1H NMR spectrum was recorded.

Conversions and yields were determined by comparing the integrals of the two terminal olefin protons (CH_2) peaks of the substrate with those of the olefinic protons of the individual products.⁹ Tests using hexamethylbenzene as internal standard have previously confirmed the reliability of this procedure.¹⁰ Some of the samples were also analyzed by gas chromatography. GC samples were prepared by either loading the previously mentioned NMR sample in a GC vial or by taking about 10 μL of reaction mixture. In both cases, the samples were diluted up to 1.5-2 ml with *n*-hexane and injected in the GC using the method described below. The area percentages obtained with samples containing metathesis products were corrected for the higher response of the FID for these products versus the response of the substrate and isomerization products. The effective carbon numbers (ECN) of the substrate and of the different products were calculated according to literature procedure, and used to determine the corrected area percentages.⁴ Standards of the starting material and of the products, either purchased from commercial sources (**6** and **10**) or prepared in our laboratory (**7-9** and **11-13**), were employed to determine the GC retention times as well as to assist the analysis of the ^1H NMR spectra. Conversions and yields obtained with the GC method were compared with those from ^1H NMR analysis, and the difference between the results was found to be within $\pm 2\%$.

Experiments in neat substrate in the presence of Hg(0). The procedure described above for experiments in neat substrate was followed, except for the fact that one drop of Hg(0) (ca. 200 mg) was added to the vial after the solvent had been removed *in vacuo* and before the addition of allylbenzene.

Experiments in solution. Under inert atmosphere (Ar) in a glove box, a stock solution of **5** was produced by dissolving 1.8 mg of **5** in 529.5 mg of DCM followed by further dilution up to 4.0 g with *n*-pentane. A stock solution of **2** in *n*-pentane/DCM (9:1) was obtained in a similar fashion. Following this, a stock solution of the substrate was produced by dissolving 52.2 mg allylbenzene in *n*-pentane to reach 4.0180 g in total. From both stock solutions (of catalyst and allylbenzene respectively), appropriate aliquots, depending on the desired substrate concentration and catalyst loading, were taken and transported into a vial (10 ml) containing the appropriate amount of *n*-pentane to reach a total volume of 4 ml. After capping the vial, the reaction mixture was placed on a standard laboratory stirrer with a stirring magnet ensured continuous agitation. At timed intervals, 0.5-1 ml of reaction mixture was transferred into a GC vial. The samples were injected in the GC without prior dilution using the method described below. The absence of metathesis products, and similar response factors of the substrate and isomerization products allows for direct use of peak area percentages. Standards of the starting material and of the products, either purchased from commercial sources (**6** and **10**) or prepared in our laboratory (**7-9** and **11-13**), were employed to determine the GC retention times.

The experiments in THF and toluene were performed according to the procedure described above using similar stock solutions of **5**, **2** and allylbenzene, in THF and toluene respectively. **General.** The catalytic performance of compounds such as **5** in ring-opening metathesis is known to improve significantly upon visible-light irradiation of the reaction vessel.¹¹ The effect of light on the present catalytic tests is expected to be very small, as the experiments were carried out inside a glovebox using glass vials that were shielded from direct light by the aluminum block in which they were placed.

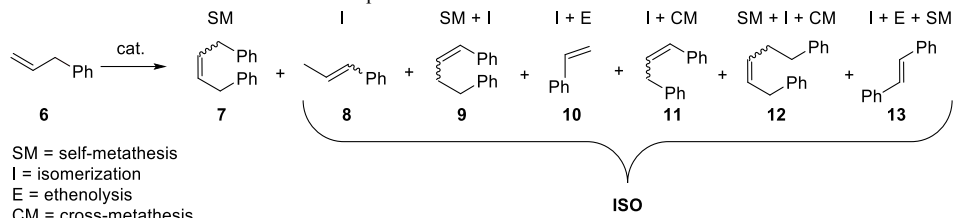
GC settings

Table S1: Configuration and settings of the GC.

Parameter	Setting
<i>Inlet port</i>	
T_{inj} (°C)	250
Type	split/constant flow
Split ratio	20:1
V_{inj} (μl)	0.1
Carrier gas	He
\bar{u} (cm/sec)	24.276
<i>Column</i>	
Type	DB-WAX
L (m) x d_c (μm) x d_f (μm)	30 × 200 × 0.2
<i>Oven program</i>	
T_0 (°C)	40
$t_{hold\ 0}$ (min)	0
$T_{ramp\ 1}$ (°C/min)	20
T_1 (°C)	230
$t_{hold\ 1}$ (min)	4
$T_{ramp\ 2}$ (°C/min)	-
T_2 (°C)	-
$t_{hold\ 2}$ (min)	-
<i>Detector</i>	
Type	FID
T_{inj} (°C)	300
V_{H_2} (ml/min)	30
V_{Air} (ml/min)	300
$V_{col+mkup}$ (ml/min)	40

SI-II

Detailed results of catalytic tests

Scheme S1: Metathesis and isomerization products identified in reaction mixtures.**Table S2:** Self-metathesis and isomerization of neat allylbenzene with **5** and **2** at high temperature.

entry	Cat.	Cat. load (ppm)	T (°C)	t (h)	Conv. ^a	7	8	9	10	11	ISO ^b (%)
1	5	1	80	1	0.7	-	0.7	-	-	-	100
				20	3.8	-	3.8	-	-	-	100
2	5	3	80	1	2.6	0.7	1.9	-	-	-	73
				4	5.5	0.8	4.7	-	-	-	85
				24	10.2	0.7	9.5	-	-	-	93
3	5	5	80	1	4.0	1.3	2.7	-	-	-	67
				4	8.6	1.5	7.1	-	-	-	83
				24	20.2	1.1	19.1	-	-	-	95
4	5	10	80	1	8.0	3.0	5.0	-	-	-	63
				4	17.4	3.6	13.8	-	-	-	79
				24	39.4	2.7	35.1	1.5	0.1	-	93
				162	48.5	3.0	43.0	1.2	0.1	0.2	94
5	5	10	100	1	12.2	3.1	9.1	-	-	-	75
				4	28.1	3.9	24.0	0.2	-	-	86
6	5	100	80	1	47.1	23.2	16.9	1.0	1.7	4.3	51
				4	9.7	7.6	2.1	-	-	-	22
7	2	1	80	1	9.7	7.6	2.1	-	-	-	22
				4	10.6	7.2	3.4	-	-	-	32
				4	97.5	71.0	11.6	12.3	0.3	2.3	27
8	2	10	80	1	82.6	76.0	3.4	1.4	0.3	1.5	8
				4	93.1	80.1	7.3	3.3	0.5	1.9	14
				4	97.5	71.0	11.6	12.3	0.3	2.3	27
9	-	-	80	4	0.0	-	-	-	-	-	
10 ^c	5	10	100	1	19.0	5.9	13.1	-	-	-	69
11 ^c	5 + Hg(0) ^d	10	100	1	33.0	5.4	27.4	-	0.2	-	84
12 ^c	5 ^e	10	100	1	28.4	4.1	24.2	-	0.1	-	86
13 ^c	5 ^e + Hg(0) ^d	10	100	1	13.2	3.5	9.7	-	-	-	74
14 ^c	5 ^f	10	100	1	39.5	1.0	38.3	-	0.2	-	97
15 ^c	Hg(0) ^d	-	100	1	0.0	-	-	-	-	-	-

^aDetermined by ¹H NMR analysis of the reaction mixture. ^bCombined yields of the primary (**8**) and secondary isomerization products (together labeled **ISO**) compared to total yields also including the self-metathesis product **7**, as determined by ¹H NMR and GC analysis. Compounds **12** and **13** were not observed. ^cAllylbenzene used in this experiment was purchased from Acros Organics (102890250, Lot A0361159) and purified according to the procedure described in the Experimental methods section. ^dReaction performed in the presence of ca. 200 mg of Hg(0). ^ePretreated by heating a solution of the catalyst in toluene at 100 °C for 1 h in absence of substrate and used after removal of the

solvent. ^JThe catalyst was preheated in toluene at 100 °C for 1 h in absence of substrate. Toluene was then removed by vacuum and *p*-cymene was added to the residual, and the resulting mixture was heated at 100 °C for 1 h. The residual, after removal of the solvent, was used as the catalyst.

Catalytic tests with thermally pretreated catalyst 5. The DFT-derived mechanism of Scheme 3 of the main paper predict that, in absence of alkene substrate, dissociation of *p*-cymene from **5** should lead to ruthenium hydrides such as **R27** and **R31**. To probe this hypothesis we have tested **5** before and after a thermal pretreatment in toluene (Table S2; compare entries 10 and 12). This heat treatment promotes exchange of the *p*-cymene ligand, as shown in ¹H NMR studies (see Figure S1) of the decomposition of **5** in anhydrous benzene-d₆.¹² Importantly, these ¹H NMR studies also revealed a weak signal (ca. 5% of the area of one proton of the initial complex) at -6.01 ppm after heating the solution for one hour at 80°C, consistent with a ruthenium hydride, see Figure S2. Ruthenium hydrides such as **R27** and **R31** are electronically and sterically unsaturated and are expected to decompose, for example *via* dimerization, to unknown species of lower energy. The assumption that the heat treatment results in decomposition is supported by the fact that the effects of the heating are not reversible. Instead, a second round of heat treatment in *p*-cymene (also this at 100°C for 1h) after the first one in toluene results in ever higher isomerization activity (compare entries 12 and 14).

Ruthenium nanoparticles have recently been shown to form during olefin metathesis and to be isomerization active.¹³ The isomerization activity of pretreated **5** is reduced in the presence of Hg(0) (compare entries 12 and 13), which strongly suggests that nanoparticles do indeed form during heat treatment of **5**. This hypothesis is also supported by the fact that the surface of the mercury changes from shiny to matt during the experiment. Interestingly, when Hg(0) is used as an additive to non-pretreated **5**, the catalytic activity almost doubled (entries 10 and 11). Hg(0) in absence of **5** is inert under identical conditions (cf. entries 11 and 15), and the gloss of the mercury surface was retained during the reaction. The effect of mercury on the catalytic performance of non-pretreated **5** is not understood. Mercury could perhaps promote the dissociation of the arene ligand, or favor the formation of one of the hydride species **R27** and **R31**. Alternatively, it could also participate as a cocatalyst in one of the two isomerization cycles depicted in Scheme 3 of the main paper. At any rate, this result confirms that nanoparticles play, if any, only a minor role in the catalytic isomerization reactions promoted by **5**. Summarizing, preheating **5** in absence of substrate leads to partial and irreversible decomposition. The decomposition products are dominated by nanoparticles, the isomerization activity of which can be reduced by Hg(0). ¹H NMR studies of the decomposition of **5** in anhydrous benzene-d₆ suggest that the decomposition initially leads to ruthenium hydrides. With decomposition reducing the amount of **5**, less alkylidene will be formed via dinuclear ruthenium alkene activation (Scheme 3). This explains the lower yields of the self-metathesis product **7** in the experiments including pretreatment.

Table S3: Self-metathesis and isomerization of neat allylbenzene with **5** and **2** at high substrate dilution and at room temperature (22 °C).

entry	Cat.	cat load (mol%)	solvent	[S] (mM)	t (h)	Conv (%) ^a	7	8	9	10	11	12	13	ISO ^{a,b} (%)
1	5	1	P/D ^c	20	1	96.4	-	96.4	-	-	-	-	-	100
					4	100.0	-	100.0	-	-	-	-	-	100
2	2	1	P/D ^c	20	1	52.2	47.1	0.3	-	1.0	2.4	-	1.3	13
					4	63.1	48.4	0.5	2.6	1.2	7.7	0.2	1.3	33
3	5	1	P/D ^c	10	1	94.0	-	94.0	-	-	-	-	-	100
					4	100.0	-	100.0	-	-	-	-	-	100
4	5	1	P/D ^c	5	1	81.4	-	81.4	-	-	-	-	-	100
					4	99.7	-	99.7	-	-	-	-	-	100
5	5	1	P/D ^c	0.25	1	49.3	-	49.3	-	-	-	-	-	100
					4	92.5	-	92.5	-	-	-	-	-	100
6	5	0.1	P/D ^c	0.25	1	3.1	-	3.1	-	-	-	-	-	100
					4	8.7	-	8.7	-	-	-	-	-	100
					26	24.7	-	24.7	-	-	-	-	-	100
7	5	1	THF	20	1	91	-	91	-	-	-	-	-	100
					4	98	-	98	-	-	-	-	-	100
8	2	1	THF	20	1	44.3	27.9	9.0	-	6.4	0.8	-	-	37
					4	83.2	30.1	31.1	-	19.5	2.3	-	-	64
9	5	1	C ₇ H ₈	20	1	50.7	39.5	1.1	-	3.8	6.3	-	-	22
					4	70.1	45.2	1.6	0.9	4.3	16.0	0.5	1.6	36
10	2	1	C ₇ H ₈	20	1	51.5	44.8	0.8	-	1.1	4.4	-	-	13
					4	75.4	56.6	0.5	2.7	1.9	11.7	0.3	1.7	25

^aDetermined by GC analysis of the reaction mixture using the effective carbon numbers (ECN) to estimate the response factors.⁴ ^bCombined yields of the primary (**8**) and secondary isomerization products (together labeled **ISO**) compared to total yields also including the self-metathesis product **7**. ^c*n*-Pentane/dichloromethane (9:1).

SI-II

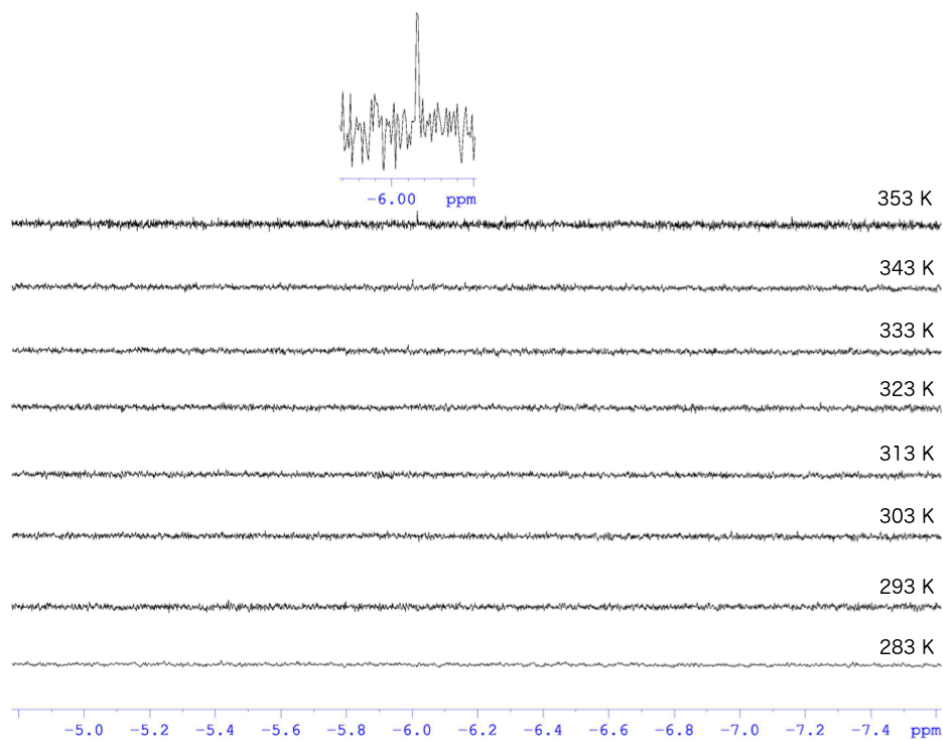
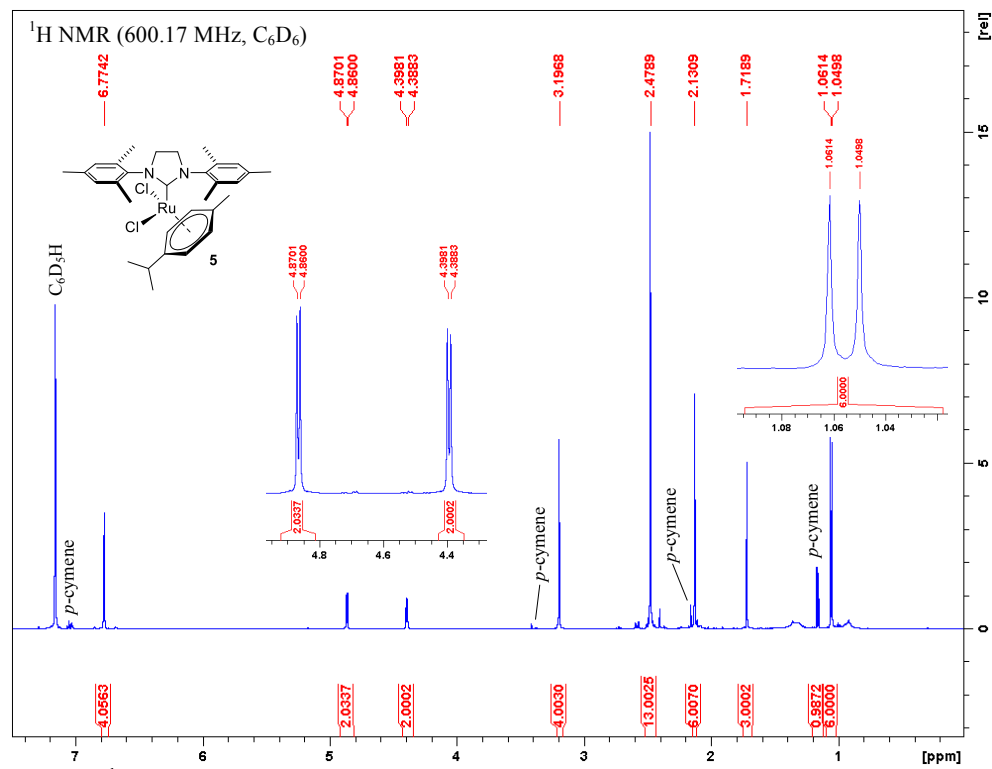


Figure S2: Stacked ^1H -spectra (from δ -4.8 to -7.6 ppm, 500.13 MHz, C_6D_6) of **5** showing formation of a hydride complex at increased temperature. Spectra non-shifted w.r.t. each other.

SI-II

Analytical data

Figure S3: ^1H NMR spectrum of **5** in C_6D_6 .

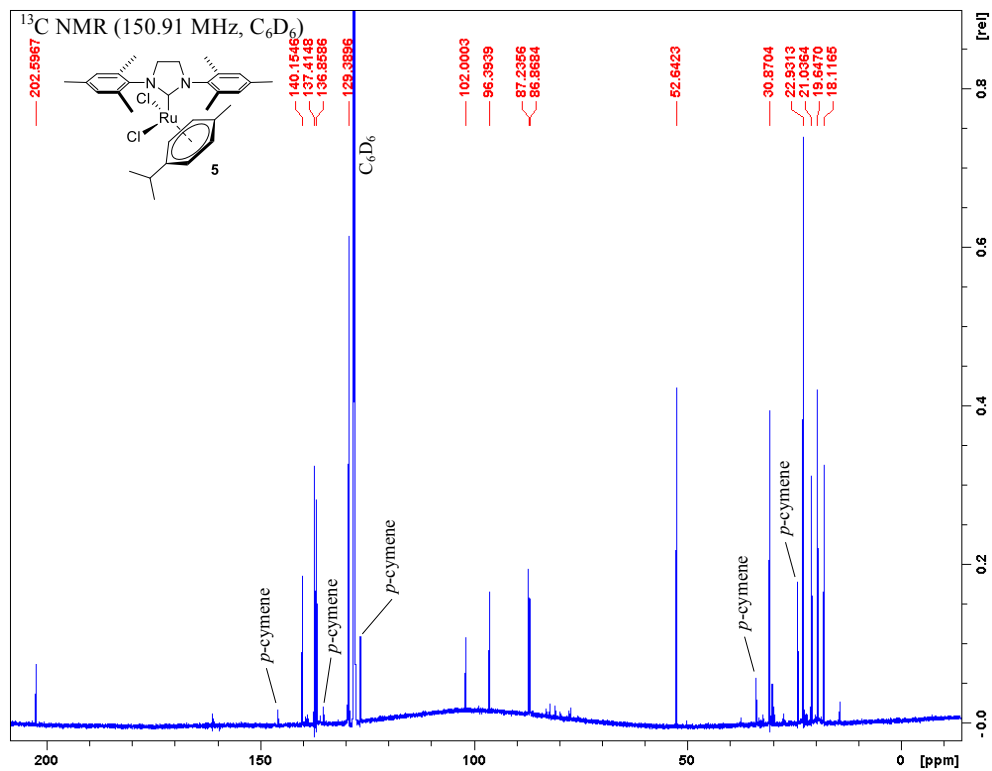


Figure S4: ¹³C NMR spectrum of **5** in C₆D₆.

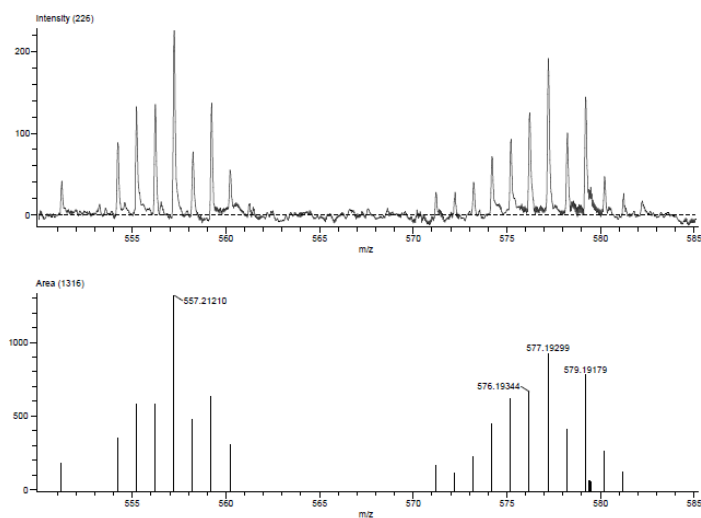


Figure S5: HRMS (DART) spectrum of **5**.

Crystallographic data

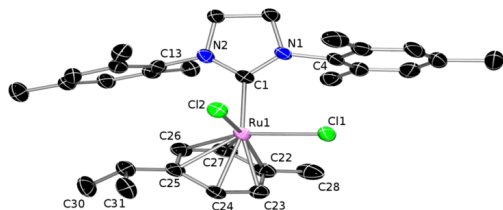


Figure S6: X-ray crystal structure of **5** with displacement ellipsoids drawn at 50% probability level. H-atoms are omitted for clarity. Selected geometrical parameters: Ru1-C1 = 2.113(4) Å, Ru1-Cl1 = 2.412(1) Å, Ru1-Cl2 = 2.405(1) Å, Ru1-C22 = 2.185(5) Å, Ru1-C23 = 2.204(4) Å, Ru1-C24 = 2.242(4) Å, Ru1-C25 = 2.233(4) Å, Ru1-C26 = 2.196(4) Å, Ru1-C27 = 2.164(4) Å, C1-Ru1-Cl1 = 92.5(1)°, C1-Ru1-Cl2 = 81.7(1)°, C1-Ru1-C22 = 117.3(2)°, C1-Ru1-C23 = 153.7(2)°, C1-Ru1-C24 = 163.6(1)°, C1-Ru1-C25 = 126.5(1)°, C1-Ru1-C26 = 100.1(1)°, C1-Ru1-C27 = 95.9(2)°, Cl1-Ru1-Cl2 = 86.25(4)°, N1-C1-N2 = 106.1(3), C1-N1-C4 = 132.6(3), C1-N2-C13 = 130.4(3).

The bond distances and angles are comparable to those of the IMes-coordinated analogue of **5**,¹⁴ although the Ru-C_{NHC} bond is slightly shorter in **5** (2.113 vs. 2.142 Å), probably reflecting the stronger back donation from ruthenium to the saturated NHC.¹⁵ The rotational conformation of the *p*-cymene ligand is also different, which is reflected, e.g., in the torsion Cl1-Ru1-C22-C28 being -35° in **5** and 101° in the IMes analogue.

Table S4: Crystal data and structure refinement for complex **5**.

Identification code	CBF	
Empirical formula	C ₃₁ H ₄₀ Cl ₂ N ₂ Ru	
Formula weight	612.62	
Temperature	103(2) K	
Wavelength	0.6999 Å	
Crystal system	Monoclinic	
Space group	P2 ₁ /n	
Unit cell dimensions	a = 8.76752(16) Å	$\alpha = 90^\circ$.
	b = 24.8251(4) Å	$\beta = 103.145(2)^\circ$.
	c = 13.7094(3) Å	$\gamma = 90^\circ$.
Volume	2905.72(10) Å ³	
Z	4	
Density (calculated)	1.400 Mg/m ³	
Absorption coefficient	0.706 mm ⁻¹	
F(000)	1272	

Crystal size	0.050 × 0.015 × 0.002 mm ³
Crystal colour/habit	Brown/Thin lath
Theta range for data collection	1.616 to 24.620°.
Index ranges	-10 ≤ h ≤ 10, -29 ≤ k ≤ 29, -16 ≤ l ≤ 16
Reflections collected	16821
Independent reflections	4808 [R(int) = 0.0500]
Completeness to theta = 24.620°	93.4 %
Absorption correction	Semi-empirical from equivalents
Max. and min. transmission	1.00000 and 0.77574
Refinement method	Full-matrix least-squares on F ²
Data / restraints / parameters	4808 / 0 / 334
Goodness-of-fit on F ²	1.027
Final R indices [I > 2σ(I)]	R1 = 0.0483, wR2 = 0.1233
R indices (all data)	R1 = 0.0596, wR2 = 0.1303
Extinction coefficient	n/a
Largest diff. peak and hole	2.100 and -0.525 e.Å ⁻³

Table S5: Bond lengths [Å] and angles [°] for complex **5**.

C(1)-N(1)	1.349(5)
C(1)-N(2)	1.353(5)
C(1)-Ru(1)	2.113(4)
N(1)-C(4)	1.440(5)
N(1)-C(3)	1.469(5)
Cl(1)-Ru(1)	2.4125(10)
Ru(1)-C(27)	2.165(4)
Ru(1)-C(22)	2.186(4)
Ru(1)-C(26)	2.196(4)
Ru(1)-C(23)	2.205(4)
Ru(1)-C(25)	2.233(4)
Ru(1)-C(24)	2.243(4)
Ru(1)-Cl(2)	2.4047(10)
C(2)-N(2)	1.484(5)
C(2)-C(3)	1.520(5)
C(2)-H(2A)	0.9900
C(2)-H(2B)	0.9900
N(2)-C(13)	1.430(5)
C(3)-H(3A)	0.9900
C(3)-H(3B)	0.9900
C(4)-C(9)	1.392(6)
C(4)-C(5)	1.402(6)
C(5)-C(6)	1.399(7)
C(5)-C(10)	1.485(7)
C(6)-C(7)	1.385(8)
C(6)-H(6)	0.9500
C(7)-C(8)	1.373(8)
C(7)-C(11)	1.525(7)
C(8)-C(9)	1.397(6)
C(8)-H(8)	0.9500
C(9)-C(12)	1.506(6)
C(10)-H(10A)	0.9800
C(10)-H(10B)	0.9800
C(10)-H(10C)	0.9800

C(11)-H(11A)	0.9800
C(11)-H(11B)	0.9800
C(11)-H(11C)	0.9800
C(12)-H(12A)	0.9800
C(12)-H(12B)	0.9800
C(12)-H(12C)	0.9800
C(13)-C(18)	1.401(6)
C(13)-C(14)	1.408(6)
C(14)-C(15)	1.403(6)
C(14)-C(19)	1.505(6)
C(15)-C(16)	1.385(6)
C(15)-H(15)	0.9500
C(16)-C(17)	1.380(7)
C(16)-C(20)	1.513(6)
C(17)-C(18)	1.393(6)
C(17)-H(17)	0.9500
C(18)-C(21)	1.499(6)
C(19)-H(19A)	0.9800
C(19)-H(19B)	0.9800
C(19)-H(19C)	0.9800
C(20)-H(20A)	0.9800
C(20)-H(20B)	0.9800
C(20)-H(20C)	0.9800
C(21)-H(21A)	0.9800
C(21)-H(21B)	0.9800
C(21)-H(21C)	0.9800
C(22)-C(27)	1.401(6)
C(22)-C(23)	1.408(6)
C(22)-C(28)	1.497(6)
C(23)-C(24)	1.387(6)
C(23)-H(23)	0.9500
C(24)-C(25)	1.423(6)
C(24)-H(24)	0.9500
C(25)-C(26)	1.406(6)
C(25)-C(29)	1.514(6)
C(26)-C(27)	1.415(6)

C(26)-H(26)	0.9500
C(27)-H(27)	0.9500
C(28)-H(28A)	0.9800
C(28)-H(28B)	0.9800
C(28)-H(28C)	0.9800
C(29)-C(31)	1.521(6)
C(29)-C(30)	1.525(6)
C(29)-H(29)	1.0000
C(30)-H(30A)	0.9800
C(30)-H(30B)	0.9800
C(30)-H(30C)	0.9800
C(31)-H(31A)	0.9800
C(31)-H(31B)	0.9800
C(31)-H(31C)	0.9800
N(1)-C(1)-N(2)	106.1(3)
N(1)-C(1)-Ru(1)	128.3(3)
N(2)-C(1)-Ru(1)	125.1(3)
C(1)-N(1)-C(4)	132.6(3)
C(1)-N(1)-C(3)	114.1(3)
C(4)-N(1)-C(3)	112.0(3)
C(1)-Ru(1)-C(27)	95.86(15)
C(1)-Ru(1)-C(22)	117.28(14)
C(27)-Ru(1)-C(22)	37.56(17)
C(1)-Ru(1)-C(26)	100.15(15)
C(27)-Ru(1)-C(26)	37.86(17)
C(22)-Ru(1)-C(26)	68.09(17)
C(1)-Ru(1)-C(23)	153.66(15)
C(27)-Ru(1)-C(23)	66.51(16)
C(22)-Ru(1)-C(23)	37.41(15)
C(26)-Ru(1)-C(23)	78.22(16)
C(1)-Ru(1)-C(25)	126.54(15)
C(27)-Ru(1)-C(25)	67.87(16)
C(22)-Ru(1)-C(25)	80.85(16)
C(26)-Ru(1)-C(25)	37.01(16)
C(23)-Ru(1)-C(25)	66.64(15)
C(1)-Ru(1)-C(24)	163.59(15)

SI-II

C(27)-Ru(1)-C(24)	78.71(15)
C(22)-Ru(1)-C(24)	67.23(15)
C(26)-Ru(1)-C(24)	66.06(15)
C(23)-Ru(1)-C(24)	36.33(15)
C(25)-Ru(1)-C(24)	37.08(15)
C(1)-Ru(1)-Cl(2)	81.75(10)
C(27)-Ru(1)-Cl(2)	151.46(13)
C(22)-Ru(1)-Cl(2)	160.63(11)
C(26)-Ru(1)-Cl(2)	114.27(12)
C(23)-Ru(1)-Cl(2)	123.23(11)
C(25)-Ru(1)-Cl(2)	90.63(11)
C(24)-Ru(1)-Cl(2)	95.58(10)
C(1)-Ru(1)-Cl(1)	92.52(10)
C(27)-Ru(1)-Cl(1)	122.30(13)
C(22)-Ru(1)-Cl(1)	89.16(13)
C(26)-Ru(1)-Cl(1)	157.10(12)
C(23)-Ru(1)-Cl(1)	81.97(11)
C(25)-Ru(1)-Cl(1)	139.94(11)
C(24)-Ru(1)-Cl(1)	103.50(10)
Cl(2)-Ru(1)-Cl(1)	86.24(4)
N(2)-C(2)-C(3)	101.4(3)
N(2)-C(2)-H(2A)	111.5
C(3)-C(2)-H(2A)	111.5
N(2)-C(2)-H(2B)	111.5
C(3)-C(2)-H(2B)	111.5
H(2A)-C(2)-H(2B)	109.3
C(1)-N(2)-C(13)	130.3(3)
C(1)-N(2)-C(2)	114.7(3)
C(13)-N(2)-C(2)	114.7(3)
N(1)-C(3)-C(2)	103.4(3)
N(1)-C(3)-H(3A)	111.1
C(2)-C(3)-H(3A)	111.1
N(1)-C(3)-H(3B)	111.1
C(2)-C(3)-H(3B)	111.1
H(3A)-C(3)-H(3B)	109.0
C(9)-C(4)-C(5)	122.3(4)

C(9)-C(4)-N(1)	119.3(4)
C(5)-C(4)-N(1)	117.8(4)
C(6)-C(5)-C(4)	116.7(5)
C(6)-C(5)-C(10)	121.7(4)
C(4)-C(5)-C(10)	121.5(4)
C(7)-C(6)-C(5)	122.4(5)
C(7)-C(6)-H(6)	118.8
C(5)-C(6)-H(6)	118.8
C(8)-C(7)-C(6)	118.9(4)
C(8)-C(7)-C(11)	121.6(6)
C(6)-C(7)-C(11)	119.5(5)
C(7)-C(8)-C(9)	121.6(5)
C(7)-C(8)-H(8)	119.2
C(9)-C(8)-H(8)	119.2
C(4)-C(9)-C(8)	118.1(4)
C(4)-C(9)-C(12)	121.0(4)
C(8)-C(9)-C(12)	121.0(4)
C(5)-C(10)-H(10A)	109.5
C(5)-C(10)-H(10B)	109.5
H(10A)-C(10)-H(10B)	109.5
C(5)-C(10)-H(10C)	109.5
H(10A)-C(10)-H(10C)	109.5
H(10B)-C(10)-H(10C)	109.5
C(7)-C(11)-H(11A)	109.5
C(7)-C(11)-H(11B)	109.5
H(11A)-C(11)-H(11B)	109.5
C(7)-C(11)-H(11C)	109.5
H(11A)-C(11)-H(11C)	109.5
H(11B)-C(11)-H(11C)	109.5
C(9)-C(12)-H(12A)	109.5
C(9)-C(12)-H(12B)	109.5
H(12A)-C(12)-H(12B)	109.5
C(9)-C(12)-H(12C)	109.5
H(12A)-C(12)-H(12C)	109.5
H(12B)-C(12)-H(12C)	109.5
C(18)-C(13)-C(14)	121.2(4)

C(18)-C(13)-N(2)	120.6(4)
C(14)-C(13)-N(2)	117.8(4)
C(15)-C(14)-C(13)	118.0(4)
C(15)-C(14)-C(19)	119.6(4)
C(13)-C(14)-C(19)	122.3(4)
C(16)-C(15)-C(14)	121.7(4)
C(16)-C(15)-H(15)	119.1
C(14)-C(15)-H(15)	119.1
C(17)-C(16)-C(15)	118.3(4)
C(17)-C(16)-C(20)	121.0(4)
C(15)-C(16)-C(20)	120.7(4)
C(16)-C(17)-C(18)	123.0(4)
C(16)-C(17)-H(17)	118.5
C(18)-C(17)-H(17)	118.5
C(17)-C(18)-C(13)	117.4(4)
C(17)-C(18)-C(21)	120.0(4)
C(13)-C(18)-C(21)	122.4(4)
C(14)-C(19)-H(19A)	109.5
C(14)-C(19)-H(19B)	109.5
H(19A)-C(19)-H(19B)	109.5
C(14)-C(19)-H(19C)	109.5
H(19A)-C(19)-H(19C)	109.5
H(19B)-C(19)-H(19C)	109.5
C(16)-C(20)-H(20A)	109.5
C(16)-C(20)-H(20B)	109.5
H(20A)-C(20)-H(20B)	109.5
C(16)-C(20)-H(20C)	109.5
H(20A)-C(20)-H(20C)	109.5
H(20B)-C(20)-H(20C)	109.5
C(18)-C(21)-H(21A)	109.5
C(18)-C(21)-H(21B)	109.5
H(21A)-C(21)-H(21B)	109.5
C(18)-C(21)-H(21C)	109.5
H(21A)-C(21)-H(21C)	109.5
H(21B)-C(21)-H(21C)	109.5
C(27)-C(22)-C(23)	117.1(4)

C(27)-C(22)-C(28)	123.4(4)
C(23)-C(22)-C(28)	119.5(4)
C(27)-C(22)-Ru(1)	70.4(2)
C(23)-C(22)-Ru(1)	72.0(2)
C(28)-C(22)-Ru(1)	129.5(3)
C(24)-C(23)-C(22)	122.6(4)
C(24)-C(23)-Ru(1)	73.3(2)
C(22)-C(23)-Ru(1)	70.6(2)
C(24)-C(23)-H(23)	118.7
C(22)-C(23)-H(23)	118.7
Ru(1)-C(23)-H(23)	130.2
C(23)-C(24)-C(25)	120.3(4)
C(23)-C(24)-Ru(1)	70.3(2)
C(25)-C(24)-Ru(1)	71.1(2)
C(23)-C(24)-H(24)	119.8
C(25)-C(24)-H(24)	119.8
Ru(1)-C(24)-H(24)	131.6
C(26)-C(25)-C(24)	117.6(4)
C(26)-C(25)-C(29)	120.0(4)
C(24)-C(25)-C(29)	122.4(4)
C(26)-C(25)-Ru(1)	70.0(2)
C(24)-C(25)-Ru(1)	71.8(2)
C(29)-C(25)-Ru(1)	131.0(3)
C(25)-C(26)-C(27)	121.1(4)
C(25)-C(26)-Ru(1)	72.9(2)
C(27)-C(26)-Ru(1)	69.9(2)
C(25)-C(26)-H(26)	119.5
C(27)-C(26)-H(26)	119.5
Ru(1)-C(26)-H(26)	130.4
C(22)-C(27)-C(26)	121.2(4)
C(22)-C(27)-Ru(1)	72.0(2)
C(26)-C(27)-Ru(1)	72.3(2)
C(22)-C(27)-H(27)	119.4
C(26)-C(27)-H(27)	119.4
Ru(1)-C(27)-H(27)	128.6
C(22)-C(28)-H(28A)	109.5

C(22)-C(28)-H(28B)	109.5
H(28A)-C(28)-H(28B)	109.5
C(22)-C(28)-H(28C)	109.5
H(28A)-C(28)-H(28C)	109.5
H(28B)-C(28)-H(28C)	109.5
C(25)-C(29)-C(31)	113.4(4)
C(25)-C(29)-C(30)	108.9(4)
C(31)-C(29)-C(30)	110.6(4)
C(25)-C(29)-H(29)	107.9
C(31)-C(29)-H(29)	107.9
C(30)-C(29)-H(29)	107.9
C(29)-C(30)-H(30A)	109.5
C(29)-C(30)-H(30B)	109.5
H(30A)-C(30)-H(30B)	109.5
C(29)-C(30)-H(30C)	109.5
H(30A)-C(30)-H(30C)	109.5
H(30B)-C(30)-H(30C)	109.5
C(29)-C(31)-H(31A)	109.5
C(29)-C(31)-H(31B)	109.5
H(31A)-C(31)-H(31B)	109.5
C(29)-C(31)-H(31C)	109.5
H(31A)-C(31)-H(31C)	109.5
H(31B)-C(31)-H(31C)	109.5

Table S6: Torsion angles [°] for complex 5.

N(2)-C(1)-N(1)-C(4)	-167.9(4)
Ru(1)-C(1)-N(1)-C(4)	20.0(6)
N(2)-C(1)-N(1)-C(3)	-2.2(4)
Ru(1)-C(1)-N(1)-C(3)	-174.4(3)
N(1)-C(1)-N(2)-C(13)	170.9(4)
Ru(1)-C(1)-N(2)-C(13)	-16.6(6)
N(1)-C(1)-N(2)-C(2)	-1.9(4)
Ru(1)-C(1)-N(2)-C(2)	170.6(3)
C(3)-C(2)-N(2)-C(1)	4.9(4)
C(3)-C(2)-N(2)-C(13)	-169.1(3)
C(1)-N(1)-C(3)-C(2)	5.2(4)
C(4)-N(1)-C(3)-C(2)	173.8(3)
N(2)-C(2)-C(3)-N(1)	-5.5(4)
C(1)-N(1)-C(4)-C(9)	76.1(5)
C(3)-N(1)-C(4)-C(9)	-89.8(4)
C(1)-N(1)-C(4)-C(5)	-113.1(5)
C(3)-N(1)-C(4)-C(5)	81.0(4)
C(9)-C(4)-C(5)-C(6)	-0.4(6)
N(1)-C(4)-C(5)-C(6)	-171.0(4)
C(9)-C(4)-C(5)-C(10)	-176.9(4)
N(1)-C(4)-C(5)-C(10)	12.5(6)
C(4)-C(5)-C(6)-C(7)	0.3(7)
C(10)-C(5)-C(6)-C(7)	176.7(4)
C(5)-C(6)-C(7)-C(8)	-1.4(7)
C(5)-C(6)-C(7)-C(11)	-179.8(4)
C(6)-C(7)-C(8)-C(9)	2.7(7)
C(11)-C(7)-C(8)-C(9)	-178.9(4)
C(5)-C(4)-C(9)-C(8)	1.7(6)
N(1)-C(4)-C(9)-C(8)	172.1(4)
C(5)-C(4)-C(9)-C(12)	-179.5(4)
N(1)-C(4)-C(9)-C(12)	-9.1(6)
C(7)-C(8)-C(9)-C(4)	-2.8(6)
C(7)-C(8)-C(9)-C(12)	178.3(4)
C(1)-N(2)-C(13)-C(18)	99.4(5)

C(2)-N(2)-C(13)-C(18)	-87.8(5)
C(1)-N(2)-C(13)-C(14)	-88.6(5)
C(2)-N(2)-C(13)-C(14)	84.2(4)
C(18)-C(13)-C(14)-C(15)	-6.1(6)
N(2)-C(13)-C(14)-C(15)	-178.1(3)
C(18)-C(13)-C(14)-C(19)	173.0(4)
N(2)-C(13)-C(14)-C(19)	0.9(6)
C(13)-C(14)-C(15)-C(16)	2.0(6)
C(19)-C(14)-C(15)-C(16)	-177.1(4)
C(14)-C(15)-C(16)-C(17)	1.3(6)
C(14)-C(15)-C(16)-C(20)	178.4(4)
C(15)-C(16)-C(17)-C(18)	-0.5(6)
C(20)-C(16)-C(17)-C(18)	-177.7(4)
C(16)-C(17)-C(18)-C(13)	-3.4(6)
C(16)-C(17)-C(18)-C(21)	171.6(4)
C(14)-C(13)-C(18)-C(17)	6.8(6)
N(2)-C(13)-C(18)-C(17)	178.6(4)
C(14)-C(13)-C(18)-C(21)	-168.1(4)
N(2)-C(13)-C(18)-C(21)	3.7(6)
C(27)-C(22)-C(23)-C(24)	-1.7(6)
C(28)-C(22)-C(23)-C(24)	179.8(4)
Ru(1)-C(22)-C(23)-C(24)	54.0(4)
C(27)-C(22)-C(23)-Ru(1)	-55.8(3)
C(28)-C(22)-C(23)-Ru(1)	125.7(4)
C(22)-C(23)-C(24)-C(25)	-0.3(6)
Ru(1)-C(23)-C(24)-C(25)	52.6(3)
C(22)-C(23)-C(24)-Ru(1)	-52.8(4)
C(23)-C(24)-C(25)-C(26)	2.6(6)
Ru(1)-C(24)-C(25)-C(26)	54.8(3)
C(23)-C(24)-C(25)-C(29)	-179.8(4)
Ru(1)-C(24)-C(25)-C(29)	-127.6(4)
C(23)-C(24)-C(25)-Ru(1)	-52.2(3)
C(24)-C(25)-C(26)-C(27)	-2.9(6)
C(29)-C(25)-C(26)-C(27)	179.4(4)
Ru(1)-C(25)-C(26)-C(27)	52.8(3)
C(24)-C(25)-C(26)-Ru(1)	-55.7(3)

C(29)-C(25)-C(26)-Ru(1)	126.6(3)
C(23)-C(22)-C(27)-C(26)	1.4(6)
C(28)-C(22)-C(27)-C(26)	179.8(4)
Ru(1)-C(22)-C(27)-C(26)	-55.2(4)
C(23)-C(22)-C(27)-Ru(1)	56.6(3)
C(28)-C(22)-C(27)-Ru(1)	-125.0(4)
C(25)-C(26)-C(27)-C(22)	0.9(6)
Ru(1)-C(26)-C(27)-C(22)	55.1(4)
C(25)-C(26)-C(27)-Ru(1)	-54.2(3)
C(26)-C(25)-C(29)-C(31)	-171.1(4)
C(24)-C(25)-C(29)-C(31)	11.3(5)
Ru(1)-C(25)-C(29)-C(31)	-82.3(5)
C(26)-C(25)-C(29)-C(30)	65.2(5)
C(24)-C(25)-C(29)-C(30)	-112.3(4)
Ru(1)-C(25)-C(29)-C(30)	154.1(3)

SI-II

Computational part

Computational methods

Geometry optimizations.

All DFT calculations were performed with the Gaussian 09 suite of programs.¹⁶ All molecular geometries were optimized using Head-Gordon's long-range- and dispersion-corrected hybrid density functional ω B97XD¹⁷ as implemented in Gaussian 09. This functional has been found to provide geometries of ruthenium-based olefin metathesis catalysts and other homogeneous catalysts in excellent agreement with those of X-ray diffraction.¹⁸ The "ultrafine" grid, a pruned grid consisting of 99 radial shells and 590 angular points per shell, was chosen for numerical integrations. Use of the internal option IOp=(1/7=67) tightened the maximum force of the geometry optimization convergence criteria from $4.50 \cdot 10^{-4}$ a.u. to $1.01 \cdot 10^{-4}$ a.u. along with the accordingly scaled maximum displacement. Dunning's correlation-consistent valence double- ζ plus polarization basis sets,¹⁹ retrieved (as cc-pVDZ) from the EMSL basis set exchange database,²⁰ were used for all elements except ruthenium, for which the Stuttgart 28-electron relativistic effective core potential (ECP28MDF)²¹ was used in combination with the accompanying correlation-consistent valence double- ζ plus polarization (EMSL: cc-pVDZ-PP)²⁰ basis set.²¹ All stationary points were characterized by the eigenvalues of the analytically calculated Hessian matrix. Finally, the minima and transition states along the favored catalyst decomposition and isomerization pathways were connected by intrinsic reaction coordinate (IRC),²² calculations. For each thus connected elementary step, the energy as a function of the path length is shown below.

Single-point energy calculations.

Single-point (SP) calculations were performed with the generalized gradient approximation (GGA) functional of Perdew, Burke and Ernzerhof (PBE) as implemented in Gaussian 09.²³ Grimme's empirical dispersion corrections with Becke-Johnson damping (D3BJ) were added to the PBE SP energies.²⁴ The PBE-D3BJ functional was chosen due to the excellent performance of the counterpoise-corrected PBE-D3BJ functional in reproducing experimental gas-phase relative energies of ruthenium-mediated olefin metathesis.²⁵ The present large SP basis sets (see below) should result in only negligibly basis set superposition errors (BSSEs), and the PBE-D3BJ energies were thus used without counterpoise corrections. In addition, to check how sensitive the calculated relative free energies are to modification of the density functional, SP calculations were performed also with the hybrid meta-GGA functional.²⁶ Of particular relevance for the present work is the fact that M06 has been parameterized to handle intermediate-range correlation, transition-metal chemistry, and transition states, and has been shown to perform excellently for ruthenium-based olefin metathesis-related chemistry.²⁷ The total energies derived from M06 are given in Table S8.

Numerical integrations were performed with the "ultrafine" grid of Gaussian 09 and the self-consistent field (SCF) density-based convergence criterion was set to 10^{-5} . Ruthenium was described by the ECP28MDF relativistic effective core potential²¹ accompanied by a correlation-consistent valence quadruple- ζ plus polarization basis set of cc-pVQZ-PP quality (primitive (14s11p10d3f2g1h), contracted [6s6p5d3f2g1h]);²¹ see below for sample Gaussian 09 input files. Carbon and hydrogen atoms were described by valence quadruple- ζ plus polarization (EMSL: cc-pVQZ)²⁰ basis sets.¹⁹ For all other atoms the valence quadruple- ζ plus polarization (cc-pVQZ) basis sets were augmented by accompanying diffuse functions^{19,28} (EMSL: aug-cc-pVQZ Diffuse).²⁰

Electrostatic and non-electrostatic solvation effects were taken into account by using the polarizable continuum model (PCM) in combination with the “Dis”, “Rep”, and “Cav” keywords and the built-in program values (dielectric constant, number density, etc.) for tetrahydrofuran.^{29,30} The solute cavity was constructed using the united atom topological model with atomic radii optimized for Hartree–Fock (termed “UAHF”)^{30,31} Gibbs free energies were calculated for a temperature of 298.15 K and a standard state corresponding to 1 M solution (but exhibiting infinite-dilution, ideal-gas-like behavior), which means that a standard-state correction $\Delta G_{\text{latm} \rightarrow 1\text{M}}^{\text{T}=298.15\text{K}} = 1.89 \text{ kcal mol}^{-1}$ ($= RT \cdot \ln(24.46)$) was added to the calculated free energy of each molecule to account for the standard-state change from 1 atm to 1 M.²⁵ Therefore, the following expressions were used to calculate the Gibbs free energies.

$$G_{\text{PBE-D3BJ}}^{\text{THF}} = E_{\text{PBE-D3BJ}}^{\text{THF}} + \Delta G_{\text{B97XD}}^{\text{T}=298.15\text{K}} + \Delta G_{\text{latm} \rightarrow 1\text{M}}^{\text{T}=298.15\text{K}} \quad \text{Equation 1}$$

$$G_{\text{M06}}^{\text{THF}} = E_{\text{M06}}^{\text{THF}} + \Delta G_{\text{B97XD}}^{\text{T}=298.15\text{K}} + \Delta G_{\text{latm} \rightarrow 1\text{M}}^{\text{T}=298.15\text{K}} \quad \text{Equation 2}$$

where $E_{\text{PBE-D3BJ}}^{\text{THF}}$ and $E_{\text{M06}}^{\text{THF}}$ are the potential energies resulting from single point calculations with PBE-D3BJ and M06 functionals, respectively, including the contributions from the implicit solvation model, $\Delta G_{\text{B97XD}}^{\text{T}=298.15\text{K}}$ is the thermal correction to the Gibbs free energy calculated at the geometry optimization level, and $\Delta G_{\text{latm} \rightarrow 1\text{M}}^{\text{T}=298.15\text{K}}$ is the standard state correction.

Minimum energy crossing points and the probability of spin crossing.

Minimum energy crossing points (MECPs) between spin singlet and triplet states were located using the program of Harvey et al. (version: November-2009)³² in conjunction with Gaussian 09.¹⁶ The functional, basis sets, and integration grid were as described above for regular geometry optimizations. MECPs were optimized to a maximum electronic energy gradient below $1.0 \cdot 10^{-4}$ a.u., similar to that of regular stationary points, and with the difference in energy between spin states below 0.00050 a.u.. All the thus optimized geometries were confirmed to be minima (and thus MECPs) on the seam of crossing, as determined from the all-positive eigenvalues of the state-averaged Hessian matrix³³ calculated using the Glowfreq program,³⁴ version November-2015. Whereas the enthalpic cost of spin inversion is associated with reaching the seam of intersection between the two spin surfaces and is represented by the MECP, the probability that the system will cross from one potential energy surface to the other can be thought of as contributing to the activation entropy of the spin-forbidden reaction. Since the spin-crossing probability is lower than unity, the effective activation free energy resulting from adding such an entropic contribution will be higher than for an analogous spin-allowed reaction.³⁵ In the present work, following the approach described by Holthausen, Schneider and co-workers,³⁶ a spin-crossing-related addition of 1-5 kcal mol⁻¹ has been used (ΔG_{pXover}), while the regular thermochemical contributions to give free energies of the MECPs have been obtained as averages for the two spin states of the minimum close to the crossing point. To summarize, the effective free energy range for MECP X is calculated as:

$$G(\mathbf{X})_{\text{PBE-D3BJ}}^{\text{THF}} = E(\mathbf{X})_{\text{PBE-D3BJ}}^{\text{THF}} + \Delta G(\mathbf{X})_{\text{B97XD}}^{\text{T}=298.15\text{K}} + \Delta G(\mathbf{X})_{\text{latm} \rightarrow 1\text{M}}^{\text{T}=298.15\text{K}} + \Delta G_{\text{pXover}} \quad \text{Equation 3}$$

where:

$$E(\mathbf{X})_{\text{PBE-D3BJ}}^{\text{THF}} = \frac{E(\mathbf{X}, S=0)_{\text{PBE-D3BJ}}^{\text{THF}} + E(\mathbf{X}, S=1)_{\text{PBE-D3BJ}}^{\text{THF}}}{2} \quad \text{Equation 4}$$

$$\Delta G(\mathbf{X})_{\omega\text{B97XD}}^{\text{T}=298.15\text{K}} = \frac{\Delta G(\mathbf{X}, S = 0)_{\omega\text{B97XD}}^{\text{T}=298.15\text{K}} + \Delta G(\mathbf{X}, S = 1)_{\omega\text{B97XD}}^{\text{T}=298.15\text{K}}}{2} \quad \text{Equation 5}$$

and ΔG_{pXover} is 1 and 5 kcal mol⁻¹ respectively for the lower and upper end of the effective free energy range.

Association and dissociation of olefins and arenes.

Whereas a DFT study of Hoveyda-Grubbs-type catalysts (**2** and analogues thereof) found decoordination of the olefinic Hoveyda ligand formed by cross-metathesis with a sterically demanding alkene substrate to give the highest-lying transition state of the catalyst initiation,³⁷ smaller alkylidenes allow much faster binding and dissociation of alkenes and other neutral ligands. For example, a DFT study of ethyl vinyl ether (EVE) coordination to a series of 14-electron ruthenium benzylidene complexes found, in all cases, smaller barriers to EVE binding than to both cycloaddition and binding of tricyclohexylphosphine to reform the 16-electron precursor.²⁵ The present alkene binding and dissociation reactions involve Ru complexes of smaller (methylidene) or no alkylidene and can be expected to require less structural rearrangement than those of (substituted) benzylidene complexes. To illustrate, even dissociation of *p*-cymene from **5** was here found, after extensive scans of the potential energy surface (PES), to occur without a potential energy barrier.

Even if some of the present bimolecular addition and dissociation reactions do not have barriers on the PES above those defined by complete separation of the two molecules, the corresponding free energy surfaces have maxima corresponding to variational transition states. Some of these, such as the dissociation of methyl styrene from ³**R25** to give ³**R21**, are of too low energy to influence the kinetics, and their energies have not been given in the schemes. The free energy of other variational transition states have been estimated by reversing the Eyring equation,³⁸ using a rate constant estimated for the addition reactions. These reactions, which do not have potential energy barriers, should proceed close to the diffusion limit, corresponding to a rate constant of ca. 4·10⁹ M⁻¹ s⁻¹ in most common solvents.³⁹ The corresponding estimate for the Eyring-derived free energy barrier of these addition reactions is thus 4.4 kcal mol⁻¹. This procedure has been followed for elementary steps (labeled **TSVAR**) where diffusion-limited association/dissociation is expected to influence the kinetics.

In general, dissociation of internal alkenes has been assumed to follow a dissociative mechanism, an example being the product release from ³**R25** after the rate-determining spin inversion from the **R25** in the allylic isomerization cycle. The main alternative, associative product release *via* allylbenzene binding to **R25**, seems unlikely judged from the fact that the bis-allylbenzene complex **R32** is 13.9 kcal mol⁻¹ less stable than the mono-allylbenzene **R22**.

Calculation of kinetic parameters.

Turnover frequencies (TOF), degrees of TOF control (X_{TOF}), and turnover numbers (TON) were estimated according to the energetic span model^{40,41} using the AUTOF program.^{40,42} Whereas the Fortran version was used for the calculation of TOF and X_{TOF} , the Excel version (kindly provided by the author) was used for the calculation of TONs. If not otherwise specified, the values of TOFs and degrees of TOF control refer to zero conversion values calculated at 298.15 K with an initial substrate concentration of 7.5 M, which corresponds to almost neat substrate.

Calculation of thermochemical corrections for **R21**.

The analytical calculation of the Hessian matrix for **R21**, performed as described above, results in a negative eigenvalue corresponding to an imaginary frequency, $i20$ cm⁻¹. This suggests that **R21** is a

transition state. However, single point energy evaluations along the corresponding mode, which was performed by single-step IRC calculations in both directions with variable step lengths, could not identify any point with lower energy than the stationary point, thus demonstrating that this is indeed a minimum (Figure S7).

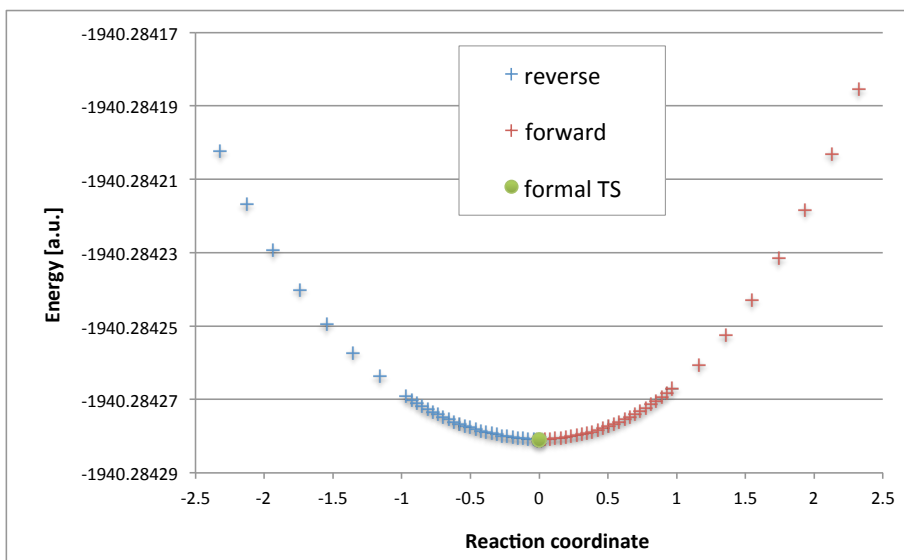


Figure S7: Energy profile generated by taking a single step of varying length in both forward and backward directions along the intrinsic reaction coordinate corresponding to the imaginary mode obtained from analytical calculation of the Hessian matrix of **R21**.

The alleged imaginary frequency resulting from the analytical calculation of the Hessian is an artifact due to the reduced-quality integration grid used in the analytical calculation of second derivatives (i.e., “SG1” rather than the “ultrafine” integration grid used for energy and gradient calculations).⁴³ The thermochemical corrections for **R21** were thus based on a numerically obtained Hessian matrix. The values corresponding to the inflexion point in the plot of this quantity against the numerical differentiation step ($N = 75$ in Figure S8) were used to calculate the free energy of **R21**. Such plots (i.e., thermochemical correction vs. numerical differentiation step length) obtained for five other complexes of this work (Figure S9 to Figure S13), show that the analytically calculated corrections are usually smaller (i.e., more stabilizing) than the inflexion points. Therefore, the choice made for **R21** is a rather conservative one: it avoids over-stabilization of this species while preventing the exceedingly high value (i.e., de-stabilization) of the thermochemical correction that would result from the inaccurate analytical Hessian (Figure S8).

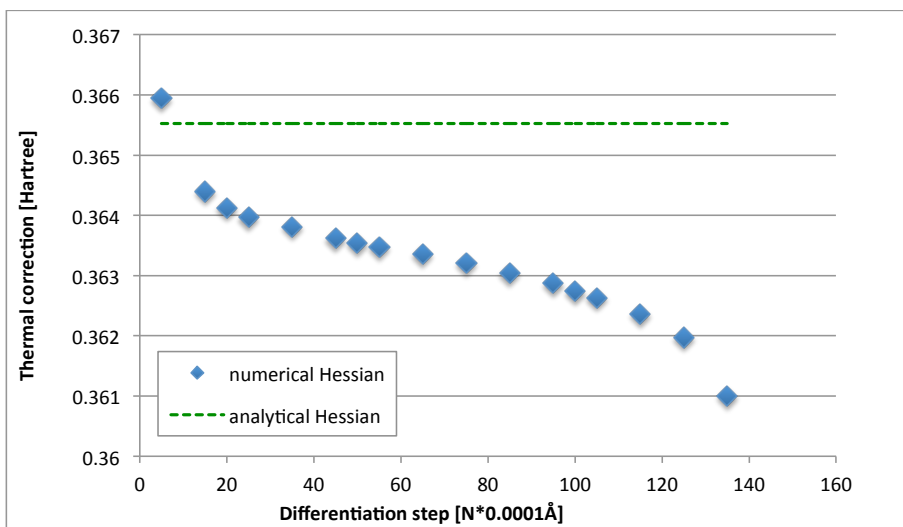


Figure S8: Thermochemical correction to the Gibbs free energy calculated for **R21** with the analytical Hessian, and with numerical Hessian obtained varying the numerical differentiation step.

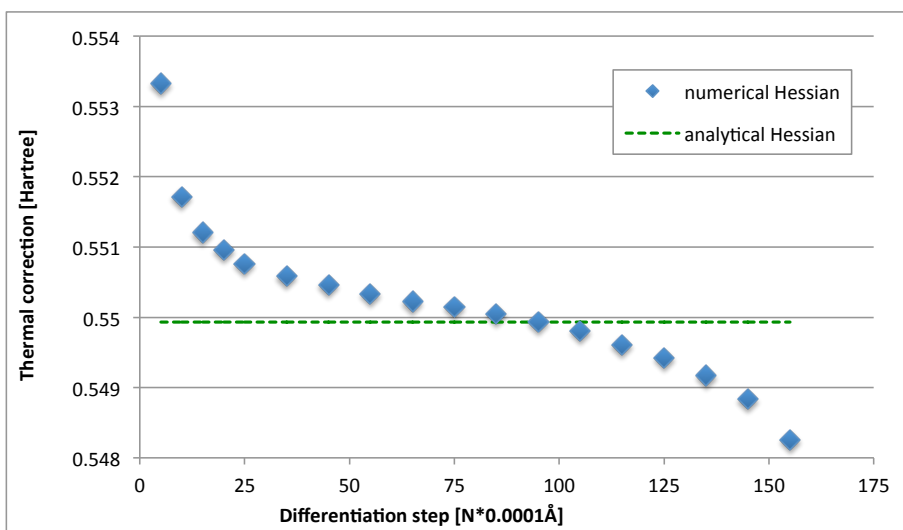


Figure S9: Thermochemical correction to the Gibbs free energy calculated for **2** with the analytical Hessian, and with numerical Hessian obtained varying the numerical differentiation step.

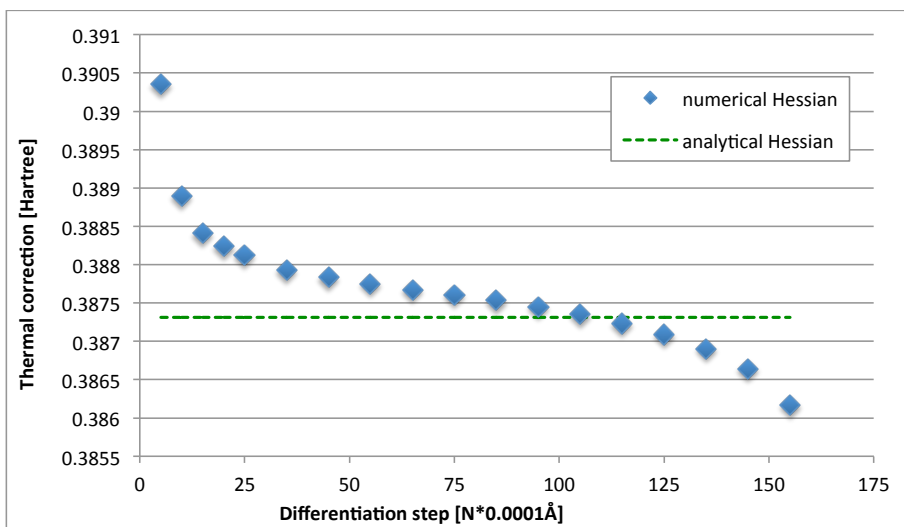


Figure S10: Thermochemical correction to the Gibbs free energy calculated for **OM5** with the analytical Hessian, and with numerical Hessian obtained varying the numerical differentiation step.

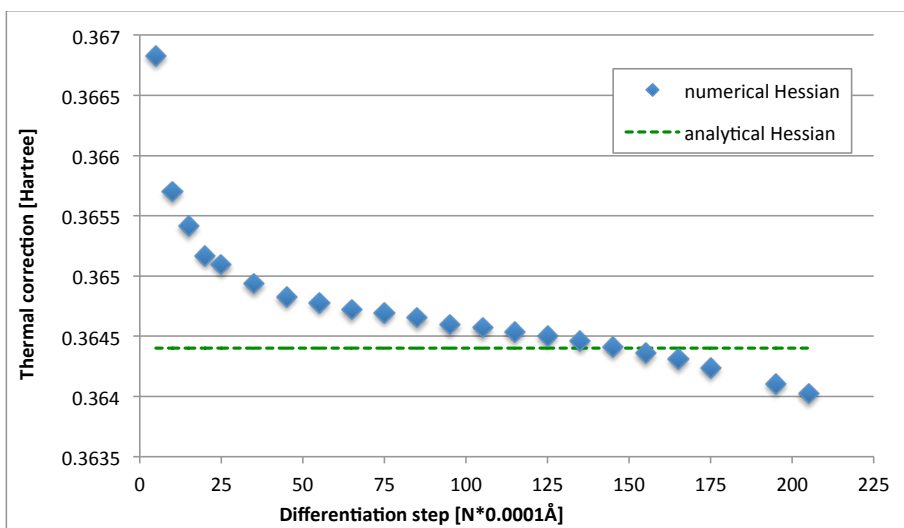


Figure S11: Thermochemical correction to the Gibbs free energy calculated for **R26A** with the analytical Hessian, and with numerical Hessian obtained varying the numerical differentiation step.

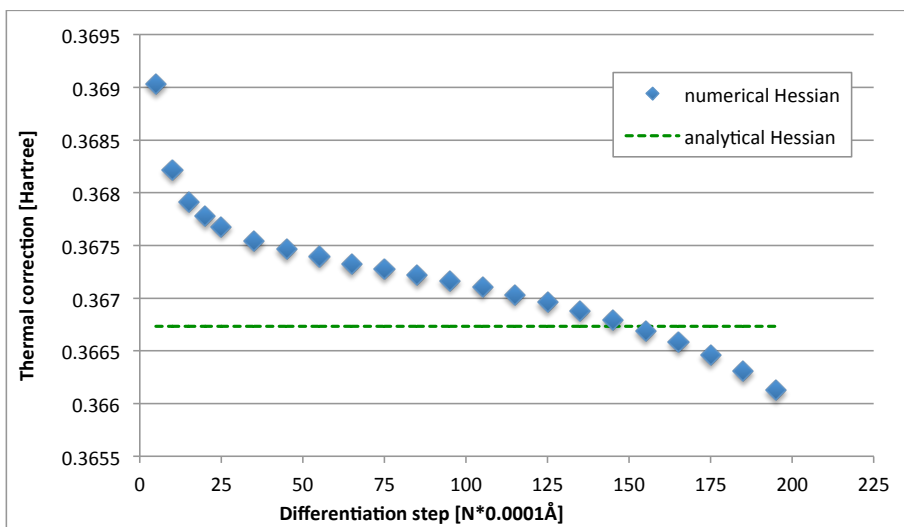


Figure S12: Thermochemical correction to the Gibbs free energy calculated for **R26** with the analytical Hessian, and with numerical Hessian obtained varying the numerical differentiation step.

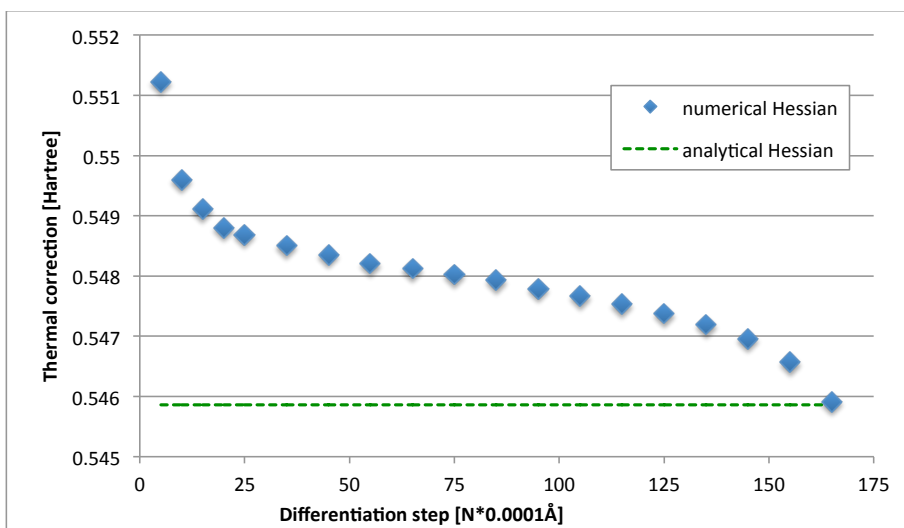


Figure S13: Thermochemical correction to the Gibbs free energy calculated for **OM7** with the analytical Hessian, and with numerical Hessian obtained varying the numerical differentiation step.

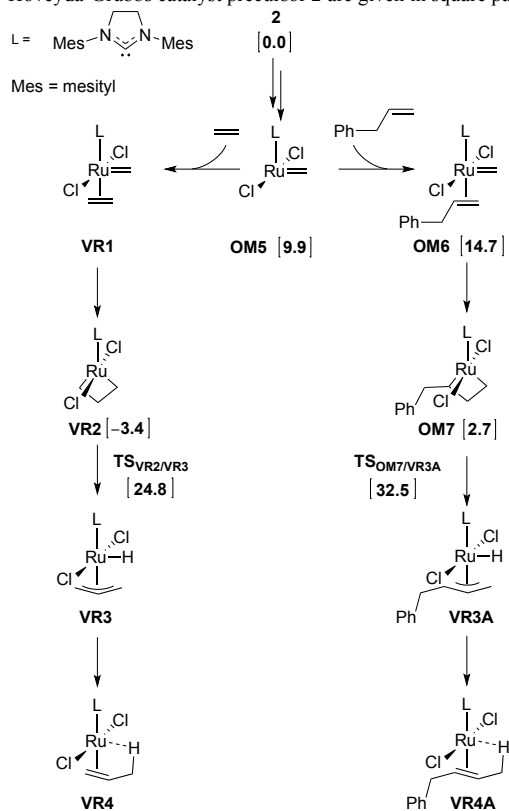
Assessment of known decomposition mechanisms

To assess whether already proposed decomposition mechanisms may compete with olefin metathesis, we first recalculated the highest-lying transition states of the well-known ruthenacyclobutane decomposition mechanisms, proposed by van Rensburg⁴⁴ and co-workers, using published DFT-optimized structures⁴⁵ as starting geometries for our own geometry optimizations (Scheme S2, left). This mechanism is operative in the presence of ethylene, an α -olefin metathesis product, and involves the unsubstituted ruthenacyclobutane intermediate **VR2**, the lowest-energy intermediate that is 3.4 kcal mol⁻¹ more stable than **2**. From **VR2** the next, crucial, step, the scission of the metallacyclobutane resulting in a hydride transfer to the ruthenium (*via* **TS_{VR2/VR3}**), requires 28.2 kcal mol⁻¹ relative to **VR2** (24.8 kcal mol⁻¹ relative to **2**), and the barrier for this decomposition mechanism is thus only 0.8 kcal mol⁻¹ higher than that of the self-metathesis of allylbenzene (main part of the paper, Scheme 1). In other words, the calculations tell that ethylene slows down metathesis by forming a stable ruthenacyclobutane, **VR2**, which acts like an energetic sink,⁴⁵ and from which catalyst decomposition is nearly as likely as continued metathesis.

The detrimental effects of ethylene are well known, and the removal of this volatile product, either by static vacuum or by argon flow, is often used to improve the efficiency of Ru-based olefin metathesis catalysts.⁴⁶ However, catalyst decomposition and isomerization are not eliminated even if ethylene is removed. In other words, although the van Rensburg mechanism explains the low stability of ruthenium alkylidene catalysts in the presence of ethylene, these catalysts face additional stability problems, a fact that strongly suggests that alkene substrates other than ethylene also may trigger catalyst decomposition.

As a first test of this hypothesis of substrate-triggered decomposition, allylbenzene was used as substrate in the van Rensburg decomposition mechanism (Scheme S2). In this case, the metallacyclobutane **OM7** (2.7 kcal mol⁻¹) is not a thermodynamic sink and the barrier to decomposition (**TS_{OM7/VR3A}**, 32.5 kcal mol⁻¹) is 8.5 kcal mol⁻¹ higher than the barrier to allylbenzene self-metathesis. But even though this means that the van Rensburg mechanism predicts catalyst decomposition to be much less likely in the absence of ethylene, the difference between the barriers to metathesis and decomposition (8.5 kcal mol⁻¹) is not far from the target range (5-7 kcal mol⁻¹) stated above among the requirements to candidate decomposition routes. The latter observation is here taken as a first indication that our hypothesis of 1-alkene-triggered decomposition could be correct, and that we should continue to look for substrate-induced decomposition reactions with even lower barriers.

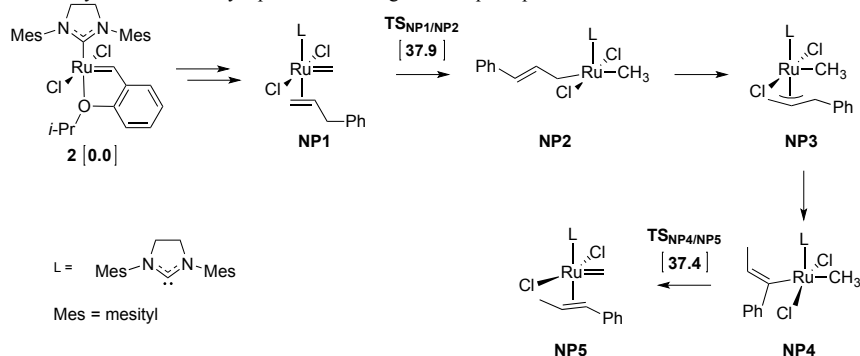
Scheme S2: Ruthenacyclobutane decomposition mechanism of van Rensburg. The Gibbs free energies relative to the Hoveyda-Grubbs catalyst precursor **2** are given in square parentheses.



The related η^3 -allyl alkyl isomerization mechanism of Nolan and Prunet⁴⁷ may also, if the cycle is not completed, act as a alkylidene-loss decomposition pathway. However, according to the current calculations, this decomposition route is disfavored compared to the above allyl-hydride mechanism, with an overall barrier of 37.9 kcal mol⁻¹ (Scheme S3).

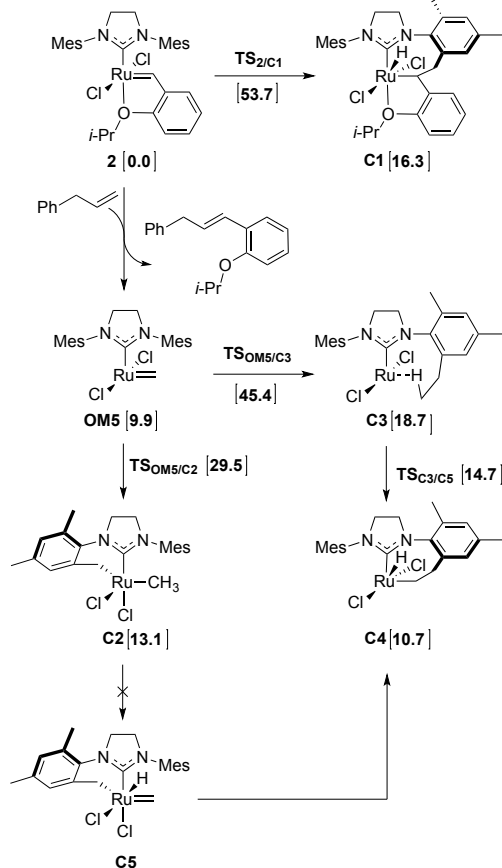
SI-II

Scheme S3: Olefin isomerization mechanism proposed by Nolan and Prunet.⁴⁷ The Gibbs free energies relative to the Hoveyda-Grubbs catalyst precursor **2** are given in square parentheses



Loss of alkylidene can also result from intramolecular activation of phenylic C–H bonds of N-phenyl substituted NHC ligands,⁴⁸ and has been studied computationally by Cavallo and co-workers.^{49,50} The rate-determining step is the addition of a hydrogen atom to the alkylidene carbon atom, resulting in the rupture of a C_{NHC}–H bond and the π -component of the alkylidene Ru=C bond and in the formation of a Ru–CNHC and a C–H bond. Extending these computational studies^{49,50} to addition of a mesityl-hydrogen to the methyldiene of **OM5**, formed after one olefin metathesis turnover, results in a relatively low barrier (29.5 kcal mol⁻¹, *via* **TS_{OM5/C2}**), see Scheme S4. However, starting from the methyl-complex **OM5** we could not obtain the hydride alkylidene oxidative addition product found in the early study of the phenyl-substituted NHC⁴⁹ with the current methyldiene/SIMes combination. The high reactivity of the methyldiene and the increased steric hindrance of the mesityl group compared to the phenyl group destabilize the hydride intermediate **C5**, thereby possibly explaining the higher stability observed for the SIMes-bearing catalyst.^{48,51} And with no stable hydride **C5**, the indirect route *via* hydrogen addition to the reactive methyldiene effectively is blocked.

Scheme S4: C–H activation pathways of the Hoveyda-Grubbs catalyst **2**. The Gibbs free energies relative to the Hoveyda-Grubbs catalyst precursor **2** are given in square parentheses.



Attempts at direct formation of a hydride *via* addition across the ruthenium-methylidene bond led instead to the agostic **C3**. The barrier to form **C3** ($45.4 \text{ kcal mol}^{-1}$, *via* $TS_{OM5/C3}$) is prohibitively high, excluding this as a viable route even though a ruthenium hydride complex, **C4**, can be obtained *via* oxidative addition in a second step. In contrast, addition to the Hoveyda-Grubbs catalyst precursor **2** led, in a single step, to a hydride complex (**C1**, see Scheme S4), although also this barrier, $53.7 \text{ kcal mol}^{-1}$ *via* $TS_{2/C1}$, is prohibitively high. Summarizing, the barriers of the C–H activation reactions of Scheme S4 are very high and these reactions can be excluded as candidate intramolecular decomposition routes to potentially isomerization-active ruthenium hydrides. However, the formation of the cyclometalated Ru-methyl complex **C2** from **OM5** is predicted to be relatively facile and it could in principle contribute to the deactivation of the ruthenium-methylidene intermediate,⁵² in particular at low substrate concentration and high temperature.

New decomposition pathways explored but not discussed in the main part of the paper

See Scheme S5 for catalyst decomposition pathways that were explored in the current work, but which were found to be less favorable.

Formation of methyl styrene from R9. The main product of allylbenzene isomerization, (*E*)- β -methylstyrene (**MS**), may be dissociated from **R10**. However, to form the methyl styrene π -complex **R10** (10.0 kcal mol⁻¹) one of the hydrogen atoms of the methyl group in ethyl styrene (**ES**) has to be shifted to the neighboring carbon atom at the same time as the bond between these two carbon atoms is broken upon formation of the ruthenium-methylidene bond. Thus, reaching the transition state for this reaction step, **TS_{R9/R10}**, requires a barrier of 60.1 kcal mol⁻¹. Starting instead from **R11**, the energy of the corresponding transition state is 43.4 kcal mol⁻¹, which is still prohibitively high, as is, with a barrier of 71.2 kcal mol⁻¹, a direct 1,2-hydrogen shift from the metallacyclopentane intermediate **R8** to the π -complex **R10**.

Decomposition routes from R12. Alternatively, the orientation of the substrate in the first π -complex, **R1**, may be reversed to give **R12** (10.0 kcal mol⁻¹), from which an isomerization pathway leading to **OM5** and liberation of **MS** is possible. However, as shown in Scheme S5 this pathway, starting with a barrier of 62.3 kcal mol⁻¹, is not competitive.

Ruthenium dialkyl species have been proposed to take part in isomerization pathways⁴⁵ and it is possible to generate the η^1 -allyl methyl complex **R20** (via **TS_{R13/R20}**) with a barrier of only 23.6 kcal mol⁻¹. In contrast, a much higher barrier (39.5 kcal mol⁻¹, via **TS_{R9/R19}**) is needed to reach the corresponding complex **R19**, which is connected to **R20** through a rearrangement of the allyl ligand. The energy difference between the transition states **TS_{R13/R20}** and **TS_{R9/R19}** can be explained by their geometries. In **TS_{R9/R19}**, steric interactions between the mesityl group of the SIMes ligand and the phenyl group of the substrate force the latter closer to the *trans* position with respect to the SIMes ligand, which is disfavored because of the strong *trans* influence of the carbene ligand.

Hydrides R6A and R6B as isomerization catalysts. Even if these ruthenium hydrides can be reached with a reasonably low overall barrier (29.5 kcal mol⁻¹ relative to **2**), they are unlikely to be active isomerization catalysts. To allow for coordination and isomerization of a new substrate, the dangling olefinic function must be released, and the dissociation from **R6A** to reach **R7** is endergonic (19.1 kcal mol⁻¹ relative to **2**). The subsequent binding of allylbenzene adds another 12.3 kcal mol⁻¹, reaching well above 30 kcal mol⁻¹ even before starting isomerization of the substrate.

Pathways to methylidene loss without ring expansion. An analogue of **R9** coordinated by 1-phenyl-2-butene (**VR4A**) may be formed directly, without having to go through ring expansion. However, the direct route is associated with a barrier (34.6 kcal mol⁻¹, via **TS_{OM7/VR4A}**; see Figure S16 for the optimized geometry) more than 5 kcal mol⁻¹ higher than the rate-determining barrier to **R9** via **TS_{R4B/R5}**. The ring rupture transition states **TS_{OM7/VR4A}** and **TS_{R8/R9}** differ in that the metallacyclopentane ring is more flexible, largely allowing the cleavage of the second ruthenium-carbon bond to be postponed until formation of the carbon-carbon double bond has started to stabilize the system. Stabilization is also obtained by ruthenium-hydrogen interaction during the 1,3-shift. In comparison, less stabilization is obtained when the smaller ruthenacyclobutane breaks up, cleaving the ruthenium-carbon bonds simultaneously via a η^3 -allylic transition state. Related allylic intermediates and transition states for rupture of the ruthenacyclobutane are also found in the van Rensburg decomposition mechanism discussed above (Scheme S2).

Regeneration of methyldiene from R9. Several pathways that close a hypothetical catalytic cycle by breaking the terminal C-C bond of the coordinated olefin of **R9** to regenerate the 14-electron ruthenium methyldiene (**OM5**) and the isomerization product β -methylstyrene (**MS**) have been explored. However, they all involve barriers of at least 39.5 kcal mol⁻¹ relative to **2**.

Abstraction of benzylic hydrogen in R12. The direct abstraction of the benzylic hydrogen from π -complex **R12**, a step that would allow access to a ring-contraction mechanism (i.e., from **R14** to **R17**) similar to the reverse of the ruthenacyclobutane ring expansion described above, is blocked by an initial barrier of 62.3 kcal mol⁻¹.

Additional intermediates and transition states of the 1-alkene-triggered decomposition pathway

See Scheme S5 for intermediates and transition states that were not included in Scheme 2 of the main part of the paper.

The rate-determining step of the ring expansion. The 1,2-shift starts by a low-barrier conformational change of the metallacyclobutane **OM7** and leads to **R4B** (6.0 kcal mol⁻¹), from which an intermediate, **R5**, with an agostic bond between one of the benzylic hydrogens of the substrate and the ruthenium, can be formed *via* **TS_{R4B/R5}** (optimized geometry in Figure S18) with a barrier of 29.5 kcal mol⁻¹ relative to **2**.

Formation of the metallacyclopentane from R5. From **R5**, the agostic hydrogen atom may be transferred to ruthenium under scission of a ruthenium–carbon bond to form the hydride alkyl complex **R6A** (12.9 kcal mol⁻¹). This octahedral complex is distorted due to the strong *trans* influence of the hydride and the alkyl group, resulting in two isomers, **R6A** and **R6B**, depending on whether the hydride is oriented closer to one or the other chloride. The hydride of **R6A** first migrates, *via* **TS_{R6A/R6B}** (23.1 kcal mol⁻¹), to form isomer **R6B** (15.1 kcal mol⁻¹). Next, the hydride is transferred *via* **TS_{R6B/R8}**, with a relatively low barrier (17.4 kcal mol⁻¹ relative to **2**), to the next carbon atom of the substrate, completing the 1,2-shift and reaching **R8**.

Additional mechanistic details of the olefin isomerization cycles

See Scheme S6 for intermediates and transition states that were not included in Scheme 3 of the main part of the paper.

Formation of the most stable η^3 -allyl hydride **R24.** Allylbenzene binding to $^3\mathbf{R21}$ leads to $^3\mathbf{R22}$ (3.9 kcal mol⁻¹, Scheme S6), which may undergo facile spin crossover⁵³ to the singlet **R22**, at -8.4 kcal mol⁻¹, which is much more stable than **R9** due to the increased η^3 -character and stronger agostic bond to ruthenium. From **R22**, with its agostic C-H bond, hydride transfer to ruthenium to reach the η^3 -allyl complex **R23** is facile, with the transition state $\mathbf{TS}_{\mathbf{R22}/\mathbf{R23}}$ at -1.7 kcal mol⁻¹. The subsequent rotation of the substrate *via* $\mathbf{TS}_{\mathbf{R23}/\mathbf{R24}}$ is, consistent with earlier studies,⁴⁵ associated with a comparably high free energy (8.3 kcal mol⁻¹) and results in the η^3 -allyl hydride **R24**.

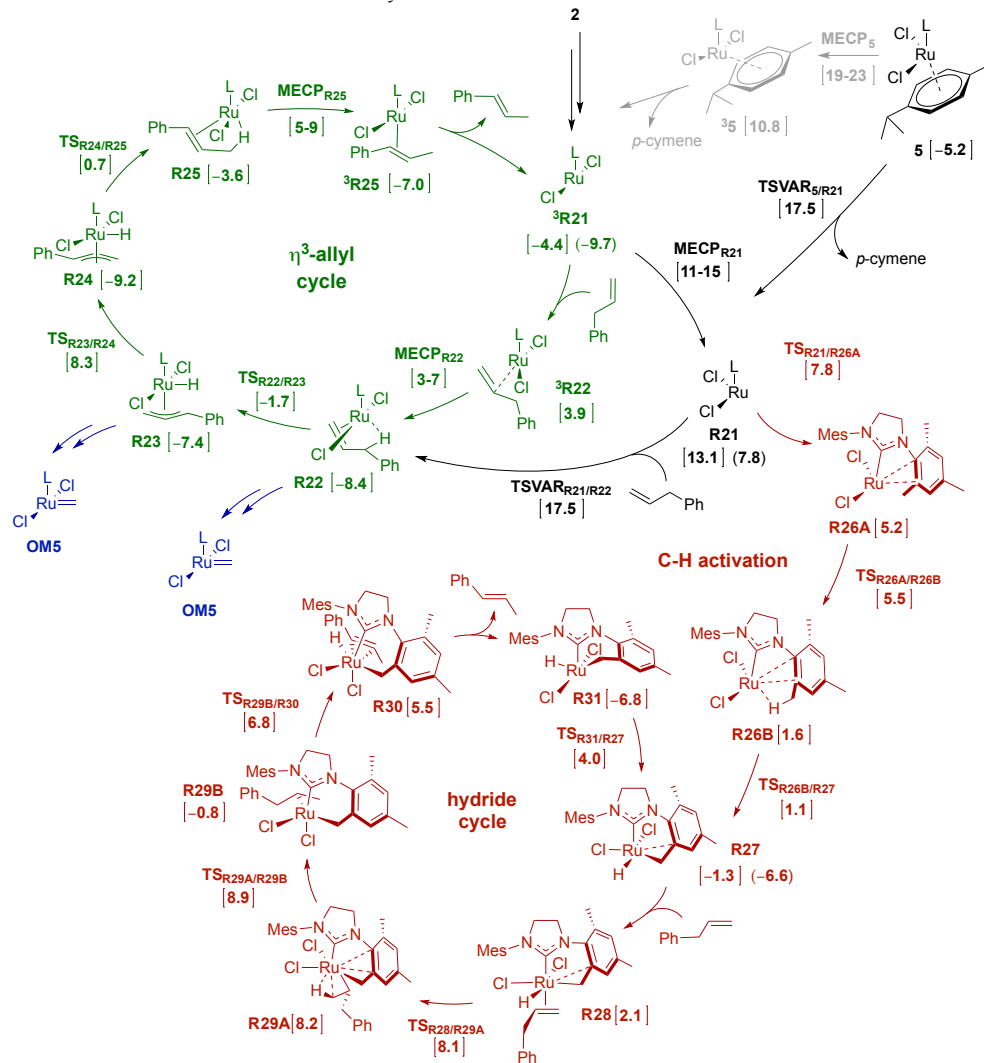
Formation and dissociation of internal alkene. From **R24**, a second hydride transfer generates the isomerized β -methylstyrene coordinated to ruthenium, **R25**. The associated transition state, $\mathbf{TS}_{\mathbf{R24}/\mathbf{R25}}$ (0.7 kcal mol⁻¹), is of higher free energy than $\mathbf{TS}_{\mathbf{R22}/\mathbf{R23}}$ (-1.7 kcal mol⁻¹) due to the added steric repulsion between the phenyl group of the substrate and the mesityl group of the carbene ligand (see Figure S33). The spin-triplet analogue of **R25** (i.e., $^3\mathbf{R25}$) is 3.4 kcal mol⁻¹ more stable than the singlet, and thus a second spin crossover brings the system back to the spin-triplet PES. However, the overall cost of this change of spin state (5-9 kcal mol⁻¹)⁵³ is likely to be high enough to contribute to determining the efficiency of the allylic isomerization cycle. Finally, $^3\mathbf{R25}$ liberates the β -methylstyrene isomerization product and regenerates $^3\mathbf{R21}$, at -9.7 kcal mol⁻¹ and thus 5.3 kcal mol⁻¹ lower than at the start of the cycle, reflecting the reaction exergonicity (see Scheme 3 of the main part of the paper).

C-H activation to form Ru hydride **R27.** In addition to mediating the above η^3 -allyl-type isomerization, the 12-electron spin-triplet $^3\mathbf{R21}$ may initiate intramolecular C-H activation and hydride-mechanism isomerization. However, this requires spin pairing, which costs 11-15 kcal mol⁻¹ relative to **2**. The resulting spin-singlet **R21** is electron deficient, very reactive, and is stabilized by almost 7 kcal mol⁻¹ by an η^2 -arene intramolecular bond with one of the NHC mesityl groups, in a barrierless⁵⁴ rearrangement to **R26A**. Next, a more stable intermediate **R26B** (1.6 kcal mol⁻¹) with an additional agostic bond involving the *o*-methyl substituent of the chelating NHC mesityl is obtained. In terms of free energy, the activation of the agostic C-H bond to form the ruthenium hydride **R27** is barrierless.⁵⁴

The hydride isomerization cycle starting from **R27.** Coordination of allylbenzene to **R27** is slightly endergonic and results in π -complex **R28** (2.1 kcal mol⁻¹), from which the substrate inserts into the ruthenium hydride bond and maintains an agostic interaction to this hydrogen in the resulting trigonal bipyramidal, σ -alkyl intermediate **R29A**. This intermediate is relatively high in energy (8.2 kcal mol⁻¹) because of the wide alkyl-Ru-NHC valence angle (137°), resulting in strong *trans* influence from the NHC. The complex reduces the *trans* influence by positioning a chloride *trans* to the NHC and the alkyl perpendicular to the NHC, in a rearrangement requiring less than 1 kcal mol⁻¹ of activation relative to **R29A** and which stabilizes the trigonal bipyramidal complex by 9.0 kcal mol⁻¹. From this more stable complex, a β -hydrogen may be eliminated, with a barrier (*via* $\mathbf{TS}_{\mathbf{R29B}/\mathbf{R30}}$) of 7.6 kcal mol⁻¹ relative to **R29B**, to give **R30**. From this π -complex hydride, the subsequent β -methylstyrene dissociation to reach

R31 is exergonic by more than 12 kcal mol⁻¹. This hydride, in turn, may isomerize to the 0.2 kcal mol⁻¹ less stable **R27** from which another isomerization cycle may begin.

Scheme S6: Olefin isomerization initiated by ³**R21**.^a



^aThe Gibbs free energies [kcal mol⁻¹] relative to the Hoveyda-Grubbs catalyst precursor **2** are given in square parentheses. This reaction scheme includes disfavored pathways, rendered in gray, and intermediates and transition states not included in Scheme 2 of the main part of the paper. See Scheme S7 for alkylidene formation pathways (rendered in blue) starting from the allylic cycle.

Additional mechanistic details of the alkylidene regeneration pathways

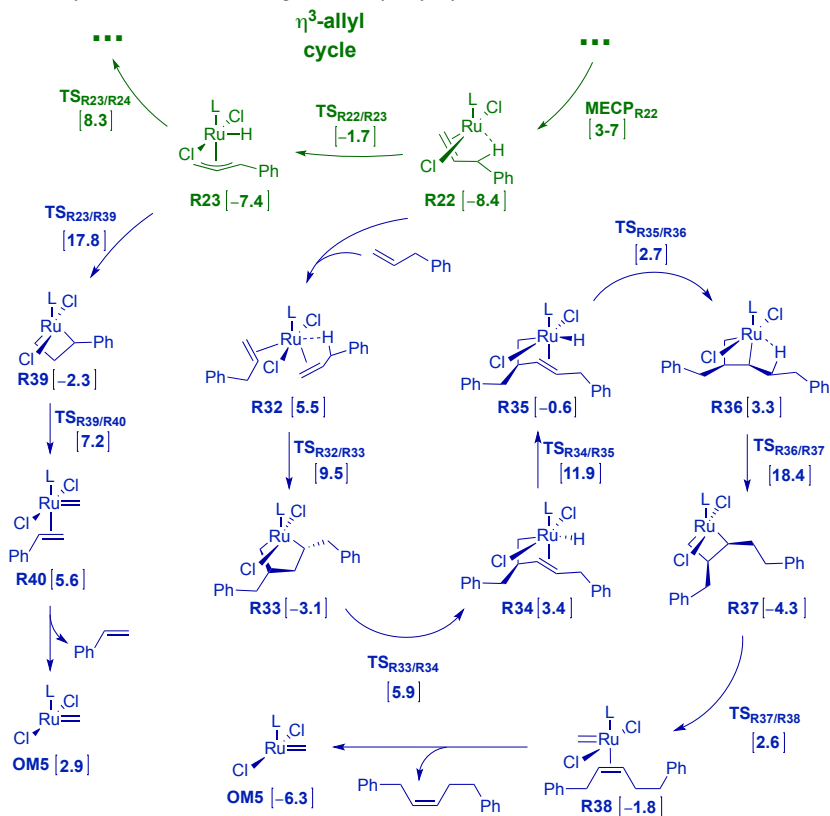
See **Scheme S7** for reactions that were not included in Scheme 3 of the main part of the paper.

Alkylidene formation mechanisms starting from the η^3 -allyl cycle. The reverse van Rensburg route proceeds *via* the allyl-hydride **R23** (-7.4 kcal mol $^{-1}$), which is obtained from **R22** by a hydride transfer to ruthenium from one of the benzylic hydrogens. **R23** evolves, *via* **TS_{R23/R39}** at 17.8 kcal mol $^{-1}$ above **2**, into the corresponding ruthenacyclobutane complex **R39** (-2.3 kcal mol $^{-1}$) *via* a second hydride transfer from ruthenium to the central carbon atom of the allylic ligand.

The ring-contraction path requires coordination of a second allylbenzene molecule to the ruthenium center, resulting in the bis-alkene complex **R32** (6.0 kcal mol $^{-1}$) from **R22**. This intermediate easily (the barrier is only 9.5 kcal mol $^{-1}$) undergoes an oxidative coupling to form the metallacyclopentane **R33** (-3.1 kcal mol $^{-1}$). Similar formation of a metallacyclopentane *via* oxidative coupling was also suggested as the key step for the substrate-induced formation of molybdenum⁵⁵ and tungsten-alkylidene⁵⁶ olefin metathesis catalysts. From **R33**, a metallacyclobutane intermediate **R37** (-4.3 kcal mol $^{-1}$) can be accessed *via* a stepwise ring contraction process, whose steps resemble those of the ring expansion discussed for 1-alkene-triggered catalyst decomposition (Scheme 2). The barrier of this pathway, *via* **TS_{R36/R37}**, is 18.4 kcal mol $^{-1}$ above **2**. Finally, the cycloreversion of the MCB intermediate **R37** leads to the Ru-methylidene complex **OM5** and 1,5-diphenyl-2-pentene.

Both the above alkylidene-formation mechanisms have to overcome transition states with a free energy ca. 18 kcal mol $^{-1}$ above that of **2**, which means that the barriers relative to **R22**, the most stable intermediate prior to the rate-determining transition states, are 26 - 27 kcal mol $^{-1}$. This is below the barrier to alkylidene loss *via* **TS_{R4B/R5}**, but much higher than the energetic cost of continuing turnovers in the allylic isomerization cycle. Energetic span models of the allylic cycle in which the two alkylidene-formation routes are treated as deactivation events, give turnover numbers (TONs) in the millions, regardless of substrate concentration (see details below). Concluding, the substrate-induced pathways from the allylic cycle probably contribute to formation of alkylidene, but they cannot be expected to be very efficient.

SI-II

Scheme S7: Alkylidene formation starting from the η^3 -allyl cycle.^a

^aThe Gibbs free energies [kcal mol⁻¹] relative to the Hoveyda-Grubbs catalyst precursor **2** are given in square parentheses. This reaction scheme includes intermediates and transition states not included in Scheme 2 of the main part of the paper.

Calculated absolute and relative energies

Table S7: Calculated absolute energies, Gibbs free energy corrections, and absolute and relative Gibbs free energy of stationary points and minimum energy crossing points (MECPs).

Molecule	$E_{\omega\text{B97XD}}^{\text{gas}}$ [a.u.] ^(a)	$\Delta G_{\omega\text{B97XD}}^{\text{T}=298.15\text{K}}$ [a.u.] ^(a)	$E_{\text{PBE-D3BJ}}^{\text{THF}}$ [a.u.] ^(b)	$G_{\text{PBE-D3BJ}}^{\text{THF}}$ [a.u.] ^(c)	$\Delta G_{\text{PBE-D3BJ}}^{\text{THF}}$ w.r.t. 2 [kcal mol ⁻¹]
2	-2403.735179	0.549931	-2402.651325	-2402.098375	0.0
AB = Allylbenzene	-348.861485	0.128707	-348.655280	-348.523554	-
TS_{OM3/OM4}	-2598.778797	0.648863	-2597.555964	-2596.904082	23.5
(E)-1,4-Diphenyl-2-butene	-619.159040	0.228487	-618.801471	-618.569965	-
OM5	-1979.586563	0.387312	-1978.744542	-1978.354211	9.9
Ethene	-78.560878	0.028980	-78.507562	-78.475563	-
VR2	-2058.195606	0.443349	-2057.297364	-2056.850996	-3.4
TS_{VR2/VR3}	-2058.143460	0.441044	-2057.250158	-2056.806095	24.8
OM6	-2328.480486	0.544815	-2327.418006	-2326.870172	14.7
OM7	-2328.499448	0.545861	-2327.438125	-2326.889246	2.7
TS_{NP1/NP2}	-2328.427952	0.541718	-2327.377911	-2326.833174	37.9
TS_{NP4/NP5}	-2328.431523	0.542649	-2327.379729	-2326.834061	37.4
TS_{OM7/VR3A}	-2328.448445	0.545619	-2327.390500	-2326.841862	32.5
TS_{2/C1}	-2403.630000	0.548191	-2402.564012	-2402.012802	53.7
C1	-2403.701795	0.554894	-2402.630270	-2402.072358	16.3
TS_{OM5/C2}	-1979.532019	0.388522	-1978.714525	-1978.322984	29.5
C2	-1979.572942	0.390564	-1978.742729	-1978.349147	13.1
TS_{OM5/C3}	-1979.513711	0.388260	-1978.688965	-1978.297686	45.4
C3	-1979.581357	0.392509	-1978.735698	-1978.340171	18.7
TS_{C3/C4}	-1979.574520	0.389817	-1978.739520	-1978.346684	14.7
C4	-1979.581429	0.391760	-1978.747738	-1978.352960	10.7
(E)-1-Isopropoxy-2-(3-phenylprop-1-en-1-yl)benzene	-772.974476	0.285170	-772.540084	-772.251895	-
R2	-2328.413183	0.539524	-2327.363839	-2326.821297	45.4
R3	-1867.596793	0.534686	-1866.712819	-1866.175115	43.4
HCl	-460.805295	-0.011109	-460.641263	-460.649353	-
TS_{OM6/OM7}	-2328.478350	0.545800	-2327.416216	-2326.867398	16.4
TS_{OM7/R4B}	-2328.495019	0.550982	-2327.435356	-2326.881355	7.7
TS_{OM7/RB}	-2328.437929	0.548463	-2327.381971	-2326.830490	39.6
TS_{OM7/VR4A}	-2328.444235	0.542549	-2327.384065	-2326.838497	34.6
R4B	-2328.495687	0.548759	-2327.435778	-2326.884001	6.0
TS_{R4B/R5}	-2328.458694	0.551165	-2327.400750	-2326.846566	29.5
R5	-2328.471590	0.549588	-2327.414292	-2326.861685	20.0
TS_{R5/R6A}	-2328.468504	0.547219	-2327.414429	-2326.864192	18.4
R6A	-2328.476340	0.547436	-2327.423446	-2326.872991	12.9
TS_{R6A/R6B}	-2328.458341	0.542595	-2327.402374	-2326.856760	23.1
R6B	-2328.473185	0.546312	-2327.418830	-2326.869500	15.1
R7	-2328.462403	0.541183	-2327.407362	-2326.863160	19.1

R7(AB)	-2677.340716	0.695342	-2676.065418	-2675.367057	31.4
TS_{R6B/R8}	-2328.456488	0.546278	-2327.415165	-2326.865868	17.4
R8	-2328.496713	0.553485	-2327.439111	-2326.882607	6.9
TS_{R8/R9}	-2328.456483	0.547487	-2327.405045	-2326.854539	24.5
TS_{R8/R10}	-2328.357623	0.542381	-2327.325598	-2326.780198	71.2
R9	-2328.497304	0.549108	-2327.424937	-2326.872810	13.0
MECP_{R9}	(d)	0.546432	-2327.420408	-2326.870957	14
³R9	-2328.522024	0.543757	-2327.440474	-2326.893698	-0.1
ES = (E)-beta-Ethylstyrene	-388.178710	0.154569	-387.939757	-387.782169	-
³R21	-1940.310425	0.357254	-1939.478726	-1939.118454	-4.4
TS_{R9/R10}	-2328.396470	0.543076	-2327.343828	-2326.797733	60.1
R10	-2328.485051	0.546033	-2327.426746	-2326.877694	10.0
R11	-2328.475632	0.543361	-2327.418599	-2326.872220	13.4
TS_{R11/(OM5+MS)}	-2328.410118	0.536083	-2327.363474	-2326.824372	43.4
MS = (E)-beta-Methylstyrene	-348.868970	0.128557	-348.663639	-348.532063	-
R12	-2328.479788	0.541740	-2327.422476	-2326.877717	10.0
TS_{R12/R13}	-2328.394290	0.542342	-2327.339589	-2326.794229	62.3
R13	-2328.484252	0.549521	-2327.411905	-2326.859365	21.5
TS_{R13/R14}	-2328.447236	0.545273	-2327.394417	-2326.846125	29.8
R14	-2328.488464	0.548138	-2327.429541	-2326.878384	9.5
TS_{R14/R15}	-2328.440212	0.545823	-2327.396278	-2326.847436	29.0
R15	-2328.469933	0.545593	-2327.414658	-2326.866047	17.3
TS_{R15/R16}	-2328.463241	0.546088	-2327.406356	-2326.857250	22.8
R16	-2328.478095	0.549606	-2327.421827	-2326.869203	15.3
R17	-2328.493801	0.548837	-2327.433362	-2326.881506	7.6
TS_{R17/R18}	-2328.477518	0.542640	-2327.420344	-2326.874686	11.9
R18	-2328.484250	0.540327	-2327.428453	-2326.885107	5.3
TS_{R9/R19}	-2328.444282	0.550754	-2327.384449	-2326.830676	39.5
R19	-2328.471086	0.549027	-2327.419609	-2326.867563	16.3
R20	-2328.481479	0.543639	-2327.429579	-2326.882921	6.7
TS_{R20/R13}	-2328.467690	0.550464	-2327.409460	-2326.855977	23.6
5	-2329.756339	0.574367	-2328.678474	-2328.101089	-5.2
MECP₅	(d)	0.568386	-2328.635322	-2328.063917	18
³5	-2329.740381	0.562405	-2328.641122	-2328.075698	10.8
p-Cymene	-389.407968	0.176107	-389.160585	-388.981459	-
R21	-1940.284273	0.363197	-1939.456764	-1939.090548	13.1
MECP_{R21}	(d)	0.360225	-1939.457960	-1939.094716	10
³R22	-2289.193045	0.512977	-2288.144676	-2287.628680	3.9
MECP_{R22}	(d)	0.516237	-2288.150733	-2287.631477	2
R22	-2289.205453	0.519496	-2288.170869	-2287.648354	-8.4
TS_{R22/R23}	-2289.182959	0.513939	-2288.154573	-2287.637615	-1.7
R23	-2289.196813	0.518004	-2288.167867	-2287.646844	-7.4
TS_{R23/R24}	-2289.165028	0.519117	-2288.143841	-2287.621705	8.3
R24	-2289.200875	0.520796	-2288.173407	-2287.649593	-9.2
TS_{R24/R25}	-2289.191744	0.519183	-2288.156057	-2287.633855	0.7
R25	-2289.202730	0.522786	-2288.166532	-2287.640727	-3.6

MECP_{R25}	(d)	0.521574	-2288.152501	-2287.627908	4
³R25	-2289.217478	0.520363	-2288.169584	-2287.646202	-7.0
TS_{R21/R26A}	-1940.280920	0.365338	-1939.467324	-1939.098967	7.8
R26A	-1940.281118	0.364400	-1939.470606	-1939.103187	5.2
TS_{R26A/R26B}	-1940.281091	0.365316	-1939.471013	-1939.102679	5.5
R26B	-1940.286513	0.366733	-1939.478632	-1939.108880	1.6
TS_{R26B/R27}	-1940.275368	0.364272	-1939.476929	-1939.109639	1.1
R27	-1940.278333	0.365621	-1939.482090	-1939.113451	-1.3
R28	-2289.163949	0.518162	-2288.152835	-2287.631654	2.1
TS_{R28/R29A}	-2289.155251	0.517137	-2288.142232	-2287.622076	8.1
R29A	-2289.162672	0.523933	-2288.148781	-2287.621830	8.2
TS_{R29A/R29B}	-2289.158356	0.524068	-2288.147880	-2287.620793	8.9
R29B	-2289.187056	0.525379	-2288.164567	-2287.636169	-0.8
TS_{R29B/R30}	-2289.155670	0.521410	-2288.148628	-2287.624199	6.8
R30	-2289.159796	0.522098	-2288.151259	-2287.626143	5.5
R31	-1940.279571	0.364718	-1939.481531	-1939.113794	-6.8
TS_{R31/R27}	-1940.264313	0.364510	-1939.464075	-1939.096547	4.0
R32	-2638.091894	0.682347	-2636.835153	-2636.149787	5.5
TS_{R32/R33}	-2638.081738	0.683000	-2636.829334	-2636.143315	9.5
R33	-2638.101869	0.680172	-2636.846708	-2636.163517	-3.1
TS_{R33/R34}	-2638.059201	0.674881	-2636.827096	-2636.149196	5.9
R34	-2638.076140	0.674091	-2636.830273	-2636.153164	3.4
TS_{R34/R35}	-2638.061952	0.672158	-2636.814743	-2636.139567	11.9
R35	-2638.080101	0.673186	-2636.835619	-2636.159415	-0.6
TS_{R35/R36}	-2638.072228	0.674418	-2636.831700	-2636.154263	2.7
R36	-2638.081791	0.678078	-2636.834395	-2636.153298	3.3
TS_{R36/R37}	-2638.065220	0.680134	-2636.812342	-2636.129189	18.4
R37	-2638.105292	0.680814	-2636.849255	-2636.165423	-4.3
TS_{R37/R38}	-2638.091682	0.678597	-2636.835937	-2636.154322	2.6
R38	-2638.093492	0.677277	-2636.841688	-2636.161393	-1.8
(E)-1,5-Diphenyl-2-pentene	-658.463094	0.256945	-658.074263	-657.814300	-
TS_{R23/R39}	-2289.150565	0.518370	-2288.127957	-2287.606568	17.8
R39	-2289.193215	0.522269	-2288.163884	-2287.638596	-2.3
TS_{R39/R40}	-2289.174227	0.520234	-2288.146675	-2287.623422	7.2
R40	-2289.176380	0.518773	-2288.147895	-2287.626103	5.6
Styrene	-309.557283	0.101291	-309.380524	-309.276214	-
TS_{S/OM1+OM5}	-4229.537241	0.917401	-4227.661531	-4226.741112	1.7
OM5	-2249.900366	0.494495	-2248.898513	-2248.400999	-

^aFrom geometry optimization. ^bSingle-point energy. ^cCalculated according to Equation 1, page 28. ^dCalculated according to Equation 3, page 28. See the Computational methods section for additional information.

Table S8: Absolute energies, Gibbs free energy corrections, and absolute and relative Gibbs free energy calculated using the M06 single-point energies for selected stationary points.

Molecule	$\Delta G_{\text{M06}}^{\text{T}=298.15\text{K}}_{\text{wB97XD}}$ [a.u.] ^(a)	$E_{\text{M06}}^{\text{THF}}$ [a.u.] ^(b)	$G_{\text{M06}}^{\text{THF}}$ [a.u.] ^(c)	$\Delta G_{\text{M06}}^{\text{THF}}$ w.r.t. 2 [kcal mol ⁻¹]
2	0.549931	-2403.596660	-2403.043710	0.0
AB = Allylbenzene	0.128707	-348.820790	-348.689064	-
TS_{OM3/OM4}	0.648863	-2598.586237	-2597.934355	19.5
(E)-1,4-Diphenyl-2-butene	0.228487	-619.085358	-618.853852	-
OM5	0.387312	-1979.480688	-1979.090357	12.9
Ethene	0.028980	-78.555498	-78.523499	-
OM6	0.544815	-2328.328499	-2327.780665	12.1
OM7	0.545861	-2328.345202	-2327.796322	2.3
TS_{NP1/NP2}	0.541718	-2328.279827	-2327.735090	40.7
TS_{NP4/NP5}	0.542649	-2328.283300	-2327.737632	39.1
TS_{OM7/VR3A}	0.545619	-2328.297527	-2327.748889	32.0
(E)-1-Isopropoxy-2-(3-phenylprop-1-en-1-yl)benzene	0.285170	-772.910110	-772.621921	-
TS_{OM6/OM7}	0.545800	-2328.324158	-2327.775339	15.4
TS_{OM7/R4B}	0.550982	-2328.343399	-2327.789398	6.6
R4B	0.548759	-2328.343914	-2327.792136	4.9
TS_{R4B/R5}	0.551165	-2328.307938	-2327.753754	29.0
R5	0.549588	-2328.319519	-2327.766912	20.7
TS_{R5/R6A}	0.547219	-2328.316849	-2327.766611	20.9
R6A	0.547436	-2328.324997	-2327.774542	15.9
R8	0.553485	-2328.342201	-2327.785697	8.9
TS_{R8/R9}	0.547487	-2328.305790	-2327.755284	28.0
ES = (E)-beta-Ethylstyrene	0.154569	-388.127420	-387.969832	-
³R21	0.357254	-1940.214661	-1939.854388	-15.2
MS = (E)-beta-Methylstyrene	0.128557	-348.830111	-348.698535	-
p-Cymene	0.176107	-389.356739	-389.177613	-
R21	0.363197	-1940.181703	-1939.815488	9.2
R22	0.519496	-2289.060201	-2288.537686	-11.6
TS_{R22/R23}	0.513939	-2289.037300	-2288.520342	-0.7
R23	0.518004	-2289.050041	-2288.529018	-6.2
TS_{R23/R24}	0.519117	-2289.028911	-2288.506775	7.8
R24	0.520796	-2289.056421	-2288.532606	-8.4
TS_{R24/R25}	0.519183	-2289.043612	-2288.521410	-1.4
R25	0.522786	-2289.056587	-2288.530782	-7.3
R26B	0.366733	-1940.197184	-1939.827432	1.7
TS_{R26B/R27}	0.364272	-1940.189060	-1939.821769	5.2
R27	0.365621	-1940.192009	-1939.823369	4.2
R28	0.518162	-2289.033445	-2288.512264	4.3
TS_{R28/R29A}	0.517137	-2289.020618	-2288.500462	11.7
R29A	0.523933	-2289.028959	-2288.502007	10.8
TS_{R29A/R29B}	0.524068	-2289.026662	-2288.499575	12.3

R29B	0.525379	-2289.045420	-2288.517022	1.3
TS_{R29B/R30}	0.521410	-2289.021192	-2288.496763	14.0
R31	0.364718	-1940.185810	-1939.818073	1.6
TS_{R31/R27}	0.364510	-1940.170306	-1939.802777	11.2
TS_{R23/R39}	0.518370	-2289.013363	-2288.491974	17.1

^aFrom geometry optimization. ^bSingle-point calculation. ^cCalculated according to Equation 2, page 28. See the Computational methods section for additional information.

```

Ru 0
ECP28MDF 4 28
G-Komponente
1
2 1.000000 0.000000
S-G
2
2 11.500590 209.786493
2 5.068575 30.214307
P-G
4
2 10.532634 48.751244
2 10.192010 97.496529
2 4.734892 7.860188
2 4.509065 15.329751
D-G
4
2 8.877977 26.967506
2 8.766122 40.432303
2 3.170196 3.340758
2 3.228851 5.256352
F-G
2
2 7.820249 -8.847525
2 7.839647 -11.835518

```

```

radii=UAHF
pcmdoc
Dis
Rep
Cav

```

Results from energetic span models

All energies and energetic spans (δE) are reported in kcal mol⁻¹. Molarity is used for concentrations, and TOFs are reported in s⁻¹. The temperature is 298.15 K, and the calculated ΔG for the isomerization reaction (AB to ME) is equal to -5.339271 kcal/mol.

η^3 -allyl pathway

Table S9: Energetic span model for the η^3 -allyl pathway with substrate concentration 7.5 M.

Step	G (int.)	G‡ (TS)	[Reac]	[Prod]	X _{TOF,int}	X _{TOF,TS}	X _{TOF,R}	X _{TOF,P}	TOF-determining states
³ R21 → ³ R22 ^(a)	0.000000	8.362788	7.5		0.00	0.00	0.00		
³ R22 → MECP _{R22}	8.362788	9.607525			0.00	0.00			
R22 → TS _{R22/R23}	-3.982624	2.756116			0.53	0.00			TDI
R23 → TS _{R23/R24}	-3.035233	12.739682			0.11	0.52			TDTS
R24 → TS _{R24/R25}	-4.759983	5.115371			0.36	0.00			
R25 → MECP _{R25}	0.803341	11.847314			0.00	0.48			TDTS
³ R25 → ³ R21 ^(a)	-2.632356	-2.632356		0.01	0.00	0.00		0.00	
δE	16.72								
TOF	1.50								

^(a)The free energy of the product of this elementary step is used as an approximation of that of the transition state.

Table S10: Energetic span model for the η^3 -allyl pathway with substrate concentration 0.02 M.

Step	G (int.)	G‡ (TS)	[Reac]	[Prod]	X _{TOF,int}	X _{TOF,TS}	X _{TOF,R}	X _{TOF,P}	TOF-determining states
³ R21 → ³ R22 ^(a)	0.000000	8.362788	0.02		0.03	0.00	0.03		
³ R22 → MECP _{R22}	8.362788	9.607525			0.00	0.00			
R22 → TS _{R22/R23}	-3.982624	2.756116			0.52	0.00			TDI

R23 → TS _{R23/R24}	-3.035233	12.739682			0.10	0.53			TDTS
R24 → TS _{R24/R25}	-4.759983	5.115371			0.35	0.00			
R25 → MECP _{R25}	0.803341	11.847314			0.00	0.47			TDTS
³ R25 → ³ R21 ^(a)	-2.632356	-2.632356		2.67E-5	0.00	0.00		0.00	
ΔE	16.72								
TOF	1.45								

^(a)The free energy of the product of this elementary step is used as an approximation of that of the transition state.

Table S11: Energetic span model for the η^3 -allyl pathway with substrate concentration 5 mM.

Step	G (int.)	G‡ (TS)	[Reac]	[Prod]	X _{TOF,int}	X _{TOF,TS}	X _{TOF,R}	X _{TOF,P}	TOF-determining states
³ R21 → ³ R22 ^(a)	0.000000	8.362788	0.005		0.11	0.00	0.11		
³ R22 → MECP _{R22}	8.362788	9.607525			0.00	0.00			
R22 → TS _{R22/R23}	-3.982624	2.756116			0.47	0.00			TDI
R23 → TS _{R23/R24}	-3.035233	12.739682			0.10	0.56			TDTS
R24 → TS _{R24/R25}	-4.759983	5.115371			0.32	0.00			
R25 → MECP _{R25}	0.803341	11.847314			0.00	0.44			
³ R25 → ³ R21 ^(a)	-2.632356	-2.632356		6.67E-6	0.00	0.00		0.00	
ΔE	16.72								
TOF	1.33								

^(a)The free energy of the product of this elementary step is used as an approximation of that of the transition state.

Table S12: Energetic span model for the η^3 -allyl pathway with substrate concentration 0.25 mM.

Step	G (int.)	G‡ (TS)	[Reac]	[Prod]	X _{TOF,int}	X _{TOF,TS}	X _{TOF,R}	X _{TOF,P}	TOF-determining states
³ R21 → ³ R22 ^(a)	0.000000	8.362788	2.50E-4		0.72	0.00	0.72		TDI
³ R22 → MECP _{R22}	8.362788	9.607525			0.00	0.00			
R22 → TS _{R22/R23}	-3.982624	2.756116			0.15	0.00			
R23 → TS _{R23/R24}	-3.035233	12.739682			0.03	0.73			TDTS
R24 → TS _{R24/R25}	-4.759983	5.115371			0.10	0.00			
R25 → MECP _{R25}	0.803341	11.847314			0.00	0.26			
³ R25 → ³ R21 ^(a)	-2.632356	-2.632356		3.34E-7	0.00	0.00		0.00	
ΔE	12.74								
TOF	0.42								

^(a)The free energy of the product of this elementary step is used as an approximation of that of the transition state.

η^3 -allyl pathway with deactivation *via* MECP_{R21}

Deactivation path departing from ³R21 *via* MECP_{R21}, activation barrier with respect to ³R21: 17.895123 kcal/mol.

Table S13: Energetic span model for the η^3 -allyl pathway with substrate concentration 7.5 M and deactivation *via* MECP_{R21}.

Step	G (int.)	G‡ (TS)	[Reac]	[Prod]	X _{TOF,int}	X _{TOF,TS}	X _{TOF,R}	X _{TOF,P}	TOF-determining states
³ R21 → ³ R22 ^(a)	0.000000	8.362788	7.5		0.00	0.00	0.00		
³ R22 → MECP _{R22}	8.362788	9.607525			0.00	0.00			
R22 → TS _{R22/R23}	-3.982624	2.756116			0.53	0.00			TDI
R23 → TS _{R23/R24}	-3.035233	12.739682			0.11	0.52			TDTS
R24 → TS _{R24/R25}	-4.759983	5.115371			0.36	0.00			
R25 → MECP _{R25}	0.803341	11.847314			0.00	0.48			TDTS
³ R25 → ³ R21 ^(a)	-2.632356	-2.632356		0.01	0.00	0.00		0.00	
ΔE	16.72								
TOF	1.50								
TON	3.7E+4								

^(a)The free energy of the product of this elementary step is used as an approximation of that of the transition state.

Table S14: Energetic span model for the η^3 -allyl pathway with substrate concentration 0.02 M and deactivation *via* MECP_{R21}.

Step	G (int.)	G‡ (TS)	[Reac]	[Prod]	X _{TOF,int}	X _{TOF,TS}	X _{TOF,R}	X _{TOF,P}	TOF-determining states
------	----------	---------	--------	--------	----------------------	---------------------	--------------------	--------------------	------------------------

³ R21 → ³ R22 ^(a)	0.000000	8.362788	0.02		0.03	0.00	0.03		
³ R22 → MECP _{R22}	8.362788	9.607525			0.00	0.00			
R22 → TS _{R22/R23}	-3.982624	2.756116			0.52	0.00			TDI
R23 → TS _{R23/R24}	-3.035233	12.739682			0.10	0.53			TDTS
R24 → TS _{R24/R25}	-4.759983	5.115371			0.35	0.00			
R25 → MECP _{R25}	0.803341	11.847314			0.00	0.47			TDTS
³ R25 → ³ R21 ^(a)	-2.632356	-2.632356		2.67E-5	0.00	0.00		0.00	
ΔE	16.72								
TOF	1.45								
TON	98								

^(a)The free energy of the product of this elementary step is used as an approximation of that of the transition state.

Table S15: Energetic span model for the η³-allyl pathway with substrate concentration 5 mM and deactivation *via* MECP_{R21}.

Step	G (int.)	G‡ (TS)	[Reac]	[Prod]	X _{TOF,int}	X _{TOF,TS}	X _{TOF,R}	X _{TOF,P}	TOF-determining states
³ R21 → ³ R22 ^(a)	0.000000	8.362788	0.005		0.11	0.00	0.11		
³ R22 → MECP _{R22}	8.362788	9.607525			0.00	0.00			
R22 → TS _{R22/R23}	-3.982624	2.756116			0.47	0.00			TDI
R23 → TS _{R23/R24}	-3.035233	12.739682			0.10	0.56			TDTS
R24 → TS _{R24/R25}	-4.759983	5.115371			0.32	0.00			
R25 → MECP _{R25}	0.803341	11.847314			0.00	0.44			
³ R25 → ³ R21 ^(a)	-2.632356	-2.632356		6.67E-6	0.00	0.00		0.00	
ΔE	16.72								
TOF	1.33								
TON	24								

^(a)The free energy of the product of this elementary step is used as an approximation of that of the transition state.

Table S16: Energetic span model for the η³-allyl pathway with substrate concentration 0.25 mM and deactivation *via* MECP_{R21}.

Step	G (int.)	G‡ (TS)	[Reac]	[Prod]	X _{TOF,int}	X _{TOF,TS}	X _{TOF,R}	X _{TOF,P}	TOF-determining states
³ R21 → ³ R22 ^(a)	0.000000	8.362788	2.50E-4		0.72	0.00	0.72		TDI
³ R22 → MECP _{R22}	8.362788	9.607525			0.00	0.00			
R22 → TS _{R22/R23}	-3.982624	2.756116			0.15	0.00			
R23 → TS _{R23/R24}	-3.035233	12.739682			0.03	0.73			TDTS
R24 → TS _{R24/R25}	-4.759983	5.115371			0.10	0.00			
R25 → MECP _{R25}	0.803341	11.847314			0.00	0.26			
³ R25 → ³ R21 ^(a)	-2.632356	-2.632356		3.34E-7	0.00	0.00		0.00	
ΔE	12.74								
TOF	0.42								
TON	1.22								

^(a)The free energy of the product of this elementary step is used as an approximation of that of the transition state.

η³-allyl pathway with deactivation *via* TS_{R36/R37}

Deactivation path departing from R22 *via* TS_{R36/R37}, activation barrier with respect to ³R21: 22.822972 kcal/mol. Substrate concentration applied to the deactivation path is equal to that reported in the tables for the first step.

Table S17: Energetic span model for the η³-allyl pathway with substrate concentration 7.5 M and deactivation *via* TS_{R36/R37}.

Step	G (int.)	G‡ (TS)	[Reac]	[Prod]	X _{TOF,int}	X _{TOF,TS}	X _{TOF,R}	X _{TOF,P}	TOF-determining states
³ R21 → ³ R22 ^(a)	0.000000	8.362788	7.5		0.00	0.00	0.00		
³ R22 → MECP _{R22}	8.362788	9.607525			0.00	0.00			
R22 → TS _{R22/R23}	-3.982624	2.756116			0.53	0.00			TDI
R23 → TS _{R23/R24}	-3.035233	12.739682			0.11	0.52			TDTS
R24 → TS _{R24/R25}	-4.759983	5.115371			0.36	0.00			
R25 → MECP _{R25}	0.803341	11.847314			0.00	0.48			TDTS
³ R25 → ³ R21 ^(a)	-2.632356	-2.632356		0.01	0.00	0.00		0.00	

δE	16.72
TOF	1.50
TON	2.7E+6

^(a)The free energy of the product of this elementary step is used as an approximation of that of the transition state.

Table S18: Energetic span model for the η^3 -allyl pathway with substrate concentration 0.02 M and deactivation via $TS_{R36/R37}$.

Step	G (int.)	G‡ (TS)	[Reac]	[Prod]	X _{TOF,int}	X _{TOF,TS}	X _{TOF,R}	X _{TOF,P}	TOF-determining states
³ R21 → ³ R22 ^(a)	0.000000	8.362788	0.02		0.03	0.00	0.03		
³ R22 → MECP _{R22}	8.362788	9.607525			0.00	0.00			
R22 → TS _{R22/R23}	-3.982624	2.756116			0.52	0.00			TDI
R23 → TS _{R23/R24}	-3.035233	12.739682			0.10	0.53			TDTS
R24 → TS _{R24/R25}	-4.759983	5.115371			0.35	0.00			
R25 → MECP _{R25}	0.803341	11.847314			0.00	0.47			TDTS
³ R25 → ³ R21 ^(a)	-2.632356	-2.632356		2.67E-5	0.00	0.00		0.00	
δE	16.72								
TOF	1.45								
TON	1.0E+9								

^(a)The free energy of the product of this elementary step is used as an approximation of that of the transition state.

Table S19: Energetic span model for the η^3 -allyl pathway with substrate concentration 5 mM and deactivation via $TS_{R36/R37}$.

Step	G (int.)	G‡ (TS)	[Reac]	[Prod]	X _{TOF,int}	X _{TOF,TS}	X _{TOF,R}	X _{TOF,P}	TOF-determining states
³ R21 → ³ R22 ^(a)	0.000000	8.362788	0.005		0.11	0.00	0.11		
³ R22 → MECP _{R22}	8.362788	9.607525			0.00	0.00			
R22 → TS _{R22/R23}	-3.982624	2.756116			0.47	0.00			TDI
R23 → TS _{R23/R24}	-3.035233	12.739682			0.10	0.56			TDTS
R24 → TS _{R24/R25}	-4.759983	5.115371			0.32	0.00			
R25 → MECP _{R25}	0.803341	11.847314			0.00	0.44			
³ R25 → ³ R21 ^(a)	-2.632356	-2.632356		6.67E-6	0.00	0.00		0.00	
δE	16.72								
TOF	1.33								
TON	4.0E+9								

^(a)The free energy of the product of this elementary step is used as an approximation of that of the transition state.

Table S20: Energetic span model for the η^3 -allyl pathway with substrate concentration 0.25 mM and deactivation via $TS_{R36/R37}$.

Step	G (int.)	G‡ (TS)	[Reac]	[Prod]	X _{TOF,int}	X _{TOF,TS}	X _{TOF,R}	X _{TOF,P}	TOF-determining states
³ R21 → ³ R22 ^(a)	0.000000	8.362788	2.50E-4		0.72	0.00	0.72		TDI
³ R22 → MECP _{R22}	8.362788	9.607525			0.00	0.00			
R22 → TS _{R22/R23}	-3.982624	2.756116			0.15	0.00			
R23 → TS _{R23/R24}	-3.035233	12.739682			0.03	0.73			TDTS
R24 → TS _{R24/R25}	-4.759983	5.115371			0.10	0.00			
R25 → MECP _{R25}	0.803341	11.847314			0.00	0.26			
³ R25 → ³ R21 ^(a)	-2.632356	-2.632356		3.34E-7	0.00	0.00		0.00	
δE	12.74								
TOF	0.42								
TON	8.1E+10								

^(a)The free energy of the product of this elementary step is used as an approximation of that of the transition state.

η^3 -allyl pathway with deactivation via $TS_{R23/R39}$

Deactivation path departing from R23 via $TS_{R23/R39}$, activation barrier with respect to ³R21: 22.237843 kcal/mol.

Table S21: Energetic span model for the η^3 -allyl pathway with substrate concentration 7.5 M and deactivation via $TS_{R23/R39}$.

Step	G (int.)	G‡ (TS)	[Reac]	[Prod]	X _{TOF,int}	X _{TOF,TS}	X _{TOF,R}	X _{TOF,P}	TOF-determining states
------	----------	---------	--------	--------	----------------------	---------------------	--------------------	--------------------	------------------------

${}^3\text{R21} \rightarrow {}^3\text{R22}^{(a)}$	0.000000	8.362788	7.5		0.00	0.00	0.00		ng states
${}^3\text{R22} \rightarrow \text{MECP}_{\text{R22}}$	8.362788	9.607525			0.00	0.00			
$\text{R22} \rightarrow \text{TS}_{\text{R22/R23}}$	-3.982624	2.756116			0.53	0.00			TDI
$\text{R23} \rightarrow \text{TS}_{\text{R23/R24}}$	-3.035233	12.739682			0.11	0.52			TDTS
$\text{R24} \rightarrow \text{TS}_{\text{R24/R25}}$	-4.759983	5.115371			0.36	0.00			
$\text{R25} \rightarrow \text{MECP}_{\text{R25}}$	0.803341	11.847314			0.00	0.48			TDTS
${}^3\text{R25} \rightarrow {}^3\text{R21}^{(a)}$	-2.632356	-2.632356		0.01	0.00	0.00		0.00	
δE	16.72								
TOF	1.50								
TON	7.5E+6								

^(a)The free energy of the product of this elementary step is used as an approximation of that of the transition state.

Table S22: Energetic span model for the η^3 -allyl pathway with substrate concentration 0.02 M and deactivation via $\text{TS}_{\text{R23/R39}}$.

Step	G (int.)	G‡ (TS)	[Reac]	[Prod]	$X_{\text{TOF,int}}$	$X_{\text{TOF,TS}}$	$X_{\text{TOF,R}}$	$X_{\text{TOF,P}}$	TOF-determining states
${}^3\text{R21} \rightarrow {}^3\text{R22}^{(a)}$	0.000000	8.362788	0.02		0.03	0.00	0.03		
${}^3\text{R22} \rightarrow \text{MECP}_{\text{R22}}$	8.362788	9.607525			0.00	0.00			
$\text{R22} \rightarrow \text{TS}_{\text{R22/R23}}$	-3.982624	2.756116			0.52	0.00			TDI
$\text{R23} \rightarrow \text{TS}_{\text{R23/R24}}$	-3.035233	12.739682			0.10	0.53			TDTS
$\text{R24} \rightarrow \text{TS}_{\text{R24/R25}}$	-4.759983	5.115371			0.35	0.00			
$\text{R25} \rightarrow \text{MECP}_{\text{R25}}$	0.803341	11.847314			0.00	0.47			TDTS
${}^3\text{R25} \rightarrow {}^3\text{R21}^{(a)}$	-2.632356	-2.632356		2.67E-5	0.00	0.00		0.00	
δE	16.72								
TOF	1.45								
TON	7.5E+6								

^(a)The free energy of the product of this elementary step is used as an approximation of that of the transition state.

Table S23: Energetic span model for the η^3 -allyl pathway with substrate concentration 5 mM and deactivation via $\text{TS}_{\text{R23/R39}}$.

Step	G (int.)	G‡ (TS)	[Reac]	[Prod]	$X_{\text{TOF,int}}$	$X_{\text{TOF,TS}}$	$X_{\text{TOF,R}}$	$X_{\text{TOF,P}}$	TOF-determining states
${}^3\text{R21} \rightarrow {}^3\text{R22}^{(a)}$	0.000000	8.362788	0.005		0.11	0.00	0.11		
${}^3\text{R22} \rightarrow \text{MECP}_{\text{R22}}$	8.362788	9.607525			0.00	0.00			
$\text{R22} \rightarrow \text{TS}_{\text{R22/R23}}$	-3.982624	2.756116			0.47	0.00			TDI
$\text{R23} \rightarrow \text{TS}_{\text{R23/R24}}$	-3.035233	12.739682			0.10	0.56			TDTS
$\text{R24} \rightarrow \text{TS}_{\text{R24/R25}}$	-4.759983	5.115371			0.32	0.00			
$\text{R25} \rightarrow \text{MECP}_{\text{R25}}$	0.803341	11.847314			0.00	0.44			
${}^3\text{R25} \rightarrow {}^3\text{R21}^{(a)}$	-2.632356	-2.632356		6.67E-6	0.00	0.00		0.00	
δE	16.72								
TOF	1.33								
TON	7.5E+6								

^(a)The free energy of the product of this elementary step is used as an approximation of that of the transition state.

Table S24: Energetic span model for the η^3 -allyl pathway with substrate concentration 0.25 M and deactivation via $\text{TS}_{\text{R23/R39}}$.

Step	G (int.)	G‡ (TS)	[Reac]	[Prod]	$X_{\text{TOF,int}}$	$X_{\text{TOF,TS}}$	$X_{\text{TOF,R}}$	$X_{\text{TOF,P}}$	TOF-determining states
${}^3\text{R21} \rightarrow {}^3\text{R22}^{(a)}$	0.000000	8.362788	2.50E-4		0.72	0.00	0.72		TDI
${}^3\text{R22} \rightarrow \text{MECP}_{\text{R22}}$	8.362788	9.607525			0.00	0.00			
$\text{R22} \rightarrow \text{TS}_{\text{R22/R23}}$	-3.982624	2.756116			0.15	0.00			
$\text{R23} \rightarrow \text{TS}_{\text{R23/R24}}$	-3.035233	12.739682			0.03	0.73			TDTS
$\text{R24} \rightarrow \text{TS}_{\text{R24/R25}}$	-4.759983	5.115371			0.10	0.00			
$\text{R25} \rightarrow \text{MECP}_{\text{R25}}$	0.803341	11.847314			0.00	0.26			
${}^3\text{R25} \rightarrow {}^3\text{R21}^{(a)}$	-2.632356	-2.632356		3.34E-7	0.00	0.00		0.00	
δE	12.74								
TOF	0.42								
TON	7.5E+6								

^(a)The free energy of the product of this elementary step is used as an approximation of that of the transition state.

Hydride pathway

Table S25: Energetic span model for the hydride pathway with substrate concentration 7.5 M.

Step	G (intermediate)	G‡ (TS)	[Reac]	[Prod]	X _{TOF,int}	X _{TOF,TS}	X _{TOF,R}	X _{TOF,P}	TOF-determining states
R27 → R28 ^(a)	0.000000	3.357300	7.5		0.05	0.00	0.13		
R28 → R29A ^(a)	3.357300	9.522203			0.00	0.03			
R29A → TS _{R29A/R29B}	9.522203	10.172489			0.00	0.10			
R29B → TS _{R29B/R30}	0.524281	8.035072			0.00	0.01			
R30 → R31 ^(a)	6.815185	6.815185		0.01	0.00	0.00		0.00	
R31 → R27 ^(a)	-5.554984	5.267529			0.94	0.87			TDI/TDTS
ΔE	10.82								
TOF	6.3E+4								

^(a)The free energy of the product of this elementary step is used as an approximation of that of the transition state.

Table S26: Energetic span model for the hydride pathway with substrate concentration 0.02 M.

Step	G (intermediate)	G‡ (TS)	[Reac]	[Prod]	X _{TOF,int}	X _{TOF,TS}	X _{TOF,R}	X _{TOF,P}	TOF-determining states
R27 → R28 ^(a)	0.000000	3.357300	0.02		0.40	0.00	0.98		
R28 → R29A ^(a)	3.357300	9.522203			0.00	0.24			
R29A → TS _{R29A/R29B}	9.522203	10.172489			0.00	0.72			TDTS
R29B → TS _{R29B/R30}	0.524281	8.035072			0.00	0.02			
R30 → R31 ^(a)	6.815185	6.815185		2.67E-5	0.00	0.00		0.00	
R31 → R27 ^(a)	-5.554984	5.267529			0.60	0.02			TDI
ΔE	10.39								
TOF	1.3E+3								

^(a)The free energy of the product of this elementary step is used as an approximation of that of the transition state.

Table S27: Energetic span model for the hydride pathway with substrate concentration 5 mM.

Step	G (intermediate)	G‡ (TS)	[Reac]	[Prod]	X _{TOF,int}	X _{TOF,TS}	X _{TOF,R}	X _{TOF,P}	TOF-determining states
R27 → R28 ^(a)	0.000000	3.357300	0.005		0.41	0.00	1.00		
R28 → R29A ^(a)	3.357300	9.522203			0.00	0.24			
R29A → TS _{R29A/R29B}	9.522203	10.172489			0.00	0.73			TDTS
R29B → TS _{R29B/R30}	0.524281	8.035072			0.00	0.02			
R30 → R31 ^(a)	6.815185	6.815185		6.67E-6	0.00	0.00		0.00	
R31 → R27 ^(a)	-5.554984	5.267529			0.59	0.00			TDI
ΔE	10.39								
TOF	325								

^(a)The free energy of the product of this elementary step is used as an approximation of that of the transition state.

Table S28: Energetic span model for the hydride pathway with substrate concentration 0.25 mM.

Step	G (intermediate)	G‡ (TS)	[Reac]	[Prod]	X _{TOF,int}	X _{TOF,TS}	X _{TOF,R}	X _{TOF,P}	TOF-determining states
R27 → R28 ^(a)	0.000000	3.357300	2.50E-4		0.41	0.00	1.00		
R28 → R29A ^(a)	3.357300	9.522203			0.00	0.24			
R29A → TS _{R29A/R29B}	9.522203	10.172489			0.00	0.73			TDTS
R29B → TS _{R29B/R30}	0.524281	8.035072			0.00	0.02			
R30 → R31 ^(a)	6.815185	6.815185		3.34E-7	0.00	0.00		0.00	
R31 → R27 ^(a)	-5.554984	5.267529			0.59	0.00			TDI
ΔE	10.39								
TOF	16								

^(a)The free energy of the product of this elementary step is used as an approximation of that of the transition state.

Hydride pathway with deactivation *via* MECPR₂₁

Deactivation path departing from R27 *via* MECPR₂₁, activation barrier with respect to R27: 14.755717 kcal/mol.

Table S29: Energetic span model for the hydride pathway with substrate concentration 7.5 M and deactivation *via* $MECP_{R21}$.

Step	G (intermediate)	G‡ (TS)	[Reac]	[Prod]	X _{TOF,int}	X _{TOF,TS}	X _{TOF,R}	X _{TOF,P}	TOF-determining states
R27 → R28 ^(a)	0.000000	3.357300	7.5		0.05	0.00	0.13		
R28 → R29A ^(a)	3.357300	9.522203			0.00	0.03			
R29A → TS _{R29A/R29B}	9.522203	10.172489			0.00	0.10			
R29B → TS _{R29B/R30}	0.524281	8.035072			0.00	0.01			
R30 → R31 ^(a)	6.815185	6.815185		0.01	0.00	0.00		0.00	
R31 → R27 ^(a)	-5.554984	5.267529			0.94	0.87			TDI/TDTS
δE	10.82								
TOF	6.3E+4								
TON	1.3E+4								

^(a)The free energy of the product of this elementary step is used as an approximation of that of the transition state.

Table S30: Energetic span model for the hydride pathway with substrate concentration 0.02 M and deactivation *via* $MECP_{R21}$.

Step	G (intermediate)	G‡ (TS)	[Reac]	[Prod]	X _{TOF,int}	X _{TOF,TS}	X _{TOF,R}	X _{TOF,P}	TOF-determining states
R27 → R28 ^(a)	0.000000	3.357300	0.02		0.40	0.00	0.98		
R28 → R29A ^(a)	3.357300	9.522203			0.00	0.24			
R29A → TS _{R29A/R29B}	9.522203	10.172489			0.00	0.72			TDTS
R29B → TS _{R29B/R30}	0.524281	8.035072			0.00	0.02			
R30 → R31 ^(a)	6.815185	6.815185		2.67E-5	0.00	0.00		0.00	
R31 → R27 ^(a)	-5.554984	5.267529			0.60	0.02			TDI
δE	10.39								
TOF	1.3E+3								
TON	34								

^(a)The free energy of the product of this elementary step is used as an approximation of that of the transition state.

Table S31: Energetic span model for the hydride pathway with substrate concentration 5 mM and deactivation *via* $MECP_{R21}$.

Step	G (intermediate)	G‡ (TS)	[Reac]	[Prod]	X _{TOF,int}	X _{TOF,TS}	X _{TOF,R}	X _{TOF,P}	TOF-determining states
R27 → R28 ^(a)	0.000000	3.357300	0.005		0.41	0.00	1.00		
R28 → R29A ^(a)	3.357300	9.522203			0.00	0.24			
R29A → TS _{R29A/R29B}	9.522203	10.172489			0.00	0.73			TDTS
R29B → TS _{R29B/R30}	0.524281	8.035072			0.00	0.02			
R30 → R31 ^(a)	6.815185	6.815185		6.67E-6	0.00	0.00		0.00	
R31 → R27 ^(a)	-5.554984	5.267529			0.59	0.00			TDI
δE	10.39								
TOF	325								
TON	8.39								

^(a)The free energy of the product of this elementary step is used as an approximation of that of the transition state.

Table S32: Energetic span model for the hydride pathway with substrate concentration 0.25 mM and deactivation *via* $MECP_{R21}$.

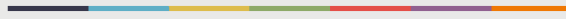
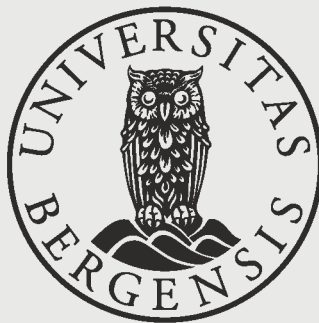
Step	G (intermediate)	G‡ (TS)	[Reac]	[Prod]	X _{TOF,int}	X _{TOF,TS}	X _{TOF,R}	X _{TOF,P}	TOF-determining states
R27 → R28 ^(a)	0.000000	3.357300	2.50E-4		0.41	0.00	1.00		
R28 → R29A ^(a)	3.357300	9.522203			0.00	0.24			
R29A → TS _{R29A/R29B}	9.522203	10.172489			0.00	0.73			TDTS
R29B → TS _{R29B/R30}	0.524281	8.035072			0.00	0.02			
R30 → R31 ^(a)	6.815185	6.815185		3.34E-7	0.00	0.00		0.00	
R31 → R27 ^(a)	-5.554984	5.267529			0.59	0.00			TDI
δE	10.39								
TOF	16								
TON	0.42								

^(a)The free energy of the product of this elementary step is used as an approximation of that of the transition state.

References

- Courchay, F. C.; Sworen, J. C.; Ghiviriga, I.; Abboud, K. A.; Wagener, K. B. *Organometallics* **2006**, *25*, 6074-86.
- Iglesias, M.; Beetstra, D. J.; Knight, J. C.; Ooi, L.-L.; Stasch, A.; Coles, S.; Male, L.; Hursthouse, M. B.; Cavell, K. J.; Dervisi, A.; Fallis, I. A. *Organometallics* **2008**, *27*, 3279-89.
- Fulmer, G. R.; Miller, A. J. M.; Sherden, N. H.; Gottlieb, H. E.; Nudelman, A.; Stoltz, B. M.; Bercaw, J. E.; Goldberg, K. I. *Organometallics* **2010**, *29*, 2176-79.
- Scanion, J. T.; Willis, D. E. *J. Chromatogr. Sci.* **1985**, *23*, 333-40.
- Dyadkin, V.; Pattison, P.; Dmitriev, V.; Chernyshov, D. *J. Synchrotron Radiat.* **2016**, *23*, 825-29.
- ChrysalisPro Software System*; Version 1.171.38.41; Rigaku Oxford Diffraction, 2015.
- Sheldrick, G. M. *Acta Crystallogr. Sect. A* **2015**, *71*, 3-8.
- Sheldrick, G. M. *Acta Crystallogr. Sect. C* **2015**, *71*, 3-8.
- Keitz, B. K.; Endo, K.; Herbert, M. B.; Grubbs, R. H. *J. Am. Chem. Soc.* **2011**, *133*, 9686-88. Krasovskaya, V.; Krasovskiy, A.; Bhattacharjya, A.; Lipshutz, B. H. *Chem. Commun.* **2011**, 47, 5717-19. Reichwein, J. F.; Pagenkopf, B. L. *J. Org. Chem.* **2003**, *68*, 1459-63. Ohmiya, H.; Makida, Y.; Tanaka, T.; Sawamura, M. *J. Am. Chem. Soc.* **2008**, *130*, 17276-77. Bandari, R.; Höche, T.; Prager, A.; Dimberger, K.; Buchmeiser, M. R. *Chem. Eur. J.* **2010**, *16*, 4650-58. Wang, Z.; Pitteloud, J.-P.; Montes, L.; Rapp, M.; Derane, D.; Wnuk, S. F. *Tetrahedron* **2008**, *64*, 5322-27. Shao, M.; Zheng, L.; Qiao, W.; Wang, J.; Wang, J. *Adv. Synth. Catal.* **2012**, *354*, 2743-50.
- Occhipinti, G.; Hansen, F. R.; Törnroos, K. W.; Jensen, V. R. *J. Am. Chem. Soc.* **2013**, *135*, 3331-34.
- Delaude, L.; Demonceau, A.; Noels, A. F. *Chem. Commun.* **2001**, 986-87.
- ¹H NMR studies of the decomposition of **5** (1 mM) in anhydrous benzene-*d*₆ with increasing temperatures (20-80 ° C) showed progressive replacement of the *p*-cymene ligand with C₆D₆. This replacement, which was completed at 70 ° C, was the dominant structural change observed in these experiments.
- Higman, C. S.; Lanterna, A. E.; Marin, M. L.; Scaiano, J. C.; Fogg, D. E. *ChemCatChem* **2016**, *8*, 2446-49.
- Lo, C.; Cariou, R.; Fischmeister, C.; Dixneuf, P. H. *Adv. Synth. Catal.* **2007**, *349*, 546-50.
- Occhipinti, G.; Björsvik, H.-R.; Jensen, V. R. *J. Am. Chem. Soc.* **2006**, *128*, 6952-64. Back, O.; Henry-Ellinger, M.; Martin, C. D.; Martin, D.; Bertrand, G. *Angew. Chem. Int. Ed.* **2013**, *52*, 2939-43.
- Frisch, M. J.; Trucks, G. W.; Schlegel, H. B.; Scuseria, G. E.; Robb, M. A.; Cheeseman, J. R.; Scalmani, G.; Barone, V.; Mennucci, B.; Petersson, G. A.; Nakatsuji, H.; Caricato, M.; Li, X.; Hratchian, H. P.; Izmaylov, A. F.; Bloino, J.; Zheng, G.; Sonnenberg, J. L.; Hada, M.; Ehara, M.; Toyota, K.; Fukuda, R.; Hasegawa, J.; Ishida, M.; Nakajima, T.; Honda, Y.; Kitao, O.; Nakai, H.; Vreven, T.; Montgomery Jr., J. A.; Peralta, J. E.; Ogliaro, F.; Bearpark, M. J.; Heyd, J.; Brothers, E. N.; Kudin, K. N.; Staroverov, V. N.; Kobayashi, R.; Normand, J.; Raghavachari, K.; Rendell, A. P.; Burant, J. C.; Iyengar, S. S.; Tomasi, J.; Cossi, M.; Rega, N.; Millam, N. J.; Klene, M.; Knox, J. E.; Cross, J. B.; Bakken, V.; Adamo, C.; Jaramillo, J.; Gomperts, R.; Stratmann, R. E.; Yazyev, O.; Austin, A. J.; Cammi, R.; Pomelli, C.; Ochterski, J. W.; Martin, R. L.; Morokuma, K.; Zakrzewski, V. G.; Voth, G. A.; Salvador, P.; Dannenberg, J. J.; Dapprich, S.; Daniels, A. D.; Farkas, Ö.; Foresman, J. B.; Ortiz, J. V.; Cioslowski, J.; Fox, D. J. *Gaussian 09*; Revision D.01; Gaussian, Inc.: Wallingford, CT, USA, 2009.
- Becke, A. D. *J. Chem. Phys.* **1997**, *107*, 8554-60. Wu, Q.; Yang, W. *J. Chem. Phys.* **2002**, *116*, 515-24. Chai, J.-D.; Head-Gordon, M. *Phys. Chem. Chem. Phys.* **2008**, *10*, 6615-20.
- Minenkov, Y.; Singstad, A.; Occhipinti, G.; Jensen, V. R. *Dalton Trans.* **2012**, *41*, 5526-41.
- Dunning, T. H. *J. Chem. Phys.* **1989**, *90*, 1007-23.
- Feller, D. *J. Comput. Chem.* **1996**, *17*, 1571-86. Schuchardt, K. L.; Didier, B. T.; Elsethagen, T.; Sun, L.; Gurumoorathi, V.; Chase, J.; Li, J.; Windus, T. L. *J. Chem. Inf. Model.* **2007**, *47*, 1045-52.
- Peterson, K. A.; Figgien, D.; Dolg, M.; Stoll, H. *J. Chem. Phys.* **2007**, *126*, 124101.
- Fukui, K. *Acc. Chem. Res.* **1981**, *14*, 363-68.
- Perdew, J.; Burke, K.; Ernzerhof, M. *Phys. Rev. Lett.* **1996**, *77*, 3865-68. Perdew, J.; Burke, K.; Ernzerhof, M. *Phys. Rev. Lett.* **1997**, *78*, 1396-96.
- Grimme, S.; Antony, J.; Ehrlich, S.; Krieg, H. *J. Chem. Phys.* **2010**, *132*, 154104. Grimme, S.; Ehrlich, S.; Goerigk, L. *J. Comp. Chem.* **2011**, *32*, 1456-65.
- Minenkov, Y.; Occhipinti, G.; Jensen, V. R. *Organometallics* **2013**, *32*, 2099-111.
- Zhao, Y.; Truhlar, D. G. *Theor. Chem. Acc.* **2008**, *120*, 215-41.
- Zhao, Y.; Truhlar, D. G. *Acc. Chem. Res.* **2008**, *41*, 157-67.
- Kendall, R. A.; Dunning, T. H.; Harrison, R. J. *J. Chem. Phys.* **1992**, *96*, 6796-806.
- Cossi, M.; Scalmani, G.; Rega, N.; Barone, V. *J. Chem. Phys.* **2002**, *117*, 43-54. Scalmani, G.; Frisch, M. J. *J. Chem. Phys.* **2010**, *132*, 114110. Tomasi, J.; Mennucci, B.; Cammi, R. *Chem. Rev.* **2005**, *105*, 2999-3094.
- Tomasi, J.; Persico, M. *Chem. Rev.* **1994**, *94*, 2027-94.
- Tomasi, J. *Theor. Chem. Acc.* **2004**, *112*, 184-203. Cramer, C. J.; Truhlar, D. G. *Acc. Chem. Res.* **2009**, *42*, 493-97. Klamt, A.; Mennucci, B.; Tomasi, J.; Barone, V.; Curutchet, C.; Orozco, M.; Luque, F. J. *Acc. Chem. Res.* **2009**, *42*, 489-92.
- Harvey, J. N.; Aschi, M.; Schwarz, H.; Koch, W. *Theor. Chem. Acc.* **1998**, *99*, 95-99.
- Koga, N.; Morokuma, K. *Chem. Phys. Lett.* **1985**, *119*, 371-74.
- Gannon, K. L.; Blitz, M. A.; Liang, C.-H.; Pilling, M. J.; Seakins, P. W.; Glowacki, D. R.; Harvey, J. N. *Faraday Discuss.* **2010**, *147*, 173-88.
- Harvey, J. N. *Phys. Chem. Chem. Phys.* **2007**, *9*, 331-43. Harvey, J. N. *Wiley Interdiscip. Rev. Comput. Mol. Sci.* **2014**, *4*, 1-14.
- Schiwek, C.; Meiners, J.; Forster, M.; Wurtele, C.; Diefenbach, M.; Holthausen, M. C.; Schneider, S. *Angew. Chem. Int. Ed.* **2015**, *54*, 15271-75.
- Núñez-Zarur, F.; Solans-Monfort, X.; Rodri'guez-Santiago, L.; Sodupe, M. *Organometallics* **2012**, *31*, 4203-15.
- McMullin, C. L.; Jover, J.; Harvey, J. N.; Fey, N. *Dalton Trans.* **2010**, *39*, 10833-36.
- Fernández-Ramos, A.; Miller, J. A.; Klippenstein, S. J.; Truhlar, D. G. *Chem. Rev.* **2006**, *106*, 4518-84.

- 40 Uhe, A.; Kozuch, S.; Shaik, S. *J. Comput. Chem.* **2011**, *32*, 978-85.
- 41 Kozuch, S.; Shaik, S. *Acc. Chem. Res.* **2011**, *44*, 101-10. Kozuch, S. *Wiley Interdiscip. Rev. Comput. Mol. Sci.* **2012**, *2*, 795-815.
- 42 Kozuch, S.; Shaik, S. *J. Am. Chem. Soc.* **2006**, *128*, 3355-65. Kozuch, S.; Shaik, S. *J. Phys. Chem. A* **2008**, *112*, 6032-41.
- 43 Martin, J. M. L.; Bauschlicher, C. W.; Ricca, A. *Comput. Phys. Commun.* **2001**, *133*, 189-201.
- 44 van Rensburg, W. J.; Steynberg, P. J.; Kirk, M. M.; Meyer, W. H.; Forman, G. S. *J. Organomet. Chem.* **2006**, *691*, 5312-25. van Rensburg, W. J.; Steynberg, P. J.; Meyer, W. H.; Kirk, M. M.; Forman, G. S. *J. Am. Chem. Soc.* **2004**, *126*, 14332-33.
- 45 Ashworth, I. W.; Hillier, I. H.; Nelson, D. J.; Percy, J. M.; Vincent, M. A. *Eur. J. Org. Chem.* **2012**, *2012*, 5673-77.
- 46 Kadyrov, R. *Chem. Eur. J.* **2013**, *19*, 1002-12.
- 47 Bourgeois, D.; Pancrazi, A.; Nolan, S. P.; Prunet, J. *J. Organomet. Chem.* **2002**, *643*, 247-52.
- 48 Hong, S. H.; Chlenov, A.; Day, M. W.; Grubbs, R. H. *Angew. Chem. Int. Ed.* **2007**, *46*, 5148-51.
- 49 Poater, A.; Cavallo, L. *J. Mol. Catal. A: Chem.* **2010**, *324*, 75-79.
- 50 Poater, A.; Bahri-Laleh, N.; Cavallo, L. *Chem. Commun.* **2011**, *47*, 6674-76.
- 51 Hong, S. H.; Wenzel, A. G.; Salguero, T. T.; Day, M. W.; Grubbs, R. H. *J. Am. Chem. Soc.* **2007**, *129*, 7961-68. Chung, C. K.; Grubbs, R. H. *Org. Lett.* **2008**, *10*, 2693-96. Leitao, E. M.; Dubberley, S. R.; Piers, W. E.; Wu, Q.; McDonald, R. *Chem. Eur. J.* **2008**, *14*, 11565-72.
- 52 The stability of **C2** is lower than that of **OM5** and the backward reaction (**C2** to **OM5**) is therefore easier, but the possibility that further transformations could lead to more stable decomposition products cannot be excluded.
- 53 Whereas the enthalpic cost of spin inversion is associated with reaching the seam of intersection between the two spin surfaces and is represented by the minimum energy crossing point (MECP), the probability that the system will cross from one PES to the other can be thought of as contributing to the activation entropy of the spin-forbidden reaction. Since the spin-crossing probability is lower than unity, the effective activation free energy resulting from adding such an entropic contribution will be higher than for an analogous spin-allowed reaction; see J. N. Harvey, *Phys. Chem. Chem. Phys.* **2007**, *9*, 331 and J. N. Harvey, *WIREs Comput. Mol. Sci.* **2014**, *4*, 1. In the present work, following the approach described in Schiwiek, C.; Meiners, J.; Forster, M.; Wurtele, C.; Diefenbach, M.; Holthausen, M. C.; Schneider, S. *Angew. Chem. Int. Ed.* **2015**, *54*, 15271, a spin-crossing-related addition of 1-5 kcal/mol has been used, while the regular thermochemical contributions to give free energies of the MECPs have been obtained as averages for the two spin states of the minimum close to the crossing point.
- 54 At the geometry optimization level, a transition state exists on the PES. With larger basis sets and thermo-chemical and solvent corrections, the final free energy surface is barrierless.
- 55 Handzlik, J.; Stosur, M.; Kochel, A.; Szymanska-Buzar, T. *Inorg. Chim. Acta* **2008**, *361*, 502-12.
- 56 Jayaraman, A.; Berner, G. M.; Mihichuk, L. M.; East, A. L. *J. Mol. Catal. A-Chem.* **2011**, *351*, 143-53.
- 57 Page, M.; Doubleday, C.; McIver, J. W. *J. Chem. Phys.* **1990**, *93*, 5634-42. Page, M.; McIver, J. W. *J. Chem. Phys.* **1988**, *88*, 922-35.
- 58 Hratchian, H. P.; Schlegel, H. B. *J. Chem. Phys.* **2004**, *120*, 9918-24. Hratchian, H. P.; Schlegel, H. B. *J. Chem. Theor. Comput.* **2005**, *1*, 61-69.



uib.no

ISBN: 9788230855867 (print)
9788230847909 (PDF)